EXPLORATION OF HEAD-DISK INTERFACE TECHNOLOGIES AT ULTRA SMALL HEAD-DISK SPACING

LIU JIN

NATIONAL UNIVERSITY OF SINGAPORE
2009

EXPLORATION OF HEAD-DISK INTERFACE TECHNOLOGIES AT ULTRA SMALL HEAD-DISK SPACING

LIU JIN

(M. Eng)

(Huazhong University of Science & Technology, P. R. China)

A THESIS SUBMITTED
FOR THE DEGREE OF DOCTOR OF PHILOSOPHY
DEPARTMENT OF ELECTRICAL & COMPUTER ENERGINEERING
NATIONAL UNIVERSITY OF SINGAPORE
2009

Abstract

Information storage is of crucial importance in the modern society. Up to now, magnetic data storage technology, represented by magnetic hard disk drive technology, has always been the dominant information storage technology for the society.

The area density or the total capacity, if the disk number and disk size are fixed, is the key performance parameter for the magnetic disk drives and magnetic data storage technology. Today, the best disk drives have reached an areal density of 100~200 Giga-bit per square inch (Gb/in^2). Researchers are developing technologies to push density to 1 Tera-bit per square inch (Tb/in^2).

High density recording requires high resolution data recording and retrieval. Such high resolution recording and retrieval are achieved by flying the read/write head as close to the disk surface as possible. An extremely low flying height of 3 nm is required for 1 Tb/in^2 areal density.

Starting from analyses of technological challenges towards such an extremely low flying height, this thesis reports author's exploration of new technologies towards 3nm flying height. The major focus areas include technologies to minimize the flying height modulation caused by disk waviness with nanometer amplitude, technologies to reduce flying height variation under various possible working altitudes, load/unload technology at extremely low flying height, nano-actuator technology for future flying height control and so on. The author is one of the pioneers in the society in exploring technology solutions towards 3 nm flying height.

Disk surface is of waviness of millimeter wavelength and nanometer amplitude. It is important to minimize the flying height modulation caused by such disk morphology or waviness in order to push technology towards 3 nm flying height.

Starting from investigating the mechanism of the flying height modulation caused by disk morphology, this thesis investigates the relationship between air-bearing design and flying height modulation. New design strategies are proposed which significantly reduce the flying height modulation. New air bearing design is, thus, proposed and demonstrated which shows the lowest flying height modulation among what were reported in public domain up to now.

Different altitudes have different air molecule densities and air bearing forces. As a result, flying height drops at a higher altitude. It is important to develop strategies and technologies to minimize the flying height change caused by working altitude, especially when the flying height is around 3 nm and the allowed maximum flying height change is merely 0.3~0.5 nm. Systematic investigations on the relationship between altitude and air-bearing force on different parts of air bearing surface, and possible air bearing designs are conducted in this thesis. Air-bearing design strategies and new air-bearing designs are proposed and developed in this thesis work. The technology developed by the author and the team makes the flying height change negligible at the targeted altitude variation range.

A multi-negative force zone technology is proposed to achieve smooth head-slider loading onto the disk surface. The simulation results show that sliders designed are of obvious advantage in achieving smooth head loading and stable flying status.

A mechanism to realize "proximity-on-demand" interface is proposed which utilizes a piezoelectric ceramic material (PZT) to adjust the curvature (crown and camber) of the air bearing surface, thus to adjust the flying height. Experimental results confirm the feasibility of such an approach.

Testing technology is of great importance for such ultra-low flying height systems. An optical constant averaging method is developed to improve the testing accuracy in flying height testing process.

The experimental study of the flying height modulation and long-term flyability are conducted with sliders of flying height around 3.5 nm. Results show that ultra-low flying height can be achieved with satisfying flyability and robustness.

Content

List of Figures

Chapter 1

Chapter 2

Chapter 3

Chapter 4

Chapter 5

Chapter 6

Chapter 7

List of Tables

Chapter 2

Chapter 3

Chapter 4

Chapter 5

Chapter 6

Chapter 7

List of Publications

1. Bo Liu, Jin Liu and Tow-Chong Chong, "Slider design for sub-3-nm flying height head-disk systems", Journal of Magnetism and Magnetic Materials, 287 (2005), pp: 339-345;
2. Bo Liu, Jin Liu, Hui Li et al., "Interface technology of 3 nm flying height and highly stable head-disk spacing for perpendicular magnetic recording", invited talk in PRMRC 2004;
3. Bo Liu, Mingsheng Zhang, Shengkai Yu, Jiang Zhou, Wei Hua, M. Yang, Hui Li, Jin Liu, "Panda III-2 femto slider with 2.5-3 nm flying height", presented in INSIC EHDR Annual Meeting 2004;
4. Bo Liu, Jin Liu, Jianfeng et.al., "Flying height modulation and femto slider design with 3.5 nm flying height", the 4th International Conference on Tribology of Information Storage Devices, Dec. 2003, Monterey, USA;
5. Jin Liu, Shengkai Yu, Bo Liu et al., "Slider design to improve dynamic response to disk waviness", Information Storage and Processing Systems, May. 2004, Santa Clara, USA;
6. Shengkai Yu, Bo Liu and Jin Liu, "Analysis and optimization of dynamic response of air bearing sliders to disk waviness", Tribology International 38 (2005), pp: 542-553;
7. Mingsheng Zhang, Shengkai Yu, Jin Liu and Bo Liu, "Flying height adjustment by slider's air bearing surface profile control", Journal of Applied Physics 97, 10P309 (2005).

Acknowledgements

I would like to extend my sincere gratitude to my advisor, Dr. LIU Bo for his continuous guidance and support throughout my Ph. D study period in Data Storage Institute (DSI), Singapore. I also gratefully acknowledge the kind support from my co-supervisor Prof. Chong Tow Chong.

Many thanks are given to Dr. YU Shengkai and Dr. ZHANG Minsheng for their helpful suggestions and guidance to my research work. I will always remember my friends and colleagues, Mr. HAN Yufei, Ms. JIANG Ying, Mr LI Hui, Ms. XIAO Peiying, Ms. ZHU Jin, Ms. ZHOU Yipin, Ms. YE Huanyi, Ms. KEK Ee Ling, Mr. TAN Boon Kee and so on, for their friendship and companionship during my staying in DSI.

Furthermore, I really appreciated DSI for providing me with their world class working environment and facilities. I would also like to specially thank National University of Singapore (NUS) and its department of electrical and computer engineering (ECE) for their research scholarship.

Finally, I am eternally grateful to my parents and my sister and brother for their unwavering support throughout these years and I will always remember all the people in DSI.

Chapter 1

Introduction

1.1 Introduction

The annual world production of unique information is between 1 and 2 exa-bytes (1 exa-byte = 1 million terabytes), as reported by the School of Information Management and Systems at the University of California in Berkeley [1]. This means that roughly 250 megabyte new and unique information will be generated every year per every man, woman, and child on earth. Regarding to the storage of such information, only 7 % of the information is stored in print (books, newspapers, photographs, etc). The rest 93 % is stored digitally with magnetic hard disks as the primary storage medium.

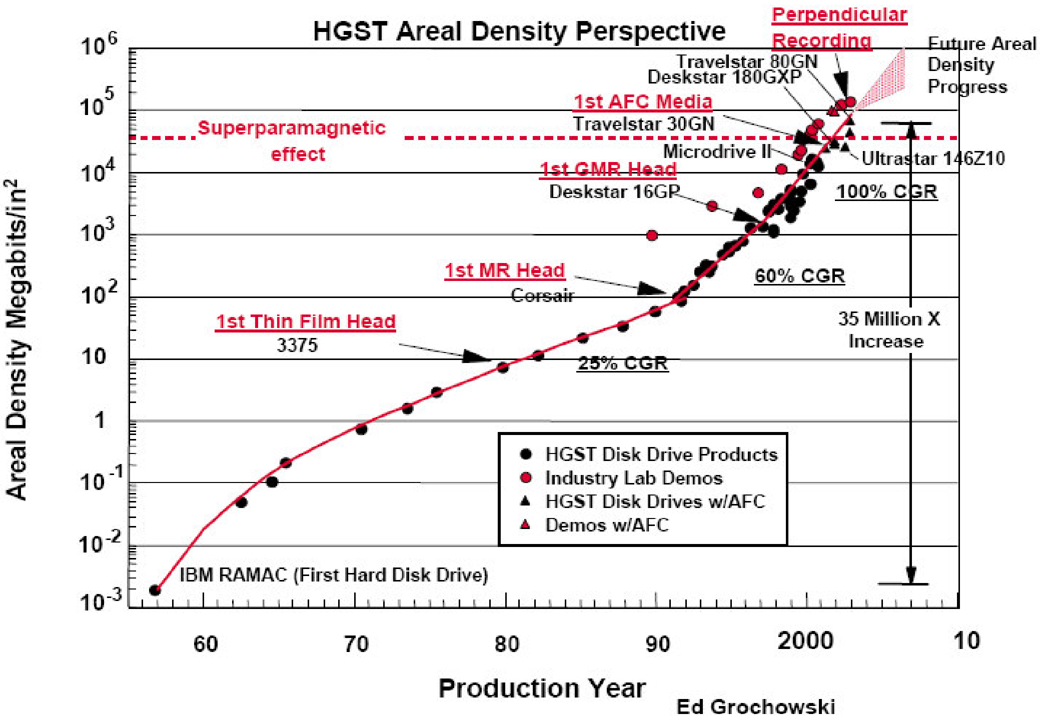

Figure 1.1 Areal density growth during the last 45 years (Chart courtesy of Ed Grochowski, Hitachi Global Storage Technology) [2]

The world’s first magnetic hard disk drive was introduced in September 1956 by the International Business Machines Corp. (IBM). The refrigerator-size product offered unprecedented performance by permitting random access to a total storage capacity of 4.4 Mbytes distributed over 50 double-sided, two-feet-diameter magnetic disks. Recording density of this first hard disk product is about 2,000 bits per square inch. The disk drive had a purchase price of $10,000,000 per giga-byte. Now, a modern 2.5" hard disk drive, e.g. used in notebook personal computers (PCs), is about the size of a deck of cards and has a capacity of 160 Giga-bytes. Its data storage density is 31 billion bits per square inch and the purchasing price of such hard disk drives is less than $1 per gigabyte [3].

Such a tremendous advancement comes from the continuous development of new technologies which increases the areal density of data storage over disk surface. In fact, the areal density of magnetic disk drives has increased by nearly eight orders of magnitude since 1956. Figure 1.1 shows the areal density of IBM products for the last 45 years [2].

New technologies and innovations are the major driving forces of the areal density increase. The magnetic disk drive enjoyed an annual areal density increase of about 25 % in its first 35 years. The invention of thin film head technology and magneto-resistive head technology led to an acceleration of this rate to about 60~100 % during 1990~2004 period. However, maintaining this incredible rate is not easy and today the technology is moving at a more sustainable pace of about 30~40 % per year.

As the technical capabilities of the hard disk drive and their range of applications expand, the impact of the hard disk drive has increased on the evolution of computing systems from mainframes to PCs to consumer electronics, such as digital entertainment systems and portable consumer devices.

1.2 Magnetic Hard Disk Drive

Figure 1.2 shows a photograph of a modern magnetic recording hard disk drive [4]. A typical hard disk drive consists of data storage media (disks to storage information), spindle motor to rotate the disks, read/write heads for data recording and retrieval, actuator to drive the read/write head to the targeted data track, and the corresponding electronics.

A hard disk drive has one or more disk platters to store data. Each platter usually has one read/write head on each of its two surfaces. The platters are made from glass or ceramic or aluminum alloy substrates. The substrates themselves are non-magnetic. With magnetic layer coated on its surface, the disks are able to record and keep information magnetically.

The disks are mounted on a spindle which is turned by the spindle motor. Most of hard disk drives nowadays spin at a speed between 5,400 and 15,000 RPM. Modern hard drives can transfer 80~100 megabytes of data per second.

The read/write heads conduct data recording and retrieval operations. The head is designed in such a way that it has high sensitivity to magnetic field. The head’s resolution is determined by the head design and the spacing between the read/write head and disk media.

The data is stored digitally as tiny magnetized regions, called bits, on the disk. A magnetic orientation in one direction on the disk could represent a "1", while an orientation in the opposite direction could represent a "0". Data is arranged in sectors along a number of concentric tracks. These tracks are arranged from the inner diameter of the disk to its outer edge. When reading head flies over the disk surface, it senses the magnetization direction and, therefore, retrieves the data recorded on disk surface by the writing head.

The read/write head is carried by a device called slider to float on a cushion of air, aiming to minimize the spacing between head and disk. The flying height of the read/write head is only a few nanometers in modern designs. As a writing head flies over the spinning disks, the head magnetizes the surface in a pattern which represents the data in a digital form.

Each head-slider is held by a triangular-shaped actuator arm (called suspension). The head arm is controlled by an actuator called voice coil motor which has to be of nanometer positioning resolution. The actuator moves the heads from the hub to the edge of the disk.

The hard disk's electronics control the movement of the actuator and the rotation of the disk, and perform reading and writing on demand from the disk controller via its interface to the computer.

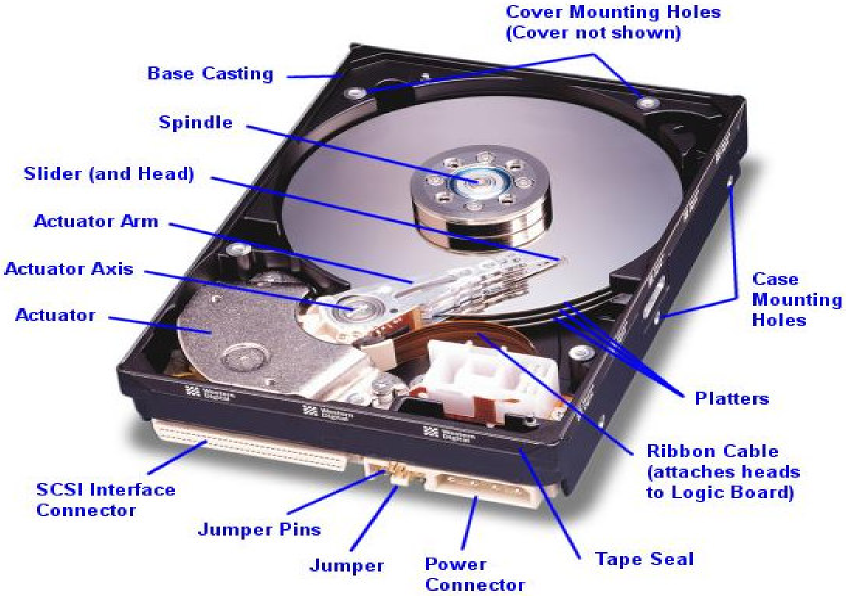

Figure 1.2 Components of a typical hard disk drive [4]

In a typical operation, the disk drive electronic circuits receive control commands from the host computer and the control signals are processed in the on-board digital signal processor (DSP). The actuator on receiving the control signal then moves and locates the read/write heads to the target locations on the disks for the read/write process to take place. During this process, the position error signals (PES) and the track numbers are read from the disk for feedback control.

1.3 Key Factors for Achieving High Areal Density

The areal density of magnetic hard disk drives is normally described by the amount of data bits stored on one unit of disk surface area. The industry standard areal density describes how many data bits can be recorded and retrieved on one square inch of disk surface.

Areal density includes two components: track density, which refers to how many tracks per inch, and bit density, which refers to how many bit per inch along one data track. Since 1997, track densities have being increased faster than linear densities, due to technology difficulties in pushing towards higher bit density.

The key factors for achieving high areal densities include the followings:

a) Nano-magnetics and advanced media technology

The recording media are made of distinct fine grains and each grain acts independently as a single magnetic domain. When an inductive write head passes over the medium, a group of particles are aligned to compose a single bit cell. Transitions between the bit cells tend to be imprecise as particles will not be perfectly aligned. The single bit cells decrease with increasing areal density, thus the magnetic particles that make up the cells must shrink accordingly, as well as the magnetic energy stored per particle. Continued decreasing this sort leads to particles too small to retain their magnetic orientation against thermal fluctuations, which is called superparamagnetism.

Increasing areal density requires to reduce the magnetic grain size, increase the thermal stability of the written bits and reduce the transition width of adjacent bit cells.

b) Nano-spintronics and advanced head and sensor technology

The size of the recording bit necessary for high bit and track densities is achieved by scaling down the dimensions of the pole tip structure to nanometer dimensions.

Increasing areal density requires read/write head designs that allow writing narrow tracks and reading information with adequate signal amplitude.

c) Nano-mechanics, nano-aerodynamics and head-disk interface technology

Achieving higher linear density and hence areal density require the read/write heads to fly closer to the disk surface. As the closer the head is to disk surface, the higher the resolution of data read/write is. Lowering the flying height allows the magnetic fields created during the writing process to be focused into a smaller area as areal density increases -- higher resolution of read/write head. More discussion can be seen in the next section.

d) Nano-actuator and high track density technology

The significant trend that track density is increasing dramatically in magnetic hard disk drives has led to a necessity for high bandwidth servo systems to enable faster system dynamics and to suppress more disturbances. One of the solutions to expand servo bandwidth is to use the dual-stage servo, in which a fine microactuator is added to the coarse actuator to accomplish the task in a high frequency range.

The work presented in this thesis covers nano-aerodynamics and nano-actuator technologies for achieving extremely high density magnetic data storage.

1.4 Head Disk Interface and Challenges to Achieve High Density

1) Head-Disk Systems

Figure 1.3 illustrates the head-disk systems. Disks are mounted on and spun by a spindle motor. The sliders, which carry the read/write transducers, are attached to suspensions. The read/write head is situated at the trailing edge of the slider. The most commonly used reading heads are called magetoresistive (MR) heads which detect the "1"s and "0"s by measuring the change in the resistance of the magnetic element as the magneto-resistance changes when the magnetic field from recorded data bit changes.

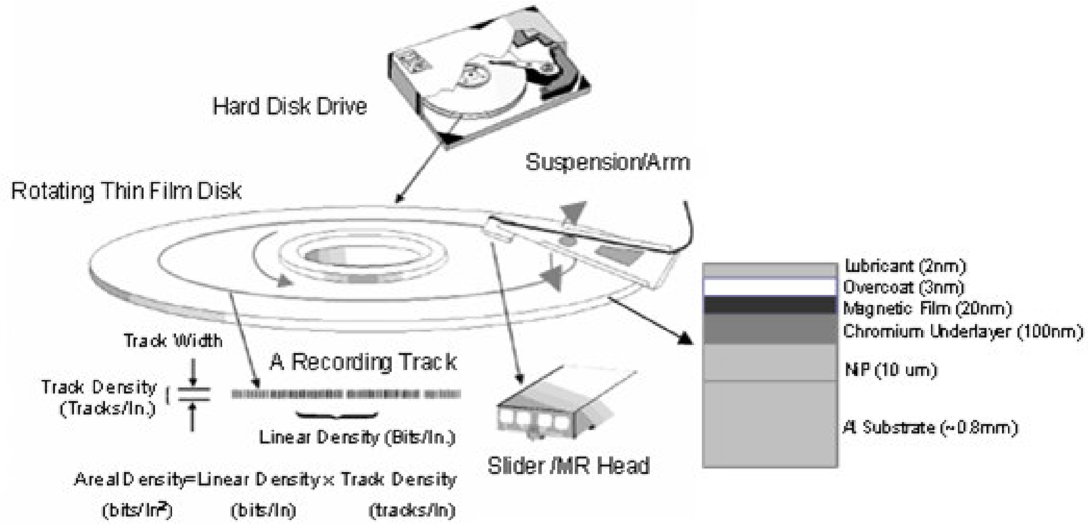

Figure 1.3 Schematic illustration of hard disk basic

Thin film disks are actually of complex multilayer structures, as shown in Figure 1.3. The aluminum substrate is plated with underlayer, such as an amorphous NiP undercoat and chromium underlayer, to help achieving the expected surface conditions and the magnetic grain structure of the magnetic recording layer. The magnetic layer (typically Co-based alloy) is the data storage layer. The magnetic layer is covered by a carbon overcoat layer and a lubricant layer, aiming at providing mechanical and chemical protection of the magnetic layer under various disk drive operation conditions. The thicknesses of the layers shown in Figure 1.3 are typical values of modern hard disk drives. Actually the thicknesses of the layers differ with different companies and different purposes. But the thicknesses of the overcoat layer and lubricant keep decreasing in order to reduce the magnetic spacing between the read/write element and disk.

High density recording requires small magnetic spacing between magnetic head and magnetic medium. The magnetic spacing is the distance between the magnetic recording head and the magnetic medium layer. The magnetic spacing includes flying height, recession of the head pole tip, the thickness of the diamond-like-carbon (DLC) film on the head surface and the thickness of the carbon overcoat and lubricant on the disk surface.

2) Slider and Its Flying Performance Parameters

The slider is the mechanical device which holds the read/write head. The modern slider is sliced from a wafer containing the head elements which are created via a semiconductor-like process. The slider's geometric dimension, the pattern design of the disk facing slider surface, called the air bearing surface or air-bearing surface (shown in Figure 1.4), the relative motion speed between slider and disk surfaces, and the gram load from suspension determine the flying height and dynamic flying performance of the slider.

Slider size and mass have evolved with time based on requirement to reduce the overall mass of the slider/suspension assembly, as illustrated in Figure 1.5 [5]. This reduction improves the dynamic response of the slider, such as shock resistance, capability in following up disk morphology and so on.

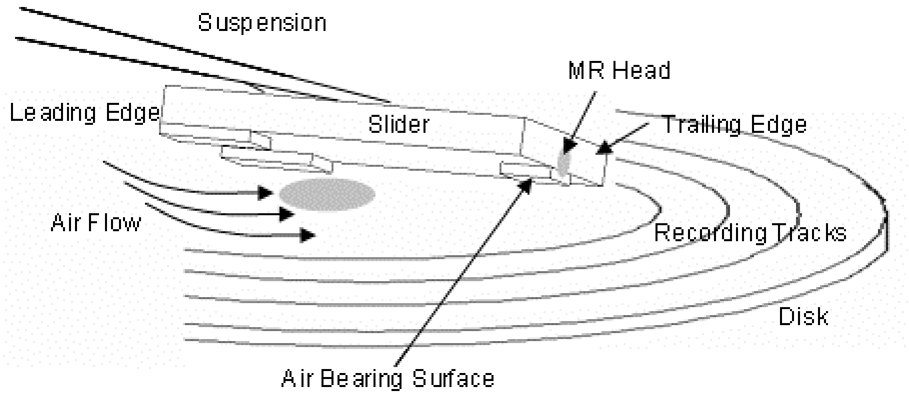

Figure 1.4 Schematic of head disk interface

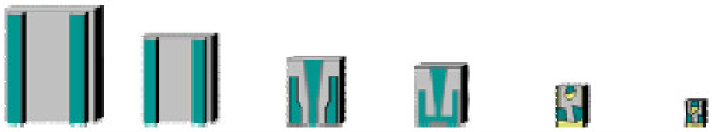

Slider Size	Mini 100%	Micro 70%	Positive Pressure Nano 62%	Negative Pressure Nano 50%	Pico 30%	Femto 20%
Intro Year	1980	1986	1991	1994	1997	2003
Dimensions, mm						
Length	4.00	2.80	2.50	2.00	1.25	0.85
Width	3.20	2.24	1.70	1.60	1.00	0.70
Height	0.86	0.60	0.43	0.43	0.30	0.23
Slider Mass, mg	55.0	16.2	7.8	5.9	1.6	0.6

Figure 1.5 Evaluation of slider size/air bearing surface (Chart courtesy of Hitachi Global Storage Technology) [5]

The slider is self-pressurized by the airflow of the rapidly spinning disk or the high speed relative motion between slider and disk. A very thin and highly compressed air bearing film is generated due to the high relative speed motion between the slider and the disk surface.

The slider has three degrees of freedom, as illustrated in Figure 1.6. It can move up and down and rotate around the point where the suspension is attached in the pitch and roll directions.

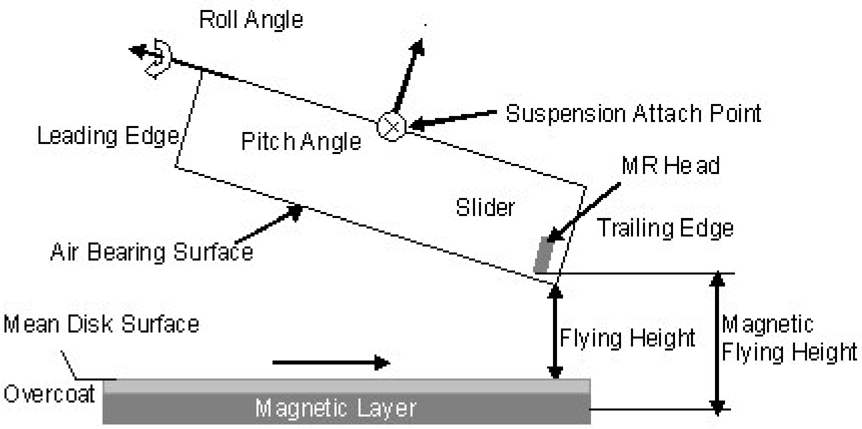

Figure 1.6 Schematic illustration of slider-disk interface and corresponding parameters

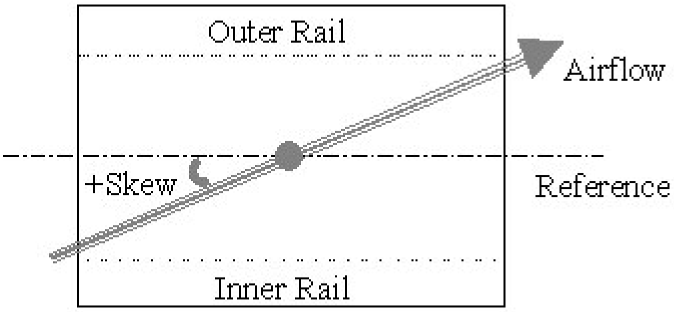

Figure 1.7 Air-flow direction, skew angle and slider's rail layout

The mechanical parameter of a flying slider includes flying height, pitch angle and roll angle. The pitch angle is the angular displacement about the slider's length. For a positive pitch, the slider-disk spacing at the leading edge of the slider is larger than that at the trailing edge of the slider. The roll angle of a slider is the angular displacement about the slider's width. For positive roll, the slider-disk spacing at the slider's inner edge (the edge closer to disk centre) is larger than that at the outer edge of the slider. Skew angle (illustrated in Figure 1.7) is the angle between the central line of the slider and the track on the disk. Positive skew refers to the case that air flows from the inner leading edge to the outer trailing edge.

The motion of the slider reaches an equilibrium when a balance is established among forces and moments generated by the air-bearing force and the force and moments exerted by a pre-load of the suspension. Other forces, such as the intermolecular force, become increasingly influential to the force/moment equilibrium if the spacing approaches a molecular distance.

3) High Density Recording and Its Requirement to Flying Height

The achievable minimum bit size is limited by the transition length of magnetization from one direction to the other, formed by writing operation of magnetic writing head. The transition length can be described as $\pi\alpha$. Here, α is the transition parameter which can be described as [6]:

$$\alpha = \frac{(1-S^{*})(T+FH+\delta/2)}{\pi Q} + \sqrt{\left[\frac{(1-S^{*})(T+FH+\delta/2)}{\pi Q}\right]^{2} + \frac{M_{r}\delta}{\pi H_{c}}\frac{(T+FH+\delta/2)}{Q}} \quad (1.1)$$

where S^{*} is the coercive squareness, H_{c} the medium coercivity, M_{r} the remanent magnetization of the magnetic medium, T the total thickness of both the overcoat (both slider and disk surfaces) and the lubricant thickness, FH the flying height of the magnetic head, δ the thickness of the magnetic layer. As can be seen from Eq. (1.1), high linear density requires small thickness T of the magnetic data recording layer and low flying height.

Meanwhile, in the reading process, the Fourier component of the readback voltage of an arctangent magnetization is given by:

$$V_{x}(k) = 2\mu_{0}vWM_{r}\delta\frac{H_{g}g}{i}e^{-k(T+FH+a)}\frac{1-e^{-k\delta}}{k\delta}\frac{\sin(kg/2)}{kg/2} \quad (1.2)$$

where μ_{0} is the permeability of free space, v the media velocity, W the track width, H_{g} is the head gap field , g the gap width, $i^{2}=-1$, k the wave number. Eq. (1.2) indicates that the readback signal at each of its harmonic decays exponentially. Here, the amplitude loss cased by factor $y = T + FH$ (the magnetic spacing) is called the magnetic spacing loss. In order to increase the readback signal, it is needed to reduce the spacing loss, which also means to reduce the flying height, the total thickness of the overcoat and lubricant.

It can be concluded that both the writing and reading processes require smaller magnetic spacing in order to achieve high linear density.

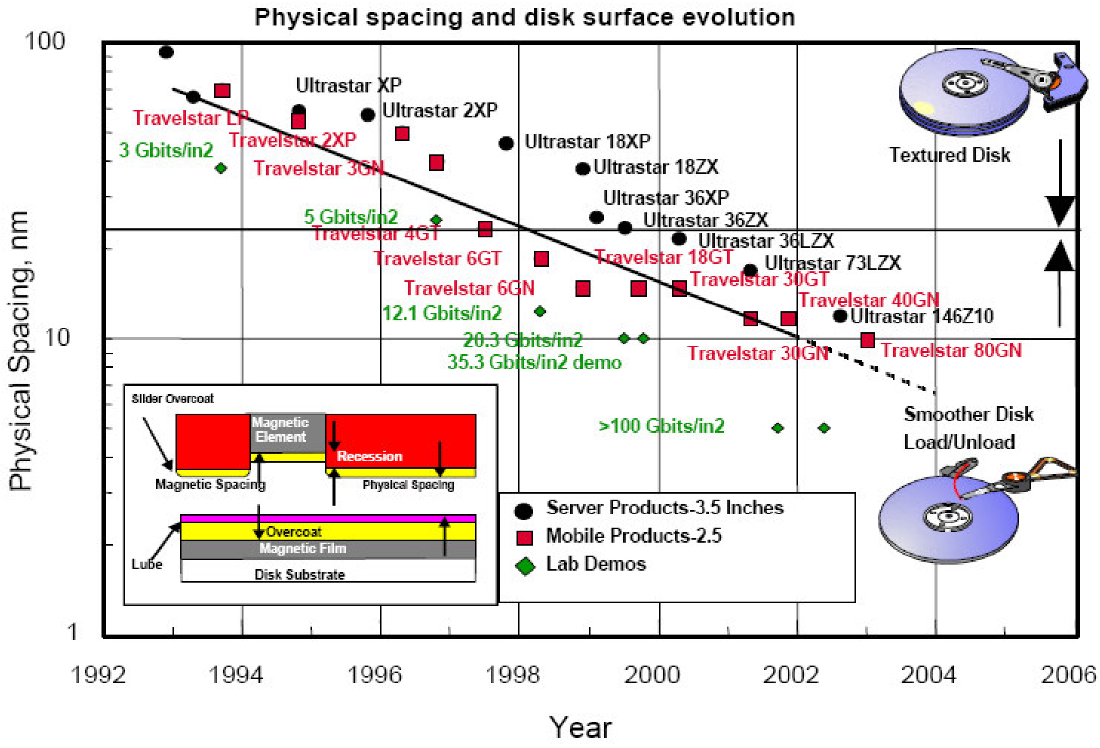

Figure 1.8 Areal density vs. head-media spacing

Magnetic spacing can be decreased by

a) Reducing the total thickness of the overcoat and the lubricant, and

b) Reducing the mechanical spacing between head-slider and disk-media – the flying height of the slider.

However, reducing the thickness of the overcoats and lubricant may subject to the development of new overcoat materials, new disk manufacturing process, and new technologies to reduce the chance of slider-disk contact and contact induced wear. The other way is to reduce the mechanical spacing between the head and the disk, which means to decrease the flying height of the slider.

Figure 1.8 shows the history of the areal density vs. flying height. Nowadays, the flying height has been reduced to merely 6~8 nm. However, a further reduction of flying height down to 2.5~3 nm is required for pushing technologies towards areal density of 1 Tera-bit per square inch (Tbit/in^2) [7].

4) Robust Head-Disk Interface at Extremely Low Flying Height

Robust and reliable operation of a modern magnetic disk drive depends critically on the robustness of head-disk interface technology. In fact, more than 90 % of disk drive failure comes from head-disk interface problems. Careful design of the air bearing and the head disk interface (HDI) is needed to provide a robust physical spacing between the head's magnetic sensors and the magnetic disk down to 10 nanometers in today's drives. This includes how to minimize the flying height fluctuation caused by disk morphology, and how to reduce the flying height changes due to altitude and other factors.

Another important factor for disk drive or head-disk interface robustness is the robustness of the dynamic load/unload (L/UL) operation – the operation to load head towards disk surface for data read/write operation and the operation to unload the head from disk surface before shutting down the disk drives. With the load/unload technology, the head is retracted off disk surface when the disk drive is not in use. The contact between slider and disk surface is minimized and, therefore, disk overcoat thickness can be reduced. However, the challenge is how to reduce the slider disk contact during load/unload operation, especially when the head-disk spacing is reduced to merely 3 nm.

The so called “proximity-on-demand” technology is another approach for increasing the robustness of the head-disk interface. The flying height is reduced to ultra-low level only when the head is going to do read/write operations. The head will be flying at higher flying height when it is not doing the read/write operations. However, the challenge for the implementation of such a technology is how to have proper micro-actuator design and working mechanism.

1.5 Problem Statement

Future high-density magnetic-disk drive requires a head-disk interface technology that can work at an extremely low flying height under various stressful working environments and flying height variation tolerance. The flying height achieved by industry in high end products today is about 12 nm when the author started this thesis work, with an areal density around 60 Giga-bit per square inch (Gb/in^2). The research target set for this thesis work is to develop technologies which can push the flying height as low as merely 3 nm so as to achieve 1000 Giga-bit per square inch (Gb/ in^2) or 1 Tera-bit per square inch (Tb/ in^2) areal density.

When the flying height moves towards 3 nm, the flying stability and the corresponding interface reliability become crucial challenges. Reliable reading and writing of magnetic data require the flying height fluctuation not more than ±10 % of the nominal flying height [8]. For 3 nm flying height case, this means a fluctuation within ±0.3 nm. The corresponding technology challenges include:

(a) How to handle factors that are negligible with higher flying height, such as intermolecular force effect and so on;

(b) How to minimize the possibility of occasional contact;

(c) How to minimize the head disk wear and friction, and

(d) How to reduce the flying height loss due to altitude.

This thesis focuses on the exploration of technologies to minimize flying height modulation and head disk contact at an extremely small flying height (3 nm). The work includes the technologies to minimize the flying height modulation caused by disk waviness, technologies to minimize the flying height sensitivity to altitude, technologies to reduce the probability of slider-disk contact during head loading process. “Proximity-on-demand” head disk interface technology is proposed and explored to reduce the head and disk contact and wear. The work also extends to the study and exploration of the flying height testing technologies for ultra-low flying height applications.

1.6 Dissertation Structure

The thesis focuses on the investigation of the key challenges and technology solutions for achieving ultra-low flying height. The thesis consists of eight chapters. Chapter 1 gives an introduction of the magnetic hard disk drives and the head-disk interface technology for the magnetic disk drives. Chapter 1 also states the challenges of the head–disk interface technology when flying height becomes extremely low. Chapter 2 discusses flying height testing technology, focusing on the working principle of intensity interferometry and the flying height testing technologies for ultra-low flying height sliders. Chapter 3 experimentally studies the flying height modulation and long-term robustness of the ultra-low flying height sliders. Chapter 4 studies the air bearing technology to reduce the flying height modulation caused by disk waviness. Chapter 5 investigates the air bearing technology to decrease the flying height sensitivity to altitude. Chapter 6 explores technologies for smooth loading operation. Multi-negative air bearing zones concept is proposed and investigated in this chapter. A new head disk interface of “proximity-on-demand” or active slider for flying height control is proposed in Chapter 7. The prototype of the slider is fabricated and experimentally test is conducted to prove the feasibility of this head disk interface. The final chapter, Chapter 8, summarizes the research work and main conclusions, as well as future work.

Chapter 2

Flying Height Testing Technologies at Extremely Small Head-Disk Spacing

Flying height is among the most critical parameter for head-disk interface design and evaluation. However, the experimental measurement of the flying height becomes more difficult than ever as technology moves to a flying height merely 2~4 nm. The commercially available flying height testers, which work well when flying height is above 10 nm, cannot provide the desired repeatability when the flying height reduces to 2~4 nm level. In fact, even the on-spot calibration process, which is a must before actual flying height testing, becomes difficult and not repeatable in the flying height testing process, when the flying height is below 10 nm.

In this chapter, the testing principle of optical flying height tester is first discussed, aiming at identifying the main cause of its difficulties in low flying height application. Then, new approaches for flying height testing are explored and proposed. Experimental results confirm that the proposed methods and approaches are effective in conducting flying height measurement at such a low flying height level.

2.1 Working Principle of Optical Interferometry for Flying Height Testing

The industry standard method for flying height measurement is one kind of optical interferometry methods. It uses a transparent glass disk to replace the magnetic disk for the flying height measurement of a head-slider. Such a replacement is acceptable in terms of evaluating the flying performance of head-slider.

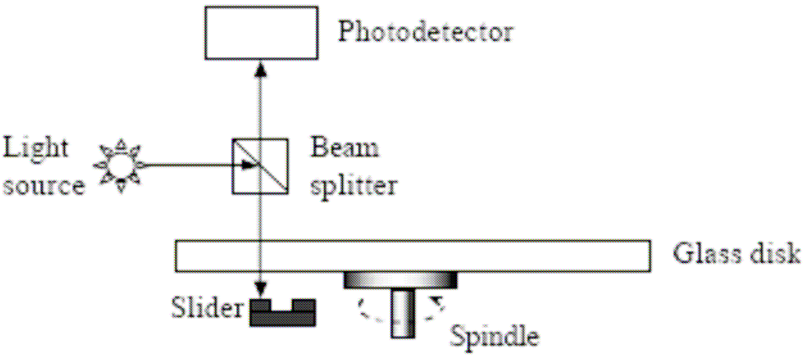

Figure 2.1 A diagram illustrating the flying height tester

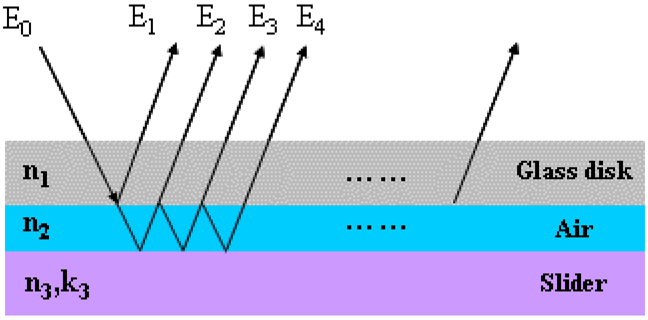

Figure 2.2 Reflections and transmissions at two interfaces

Figure 2.1 illustrates the system configuration of the industry standard optical flying height tester setup. Light from the mercury arc lamp is directed through the transparent glass disk and onto the slider. Reflected light, containing information about the spacing between slider and glass disk, is received by the photo-detector for flying height measurement and analyses [9, 10].

Figure 2.2 illustrates the optical working principles of such interferometry [10-12]. Considering the bottom surface of the glass disk, air bearing and the slider surface, there are two interfaces in this structure. The resultant reflected waves returning to glass disk consist of light which is initially reflected from the glass-air (E1) and air-slider (E2) interfaces as well as the multi-reflection components (E3, E4, …). Each successive transmission back into glass disk is smaller than the last, and the infinite series of partial waves makes up the resultant reflected wave. The amplitude of the resultant reflected wave is $E_{tot} = E_1 + E_2 + E_3 + \ldots$

The ratio of the amplitude of the outgoing resultant wave to the amplitude of the incoming wave is defined as the total reflection coefficient, and is analogous to the Fresnel reflection coefficients for a single interface. For a single film including two interfaces and considering the normal incidence (incident angle is zero), the total reflection coefficient is

$$R = \frac{E_{tot} \cdot E_{tot}^{*}}{E_0 \cdot E_0^{*}} = r \cdot r^{*} = \frac{r_{12}^{2} + |r_{23}|^{2} + 2r_{12}|r_{23}|\cos\left(\frac{4\pi n_2 d}{\lambda} - \phi_{23}\right)}{1 + r_{12}^{2}|r_{23}|^{2} + 2r_{12}|r_{23}|\cos\left(\frac{4\pi n_2 d}{\lambda} - \phi_{23}\right)} \tag{2.1}$$

where

$$r = \frac{r_{12} + r_{23}\exp\left(-j\frac{4\pi n_2 d}{\lambda}\right)}{1 + r_{12} r_{23}\exp\left(-j\frac{4\pi n_2 d}{\lambda}\right)} \tag{2.2}$$

$$r_{12} = \frac{\tilde{n}_1 - \tilde{n}_2}{\tilde{n}_1 + \tilde{n}_2} = \frac{n_1 - n_2}{n_1 + n_2} \qquad (k_1, k_2 = 0) \tag{2.3}$$

$$r_{23} = \frac{\tilde{n}_2 - \tilde{n}_3}{\tilde{n}_2 + \tilde{n}_3} = \frac{n_2 - n_3 + jk_3}{n_2 + n_3 - jk_3} \qquad (k_3 \neq 0) \tag{2.4}$$

$$\varphi_{23} = \tan^{-1}\left(\frac{2n_2 k_3}{n_2^{2} - n_3^{2} - k_3^{2}}\right) \tag{2.5}$$

Here, n_1, n_2 are the refractive indices of the glass disk and the air, respectively, and $(n_3 - j \cdot k_3)$ the complex index of refraction for the slider, d the flying height and λ is the wavelength of the incident light.

To find the flying height is just to rephrase the question. Rewrite Eq. (2.1), the flying height can be expressed as Eq. (2.6) for the first order fringe.

$$d = \left[\phi_{23} - \frac{r_{12}^{\ 2} + |r_{23}|^2 - \left(1 + r_{12}^{\ 2}|r_{23}|^2\right)\cdot R}{2r_{12}|r_{23}|\cdot(1-R)} \right] \cdot \frac{\lambda}{4\pi} \tag{2.6}$$

The optical constants (n, k) for slider and glass disk can be determined by an ellipsometer. With those known values, we can use Eqs. (2.3) to (2.5) to calculate r_{12}, r_{23} and ϕ_{23}. If the total reflection coefficient R associated with that flying height is known, the flying height can be calculated from Eq. (2.6).

In flying height tester, the reflected light goes into a photo-detector that converts the photon energy into electrical energy, and the output signal of the photo-detector is in voltage. This voltage is then converted to digital data by an A/D converter connected to the photo-detector.

One part of the reflected light is further reflected from the optical components before it reaches the photo-detector. Moreover, the light from the background and the light reflected from the top surface of the glass disk also go into the photo-detector, which are not counted in Eq. (2.6). It should be appreciated that all the uncertainties can be treated as constants for every testing and therefore, we can write the output voltage in terms of the total reflection coefficient as,

$$V = G \cdot R + C \tag{2.7}$$

It is easy to obtain the voltage value V for a certain flying height. We still need the overall gain G and the offset C to find out R. If two more voltage values are known, e.g., the maximum and minimum voltages that correspond to interference maximum and minimum in this case, the total reflection coefficient R can be determined from Eqs. (2.8) and (2.9), and it can be expressed as Eq. (2.10).

$$V_{\max} = G \cdot R_{\max} + C \tag{2.8}$$

$$V_{\min} = G \cdot R_{\min} + C \tag{2.9}$$

Then, the instant value of *R* in Eq. (2.1) can be calculated as:

$$R = \frac{V - V_{\min}}{V_{\max} - V_{\min}} \left(R_{\max} - R_{\min} \right) + R_{\min} \tag{2.10}$$

Thus, flying height can be obtained.

The calibration procedure in the flying height tester is hence a means to determine the maximum and minimum voltages, which in turn determine the overall gain and offset of the optical and electrical systems in the flying height tester.

The industry standard flying height measurement technique, represented by the Dynamic Flying Height Tester (DFHT) from a company called Phasemetrics, conducts the calibration (measuring the maximum and minimum voltages) by capturing the maximum and minimum interference signals when load or unload the slider onto or from the disk surface.

2.2 Sample Preparation

2.2.1 Slider Sample and Its Parameters

A femto slider, Panda II slider, designed and fabricated by researchers in the Data Storage Institute [13], was used for the experiments. The air-bearing surface design of such slider is shown in Figure 2.3. The targeted flying height of such slider is 3.5 nm. Figure 2.3 (a) illustrates the air bearing surface of the slider and the plot of the dual shallow steps in Figure 2.3 (b). The slider is of a negative pressure zone and five positive pressure pads: one trailing pad, two side pads and two leading pads. The negative pressure is formed in the main recess area which is in the middle of the slider. The air bearing surface has three etching steps: the outmost surface (small trailing pad and leading pads), the sub-shallow step which is 15 nm lower from the outmost surface (middle trailing pad and side pads) and the main-shallow step which is 82 nm lower from the outmost surface. The base recess is of 1540 nm from the outmost surface.

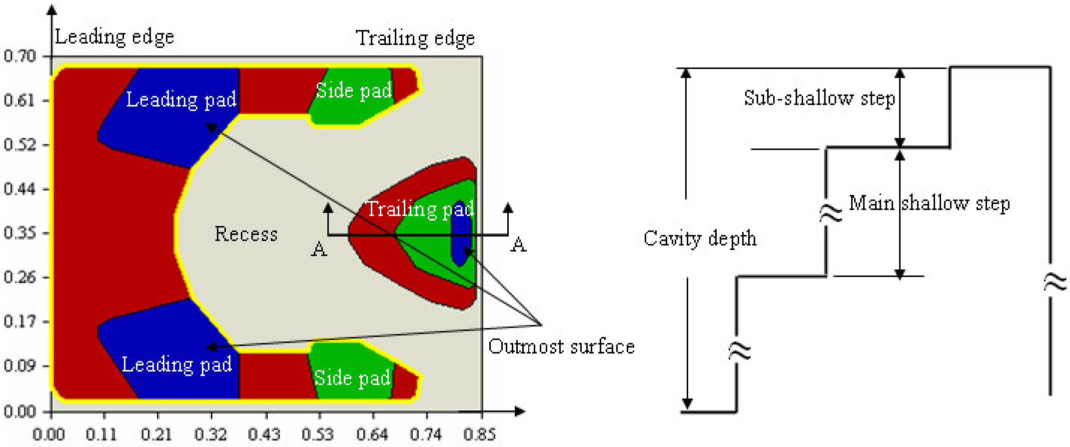

(a) Air bearing surface (b) A-A plot of the dual shallow steps

Figure 2.3 The air-bearing surface layer of the Panda II slider

Table 2.1 Static flying attitude of Panda II slider

Radius (mm)	Skew (°)	RPM	Pitch (μrad)	Roll (μrad)	FH (0.83, 0.35) (nm)
27.94	11.44	10000	189.42	2.79	3.45
20.35	4.26	10000	188.77	0.59	3.55
14.83	-2.45	10000	174.94	-2.23	3.47

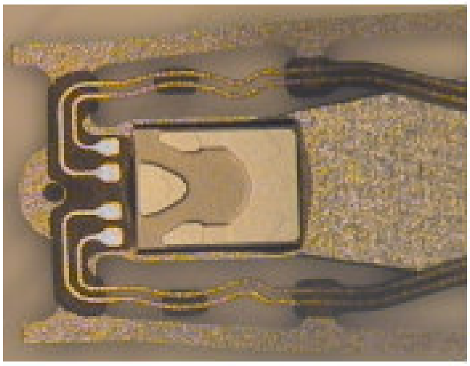

Figure 2.4 Fabricated slider-suspension assembly of Panda II slider

Table 2.1 lists the design parameters of Panda II slider. It is shown that the flying height profile of the slider is quite smooth over the whole disk surface. The design parameters are obtained by the design and evaluation platform from the Computer Mechanics Laboratory (CML) at University of California at Berkeley, the most used design and modeling platform in the industry. Figure 2.4 shows the fabricated slider-suspension assembly of the Panda II slider.

2.2.2 Glass Disk and Disk Characterization

Glass disks are used for the optical flying height testing. One critical parameter for glass disk selection is the disk surface roughness. The roughness (*Ra*) of the disk should be as small as possible for flying height measurement. Figure 2.5 shows the disk surface profile, measured by atomic force microscope (AFM). The *Ra* value of such glass disks is 0.34 nm, the best possible disk at the time of experimental work.

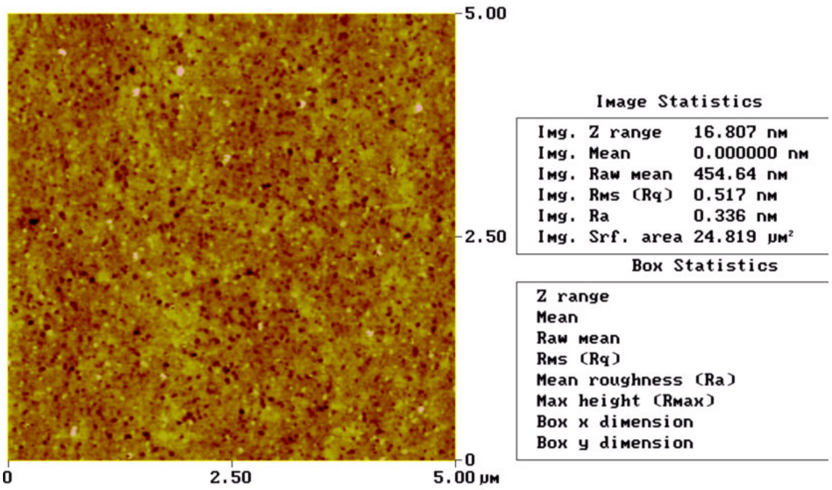

Image Statistics

```
Img. Z range    16.807 nm
Img. Mean       0.000000 nm
Img. Raw mean   454.64 nm
Img. Rms (Rq)   0.517 nm
Img. Ra         0.336 nm
Img. Srf. area  24.819 µm²
```

Box Statistics

```
Z range
Mean
Raw mean
Rms (Rq)
Mean roughness (Ra)
Max height (Rmax)
Box x dimension
Box y dimension
```

Figure 2.5 Glass disk surface tested by AFM

We noticed that it is necessary to have a layer of lubricant over the glass disk surface, in order to prevent slider or disk surface damage caused by casual slider-disk contact when loading slider to disk surface or during calibration or testing process. The glass disks used in the experimental work of this chapter are lubed and the thickness of lubricant is about 1~1.5 nm.

2.3 Approaches to Improve Flying Height Testing Accuracy

2.3.1 Optical Constants and Flying Height Testing Error

One phenomenon noticed by the author in the experimental measurement of the flying height is the poor repeatability of flying height readings even for the same slider and at the same testing spot on the slider surface. The author believes that this is due to the combined effect of both the refractive indices of slider and the calibration process.

The parameters used in the calculation of r_{12}, r_{23} and φ_{23} (in Eqs. (2.3) - (2.5)) are the indices of refraction for the glass disk, the air and the slider. Any error in the determination of these indices leads to an error of flying height measurement. It is easy to determine the index of refraction for homogenous materials, so the index of refraction for the glass disk can be determined accurately. The index of refraction for the air is close to 1.0. The precision of the index of refraction for the slider is most questionable because the slider substrate is formed by composite materials and its index of refraction varies form spot to spot.

Quantitative analysis of the error caused by refractive index measurement of the slider is carried out. Figure 2.6 shows the flying height changes versus (n, k) value variations when the actual flying height is fixed at 5 nm. It can be observed that a variation of n value by 0.02 produces a flying height measurement error around 0.2 nm, and a variation of k value by 0.01 generates more than 0.2 nm flying height measurement error.

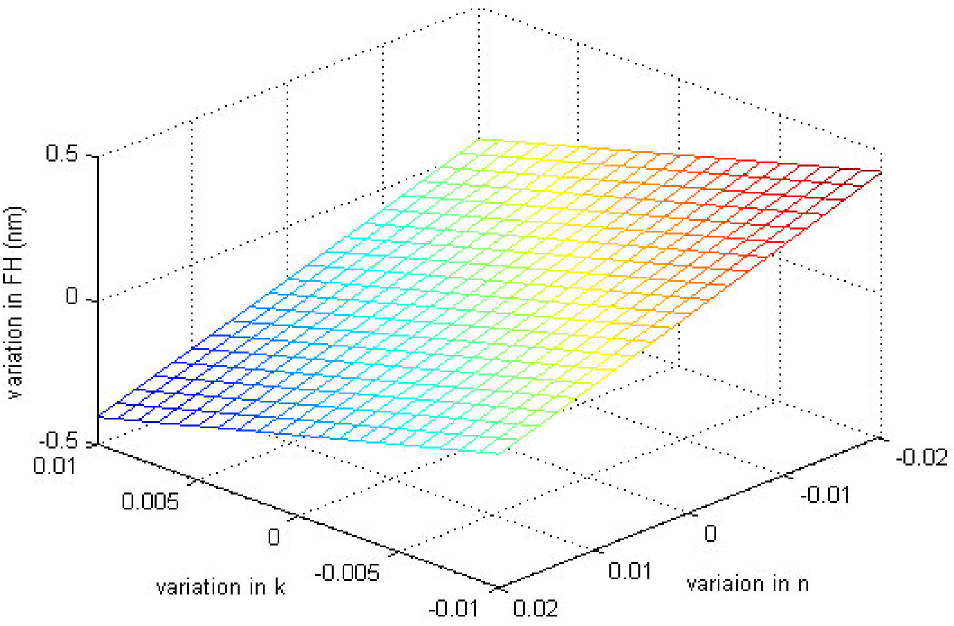

Figure 2.6 Flying height testing error caused by variation of (n, k) value

In the flying height testing process of commercial flying height tester, only one (n, k) value is typed into the system. However, the actual (n, k) values for different sliders are slightly different. Also, different points of the slider surface are of slightly different (n, k) values as well. Such differences cause flying height testing error. Furthermore, the light beam spot size of the commercial flying height tester is a square of about 25 μm [12], whilst the measurement spot of the ellipsometer (M-2000) is of an ellipse shape and minimum spot size of 60 μm x 25 μm [14]. It means that the reading from the ellipsometer is more like an average value, comparing with the beam spot size of optical flying height tester.

Table 2.2 lists the (n, k) values tested point by point at 10 μm interval. It can be seen that the variation of (n, k) values can easily lead to more than 0.5 nm difference even if we assume that the spot size for flying height testing is as big as the spot size of the ellipsometer

Table 2.2 Complex refractive indices around the testing point on a slider pad

	n@450	n@550	n@650	k@450	k@550	k@650
Point 1	2.203	2.232	2.189	0.569	0.495	0.476
Point 2	2.223	2.246	2.206	0.545	0.486	0.460
Point 3	2.223	2.227	2.181	0.513	0.428	0.414
Point 4	2.237	2.249	2.207	0.528	0.463	0.434
Point 5	2.229	2.228	2.184	0.501	0.428	0.411
Point 6	2.244	2.253	2.211	0.536	0.456	0.443
Point 7	2.233	2.253	2.213	0.528	0.474	0.455
Point 8	2.220	2.228	2.197	0.493	0.437	0.429
Point 9	2.239	2.244	2.201	0.514	0.448	0.424
Average:	2.228	2.240	2.199	0.525	0.457	0.438
Minimum:	2.203	2.227	2.181	0.493	0.428	0.411
Maximum:	2.244	2.253	2.213	0.569	0.495	0.476
Std	0.012	0.011	0.012	0.023	0.024	0.022

2.3.2 Calibration and Flying Height Testing Error

1. Calibration Method

Calibration is critical for flying height testing accuracy as mentioned in previous section. For the industry standard dynamic flying height tester (DFHT), the calibration is achieved through capturing reflected light intensities while varying the spacing between the slider and the glass disk. A spacing change of at least ten micro-inches (250 nm) is required so that the true minimum and maximum light intensities for each measurement wavelength can be collected [11, 15].

Two methods can be employed to vary the flying height for such a calibration purpose: retracting and RPM ramp. Additionally, both techniques can be used together as a hybrid calibration.

The retract method is the major method used for flying height testing calibration. It utilizes the head load/unload mechanism to unload the slider from the glass disk. In general, flying height changes when the spindle speed is increased. The RPM calibration method utilizes an increase of spindle speed to alter the slider to disk spacing.

A spacing change of at least ten micro-inches is required in the calibration process in order to obtain the minimum and maximum intensities. However, due to the strong negative pressure of the modern sliders, it is difficult to achieve such a spacing variation even if the RPM is increased to the maximum of the tester (20,000 RPM). Therefore, we applied the retract method in our testing.

2. Reliable Calibration for Flying Height Testing

An example of a good extracting calibration plot is shown in Figure 2.7. The primary factor for achieving reliable calibration is to assure that the first peak and valley of the intensity plot is apparent and not spiked.

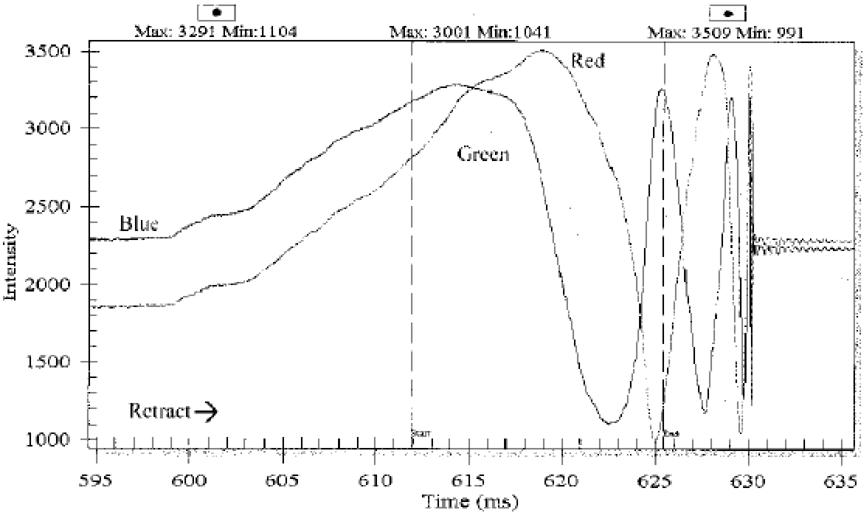

Figure 2.7 Example of a good calibration plot [16]

When the flying height reduces to about 3.5 nm, it is very difficult to get a good calibration performance and desired repeatability, as can be seen from the following case descriptions (calibration radius of 20.35 mm, skew angle of 4.26° and RPM of 10000).

One calibration plot is shown in Figure 2.8. It can be seen that the whole curve of the calibration vibrates. The first-order peaks and valleys are sharp and not apparent.

Another example of the calibration is shown in Figure 2.9. It is shown that the extracting process of the slider is long and not smooth. As a result, the confidence on the accuracy of minimum intensity value cannot be high.

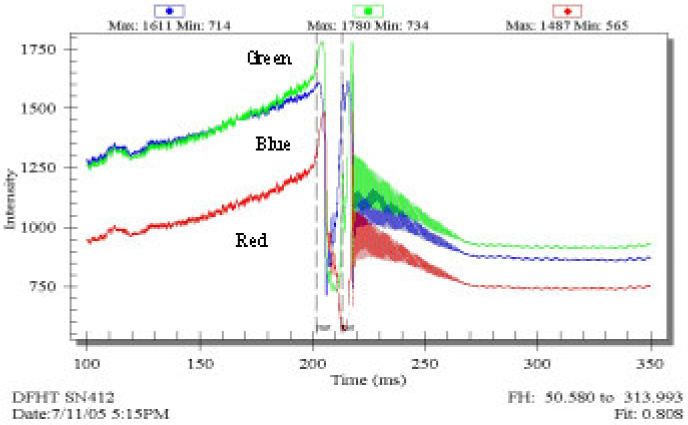

Figure 2.8 Example 1 of poor calibration plot

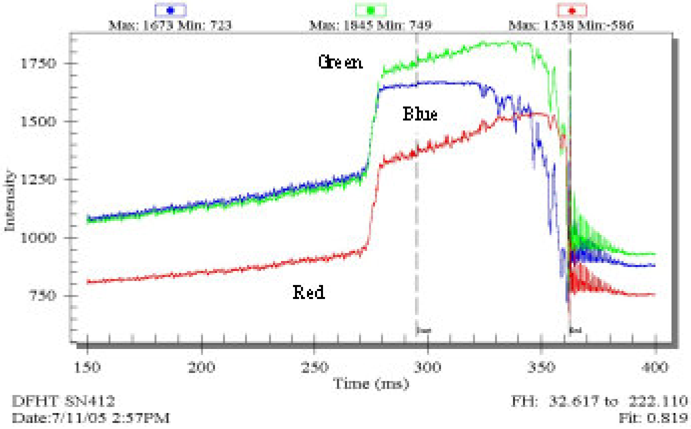

Figure 2.9 Example 2 of poor calibration plot

3. Parameters Selection for Calibration

Further investigations are carried out to understand more about how to get reliable calibration curve.

1) RPM Effect

Figure 2.10 shows the RPM effects on the flying height and the negative force at the radius of 20.35 mm for the Panda II type of sliders. It is shown that when the RPM increases from 1000 to 10000, the negative force increases from 0.46 g to 1.62 g. The flying height increases, reaches a peak at about 2000 RPM, decreases till 8000 RPM and starts to increase again when the spindle speed further increases. The results suggest that we can do flying height calibration at a lower RPM (higher flying height) and do flying height testing at the working RPM of the slider.

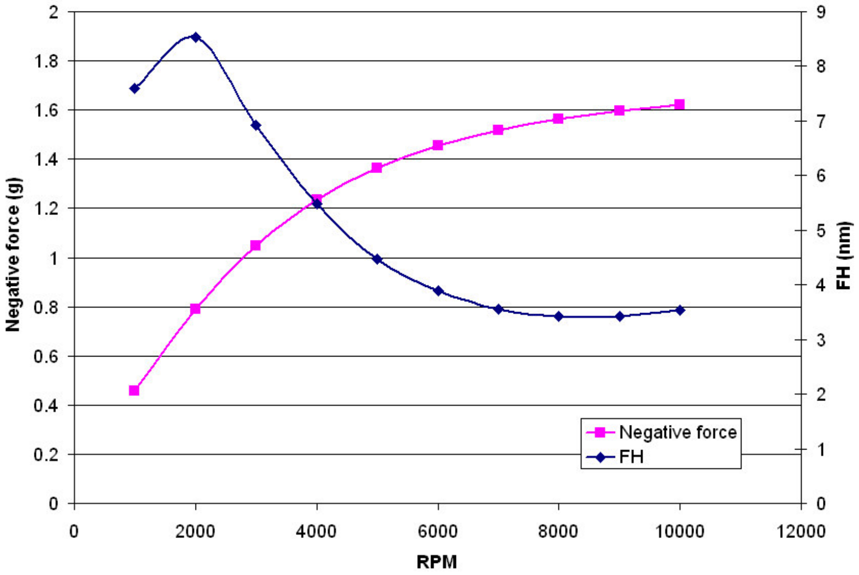

Figure 2.10 RPM effect on the flying height and negative force

2) Skew Angle Effect

Figure 2.11 shows the skew angle's effect on the flying height and the roll angle of a slider. The simulation radius is at 20.35 mm and RPM of 10000. It is shown that for the Panda II slider, the maximum flying height happens when skew angle is 0°. The flying height reduces when the skew angle becomes positive or negative. On the other hand, the effects of the skew angle on roll angle are not significant. But small skew angle is preferred as the flying height is higher and the roll angle is smaller – fewer chance of slider-disk contact.

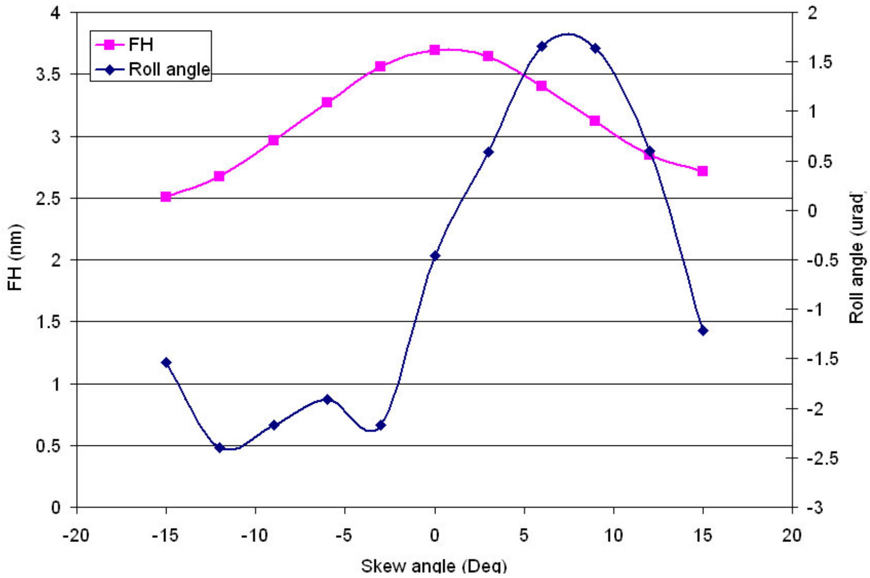

Figure 2.11 Skew angle effect on the flying height and roll angle

3) Further Discussion

From the above analysis, the RPM has a significant effect on the change of the suction force and the flying height. For this special slider case, lower RPM can greatly reduce the suction force and increase the flying height. Larger radius and smaller skew angle can result in larger flying height. Thus in order to reduce or avoid contacts between the slider and disk during calibration, the calibration can be done with a lower RPM (for this slider design), larger radius and smaller skew angle. Here, we should note that though the RPM, radius and skew angle effects on the flying height differs with different air bearing surface designs, we can do the similar analyses to optimize parameters' effects on the calibration process.

2.4 Flying Height Testing Results

2.4.1 Flying Height Extrapolation

When the flying height reduces to lower than 5 nm, the commercially available flying height testers can hardly provide the desired repeatability and it is not easy to pass the required on-spot calibration in the flying height testing process.

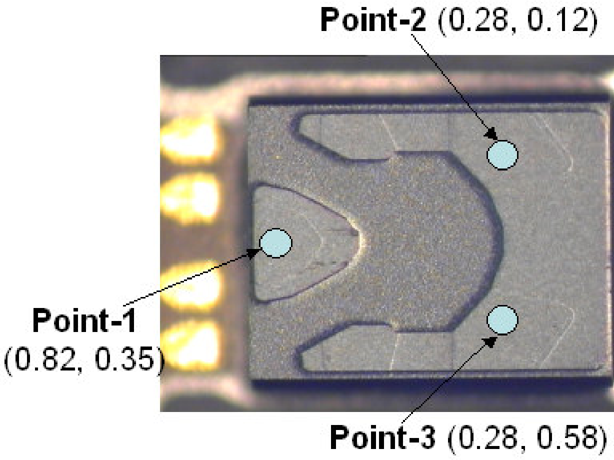

Figure 2.12 Measurement points on the slider pads

The author tried to test slider-disk spacing at the points with higher flying height, as far as high quality calibration can be carried out. Then, extrapolation is adopted to get the gap flying height. The extrapolation is based on the surface profile measurement of the slider sample, measured with an optical profilometer.

The flying heights on the selected testing points, as illustrated in Figure 2.12 are measured. Then, the gap flying height is derived by extrapolation, based on the measured slider surface profile and the slider-disk spacing (FH) at the 3 selected testing points [17].

2.4.2 Flying height testing procedure

The procedures of the flying height testing with 3.5 nm of clearance are summarized below:

(1) Prepare glass disk and slider. The disk is lubed and measured with atomic force microscopy (AFM) for the roughness. The optical constants (n, k) of the sliders are measured with the ellipsometer.

(2) Setup the relevant parameters, including suspension parameters, disk radius and testing track, testing point locations on slider surface, the calibration conditions and testing parameters (including (n, k) values).

(3) Interface status monitoring. It is important to make sure that there is no detectable contact between the slider and the disk. Therefore, an AE is attached to the clamping cartridge to monitor if there is contact.

(4) The calibration curve should be smooth, the first peak and valley should be broad and obvious.

(5) After the calibration is done, testing can be performed.

2.4.3 Flying Height Testing Results

Experiments are carried out with Panda II sliders. Figure 2.13 shows the typical calibration plot for the slider. The calibration is finished at the radius of 30 mm, RPM of 10000, and skew angle of 0°. The curve is quite smooth, the peaks for three colors are broad, the valleys are narrow and the intensity falloffs are obvious. Tables 2.3 and 2.4 list the testing results of two Panda II sliders. The fourth column MPS means the linear velocity of the disk, and the fifth, sixth and seventh columns mean the testing flying height at the points of Point-1, Point-2, and Point-3 shown in Figure 2.12 respectively. The last columns show the gap flying height attained by extrapolation.

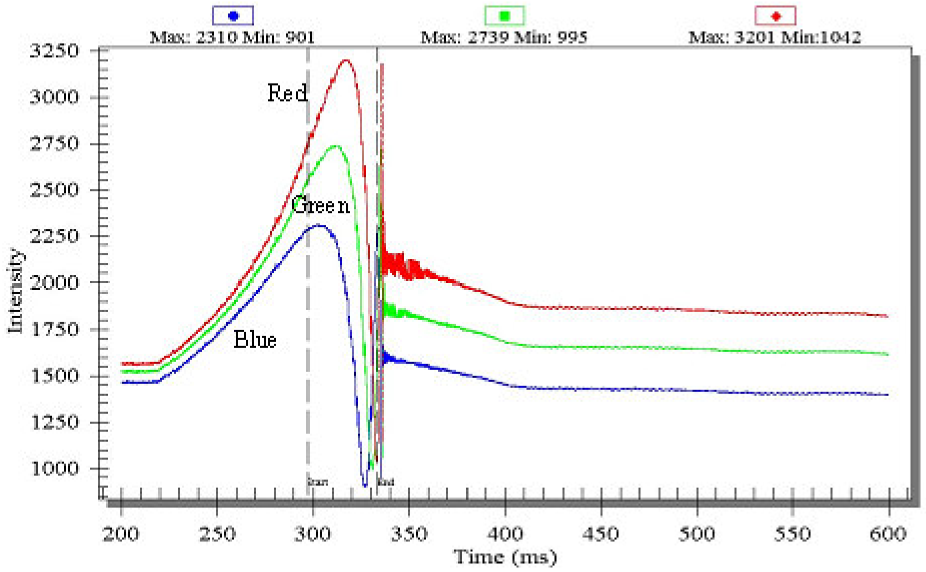

Figure 2.13 Calibration plot for Panda II slider

Table 2.3 Flying height testing result of slider I

Radius (mm)	Skew (°)	RPM	MPS (m/s)	P1 (nm)	P2 (nm)	P3 (nm)	Gap FH (nm)
30	0	10000	31.42	5.16	110.76	114.44	3.17
30	0	11000	34.56	5.93	128.71	131.53	3.63
30	0	12000	37.70	7.74	134.32	135.87	5.38
30	0	13000	40.84	9.86	137.15	138.00	7.49
30	0	10000	31.42	5.41	112.16	113.03	3.42
30	0	11000	34.56	5.49	124.43	125.16	3.28
30	0	12000	37.70	7.28	136.93	137.60	4.87
30	0	13000	40.84	9.29	139.52	136.26	6.91
30	0	10000	31.42	5.19	111.37	113.27	3.21
30	0	11000	34.56	5.97	124.86	125.71	3.76
30	0	12000	37.70	7.69	137.14	137.94	5.29
30	0	13000	40.84	9.82	139.81	140.56	7.40

Table 2.4 Flying height testing result of slider II

Radius (mm)	Skew (°)	RPM	MPS (m/s)	P1 (nm)	P2 (nm)	P3 (nm)	Gap FH (nm)
30	0	10000	31.42	5.36	130.76	131.44	3.03
30	0	11000	34.56	6.43	138.71	139.53	3.97
30	0	12000	37.70	7.34	144.32	145.88	4.79
30	0	13000	40.84	8.86	147.15	148.00	6.23
30	0	10000	31.42	5.41	132.16	133.04	3.05
30	0	11000	34.56	6.49	141.43	142.16	3.98
30	0	12000	37.70	7.28	146.93	147.60	4.68
30	0	13000	40.84	9.09	149.52	150.26	6.48

30	0	10000	31.42	5.39	131.37	133.27	3.04
30	0	11000	34.56	6.37	140.86	142.71	3.86
30	0	12000	37.70	7.59	145.14	157.94	4.92
30	0	13000	40.84	8.72	149.81	149.56	6.10

2.5 Summary

In this chapter, the principle of intensity interferometer of flying height testing technology is first illustrated. The variation of optical constants (n, k) on the air bearing surface and the accuracy of calibration curve brings into errors during the flying height testing process. Optical constant averaging method is adopted to reduce the variation of optical constants effects. To carefully select the parameters for calibration process is important to improve the accuracy of the calibration curve.

Since the available flying height tester (the industry standard) cannot provide the desired repeatability and it is not easy to pass the required on-spot calibration in the flying height testing process, a method of extrapolation is introduced to achieve the gap flying height. Then the flying height testing procedure for flying height below 5 nm is developed and confirmed experimentally.

Chapter 3

Experimental Studies of Flying Height Modulation and Long-Term Flyability

Flyability and flying stability are key issues for achieving a stable head-disk interface. They are becoming more and more critical with lower and lower flying height. It is believed that reliable reading and writing of magnetic data would require the transducer location on the slider fluctuate by no more than 10 % of the nominal flying height [18-21]. Many factors, such as surface roughness, disk waviness, flying contact, dynamic lube bridging, inter-molecule level interaction, and disk topographic features, may affect the flying stability of the slider.

Researches have been reported which investigated lubricant redistribution, deformation and modulation induced by flying sliders. But all these works [22-25] are limited to those head-disk systems with rather high flying height (above 10 nm). In order to achieve areal density of 1 Tera-bit per square inch (Tb/in^2) and beyond, the flying height will have to be reduced to 2~4 nm. Also, technology requires a lubricant thickness around 1.0 nm and high slider-disk motion velocity (30 m/s).

Research results were also reported about the investigation of slider's flying characteristics and flying height modulation caused by disk waviness [26-30]. However, most of them are limited to rather high flying height and computer modeling.

Starting from discussion on disk surface morphology characteristics and its effects on flying height modulation, a platform is set up to experimentally investigate the flying height modulation caused by disk waviness when the flying height is merely 3.5~4 nm. Then, long-term flyability test is performed in order to investigate the robustness of the head-disk interface at such a small head-disk spacing.

3.1 Surface Morphology and Flying Height Modulation

Disk surface morphology can be classified according to the wavelength. The definition used by THôT [35] is adopted in this thesis to describe disk surface morphology, as listed in Table 3.1. THôT is the major instrumentation company providing equipment for disk surface morphology analyses. The definition from THôH is the most widely accepted definition in the industry up to now.

Table 3.1 THôT's surface morphology definition

Ra (µm)	Low Freq. Ra (µm)	µ-Waviness (µm)	Waviness (µm)	Macro-waviness (µm)	Flatness (µm)
<40	40 to 100	100 to 400	400 to 2,000	2,000 to 4,000	>4,000

A full spectrum of disk surface morphology is illustrated in Figure 3.1, which is a typical spectrum analysis of disk surface profile on a given track (given radius). It can be seen that the spectrum contains morphology from the roughness level (Ra, micron or sub-micron wavelength) to disk flatness (10's millimetre in wavelength). Figure 3.2 is an illustration of disk micro surface morphology, tested by an atomic force microscope (AFM). It can be observed that the disk surface is not absolute smooth but has surface roughness.

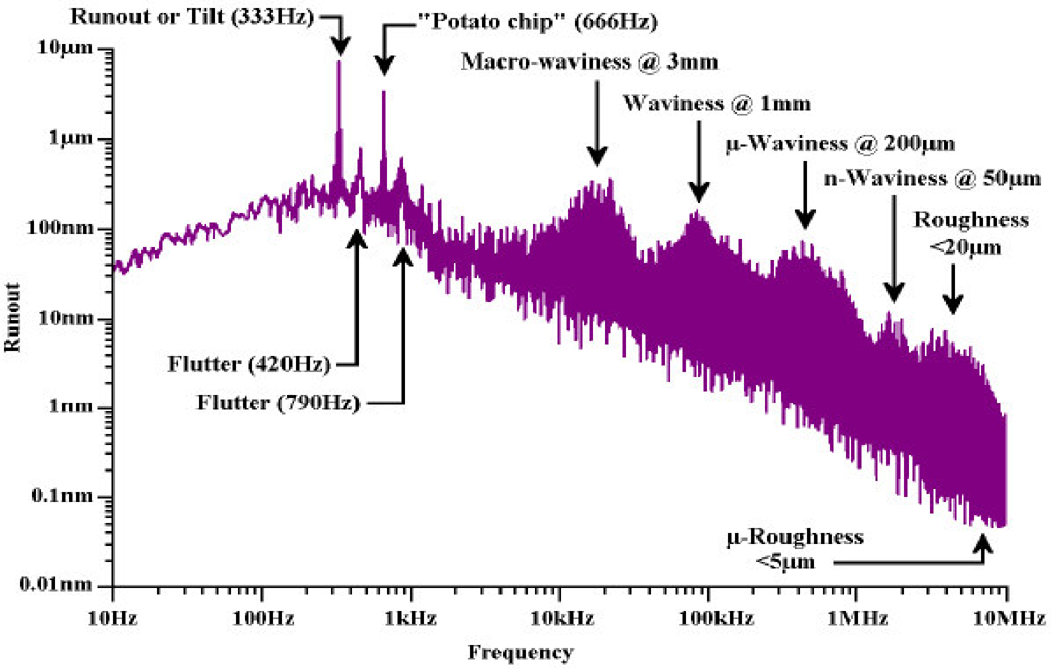

Figure 3.1 Frequency spectrum of disk surface morphology measured at a given track

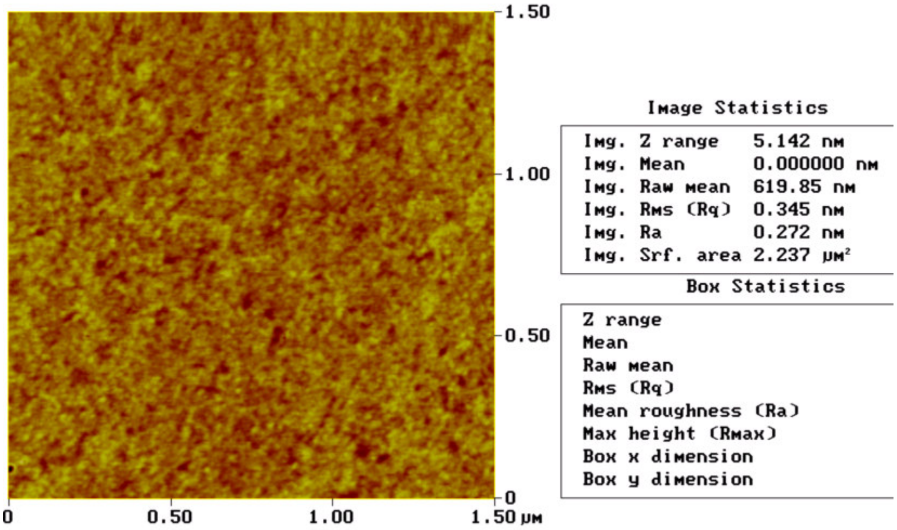

```
Image Statistics
Img. Z range    5.142 nm
Img. Mean       0.000000 nm
Img. Raw mean   619.85 nm
Img. Rms (Rq)   0.345 nm
Img. Ra         0.272 nm
Img. Srf. area  2.237 µm²
Box Statistics
Z range
Mean
Raw mean
Rms (Rq)
Mean roughness (Ra)
Max height (Rmax)
Box x dimension
Box y dimension
```

Figure 3.2 Disk morphology tested by AFM

Table 3.2 Surface morphology descriptions by wavelength and frequency

Features	Wavelength range	Frequency range
Flatness	> 4 mm	< 6 kHz
Macro-waviness	2 ~ 4 mm	6 ~ 12 kHz
Waviness	0.4 ~ 2 mm	12 ~ 60 kHz
µ-waviness	0.1 ~ 0.4 mm	60 ~ 240 kHz
Long wave roughness	40 ~ 100 µm	240 ~ 600 kHz
Roughness	< 40 µm	> 600 kHz

Table 3.2 lists the corresponding frequency bandwidth converted from the wavelength based definition when the linear velocity of the testing track is 24 m/s (at radius of 1.25 inch and with disk spindle speed of 7200 rpm), typical number for modern 3.5” disk drives for desktop computer applications.

When a slider flies over a disk surface, the magnetic spacing (or flying height) at the transducer fluctuates with respect to the disk morphology. These fluctuations (which are called flying height modulation) influence both the readback signal amplitude and the reading or writing resolution of the read/write head. Therefore, the slider air bearing surface must be designed in such a way that the slider would be able to follow up as high percentage of disk morphology as possible and reduce the flying height fluctuation caused by disk morphology to a negligible level.

When the magnetic spacing of the head disk interface reduces, the allowed flying height fluctuation or flying height modulation reduces. As mentioned above, the flying height fluctuation would be as low as ± 0.3 nm when flying height is targeted at 3 nm. Thus it is important to minimize the flying height modulation caused by disk morphology.

3.2 Flying Height Modulation Caused by Disk Morphology

The slider’s disk surface following capability is different for different disk surface morphology wavelengths.

When the disk wavelength is significantly longer than the length of the slider, the slider can follow the disk waviness. For a fixed wavelength of the disk waviness, the flying height modulation increases when the length of the slider increases [26].

When the wavelength reduces to about the sliders' dimension, the flying height modulation will be determined by the air-bearing design of the slider and air-pressure arrangement over slider's air bearing surface.

Thornton, et al [30] investigated the flying height modulation of both pico and femto sliders. They observed that the large flying height modulation is resulted from a phase shift between the sliders' response and the disk waviness. The phase shift becomes larger when the pitch angle of a flying slider is small. They concluded that a flying height modulation is not just a function of the sliders' overall length but also a function of the sliders' attitude and air bearing surface design. Higher pitch angle is helpful to reduce the flying height modulation and shifting the high pressure zone to the transducer area is beneficial for reducing the flying height modulation.

When the wavelength is much shorter than the slider dimension (such as disk roughness case), the slider will not be able to adjust itself promptly to follow the surface profile at such a wavelength and the flying height modulation will equal to the disk roughness. Also, certain disk waviness or micro-waviness corresponds to slider's air-bearing resonance frequency and can excite the air bearing resonance. The flying height modulation, in this situation, depends on the dynamics of the mechanical system [26-27].

It is expected that femto form-factor sliders will be favored over the most commonly used pico sliders of current hard disk drives in terms of reducing flying height modulation, due to its reduced slider dimension, comparing with pico form-factor sliders. Simulation and experimental work from Liu, et al confirmed the advantages of the femto sliders [31, 32].

The Laser Doppler Vibrometer (LDV) is widely used to experimentally study the flying height modulation of the slider, due to its super high displacement resolution (sub-nm) and high bandwidth. Q. H. Zeng, et al [28-29] stated that averaging is critical for using the LDV to measure the flying height modulation in the time domain. Increasing the times of averaging operations can increase the accuracy of the testing, but of course will take longer time for testing. Thus a suitable averaging number should be determined for a specific experimental system. Also much better displacement data can be obtained from velocity output of the LDV by using numerical integration [29]. The experimental results were reported for the investigation of the flying height modulation as a function of flying height. They utilized the flying height loss vs. flying height to evaluate the flying height effects on the flying height modulation. Their results showed that for the same disk rotating speed, the percentage of fly height loss is much more significant at the lower fly height, and the rate of growth is not linear.

Experimental investigations were conducted in [28] to investigate repeatable flying height modulation as a function of RPM. It was found that the minimal flying height modulation occurs when the slider begins to be flying without intermittent contact, and the flying height modulation increases as RPM increases. But the ratio of the flying height modulation to the flying height stays approximately constant.

From the previous research works, most of the simulation and experimental results were conducted with flying height above 5 nm. In order to investigate the flying height modulation of head disk spacing of 2~4 nm, it is necessary to build up a head disk interface system with such an ultra-low flying height for achieving areal density of 1 Tb/in^2.

3.3 Experiments of Flying Height Modulation

Experimental investigations of the flying height modulation are carried out with Panda II slider, which was described in Chapter 2. The experimental setup, procedure and some testing results will be discussed in the following.

3.3.1 Experimental Setup

As discussed above, a Laser Doppler Vibrometer (LDV) is widely used to measure the flying height modulation of the sliders. There are two methods to measure the flying height modulation by using LDV [28-29]: dual beam measurement and single beam measurement. The single beam LDV measurement method can provide the absolute motion of the disk surface under the slider as well as the absolute motion of the slider. Not only a higher resolution can be obtained, but also it is easier to directly compare experimental and simulation results. Thus in our experiments, we adopted the single beam measurement and the velocity output of the LDV is utilized and the displacement is attained by integration.

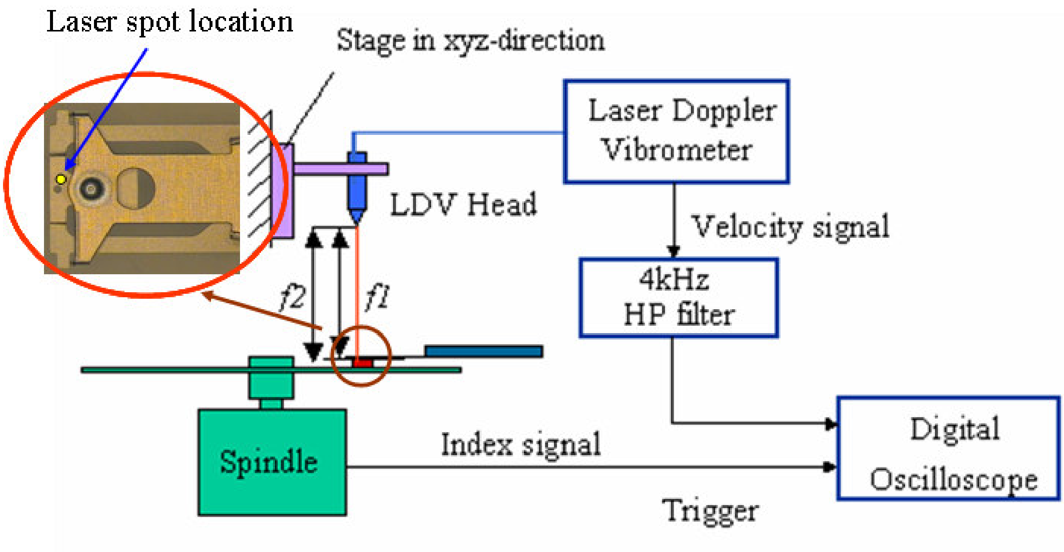

Figure 3.3 Experimental setup for testing flying height modulation

Figure 3.3 shows the schematic diagram of our experimental system. A Guzik spinstand, the industry standard head-disk testing platform, is used as the testing platform. The spinstand is of a precision air-bearing spindle and a built-in signal when the spindle rotates one round, which we can use as a trigger instead of using a scratch in the inner disk track [28]. A single beam LDV (Polytec 512) is used and the output velocity signal of the LDV is fed into a high-pass filter with a cutoff frequency of 4 kHz. The stage of xyz direction can be used to adjust the laser spot on the slider and the disk. Data acquisition is accomplished using a LeCroy oscilloscope sampled at 1 MHz and with desired averaged times. All data postprocessing is carried out using MATLAB.

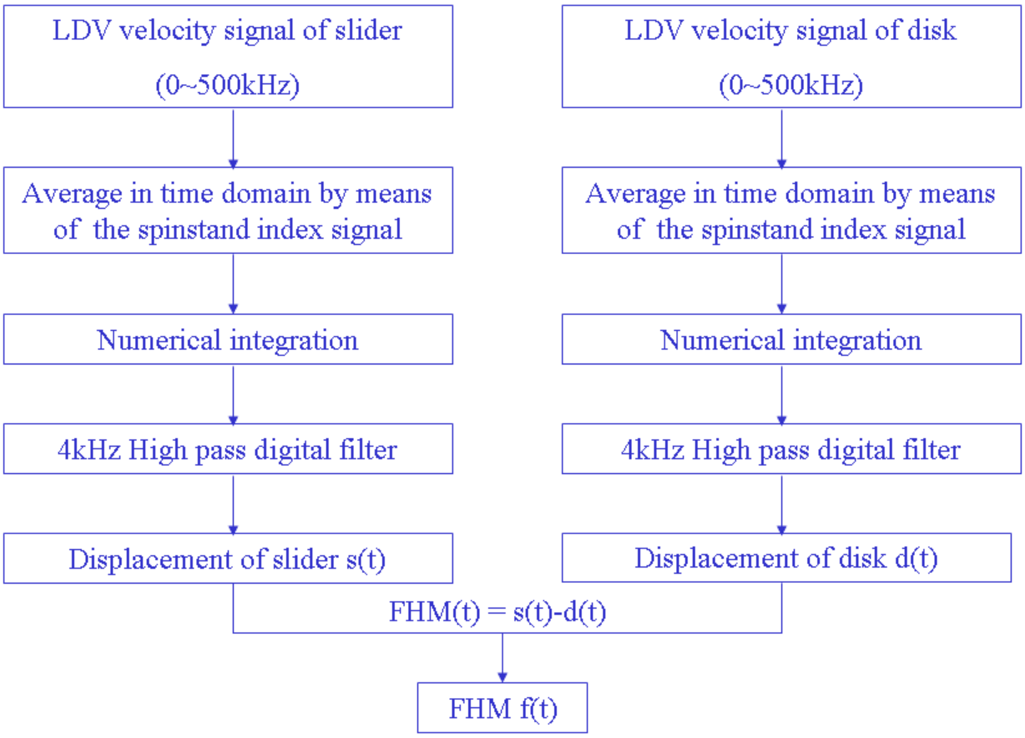

Figure 3.4 Schematic illustration of signal analysis process

The data analysis process is illustrated in Figure 3.4. The velocity signals of the slider and the disk from the LDV are acquired using the oscilloscope and with 100 averaging. Then the displacements are attained with numerical integration. However, the displacement data from the velocity measurement obtained by integration is quite different from the directly measured displacement in the time domain, because there are some low frequency components after the integration. A high order Finite Impulse Response filter (800 orders, MATLAB function FIR1) is used to remove these low frequency components. The frequency of the high-pass filter is selected to be 4~500 kHz so that the data is for the waviness with wavelength comparable or smaller than the slider size. The difference of the displacements measured from the disk and the backside of the slider reflects the variation of the head-disk spacing.

3.3.2 Experimental Procedure

The experimental procedure is as follows:

(1) Test the disk roughness characteristics with AFM. Then the disk is mounted onto a spinstand (GUZIK).

(2) Test flying height of the slider sample with the dynamic flying height tester (DFHT), with at least 5 times of averaging and under satisfying calibration accuracy (refer to Chapter 2 for Panda II slider flying height testing).

(3) Evaluate the flyability of the head disk system. Firstly, fly the slider at higher flying height. This is achieved by increasing the relative motion speed between slider and disk --- letting the slider to work at outer diameter of the disk and at high RPM (12,000). Stop the experiment if there is detectable AE signal which indicates slider-disk contact. If no detectable AE signal, then, reduce the spindle speed from 12000 RPM to 8000 RPM and move the slider from radius of 30 mm to 20 mm, monitoring the AE signal. The experimental study can be carried out if there still is no AE detectable slider-disk contact

(4) Monitoring system setup. Table 3.3 lists the parameters for the testing. In the experiment, the slider is tested at radius of 30 mm, RPM of 10000 and skew angle of 0°. It takes 6 ms for the slider to run the whole track, thus we can set the total time for sampling as 10 ms. At a sample frequency of 1 MHz, we can get 10,000 samples on the track.

Table 3.3 Parameters for the flying height modulation testing

Average times	100
Filter	4k Hz high pass filter
Sample frequency	1M Hz
Sample time	10 ms

(5) Flying height modulation measurement. Firstly, the laser is focused onto the slider back as close to the read/write transducer as possible (as shown in Figure 3.3) to measure the vertical motion velocity of the slider (S' (t)). Then the slider is offset to a different radius, but holding the measurement beam in place. The velocity of the disk is measured (D' (t)). Here, we only consider the repeatable part of slider motion, disk motion and flying height modulation.

(6) Data processing. After getting the velocity data, the displacement data S (t) and D (t) are attained by numerical integration and digital filtering is carried out. Then flying height modulation is obtained by subtracting D (t) from S (t).

3.3.3 Experimental Results

Averaging is important when using the LDV to measure the flying height modulation in the time domain. It aims to remove the data caused by random factors. It is necessary to identify an averaging number that is suitable to attain stable testing data. Too small averaging number brings many random data into the testing data, and too big averaging number increases the experimental and processing time.

Figure 3.5 (a) shows the relationship between the averaging number and the 3σ value of the disk waviness amplitude. The experiment is carried out at a rotation speed of 10000 RPM, skew angle of 0° and radius of 30 mm. It is seen that the 3σ value of the disk waviness amplitude reduces when the averaging number increases, but when the averaging number is more than 100, the variation of 3σ is very small. Thus we may conclude that at least 100 averages are required for the disk morphology testing.

Figure 3.5 (b) is the probability density function of the disk morphology amplitude, the mean value and the standard deviation is 0 and 0.163, respectively. The line is the normal distribution function based on the mean value and standard deviation of the testing disk morphology. It is clear that the bar of the probability density function correlates very well with the normal distribution function.

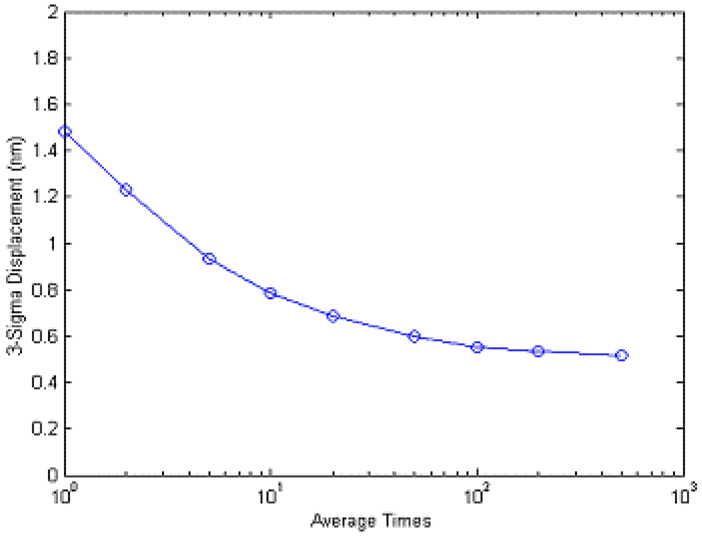

(a) Averaging number vs. 3σ of disk displacement amplitude

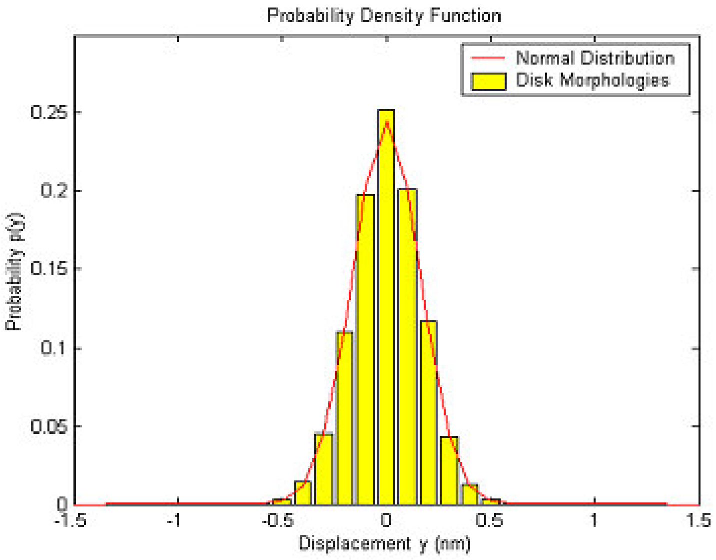

(b) Histogram of the disk morphology amplitude

Figure 3.5 Testing results of disk morphology

Figure 3.6 (a) shows the displacements of the slider and the disk in time domain with 100 averages. It is shown that the slider can follow the disk morphology of long wavelength, but can not follow short wavelength components. Figure 3.6 (b) is the flying height modulation attained by subtracting the disk amplitude from the slider amplitude shown in Figure 3.6 (a). It is observed that most of the flying height modulation is in the range of -0.3 nm ~ +0.3 nm.

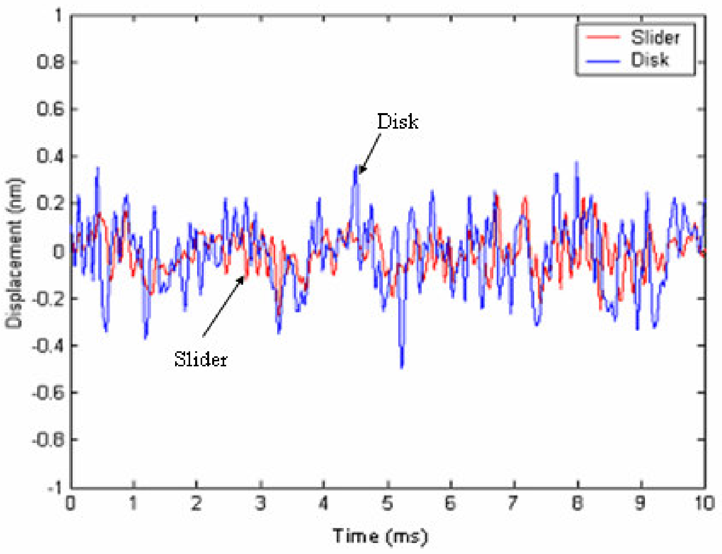

(a) Testing amplitude of slider and disk

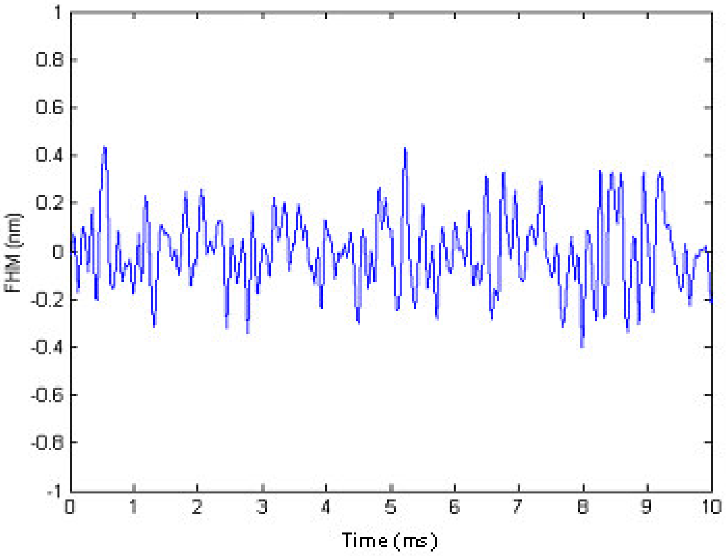

(b) Flying height modulation with 100 averaging

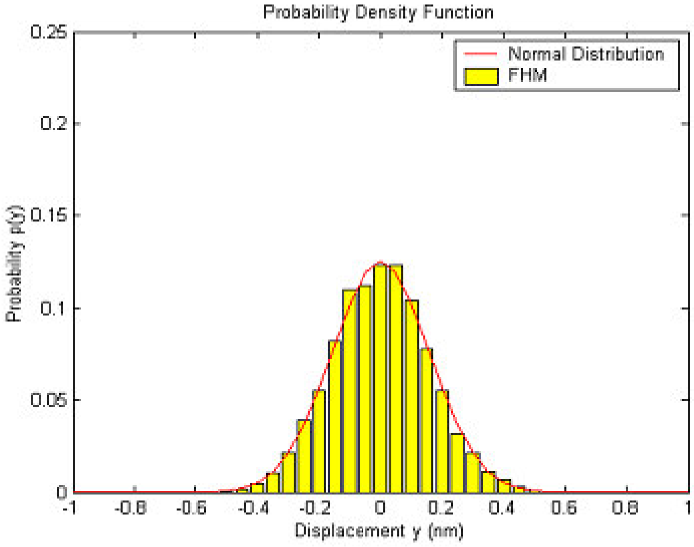

(c) Histogram of flying height modulation

Figure 3.6 Experimental results of flying height modulation

Figure 3.6 (c) shows the probability density function of flying height modulation, where the mean value and the standard deviation are 0 and 0.159, respectively. The line is the normal distribution function based on the mean value and standard deviation of the flying height modulation. It is clear that the bar of the probability density function of the flying height modulation also correlates very well with the normal distribution function.

3.4 Experiments of Long-Term Flyability

Long-term (14 days) flyability study was carried out, aiming to study the long-term robustness of the interface between Panda II slider and a super-smooth disk. The characteristic of the disk is the same as illustrated in Figure 3.2. Before the experiments, the disk was dipped with a layer of lubricant of 1~1.5 nm thickness.

Long sweep and tracking following tests were carried out to study the durability of padded and load/unload pico sliders [33, 34]. It was found that after two long sweep cycles (one cycle of 7 days, which consists of 6-day sweep and 24 hour rest time), the contact signals decreased to a relatively stable value and smears could be observed on the air-bearing surface.

In hard disk drive, the probabilities of the read/write head accessing various tracks are the same in actual operating conditions, it can be denoted as $f(x) = 1/N$, where N (from No at outer diameter (OD) to Ni at inner diameter (ID)) is the amount of tracks on the disk surface. The disk radius from OD to ID is denoted as Ro to Ri, respectively, and the width of the slider is denoted as w. If the slider can fly at one radius for 14 days (L) with no scratches and no obvious disk wear, then in the normal operating conditions, the durability of the head and the disk can be approximated by integrating over the whole disk surface.

$$F = \int_{Ni}^{No} \frac{1}{N} \frac{R_o - R_i}{w} L dx \tag{3.1}$$

If $Ro = 32$ mm, $Ri = 14$ mm, $w = 0.85$ mm, and $L = 14$ day, we can get the F about 296 days.

3.4.1 Experimental Platform

The test platform for the flyability test is the same as shown in Figure 3.3. An optical surface analyzer (OSA, Candela Instruments) was used to determine the lubricant thickness, carbon wear and disk wear, as illustrated in Figure 3.7 [36].

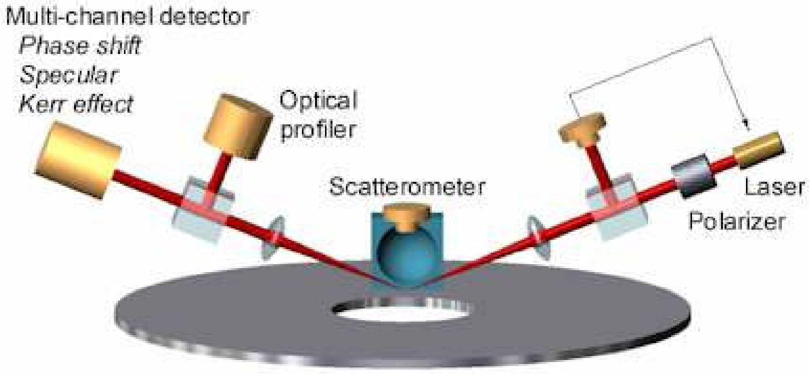

Figure 3.7 Diagram of the optical system of OSA

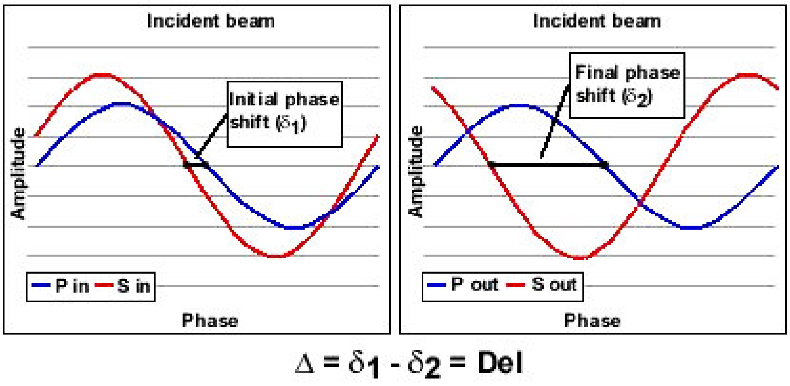

$$\Delta = \delta_1 - \delta_2 = \mathrm{Del}$$

Figure 3.8 Phase changes of OSA

The OSA systems use Q-polarized light, a proprietary combination of P and S linearly polarized light, and can be equipped with up to five measurement methods of detection: (1) phase shift detection (ellipsometer); (2) specular light detector (reflectometer); (3) scattered light detector (scatterometer); (4) magnetic (Kerr effect); (5) surface topography (optical profiler).

When a Q-polarized optical wave strikes a surface, the phase between the P and S components of the wave changes depending upon the properties of the surface. The change in phase shift, or Del, provides a highly sensitive way to characterize the surface (shown in Figure 3.8).

The P-specular image is very sensitive to carbon wear and very weakly sensitive to variations in the lubricant layer. Therefore, the P-specular image shows carbon wear but not lubricant variations. On the other hand, the Phase-Shift image is very sensitive to both lubricant variations and carbon wear. If carbon wear is present, bright tracks appear in both the P-specular and the Phase-Shift images. Lubricant variations only appear in the Phase-Shift image. The same area can be simultaneously analyzed with the P-specular and the Phase-Shift channels to determine whether carbon wear, lubricant variations, or both are present [36].

3.4.2 Experimental Procedure

The experimental procedure of the long-term flyability is illustrated in Figure 3.9:

(1) Test the flying height of the slider with dynamic flying height tester (DFHT). Accuracy control criteria: with at least 5 times of averaging and under satisfying calibration accuracy (refer to Chapter 2 for the flying height testing of Panda II slider).

(2) Test the disk roughness characteristics with AFM. At least three areas on the disk are tested and the values of roughness (Ra) should be all smaller than 0.4 nm. Then the disk is mounted onto a spinstand (GUZIK). The rotation speed is set to the desired value (in this case is 10000 RPM).

(3) The slider is then loaded onto the disk at a radius of 28 mm using Load/Unload technology. Load/Unload radius is set to be smaller than the testing radius to avoid possible scratches caused by Load/Unload process.

Then the slider is positioned to the desired testing track (30 mm) and is kept flying.

(4) After a given flying time (24 hours), the slider is moved to radius of 28 mm and unloaded from the disk. Then the disk is mapped with the OSA. If the slider is crashed, the experiment is stopped. Otherwise the disk is again mounted onto the spinstand and the slider is loaded and positioned onto the testing radius.

(5) Repeat step (4) until the slider has been flying for 14 days or when the slider is crashed. If the slider keeps flying above the disk for more than 7 days before it crashes, we still consider it passes the robustness test and can be used for analyses.

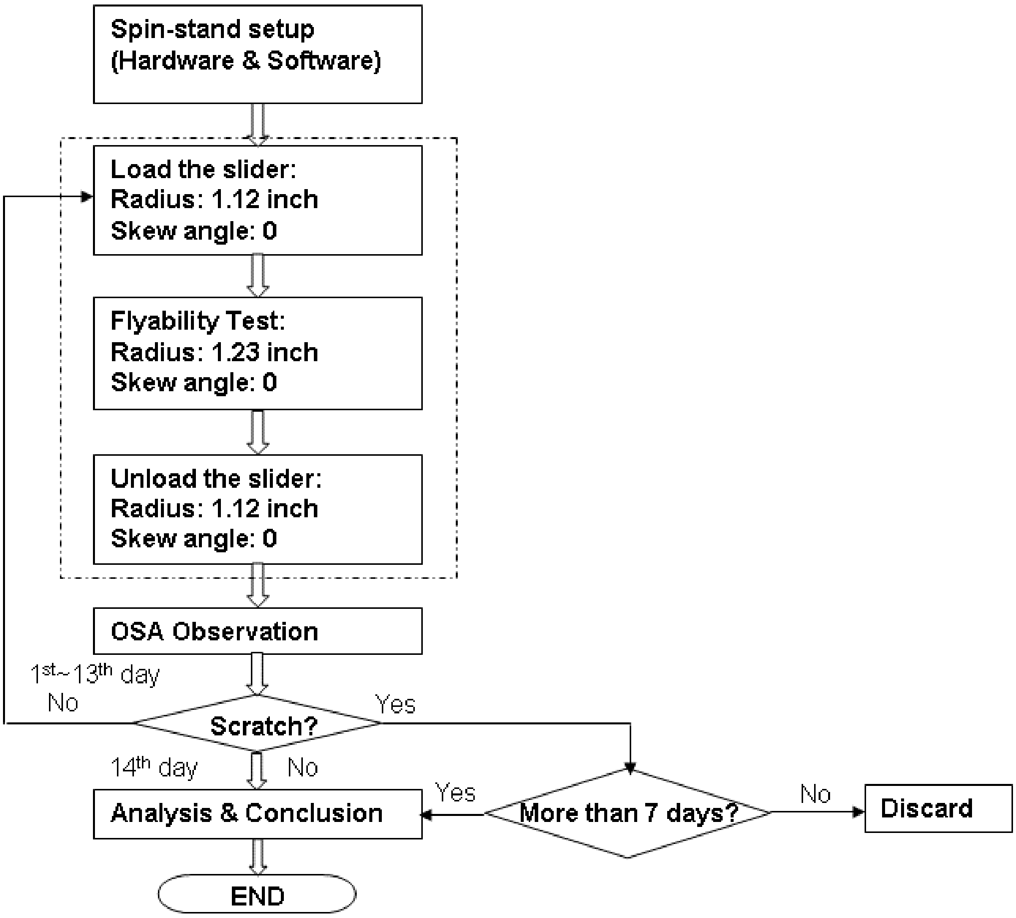

Figure 3.9 Flyability test procedure

3.4.3 Experimental Results

Figure 3.10 shows the sequential OSA images of flying track conditions of the Phase-Shift channel (a) and the P_specular channel (b) with flying time on track. According to the principle of OSA imaging, since no bright tracks appear in the P-specular images, we may conclude that there is no obvious carbon wear after long time flying of the slider. But from the Phase-Shift images, lubricant redistribution is evident.

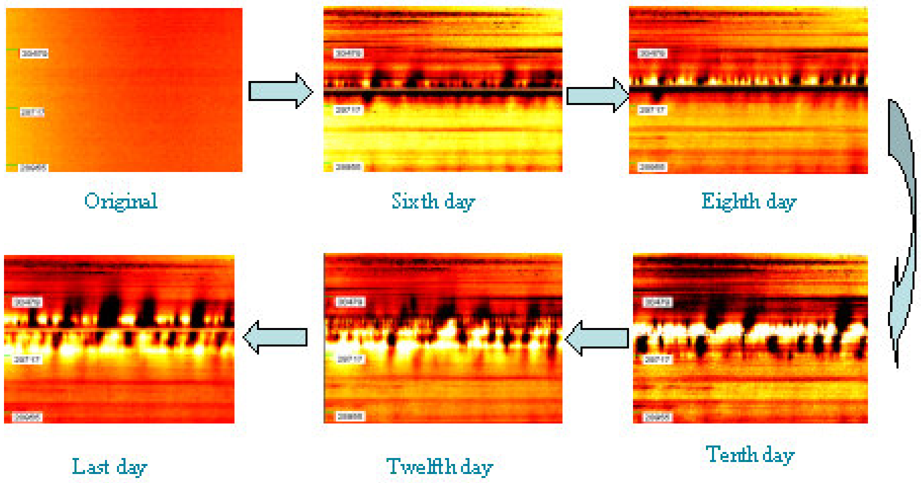

(a) Images of Phase Shift channel

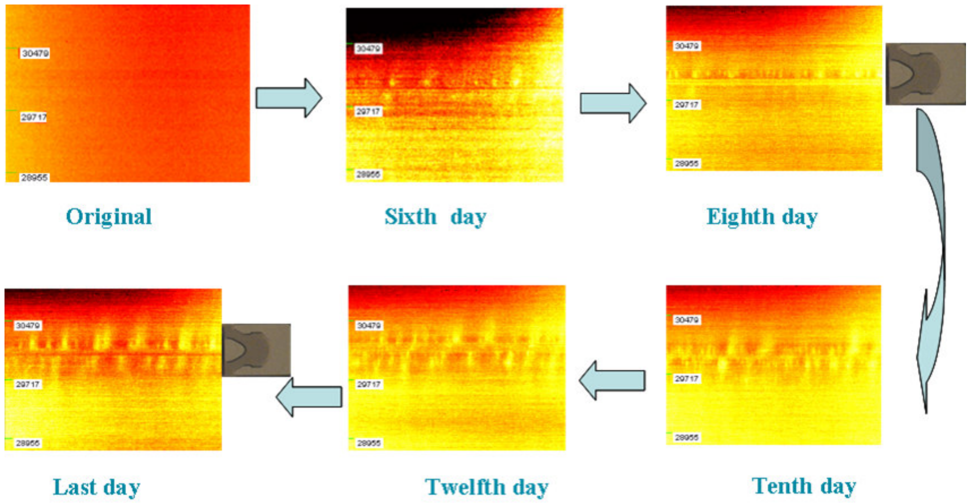

(b) Images of P-polarized light channel

Figure 3.10 Disk track variations during 14 days' flyability testing

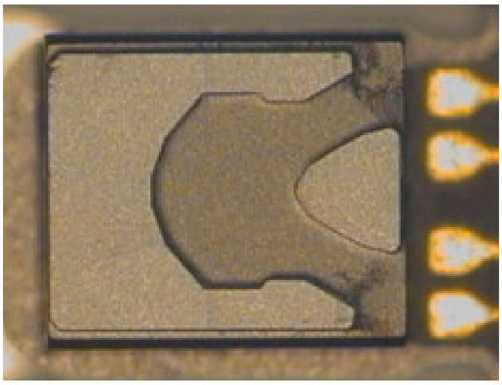

Figure 3.11 Air-bearing surface after 14 days' flyability test

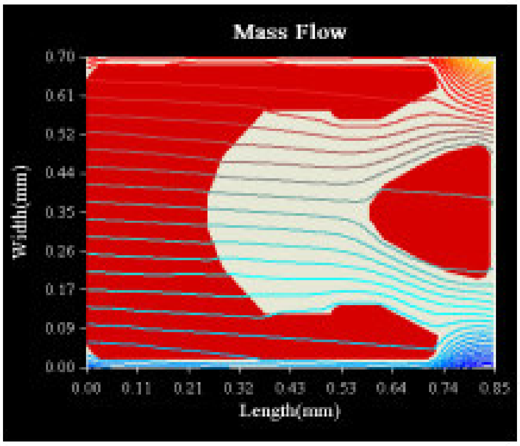

Figure 3.12 Air-flow on air bearing surface

Figure 3.11 shows the air-bearing surface after 14 days' flyability test. It is shown that there is accumulation of lubricant around the trailing end of the two side rails of the Panda II slider. This is because the high pressure at the trailing pad pushes the air to flow towards sides of the air-bearing surface, shown in Figure 3.12. Flying height of the slider is tested after the experiments. The result shows that the flying heights increase by 1~2 nm. This may be due to the transferring of degraded lubricant to slider surface.

3.5 Summary

In this chapter, the disk morphology characteristics and its effects on flying height modulation were first discussed. Then a testing platform was set up to experimentally study the flying height modulation caused by disk waviness with a flying height of 3.5 ~ 4 nm. The results show that the flying height modulation (Panda II slider) caused by disk waviness is in the range of -0.3 nm ~ +0.3 nm. Lastly, long-termed flyability test was carried out to study the long termed robustness of the head disk interface between the Panda II slider and a super-smooth disk. The results suggest that the Panda II slider could pass the long-term flyability test without observable surface damage over the testing track.

Chapter 4

Exploration of Technologies Towards Small Flying Height Modulation

Reliable reading and writing of magnetic data would require the transducer location on the slider fluctuate no more than ±10 % of the nominal flying height, which means fluctuation of no more than ±0.2~0.4 nm when the flying height reduces to 2~4 nm in order to achieve areal density of 1 Tera-bit per square inch (Tbit/in^2)[37].

The experimental results in Chapter 3 show that the flying height modulation caused by disk morphology of the Panda II slider is in the range of -0.3~+0.3 nm. This range of the flying height modulation is still too large for achieving areal density of 1 Tbit/in^2, since except for the disk morphology, there are many other factors (such as flying contact, inter-molecular interaction etc) that will affect the flying stability of the slider and make the flying height modulation easily exceed the fluctuation range of ±0.2~0.4 nm. Thus it is necessary to optimize the air bearing surface design to minimize the flying height modulation caused by disk waviness.

In this chapter, the mechanism of the flying height modulation caused by disk waviness is first investigated by using an analytical model. Then the parameters' effects on the flying height modulation are analyzed and optimization of air-bearing surface is investigated. Based on the analytical and optimization results, a new kind of air bearing surface design is developed which shows the smallest flying height modulation according to available literatures published.

4.1 Dynamic Response of Air Bearing Sliders Due to Disk Waviness

4.1.1 Slider-Air Bearing System

Slider air bearing system is actually a mechanical system. The disk waviness can be considered as a kind of excitation (input) and the vibrations of the slider as the response (output), as illustrated in Figure 4.1 [38].

Figure 4.1 Schematic drawing of a controlled system

In a controlled system, frequency response function (FRF) is normally used to characterize the input-output relationship of the system. It can be expressed as:

$$G(i\omega) = \frac{Y(i\omega)}{X(i\omega)} \tag{4.1}$$

Here, $i^2 = -1$, ω is the angular velocity which equals to 2π times of the waviness frequency, *X* is the input which is the disk waviness in this case and *Y* is the output function which is the flying height modulation. *G* is the frequency response function of the system, which is determined by the system's modal parameters, i.e., its mass, air bearing stiffness and damping.

For a kind of slider air bearing surface, if the frequency response function of its air bearing system *G* is derived, the flying height modulation *Y* can be obtained directly for a kind of disk waviness *X* by

$$Y(i\omega) = G(i\omega) \times X(i\omega) \, . \tag{4.2}$$

Thus, one important thing is to derive the frequency response function of a slider air bearing system.

In the following, the dynamic characteristic of the slider is investigated, which is necessary for further investigation to attain the frequency response function of the slider air bearing system. Then a random disk surface is generated which can be used to quantitatively describe the surface smoothness of the disk morphology.

4.1.2 Dynamic Characteristics of Air Bearing Sliders

As a rigid body, the slider generally has 3 degree of freedoms (3-DOF) of vertical translation, pitch and roll angular motions. Figure 4.2 shows the slider geometry and coordinate system [39, 40].

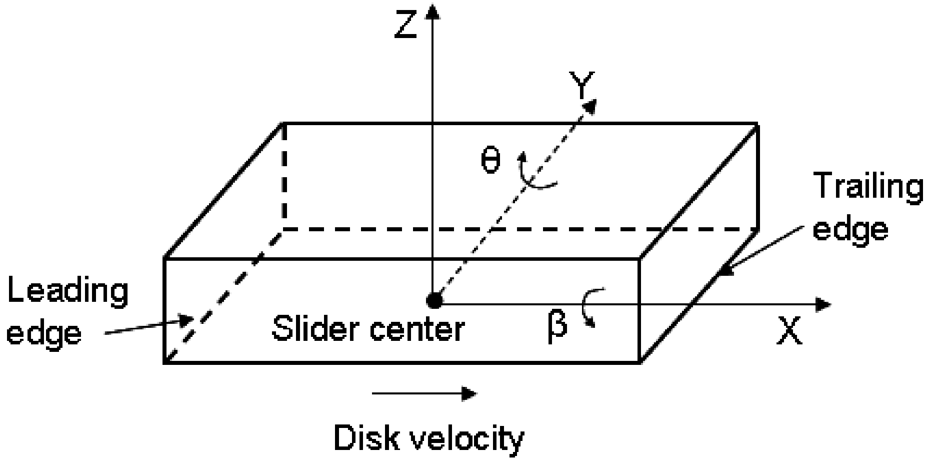

Figure 4.2 Schematic diagram of the slider geometry and coordinate system

Assuming the slider vibrates in the range near its steady flying state, the governing equations for the motion of the slider can be expressed as:

$$m\frac{d^2z}{dt^2}+c_z\frac{dz}{dt}+k_z z=f_z(t)+\iint_A (p-p_s)dA \tag{4.3}$$

$$J_\theta\frac{d^2\theta}{dt^2}+c_\theta\frac{d\theta}{dt}+k_\theta\theta=f_\theta(t)-\iint_A (p-p_s)xdA \tag{4.4}$$

$$J_\varphi\frac{d^2\varphi}{dt^2}+c_\varphi\frac{d\varphi}{dt}+k_\varphi\varphi=f_\varphi(t)-\iint_A (p-p_s)ydA \tag{4.5}$$

Here, z, θ, and φ are the slider's vertical displacement (from the steady flying condition) at the slider's center, and its pitch and roll angles; m, J_θ, and J_φ are the mass and inertia moments of the slider; $k_z, k_\theta, k_\varphi, c_z, c_\theta$ and c_φ are stiffness and damping coefficients of the suspension in the three directions. $f_z(t), f_\theta(t)$ and $f_\varphi(t)$ are external excitation forces; p and p_s are pressure profiles in the vibration state and steady flying state, governed by the generalized Reynolds equation:

$$\frac{\partial}{\partial x}\left(ph^3Q\frac{\partial p}{\partial x}\right)+\frac{\partial}{\partial y}\left(ph^3Q\frac{\partial p}{\partial y}\right)=6\mu V_x\frac{\partial(ph)}{\partial x}+6\mu V_y\frac{\partial(ph)}{\partial y}+12\mu\frac{\partial(ph)}{\partial t} \tag{4.6}$$

where h is the air bearing thickness; μ the ambient gas viscosity; V_x and V_y the gas velocity components in the x and y directions; Q a flow factor to account for gaseous rarefaction effects. Simultaneously solving these equations, the vibration responses for given disturbances can be obtained.

For small disturbances to its steady flying state, assuming the system is linear, time-invariant, self-adjoint, and with viscous damping, Eqs. (4.3) to (4.5) can be written as:

$$[M]\{\ddot{u}\}+[C]\{\dot{u}\}+[K]\{u\}=\{f(t)\} \tag{4.7}$$

where

$$\mathbf{M}=\begin{bmatrix} m & & \\ & J_\theta & \\ & & J_\varphi \end{bmatrix} \quad \mathbf{C}=\begin{bmatrix} c_{11} & c_{12} & c_{13} \\ & c_{22} & c_{23} \\ sym & & c_{33} \end{bmatrix} \quad \mathbf{K}=\begin{bmatrix} k_{11} & k_{12} & k_{13} \\ & k_{22} & k_{23} \\ sym & & k_{33} \end{bmatrix} \tag{4.8}$$

here m, J_θ and J_φ are the mass, pitch moment of inertia and roll moment of inertia of the slider, respectively, [C] and [K] are symmetric matrices, and $\{u\}=\{z,\theta,\varphi\}^T$ is the vibration displacement vector of the slider.

The Parameter Identification Program (PIP), developed by the Computer Mechanics Lab (CML) of the University of California at Berkeley, uses the system identification method to estimate the system's parameters [39]: the physical matrices of the mass$[M]$, stiffness $[K]$and damping$[C]$. Such a program is used in this thesis for the dynamic performance analysis of the slider.

Firstly, the steady solution is obtained from Eq. (4.7). Next, a small initial velocity $\dot{z}_0$ of the slider in the vertical direction is specified. It is characterized as an impulse force $m\dot{z}_0\delta(t)$ ($\delta(t)$ is Dilac's delta function). The responses of the slider in the three motion directions are calculated, and they are subtracted from the steady solution to obtain the vibration responses$\{u(t)\}$. Then, the impulse response function (IRF) of the system, defined by

$$\{h(t)\} = \frac{\{u(t)\}}{m\dot{z}_0} \tag{4.9}$$

is calculated. The Fourier transformations of the impulse response functions for this disturbance are the frequency response functions (FRFs) H_{11}, H_{21}, and H_{31}. Through a similar procedure, $H_{\kappa\lambda}$ (k=1, 2, 3; λ=2, 3) can also be calculated by separately giving an impulse in the pitch and roll directions. As a result, all elements of the frequency response functions matrix $[H]_{3x3}$ of the system are obtained.

From Eq. (4.8), relationships between the frequency response functions and the modal parameters can be found as

$$\left[\bar{H}\right]_{3\times3} = \sum_{j=1}^{3}\left[\frac{\{\varphi\}_j\{\varphi\}_j^T}{i(i\omega - s_j)} - \frac{\{\varphi^*\}_j\{\varphi^*\}_j^T}{i(i\omega - s_j^*)}\right] = \frac{[N(s)]_{3\times3}}{[D(s)]_{3\times3}} \tag{4.10}$$

$$s_j = -2\pi\zeta_j f_j + i2\pi\sqrt{1-\zeta_j^2}\, f_j \tag{4.11}$$

where ζ_j, f_j and $\{\varphi\}_j$ are the modal damping ratio, frequency and shape of mode j. *D(s)* and *N(s)* are orthogonal polynomials of order 2 and 1+n_a, respectively, and n_a is an additional order to compensate for nose effects ($n_a \geq 0$).

Let $s = i2\pi f$, the six roots $s_j (j = 1, 2, \ldots 6)$ can be found from $\left\| [D(s)] \right\| = 0$. Then

$$\{\varphi\}_j \{\varphi\}_j^T = i \frac{[N(s)]}{d[D(s)]/ds} |_{s=s_j}, j = 1, 2, 3 \tag{4.12}$$

Three estimations of each $\{\varphi\}_j$ can be directly obtained from Eq. (4.12), and the averaged results are then used as the final estimation of the mode shape.

The estimated modal parameters should satisfy the following orthogonality properties

$$[\Psi]^T \begin{bmatrix} C & M \\ M & 0 \end{bmatrix} [\Psi] = i \begin{bmatrix} [I] & 0 \\ 0 & -[I] \end{bmatrix}$$

$$[\Psi]^T \begin{bmatrix} K & 0 \\ 0 & -M \end{bmatrix} [\Psi] = \begin{bmatrix} -i[\Lambda] & 0 \\ 0 & i[\Lambda]^* \end{bmatrix} \tag{4.13}$$

where

$$[\Psi] = \begin{bmatrix} [\phi] & [\phi]^* \\ [\phi][\Lambda] & [\phi]^*[\Lambda]^* \end{bmatrix}, \ [\phi] = \left[\{\varphi\}_1, \{\varphi\}_2, \{\varphi\}_3 \right]$$

$$[\Lambda] = \begin{bmatrix} s_1 & & \\ & s_2 & \\ & & s_3 \end{bmatrix}, \ [I] = \begin{bmatrix} 1 & & \\ & 1 & \\ & & 1 \end{bmatrix} \tag{4.14}$$

Thus we can calculate the physical (mass, stiffness and damping) matrices. For the suspension-slider-air bearing system, the estimated $[M]$, $[K]$ and $[C]$ are effective mass, stiffness and damping matrices of the system.

Table 4.1 lists the estimated results of the physical matrices of the Panda II slider. The slider is flying at the radius of 30 mm, disk RPM of 10000, and skew angle of 0°.

Normally, the modal frequency and damping ratios are used to indicate the dynamic characteristics of one system. The estimated modal frequency and damping ratios of the Panda II slider are listed in Table 4.2 and Figure 4.4 shows the nodal lines of the three mode shapes [39].

Table 4.1 Estimated stiffness and damping matrices of Panda II slider (kg, m, s)

Damping	5.44E-2	-5.67E-6	1.21E-7
	-5.67E-6	3.73E-9	4.79E-11
	1.21E-7	4.29E-11	1.43E-9
Stiffness	1.84E6	-4.94E2	4.07E0
	-4.94E2	2.09E-1	-1.29E-4
	4.07E0	-1.29E-4	3.25E-2
Mass	5.82E-7	0	0
	0	4.53E-14	0
	0	0	3.40E-14

Table 4.2 Estimated modal parameters of Panda II slider

Modes	Frequency (kHz)	Damping (%)
#1: 1st pitch	139.4	3.14
#2: roll	155.5	2.15
#3: 2nd pitch	421.9	2.29

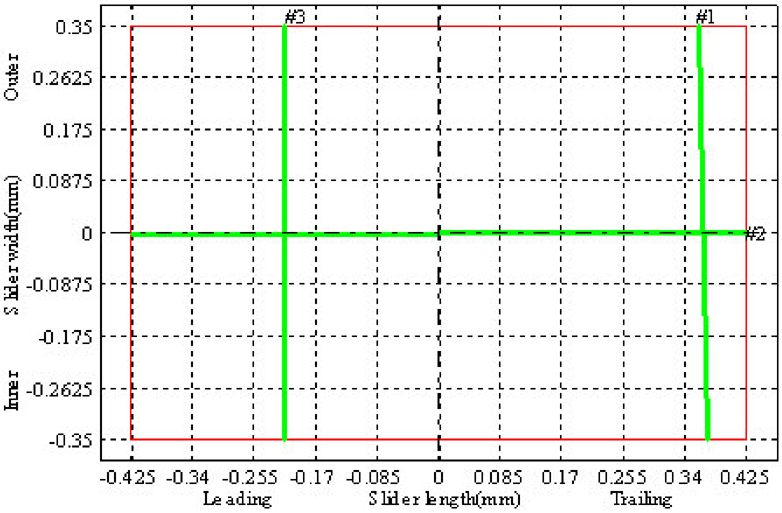

Figure 4.3 Dynamic characteristics of the Panda II slider

From the results, it can be observed that the system has three air bearing vibration modes. The first and the third modes at frequencies of 139.4 kHz and 421.9 kHz, respectively, are coupled with vertical and pitch motion, which can be represented as a rotation of the slider with respect to the nodal lines #1 and #3, respectively. The slider also has a pure roll mode at 155.5 kHz, which is a rotational motion with respect to the nodal line of #2. Because the transducer location is close to the nodal lines of #1 and #2, the effects of modes of #1 and #2 on the flying height modulation are small, but mode #3 has significant influence on the flying height modulation.

4.1.3 Disk Surface Generation

The disk surface used for the simulation can be attained from testing results or by numerical generation. In order to easily compare the effects of the disk features on the flying height modulation, numerical generated disk surface is utilized.

Midpoint displacement method [41, 42] is widely used to generate the random disk surface since it can easily generate self-defined Gaussian random surfaces in spatial and time domains with different frequency characteristics in a prescribed frequency range.

The mathematical description of the random midpoint displacement algorithm is formulated in the following way:

Assume that values $X(0)=0$ and $X(1)$ are given and $X(1)$ is obtained as a Gaussian random number. The interval [0, 1] can be partitioned into two subintervals: [0, 1/2], [1/2, 1], and $X(1/2)$ is defined as the mean of $X(0)+X(1)$ plus a displacement *D* as the Gaussian. The big subdivision gets a big displacement, while the smaller subdivisions get smaller displacement, what makes the line fractal. The initial three steps of the midpoint displacement algorithm are presented as:

$$
\begin{aligned}
X(1/2) &= [X(0)+X(1)]/2+D1 \\
X(1/4) &= [X(0)+X(1/2)]/2+D2 \\
X(3/4) &= [X(1/2)+X(1)]/2+D3 \qquad (4.15)
\end{aligned}
$$

This process is continued with displacements D_n having variance σ_n^2.

The entire process of the random midpoint displacement is based on randomly generated numbers and usually controlled by three variables: the number of iterations, roughness and the number of initial points.

Random number---is generated by the computer using a function called “random number generator”. The random number generator follows a normal random distribution function, with mean $\mu=0$ and variance $\sigma^2=1$.

Roughness---is the factor by which the perturbations are reduced on each iteration. Higher values result in a smoother surface while lower values result in a rougher surface. Roughness (R) is also related to scale (S) by the exponential relationship: $S=(1/2)^R$. Thus, a larger scale means a smaller roughness value and a rougher surface.

Initial points---points where the line is broken during its formation. They are specified to provide some degree of control over the appearance of the surface.

Number of iterations---indicate how many times the process of the midpoint displacement is repeated. At n iterations, there will be 2^n segments of the line.

The procedure for computer iteration is described as following:

```
Start with a single horizontal line segment.
Repeat for a sufficiently large number of times {
    Repeat over each line segment {
        Find the midpoint of the line segment.
        Displace the midpoint in Y by a random amount.
        Reduce the range for random number. }}
```

In our case, firstly, the velocity ν of the disk movement and the interested frequency range f are defined. With the velocity and frequency, the corresponding wavelength (λ) and sampling period (T) can be calculated by:

$$T = \frac{1}{f} = \frac{\lambda}{v} \tag{4.16}$$

At the initial step, a series of discrete random displacements are generated with fundamental period T_0. The displacement values have Gaussian distributions with standard deviation σ_0 and variance σ_0^2. Next these displacements are interpolated with random number at the midpoints of the fundamental period. The variance of additional random displacement is subject to the relationship of the form:

$$\sigma_{n+1}^2 = \left(\frac{1}{2}\right)^p \sigma_n^2 \tag{4.17}$$

where p is the scaling parameter which determines the roll-off characteristics of the amplitude and power spectral of the surface of the disk.

The higher frequency components can be reduced by increasing the p value. If the mean amplitude spectrum $A(f)$ at frequency f is represented by:

$$A(f) = Bf^{-\beta} \tag{4.18}$$

the relationship between p and β can be written as $\beta = (p+1)/2$.

If the disk velocity v is chosen as 30 m/s, the initial sampling period T_0 is 32 μs, which corresponds to a sampling distance or wavelength λ_0 of 960 μm. Sampling 196 points can cover 6.272 ms and 188.16 mm. After repeating 5 times of mid-point interpolation, the sampling period of $T_5=1$ μs corresponds to a sampling distance or wavelength λ_5 of 30 μm.

Thus the initial sampling corresponds to the frequency of 31.25 kHz and after 5 times of itineration, it corresponds to the frequency of 1 MHz.

From the results above, a random disk surface, with amplitude spectrum of roll-off characteristics in the range of 31.25 kHz ~1 MHz has been generated. The disk smoothness features can be adjusted by changing the scaling parameter p. The amplitude spectrum of the disk with frequency lower than 31.25 kHz is considered to be constant. Figure 4.4 shows the generated disk surface, where the scaling parameter p is 2.

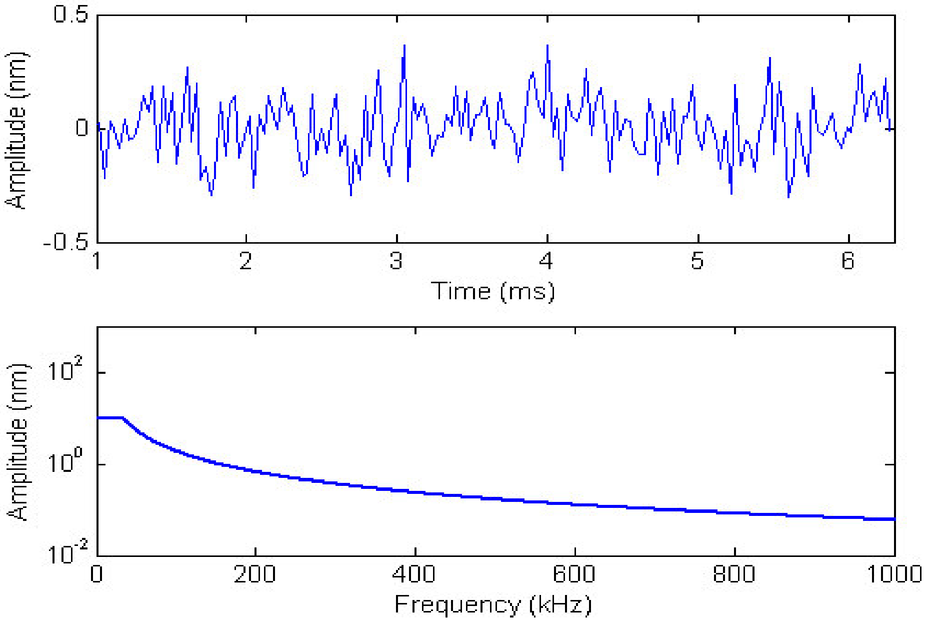

Figure 4.4 Generated disk surface (top: spatial domain; bottom: frequency spectrum)

4.2 Analytical Model for Slider Air Bearing System

From the results above, the random disk surface morphology has been generated, and the dynamic characteristics of the slider have been attained. The next step is to investigate the mechanism of the flying height modulation caused by the disk waviness. The Panda II slider is used again for this analysis.

The equation of motion of the slider can be described in Eq. (4.7), or re-written as

$$\mathbf{M}\ddot{\mathbf{u}} + \mathbf{C}\dot{\mathbf{u}} + \mathbf{K}\mathbf{u} = \mathbf{F} \tag{4.19}$$

Matrices $[M]$, $[K]$ and $[C]$ are illustrated in Eq. (4.8). They have been attained using the Parameter Identification Program (PIP) simulator developed by the Computer Mechanics Lab of the University of California at Berkeley and listed in Table 4.1. In the following, an analytical model is utilized to study how these stiffness and dampers are distributed on the air bearing surface of the slider.

Figure 4.5 shows the analytical model of a slider-air bearing system. The slider is considered as a rigid block with mass *m*, pitch moment of inertia J_θ and roll moment of inertia J_φ. The suspension is modeled as 3 springs (k_z, k_θ, k_φ) and dampers (c_z, c_θ, c_φ).

Researches have been reported to model the air bearing effect between the slider and the disk. K. Iida et al. [43-47] et al. modeled the air bearing of a tri-pad slider as two lumped linear springs and dampers. S. Yu et al. [38] modeled the air bearing of a five-pad slider as six lumped linear springs and dampers, and they are fixed at the air bearing pressure centers of the air bearing pads and the recess. These models can be used to investigate the pads' location effects on the waviness following ability of the slider, but cannot be used to study the pads' size effects.

In our model, the effects of both the pad location and the pad size (length along the track direction) on the flying height modulation caused by disk waviness are taken into account. Figure 4.6 shows the schematic illustration of the air bearing surface of the Panda II slider. Firstly, the air bearing pressure centers of the trailing pad, side pads, leading pads and the recess area are obtained, indicated as c_t, c_s, $c_s^{'}$, c_l, $c_l^{'}$ and c_n, respectively, using CML simulator. In order to study the effects of the pads' length, lines are drawn through the centers of the trailing pad, side pads and leading pads along the track direction, denoted as lines *a*, *b*, *b'*, *c* and *c'*, respectively. And the air bearing forces at the trailing pad, side pads and leading pads are supposed to be distributed along these lines. Since the air bearing surface design of Panda II slider is symmetric, ignoring the effects of the skew angle and roll angle, we can only analyze the characteristics of three lines: *a*, *b*, and *c*. The distance from the center of the slider to the edges of the air bearing pads are denoted as $d_{T1}, d_{T2}, d_{T3}, d_{C1}, d_{C2}, d_{L1}, d_{L2}$, and the distance from the slider center to the transducer and the recess are denoted as d_H and d_N, respectively. Table 4.3 lists these geometric parameters of the Panda II slider.

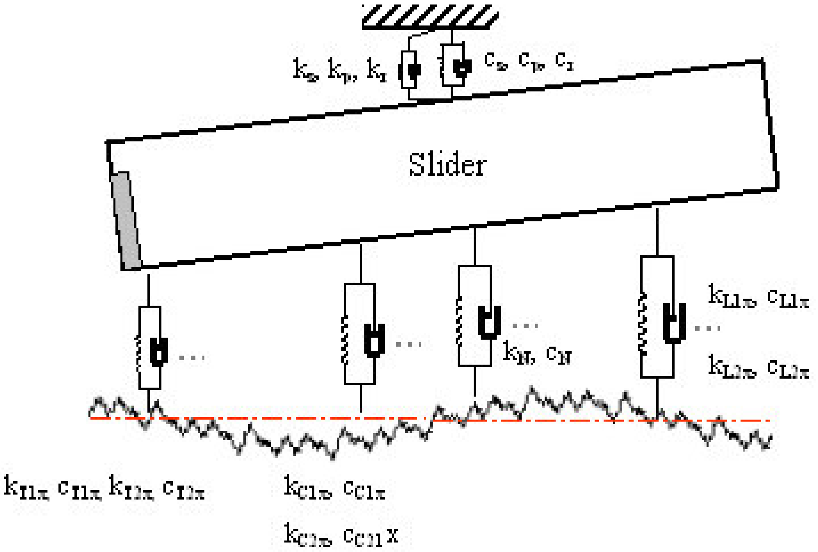

Figure 4.5 Analytical model of a slider-air bearing

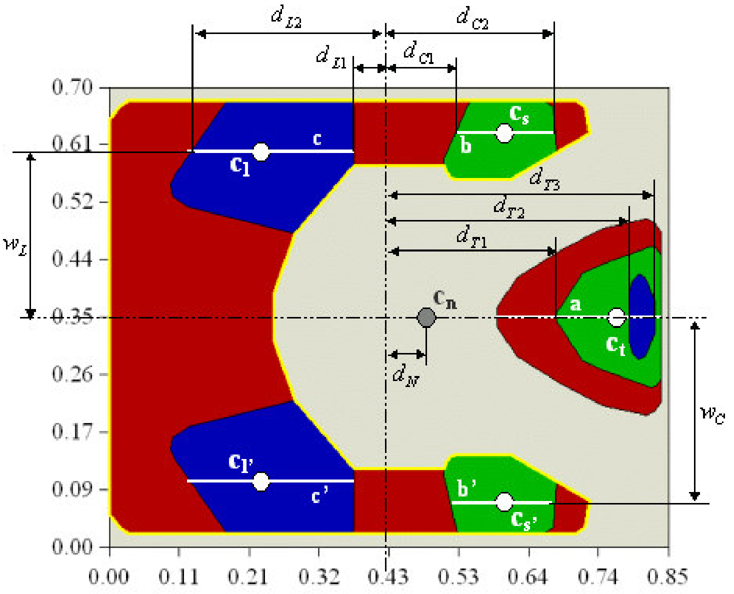

Figure 4.6 Schematic illustration of pad locations and lengths of Panda II slider

Table 4.3 Estimated geometric parameters of Panda II slider (m)

d_{T1} = 0.255 E-3	d_{T2} = 0.365 E-3

d_{T3} = 0.405 E-3	d_{C1} = 0.105 E-3
d_{C2} = 0.235 E-3	d_{L1} = 0.060 E-3
d_{L2} = 0.245 E-3	w_C = 0.290 E-3
d_N = 0.160 E-3	w_L = 0.230 E-3

The air bearing effects along lines *a*, *b* and *c* are modeled as lumped linear springs $k_{T1}(x)$, $k_{T2}(x)$, $k_{C1}(x)$, $k_{C2}(x)$, $k_{L1}(x)$, $k_{L2}(x)$ and dampers $c_{T1}(x)$, $c_{T2}(x)$, $c_{C1}(x)$, $c_{C2}(x)$, $c_{L1}(x)$, $c_{L2}(x)$, where *x* is the distance to the slider center, which means the stiffness and dampers are functions of their distances to the slider center. And the distribution profiles of the springs and dampers are supposed to be the same as the distribution profiles of the air bearing pressure along the lines *a, b,* and *c*, respectively. If the pressure at any location along the lines *a, b,* and *c* is denoted as *p(x)*, then the stiffness *k(x)* can be expressed as $q \times p(x)$, where *q* is a coefficient which we should attain. Similar expression can be obtained for the coefficients of the dampers.

In the following modeling, the coefficients of the stiffness at the trailing pad sub-shallow step and outmost surface, side pads and leading pads are denoted as $q_{T1k}, q_{T2k}, q_{C1k}, q_{C2k}, q_{L1k}, q_{L2k}$ respectively. In the same manner, the coefficients of the dampers at the trailing pad sub-shallow step and outmost surface, side pads and leading pads are denoted as $q_{T1c}, q_{T2c}, q_{C1c}, q_{C2c}, q_{L1c}, q_{L2c}$ respectively.

In order to obtain the coefficients of the stiffness and dampers, we first obtain the air bearing pressure profiles along the lines *a*, *b* and *c*.

Figure 4.7 shows the air bearing pressure profile of the Panda II slider. It can be observed that there is a very high pressure at the trailing pad near the transducer, moderate pressure at two side pads and two leading pads. In addition, the negative pressure is also observed at the recess area of the slider. The vibrations of the slider are induced by the disk waviness through these air bearings.

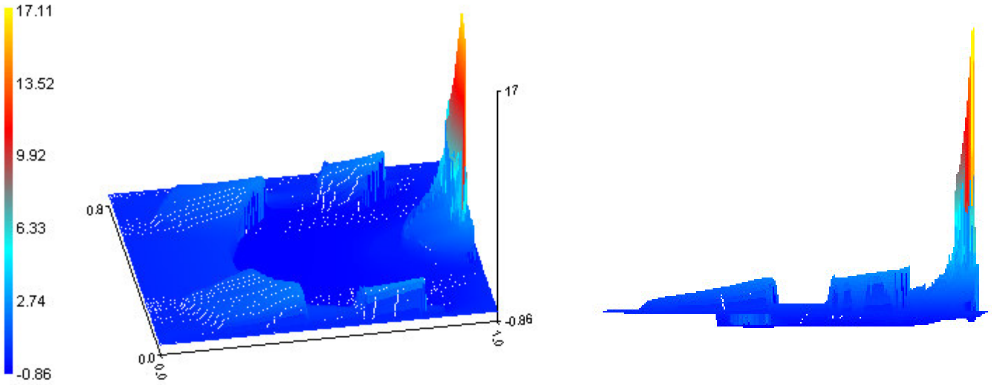

Figure 4.7 Air bearing pressure profile of Panda II slider

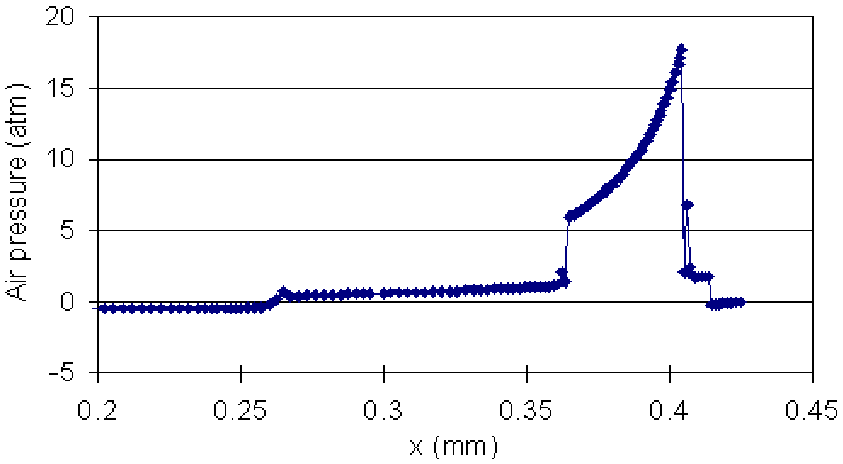

Figure 4.8 Air bearing pressure along line a

Figure 4.8 shows the air bearing pressure profile along the line *a* of the trailing pad, where coordinate *x* is the distance from the slider center, and coordinate *y* is the air bearing pressure relative to ambient pressure. It is observed that there is a pressure jump between the outmost surface area and sub-shallow step area. Thus we model these two areas as separate sets of springs and dampers. The profiles at the sub-shallow step and the outmost surface at the trailing pad are shown in Figure 4.9 (a) and (b), respectively, and they can be fitted to be two-order polynomials. In the same manner, the pressure profiles along lines b and c are attained, as illustrated in Figures 4.10 and 4.11. They both have linear relationships to the x coordinate.

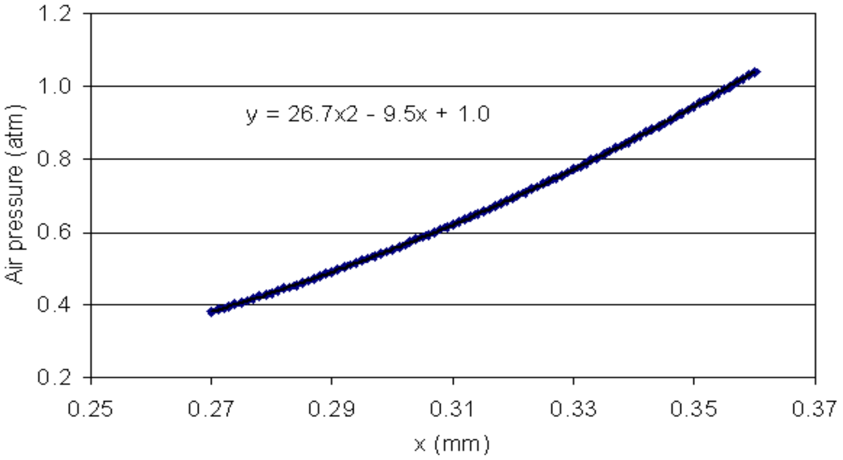

(a) Sub-shallow step

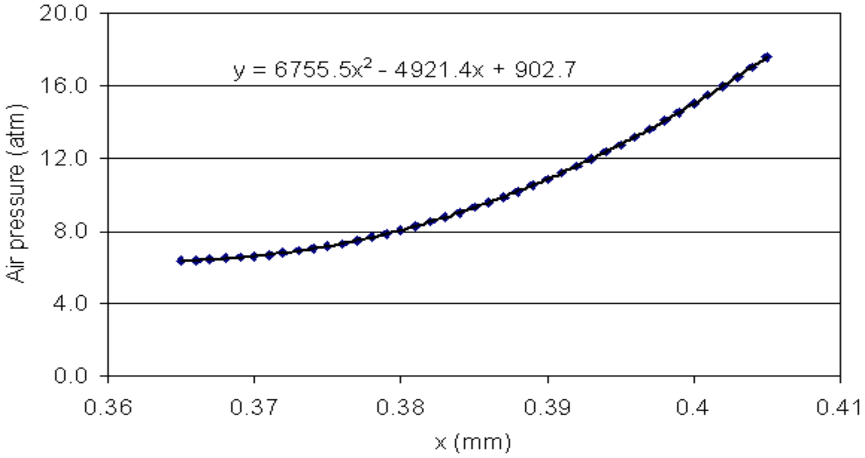

(b) Outmost surface

Figure 4.9 Air bearing pressure profile along the line *a*

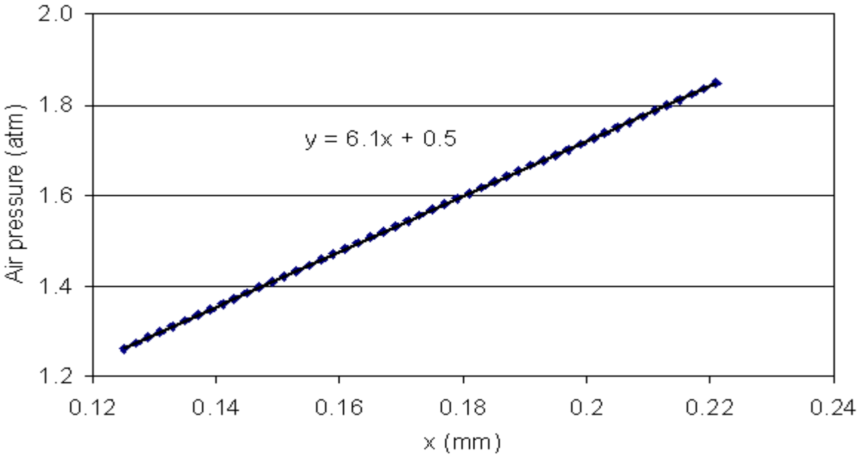

Figure 4.10 Air bearing pressure profile along the line *b*

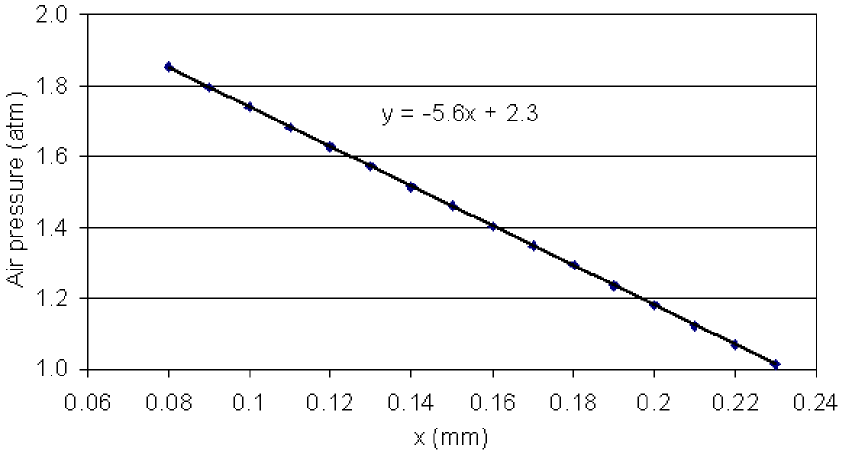

Figure 4.11 Air bearing pressure profile along the line *c*

Then the stiffness on the trailing pad sub-shallow step and outmost surface, side pads and leading pads can be expressed by:

$$k_{T1}(x) = q_{T1k} \times (26.7x^2 - 9.5x + 1.0)$$

$$k_{T2}(x) = q_{T2k} \times (6755.5x^2 - 4921.4x + 902.7)$$

$$k_{C1}(x) = q_{C1k} \times (6.1x + 0.5)$$

$$k_{C2}(x) = q_{C2k} \times (6.1x + 0.5)$$

$$k_{L1}(x) = q_{L1k} \times (-5.6x + 2.3)$$

$$k_{L2}(x) = q_{L2k} \times (-5.6x + 2.3) \qquad (4.20)$$

The dampers at the trailing pad sub-shallow step and outmost surface, side pads and leading pads can be expressed by similar manner, but with coefficients of $q_{T1c}, q_{T2c}, q_{C1c}, q_{C2c}, q_{L1c}, q_{L2c}$ respectively.

With those geometric parameters shown in Table 4.3 and stiffness and dampers, the components in matrices of [*K*] and [*C*] in Eq. (4.8) can be expressed as follows:

$$
\begin{aligned}
k_{11} &= k_S + \int_{dT1}^{dT3} k_T(x)dx + \int_{dC1}^{dC2} k_{C1}(x)dx + \int_{dC1}^{dC2} k_{C2}(x)dx + \int_{dL1}^{dL2} k_{L1}(x)dx + \int_{dL1}^{dL2} k_{L2}(x)dx + k_N \\
k_{12} &= k_{21} = -\int_{dT1}^{dT3} k_T(x)xdx - \int_{dC1}^{dC2} k_{C1}(x)xdx - \int_{dC1}^{dC2} k_{C2}(x)xdx + \int_{dL1}^{dL2} k_{L1}(x)xdx + \int_{dL1}^{dL2} k_{L2}(x)xdx - k_N d_N \\
k_{13} &= k_{31} = \int_{dC1}^{dC2} k_{C1}(x)dxw_C - \int_{dC1}^{dC2} k_{C2}(x)dxw_C + \int_{dL1}^{dL2} k_{L1}(x)dxw_L - \int_{dL1}^{dL2} k_{L2}(x)dxw_L \\
k_{22} &= k_\theta + \int_{dT1}^{dT3} k_T(x)x^2dx + \int_{dC1}^{dC2} k_{C1}(x)x^2dx + \int_{dC1}^{dC2} k_{C2}(x)x^2dx + \int_{dL1}^{dL2} k_{L1}(x)x^2dx + \int_{dL1}^{dL2} k_{L2}(x)x^2dx + k_N d_N^2 \\
k_{23} &= k_{32} = -\int_{dC1}^{dC2} k_{C1}(x)xdxw_C + \int_{dC1}^{dC2} k_{C2}(x)xdxw_C + \int_{dL1}^{dL2} k_{L1}(x)xdxw_L - \int_{dL1}^{dL2} k_{L2}(x)xdxw_L \\
k_{33} &= k_\varphi + \int_{dC1}^{dC2} k_{C1}(x)dxw_C^2 + \int_{dC1}^{dC2} k_{C2}(x)dxw_C^2 + \int_{dL1}^{dL2} k_{L1}(x)dxw_L^2 + \int_{dL1}^{dL2} k_{L2}(x)dxw_L^2
\end{aligned}
\tag{4.21}
$$

$$
\begin{aligned}
c_{11} &= c_S + \int_{dT1}^{dT3} c_T(x)dx + \int_{dC1}^{dC2} c_{C1}(x)dx + \int_{dC1}^{dC2} c_{C2}(x)dx + \int_{dL1}^{dL2} c_{L1}(x)dx + \int_{dL1}^{dL2} c_{L2}(x)dx + c_N \\
c_{12} &= c_{21} = -\int_{dT1}^{dT3} c_T(x)xdx - \int_{dC1}^{dC2} c_{C1}(x)xdx - \int_{dC1}^{dC2} c_{C2}(x)xdx + \int_{dL1}^{dL2} c_{L1}(x)xdx + \int_{dL1}^{dL2} c_{L2}(x)xdx - c_N d_N \\
c_{13} &= c_{31} = \int_{dC1}^{dC2} c_{C1}(x)dxw_C - \int_{dC1}^{dC2} c_{C2}(x)dxw_C + \int_{dL1}^{dL2} c_{L1}(x)dxw_L - \int_{dL1}^{dL2} c_{L2}(x)dxw_L \\
c_{22} &= c_\theta + \int_{dT1}^{dT3} c_T(x)x^2dx + \int_{dC1}^{dC2} c_{C1}(x)x^2dx + \int_{dC1}^{dC2} c_{C2}(x)x^2dx + \int_{dL1}^{dL2} c_{L1}(x)x^2dx + \int_{dL1}^{dL2} c_{L2}(x)x^2dx + c_N d_N^2 \\
c_{23} &= c_{32} = -\int_{dC1}^{dC2} c_{C1}(x)xdxw_C + \int_{dC1}^{dC2} c_{C2}(x)xdxw_C + \int_{dL1}^{dL2} c_{L1}(x)xdxw_L - \int_{dL1}^{dL2} c_{L2}(x)dxw_L \\
c_{33} &= c_\varphi + \int_{dC1}^{dC2} c_{C1}(x)dxw_C^2 + \int_{dC1}^{dC2} c_{C2}(x)dxw_C^2 + \int_{dL1}^{dL2} c_{L1}(x)dxw_L^2 + \int_{dL1}^{dL2} c_{L2}(x)dxw_L^2
\end{aligned}
\tag{4.22}
$$

Here, the nonlinear effects of the air bearing stiffness are not taken into account, as we only consider an infinitely small flying height modulation of the slider.

Since there are only six equations, we assume $q_{T1k} = q_{T2k}$. Solving these equations, the coefficients of the stiffness and dampers can be obtained and they are listed in Table 4.4.

Table 4.4 Results of the coefficients for Panda II slider

q_{Tk} = 3.037 E 4	q_{L1k} = 6.343 E 3
q_{C1k} = 3.630 E 3	q_{L2k} = 6.703 E 3

q_{C2k} = 4.605 E 5	k_N = -1.505 E 5
q_{Tc} = 4.569 E -4	q_{L1c} = 4.748 E -4
q_{C1c} = 2.099 E -5	q_{L2c} = 4.427 E -4
q_{C2c} = 3.769 E -5	c_N = 5.375 E -3

Up to now, we have already calculated the left side of Eq. (4.19). In order to calculate the right side of the equation, suppose there is no contact between the slider and the disk, and the disk surface displacements correspond to the points on the lines *a*, *b* and *c* at the trailing pad, side pads, leading pads, the recess and the point related to the transducer are represented as $z_{dTx}, z_{dC1x}, z_{dC2x}, z_{dL1x}, z_{dL2x}, z_{dN}$ and z_{dH}, respectively. F is equal to the air bearing force vector and it can be calculated by

$$\mathbf{F} = \begin{bmatrix} A_T & A_{C1} & A_{C2} & A_{L1} & A_{L2} & A_N \end{bmatrix} \begin{Bmatrix} z_{dTx} \\ z_{dC1x} \\ z_{dC2x} \\ z_{dL1x} \\ z_{dL1x} \\ z_{dN} \end{Bmatrix} + \begin{bmatrix} B_T & B_{C1} & B_{C2} & B_{L1} & B_{L2} & B_N \end{bmatrix} \begin{Bmatrix} \dot{z}_{dTx} \\ \dot{z}_{dC1x} \\ \dot{z}_{dC2x} \\ \dot{z}_{dL1x} \\ \dot{z}_{dL2x} \\ \dot{z}_{dN} \end{Bmatrix} \tag{4.23}$$

where

$$A_T = \begin{Bmatrix} \int_{d_{T1}}^{d_{T3}} k_T(x)dx \\ -\int_{d_{T1}}^{d_{T3}} k_T(x)xdx \\ 0 \end{Bmatrix} \quad A_{C1} = \begin{Bmatrix} \int_{d_{C1}}^{d_{C2}} k_{C1}(x)dx \\ -\int_{d_{C1}}^{d_{C2}} k_{C1}(x)xdx \\ 0 \end{Bmatrix} \quad A_{C2} = \begin{Bmatrix} \int_{d_{C1}}^{d_{C2}} k_{C2}(x)dx \\ -\int_{d_{C1}}^{d_{C2}} k_{C2}(x)xdx \\ 0 \end{Bmatrix}$$

$$A_{L1} = \begin{Bmatrix} \int_{d_{L1}}^{d_{L2}} k_{L1}(x)dx \\ -\int_{d_{L1}}^{d_{L2}} k_{L1}(x)xdx \\ 0 \end{Bmatrix} \quad A_{L2} = \begin{Bmatrix} \int_{d_{L1}}^{d_{L2}} k_{L2}(x)dx \\ -\int_{d_{L1}}^{d_{L2}} k_{L2}(x)xdx \\ 0 \end{Bmatrix} \quad A_N = \begin{Bmatrix} k_N \\ -k_N d_N \\ 0 \end{Bmatrix}$$

$$B_T = \begin{Bmatrix} \int_{d_{T1}}^{d_{T3}} c_T(x)dx \\ -\int_{d_{T1}}^{d_{T3}} c_T(x)xdx \\ 0 \end{Bmatrix} \quad B_{C1} = \begin{Bmatrix} \int_{d_{C1}}^{d_{C2}} c_{C1}(x)dx \\ -\int_{d_{C1}}^{d_{C2}} c_{C1}(x)xdx \\ 0 \end{Bmatrix} \quad B_{C2} = \begin{Bmatrix} \int_{d_{C1}}^{d_{C2}} c_{C2}(x)dx \\ -\int_{d_{C1}}^{d_{C2}} c_{C2}(x)xdx \\ 0 \end{Bmatrix}$$

$$B_{L1} = \begin{Bmatrix} \int_{d_{L1}}^{d_{L2}} c_{L1}(x)dx \\ -\int_{d_{L1}}^{d_{L2}} c_{L1}(x)xdx \\ 0 \end{Bmatrix} \quad B_{L2} = \begin{Bmatrix} \int_{d_{L1}}^{d_{L2}} c_{L2}(x)dx \\ -\int_{d_{L1}}^{d_{L2}} c_{L2}(x)xdx \\ 0 \end{Bmatrix} \quad B_N = \begin{Bmatrix} c_N \\ -c_N d_N \\ 0 \end{Bmatrix} \tag{4.24}$$

Because the side pads and the leading pads are not located on the same track as the transducer, only z_{dTx} has a relation with z_{dH} as follows:

$$z_{dTx}(t) = z_{dH}\left(t + \frac{d_H - d_{Tx}}{V}\right) \tag{4.25}$$

where V is the linear velocity of disk rotation and t is the time.

Substituting Eqs. (4.24) and (4.25) into Eq. (4.23), we have

$$\mathbf{F} = \mathbf{A_T} z_{dH}\left(t + \frac{d_H - d_{Tx}}{V}\right) + B_T \dot{z}_{dH}\left(t + \frac{d_H - d_{Tx}}{V}\right) \tag{4.26}$$

Substituting the Eqs. (4.21), (4.22) and (4.26) into Eq. (4.19), the displacement of the slider center u can be solved.

In order to obtain the flying height modulation at the transducer location of the slider, let

$$\mathbf{v} = \begin{Bmatrix} \mathbf{u} \\ \dot{\mathbf{u}} \end{Bmatrix}, \ \mathbf{w} = \{z_{dH}\} \text{ and } \ \mathbf{y} = \{z_H - z_{dH}\} \tag{4.27}$$

Here, z_H is the displacement of the slider at the transducer location, w is the disk waviness (input) and y is the flying height modulation at the transducer location (output). Thus Eq. (4.19) can be rewritten in state space form as:

$$\begin{aligned}\dot{\mathbf{v}} &= \mathbf{A}\mathbf{v} + \mathbf{B}\mathbf{w} \\ \mathbf{y} &= \mathbf{C}\mathbf{v} + \mathbf{D}\mathbf{w}\end{aligned} \tag{4.28}$$

where

$$A = \begin{bmatrix} 0 & 1 \\ -M^{-1}K & -M^{-1}C \end{bmatrix} \qquad B = \begin{bmatrix} 0 \\ M^{-1} \end{bmatrix}(A_T + sB_T)$$

$$C = \begin{bmatrix} 1 & -d_H & 0 & 0 & 0 & 0 \end{bmatrix} \qquad D = \begin{bmatrix} -e^{\frac{dT-dH}{V}s} \end{bmatrix} \tag{4.29}$$

where $s = i2\pi f$, f is the frequency. Finally, the close form frequency response functions of the slider-air bearing system can be obtained as follows:

$$G(i\omega) = \frac{Y}{W} = \mathbf{C}[i\omega\mathbf{I} - \mathbf{A}]^{-1}\mathbf{B} + \mathbf{D} \tag{4.30}$$

Figure 4.12 shows the frequency response function of the Panda II slider. From Eq. (4.30), the values of the frequency response function are complex numbers and they are represented by the gain and phase. The gain means the amplifying (reducing) effects of the system for an excitation in the amplitude and the phases describe the phase differences between the response and excitation in the frequency domain.

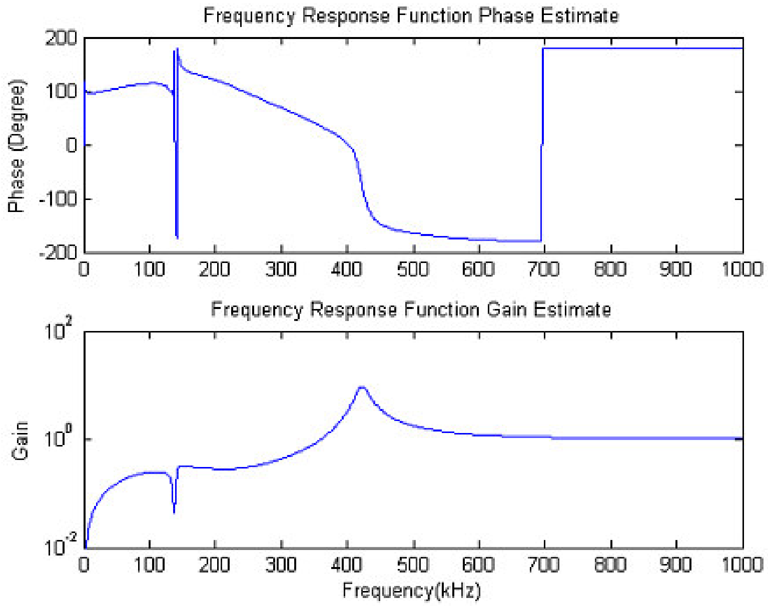

Figure 4.12 Frequency response function of the Panda II slider

From Figure 4.12, the low frequency components of frequency response function are small, which means that low frequency flying height modulation components due to disk waviness are small, or the slider can well follow the disk waviness of long wavelengths. In addition, the frequency response function gain approaches one at high frequencies, which means the flying height modulation components at this range mainly come from the disk waviness, or the slider cannot respond to the disk waviness of short wavelengths. It is also noted that the flying height modulation significantly increases if the air bearing mode of the 2nd pitch (421.9 kHz) is excited.

From the analysis above, the frequency response function of the slider air bearing system has been derived. Then the relationship of the response to the excitation in frequency domain can be described by Eq. (4.2).

4.3 Parameters Effects on Flying Height Modulation

4.3.1 Flying Height Modulation to Waviness Ratio

In order to evaluate the waviness following characteristics, the flying height modulation to waviness ratio is proposed as a measurement of the waviness following ability of a slider, which is defined as:

$$\rho = \frac{\sigma_H}{\sigma_D} \tag{4.31}$$

where the σ_H and σ_D are root mean square (rms) amplitude of the flying height modulation and disk waviness, respectively. Based on the Parseval's theorem, it is known that the rms value of a signal can be estimated from its amplitude spectrum. Considering Eqs. (4-30) and (4-31), we have:

$$\rho = \sqrt{\frac{\sum_{k=0}^{N-1} |Z_{dk}(s)|^2 |G_k(s)|^2}{\sum_{k=0}^{N-1} |Z_{dk}(s)|^2}} \tag{4.32}$$

where Z_{dk} and G_k are the discrete-time Fourier transform (DTFT) of z_d and G, respectively, both of length N, and $s = i2\pi f$, f is the frequency. For a slider air bearing system whose frequency response function is known, we can use the flying height modulation to waviness ratio to evaluate its waviness following ability. In the following section, the effects of the disk surface feature, air bearing stiffness and damping, and air bearing surface design parameters are studied by analyzing the Panda II slider.

4.3.2 Effect of Disk Surface Features

To compare the effects of disk surface features on the flying height modulation, three types of disk surfaces are generated and plotted in Figure 4.13 (top). Their smooth parameters are 1.0, 1.5 and 2.0, respectively. It can be observed that the disk surface has smaller amplitude when the smooth parameter increases.

The gain of the frequency response function and the amplitude spectrum of the flying height modulation are also plotted in Figure 4.13 (middle and bottom). In the simulation, the modal parameters are the same as those listed in Table 4.2.

Figure 4.14 shows the flying height modulation to waviness ratio when the parameter p varies from 1.0 to 2.0. Smoothing the disk surface can result in decreasing the flying height modulation to waviness ratio, and thus increase the waviness following ability of the slider.

The reason may include two parts. From the frequency response function plot, the slider cannot follow the disk waviness at the high frequencies. Smoothing the disk surface can reduce the waviness amplitude at high frequencies and thus reduce the flying height modulation. In addition, the system has a resonance mode at a frequency of 421.9 kHz. The waviness components at this range leads to big components in the flying height modulation spectrum. Reducing waviness amplitude at this range also decreases the flying height modulation components, and therefore, contributes more to the reduction of root mean square value of the flying height modulation.

From these results, it can be concluded that smoothing the disk surface, especially reducing the waviness components around the frequency of resonance mode of slider air bearing system, can reduce the flying height modulation.

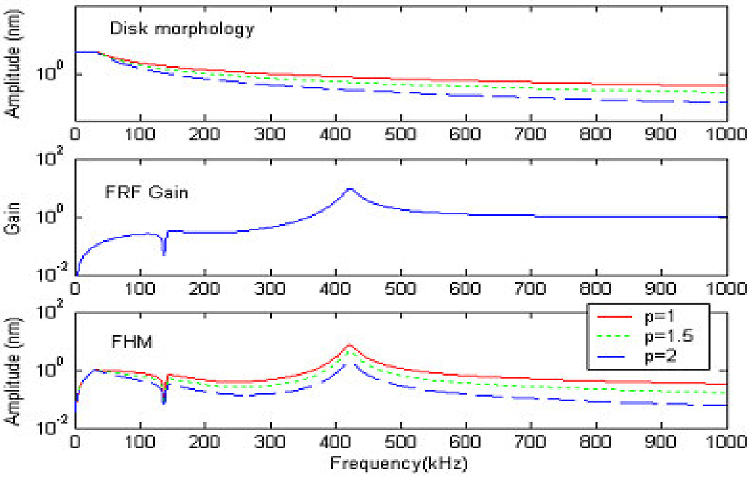

Figure 4.13 Effects of disk surface features on flying height modulation

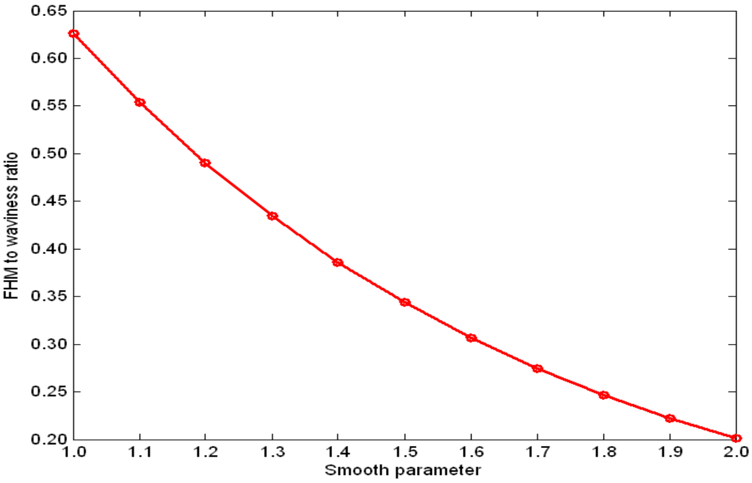

Figure 4.14 Effects of disk surface features on flying height modulation, showing that smoothing the disk surface reduces flying height modulation

4.3.3 Effect of Air Bearing Stiffness and Dampers at Trailing Pad

After the coefficient q_{Tk} is attained, we can calculate the total stiffness at the trailing pad by integrating $k_T(x)$ over the line a. Figure 4.15 shows the frequency response functions and the flying height modulation amplitudes by changing the total stiffness at the trailing pad, where the smoothing parameter of the disk surface p is 1. Figure 4.16 shows the flying height modulation to waviness ratio when the stiffness ranges from 0.5 kT0 to 1.5 kT0, where kT0 is the initial total stiffness at the trailing pad and it is supposed that the slider flies with fixed flying attitude.

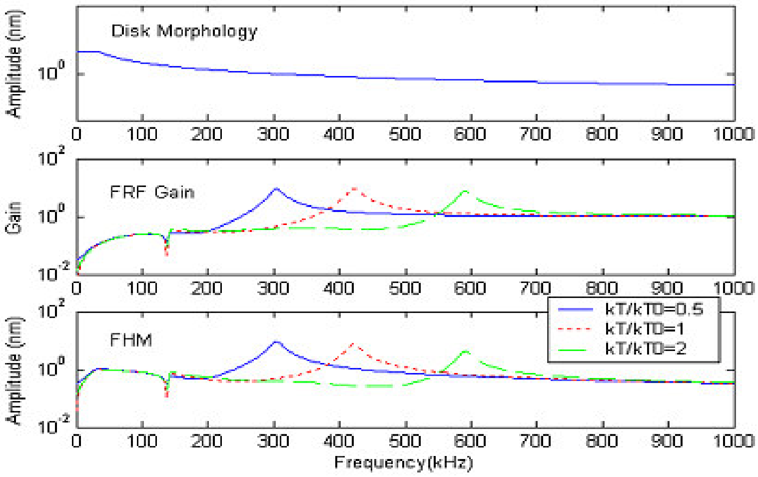

Figure 4.15 Effects of the trailing pad stiffness on flying height modulation

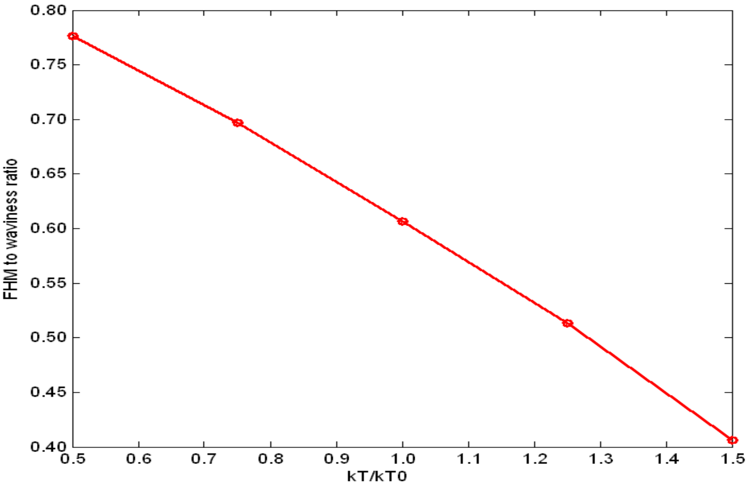

Figure 4.16 Effects of the trailing pad stiffness on flying height modulation, showing that increasing the stiffness reduces flying height modulation

It is apparent that increasing the stiffness at the trailing pad can increase the resonance frequency of the 2nd pitch mode, thus induces better waviness following ability of the slider.

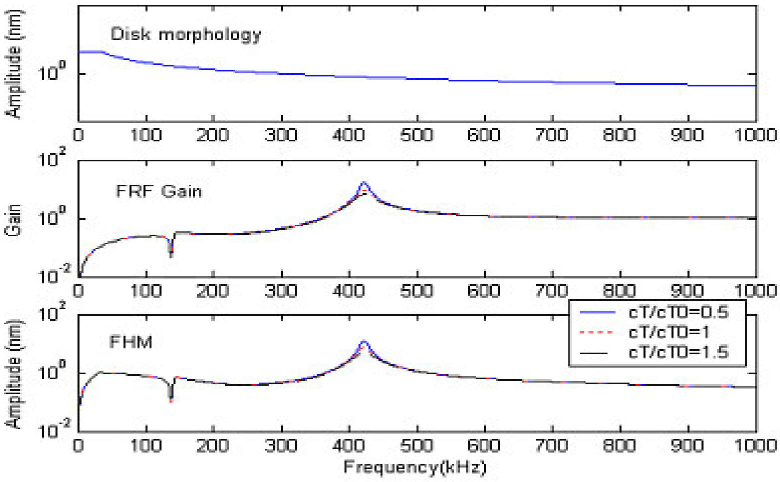

Figure 4.17 Effects of the trailing pad damping on flying height modulation

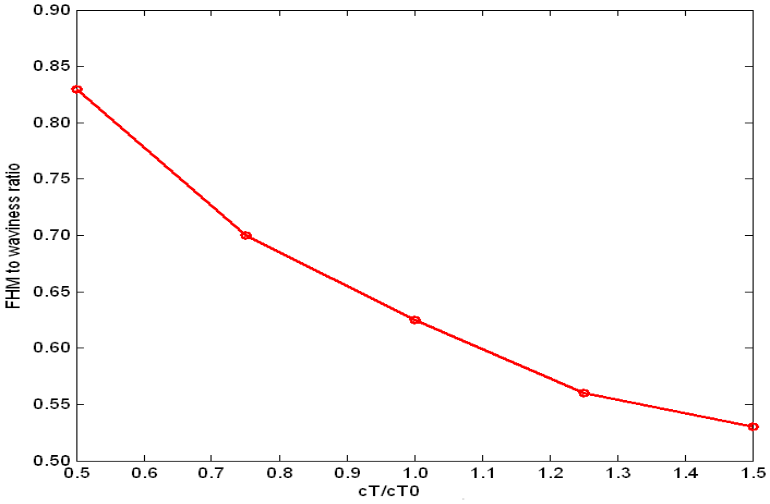

Figure 4.18 Effects of the trailing pad damping on flying height modulation, showing that increasing the damping reduces flying height modulation

The effects of air bearing damping at the trailing pad on the flying height modulation are analyzed and the results are shown in Figures 4.17 and 4.18. From Figure 4.18, the flying height modulation to waviness ratio is reduced from 0.83 to 0.53 when the damping at the trailing pad is increased from 0.5 cT0 to 1.5 cT0, where cT0 is the initial total damping at the trailing pad. From Figure 4.17, higher damping at the trailing pad can reduce the peak of the 2nd pitch mode. Since the flying height modulation components around the 2nd pitch mode are dominant, reduction of the peak amplitude leads to a significant decrease of the flying height modulation and increase of waviness following ability.

4.3.4 Effect of Transducer Position

The location of air bearing center at the trailing pad d_T can be attained by solving the following equation:

$$\int_{d_{T1}}^{d_T} k_T(x)\,dx = \int_{d_T}^{d_{T3}} k_T(x)\,dx \tag{4.33}$$

Figure 4.20 shows the change of the flying height modulation to waviness ratio when the distance ($d_H - d_T$) varies from 0.01 mm to 0.03 mm, where d_H is the distance from the transducer to the slider center. It is seen that a smaller distance between the transducer and the trailing pad air-bearing center results in better waviness following ability of the slider. From Figure 4.19, when the air bearing center at the trailing pad moves to the transducer, it shows better tracking ability in the lower frequency range. And the resonance frequency of the 2nd pitch mode increases as well. This is because smaller distance between the transducer and the trailing pad air-bearing center yields smaller phase delay of the response to the disk waviness of these two points [30].

From analysis above, we conclude that the distance between the transducer position and the trailing pad air-bearing center should be made as small as possible.

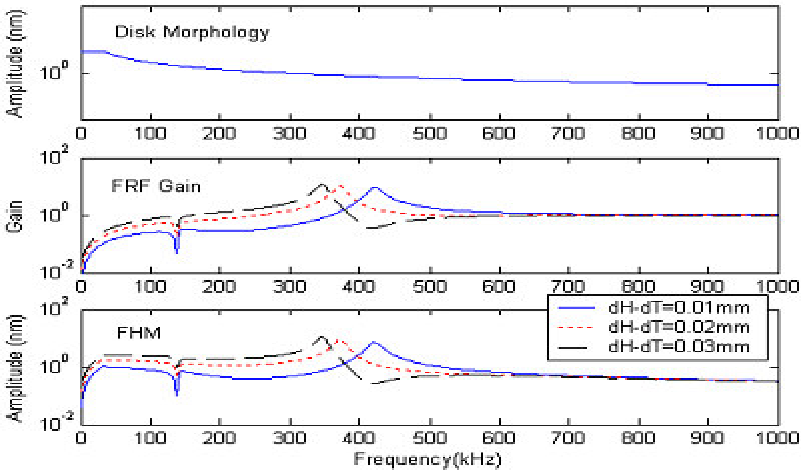

Figure 4.19 Effects of head-gap position on flying height modulation

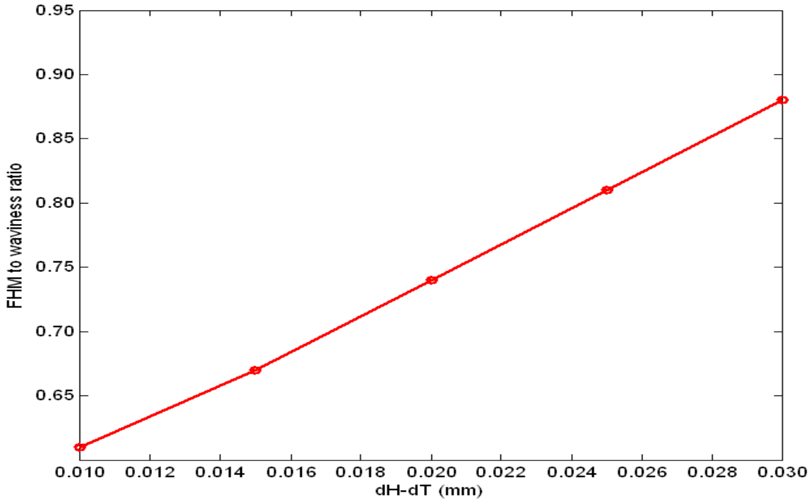

Figure 4.20 Effects of head-gap position on the flying height modulation, showing that reducing the distance between head-gap position and the trailing pad air-bearing centre reduces the flying height modulation

4.3.5 Effect of Trailing Pad Length

In order to investigate the effects of the trailing pad length on the flying height modulation, it is assumed that the slider flies at a fixed attitude. From Figure 4.22, the slider shows best waviness following ability when the length of the outmost surface ranges from 0.05 mm to 0.07 mm. From Figure 4.21, when the length of the outmost surface at the trailing pad reduces from 0.08 mm to 0.02 mm, the slider can follow waviness of low frequency with better performance, while the resonance frequency of the 2nd pitch mode reduces and peak amplitude increases. The reason for the resonance amplitude depressed with longer outmost surface length is that the resultant force of the trailing pad is partly cancelled by the averaging effect of the local restoring force over the trailing pad air-bearing surface. However, if the length is much longer than the wavelength of the 2nd pitch mode resonance frequency, the cancellation of the restoring force occurs in frequency range less than the resonance frequency, and the slider cannot follow the low frequency component of the disk surface.

On the other hand, if the length of the outmost surface of the trailing pad is much shorter than the wavelength of the 2nd pitch mode resonance frequency, the wavelength component corresponding to the 2nd pitch mode resonance frequency of the disk surface strongly excites the 2nd pitch resonance mode of the slider air-bearing system, thus increasing the resonance amplitude.

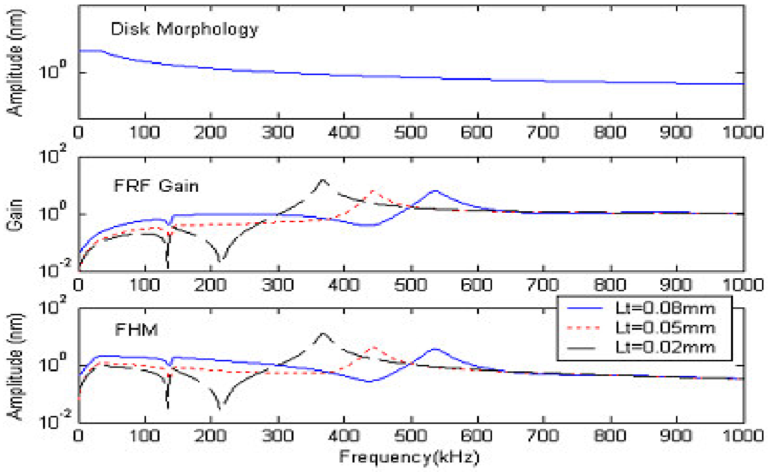

Figure 4.21 Effects of top surface length at trailing pad on flying height modulation

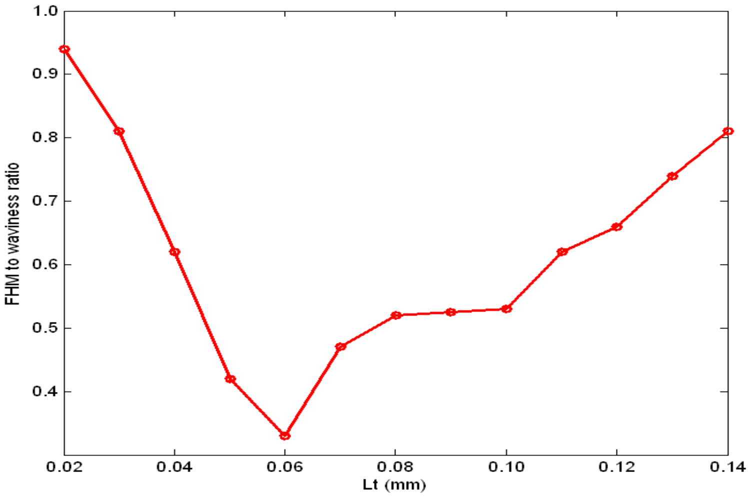

Figure 4.22 Effects of top surface length at trailing pad on flying height modulation, showing that minimum flying height modulation occurs when the top surface length of trailing pad is 0.05 mm

From analysis above, we conclude that the length of the outmost surface at the trailing pad should be designed to be comparable to or shorter than the wavelength of the 2nd pitch mode resonance frequency.

Figures 4.23 and 4.24 show the changes of the flying height modulation and the flying height modulation to waviness ratio when the length of the sub-shallow step layer at the trailing pad changes. It is shown that longer sub-shallow step length improves the waviness following capability of the slider. This is because that longer sub-shallow step length results in the increase of the stiffness. But from these two figures, the effects of changing the sub-shallow step length on the flying height modulation are small compared to the effects of changing the outmost surface length at the trailing pad. This is because the air bearing pressure or stiffness at the outmost surface is much higher than that at the sub-shallow step area at the trailing pad.

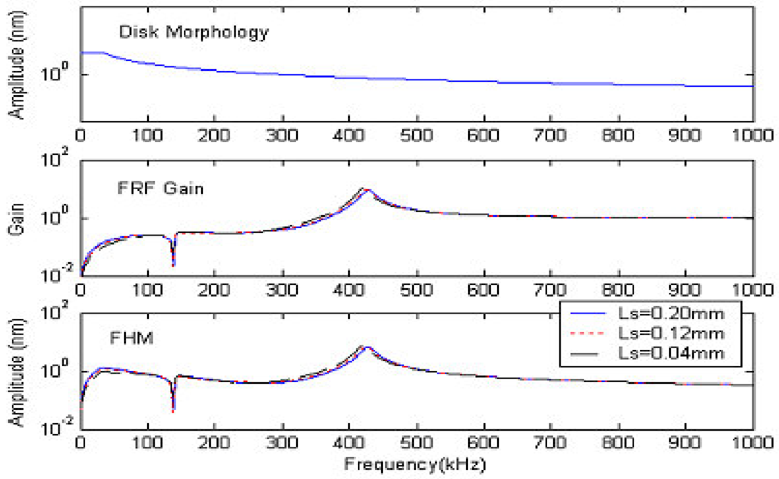

Figure 4.23 Effects of sub-shallow step length at trailing pad on flying height modulation

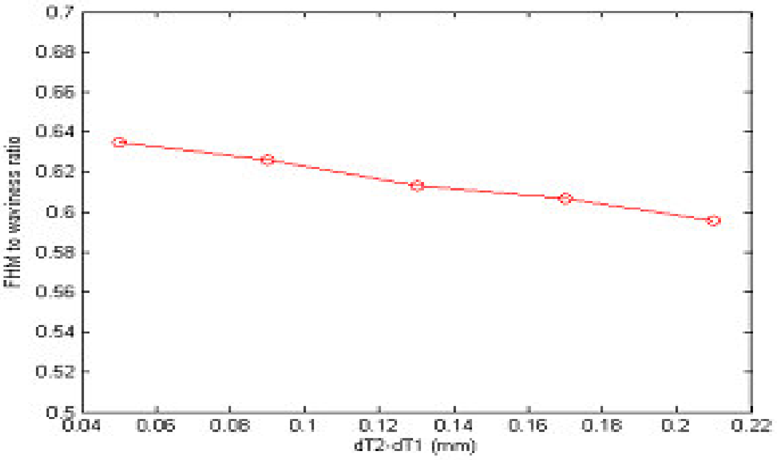

Figure 4.24 Effects of sub-shallow step length at trailing pad on flying height modulation, showing that longer sub-shallow step reduces the flying height modulation

4.3.6 Effect of Side Pad Location and Length

In the same manner, the air bearing centers of the side pads can be obtained by solving the following equation:

$$\int_{d_{C1}}^{d_C} k_C(x)dx = \int_{d_C}^{d_{C2}} k_C(x)dx \tag{4.34}$$

Figure 4.25 shows the flying height modulation to waviness ratio when the air-bearing centers of the side pads change, it can move backward to the trailing edge (to nodal line #1), or it can move forward to the leading edge (to nodal line #3). From Figure 4.3, the distance of nodal line #1 to slider center is about 0.36 mm, and the distance of nodal line #3 to slider center is about 0.21 mm. It is shown that reducing the distance of the air-bearing center of the side pads to nodal lines of #1 and #3 can both decrease the flying height modulation to waviness ratio. The *x* coordinate in Figure 4.25 (b) is negative, which means the air-bearing center of the side pads are moved to the leading edge.

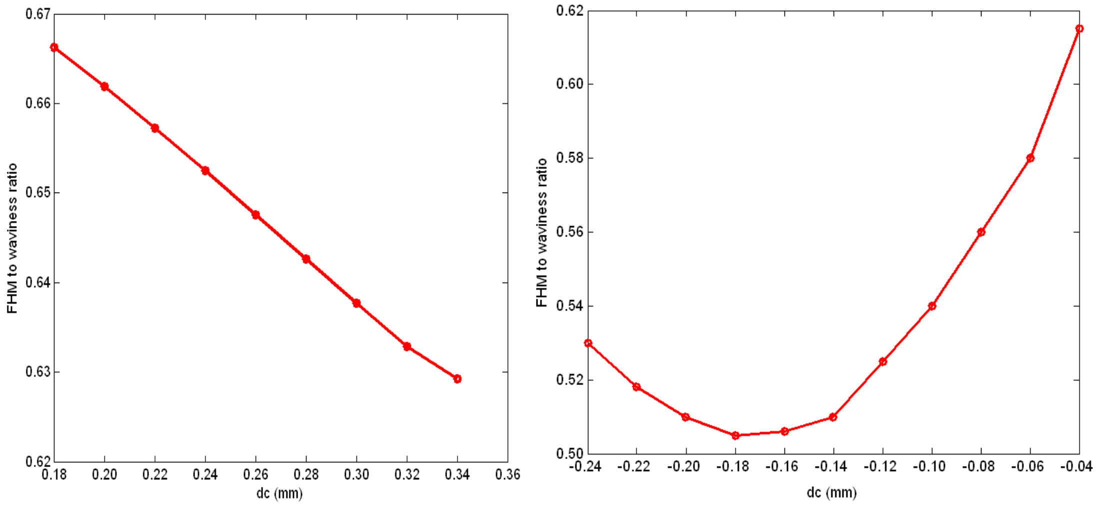

(a) (b)

Figure 4.25 Effects of side pad position on flying height modulation, (a) Center of side pad moves to nodal line #1, (b) Center of side pad moves to nodal line #3, showing that moving the side pad center to the nodal lines reduces flying height modulation

This is also because smaller distance between the side pad centers and the nodal lines yields smaller phase delay of the response to the disk waviness of these two points, which results in smaller flying height modulation. But moving the side pads towards the nodal line of #1 or towards the trailing edge increases the probability of the slider and disk contact.

Figure 4.26 shows the changes of the flying height modulation to waviness ratio when the lengths of the side pads range from 0.06 mm to 0.3 mm, where the side pad center d_c =0.18 mm. It is observed that increasing the length of the side pads improves the waviness following ability of the slider. This is because longer side pads result in the increase of the stiffness and can depress the effects of disk waviness. But the effects of increasing the length of the side pads on waviness following ability are not significant.

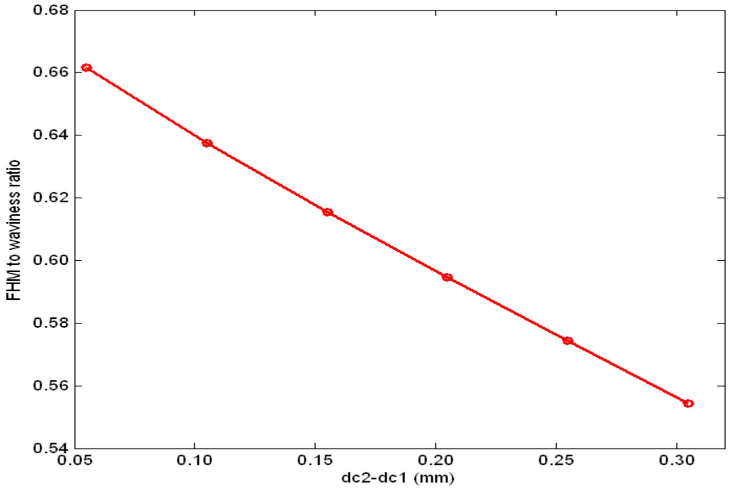

Figure 4.26 Effects of side pads length on flying height modulation, showing that longer side pads reduces flying height modulation

4.3.7 Effect of the Leading Pad Location and Length

Figures 4.27 and 4.28 show the flying height modulation to waviness ratio when the leading pads air-bearing centers and lengths change. It is observed that the effects of the leading pad location and length on the flying height modulation are negligible comparing to the changes of the trailing pad and the side pads. It is because that the leading pad is far away from the transducer position and the flying height is much higher than those at the trailing pad and side pads.

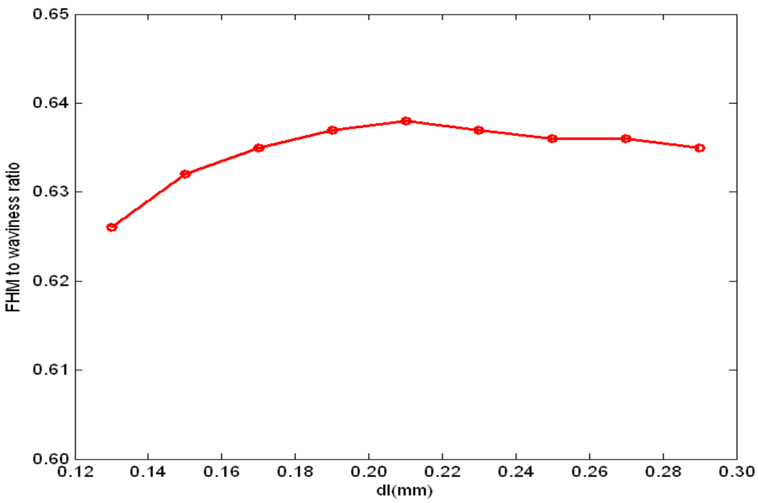

Figure 4.27 Effects of leading pad position on flying height modulation, showing very small effect

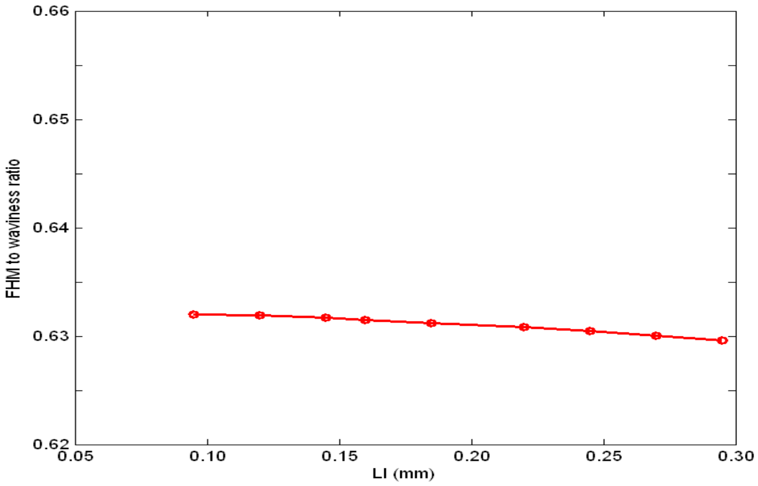

Figure 4.28 Effects of leading pad length on flying height modulation, showing that the effect is negligible

From the above analysis, the length of the outmost surface at the trailing pad and the transducer position have significant effects on the flying height modulation caused by disk waviness. The length of the outmost surface at the trailing pad should be made comparable to or shorter than the wavelength of the 2nd pitch mode resonance frequency, which is about 60 μm for the Panda II slider. On the other hand, the distance between the transducer position and the air bearing center at the trailing pad should be made as small as possible. This can be achieved by having three etching depths at the trailing pad. The air-bearing pressure on the outmost surface at the trailing pad is much higher than other location of the air bearing surface and so is the corresponding stiffness, which makes much shorter distance from the transducer position to the trailing pad air-bearing center possible, comparing the conventional air-bearing surface designs of two etching steps. Though the position and length of side pads and leading pads also have effects on the waviness following ability, the effects are small comparing to that of the trailing pad.

4.4 Air-Bearing Surface Design Optimization for Minimizing Flying Height Modulation Caused by Disk Waviness

4.4.1 Optimization Definition

From the results in the last section, the air bearing pads' locations and lengths or the distribution of air bearing pressure at air bearing surface determine the slider's disk waviness following capability. It is possible to optimize the air bearing pads' locations and lengths to minimize the flying height modulation of the slider caused by disk waviness.

To describe an optimization problem, the design variables must be defined. A vector $\mathbf{x} = \{x_1, x_2, x_3, x_4, x_5, x_6, x_7\}^T$ is employed as the design variable vector, which is defined by the following equations:

$$d_{T3} = x_1 + d_{T30}, d_{T2} = x_2 + d_{T20}, d_{T1} = x_3 + d_{T10}, d_{C2} = x_4 + d_{C20}$$

$$d_{C1} = x_5 + d_{C10}, d_{L2} = x_6 + d_{L20}, d_{L1} = x_7 + d_{L10} \tag{4.35}$$

For panda II slider, the initial values of $d_{T30}, d_{T20}, d_{T10}, d_{C20}, d_{C10}, d_{L20}, d_{L10}$ are listed in Table 4.3.

Then the optimization problem is to minimize the flying height modulation to waviness ratio, while the design variable **x** is constrained between x_b and x_u since the pads at the air bearing surface have limited locations and lengths. The optimization relations can be described as:

$$\text{Minimize: } \rho \tag{4.36}$$

Subject to: $\mathbf{x}_b \leq \mathbf{x} \leq \mathbf{x}_\mathbf{u}$

$$\& \begin{cases} d_{T3} - d_{T2} \geq 0.01e-3 \\ d_{T2} - d_{T1} \geq 0.02e-3 \\ d_{C2} - d_{C1} \geq 0.00e-3 \\ d_{L2} - d_{L1} \geq 0.05e-3 \end{cases}$$

4.4.2 Sequential Quadratic Programming Method

Sequential quadratic programming (SQP) [32] is utilized to find the solution of:

$$f(x^*) = \min_x f(x) \tag{4.37}$$

Subject to: $c_i(x) \geq 0, i = 1, \ldots, m$

Sequential quadratic programming methods attempt to solve a nonlinear program directly. The basic idea is: At each step, a local model of the optimization problem is constructed and solved, yielding a step toward the solution of the original problem.

A quadratic approximation of the function is introduced to optimize and search for the minimum of this quadratic. The function to be approximated will be the Lagrangian function $\Im$.

$$\begin{aligned} &\Im(x_k+\delta_x, \lambda_k+\delta_\lambda) \approx Q(\delta_x, \delta_\lambda) \\ &= \Im(x_k, \lambda_k) + \nabla\Im(x_k, \lambda_k)\begin{pmatrix}\delta_x \\ \delta_\lambda\end{pmatrix} + \frac{1}{2}(\delta_x\ \delta_\lambda)\left[\nabla^2\Im(x_k, \lambda_k)\right]\begin{pmatrix}\delta_x \\ \delta_\lambda\end{pmatrix} \\ &\Leftrightarrow Q(\delta_x, \delta_\lambda) = \Im(x_k, \lambda_k) + (g_k + A_k\lambda_k\ c_k)\begin{pmatrix}\delta_x \\ \delta_\lambda\end{pmatrix} + \frac{1}{2}(\delta_x\ \delta_\lambda)\begin{bmatrix}H_k & -A_k \\ -A_k & 0\end{bmatrix}\begin{pmatrix}\delta_x \\ \delta_\lambda\end{pmatrix} \end{aligned} \tag{4.38}$$

with A_k is the Jacobian matrix of the constraints evaluated at x_k:

$$(A_k)_{i,j} = \frac{\partial c_i(x)}{\partial j}$$

and H_k is the Hessian matrix of the Langrangian function:

$$\nabla_x^2 \Im(x_k, \lambda_k) = H_k = \nabla_x^2 f(x_k) - \sum_i (\lambda_k)_i \nabla^2 c_i(x_k)$$

The full Hessian W_k of $\Im$ is thus:

$$W_k = \begin{bmatrix} H_k & -A_k \\ -A_k & 0 \end{bmatrix} \tag{4.39}$$

If it is on the boundary of the i^{th} constraint, we will have $(\delta_x)^t \nabla c_i(x) = 0$, thus on the constraints boundaries: $A_k \delta_x \approx 0$ (4.40)

Thus the problem is that we want to find δ_x which minimize $Q(\delta_x, \delta_\lambda)$, subject to the constraints $c_i(x) \geq 0, i = 1, \ldots, m$.

From Eqs. (4.38) and (4.40), we obtain:

$$\min_{\delta_x} Q, \qquad \text{Subject to } c_j(x_k + \delta_x) \geq 0, j = 1, \ldots, r$$

$$\overset{approx.}{\Leftrightarrow}$$

$$\min_{\delta_x} g_k^t \delta_x + \frac{1}{2} \delta_x^t H_k \delta_x, \quad \text{Subject to } c_j(x_k + \delta_x) \geq 0, j = 1, \ldots, r \tag{4.41}$$

Using a first order approximation of the constraints around x_k, we have the Quadratic Program (QP):

$$\min_{\delta_x} g_k^t \delta_x + \frac{1}{2} \delta_x^t H_k \delta_x$$

$$\text{Subject to } c_j(x_k) + (\delta_x)^t \nabla c_j(x_k) \geq 0, j = 1, \ldots, r \tag{4.42}$$

A Quadratic Program (QP) is a function that finds the minimum of a quadratic subject to linear constraints.

Thus for solving a sequential quadratic programming problem, we can define the algorithm:

a. Solve the quadratic programming subproblem described on Eq. (4.38) to determine δ_x and let λ_{k+1} be the vector of the Lagrange multiplier of the linear constraints obtained from the quadratic programming.
b. Set $x_{k+1} = x_k + \delta_x$
c. Increase k . Stop if $\nabla\Im(x_k, \lambda_k) \approx 0$. Otherwise, go to step a.

4.4.3 Optimization Results

The simulations show that different ranges of parameters result in different results since the locations and lengths of the side pads and the leading pads both affect the waviness following ability at low frequency range and resonance amplitudes. But only the effects of the length and location of the outmost surface area at the trailing pad are significant, and all of the geometric parameters are subject to the limits of the size of the slider.

If:

$$\mathbf{x}_b = \{\text{-0.01e-3,-0.05e-3,-0.08e-3,-0.2e-3,-0.2e-3,-0.2e-3,-0.2e-3,-0.2e-3}\}^{\mathrm{T}},$$

$$\mathbf{x}_u = \{\text{0.01e-3, 0.05e-3, 0.08e-3, 0.1e-3, 0.1e-3, 0.1e-3, 0.1e-3, 0.1e-3}\}^{\mathrm{T}}.$$

The optimum solution $\mathbf{x}^*$ is obtained:

$$\mathbf{x}^* = \{\text{0.01e-3, -0.01e-3, 0.08e-3, -0.2e-3, -0.06e-3, -0.03e-3, -0.1e-3}\}^{\mathrm{T}} \qquad (4.43)$$

In this case, the side pads and leading pads are emerged into one pad, which means that three-pad air-bearing slider may have better tracking ability to disk waviness since the effects of the side pads on flying height modulation are eliminated. Figure 4.29 shows the frequency response functions and amplitude spectrums of the initial design and of the optimized design. The flying height modulation to waviness ratio is reduced from 0.626 for the initial design to 0.448 for the optimal design.

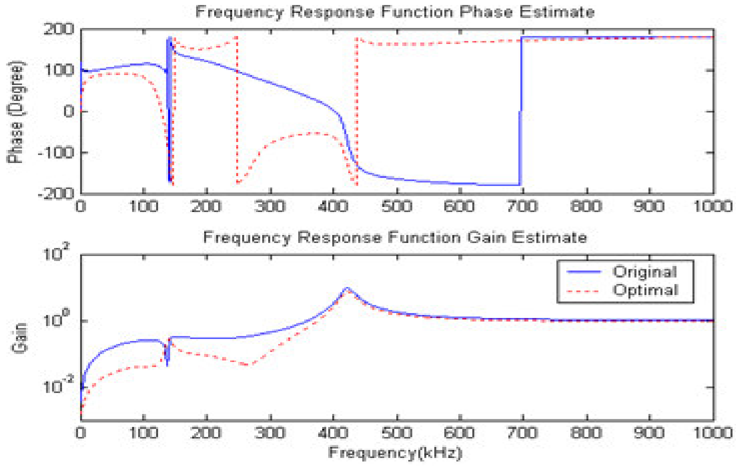

Figure 4.29 Frequency response functions of initial and optimized slider

4.5 New Slider Design with Extremely Small Flying Height Modulation

From the analytical and optimized results above, a new kind of air-bearing surface design is developed, named Panda III slider [17, 48], as shown in Figure 4.30. This is a three-pad and three etching steps negative slider. There are three etching depth at the trailing pad of the slider. The sub-shallow step is 15 nm, the main shallow step is 160 nm, and the base recess is 1.85 μm deeper from the outmost surface, respectively.

In order to evaluate the waviness following ability of the Panda III slider, we compare the flying height modulation caused by disk waviness of the Panda III, Panda II and one two-step slider which is modified from the Panda II slider (shown in Figure 4.31).

The flying attitudes of these three kinds of sliders are listed in Table 4.5. It is seen that Panda II and Panda III sliders have much smoother flying height profiles over the whole disk than the two-step slider.

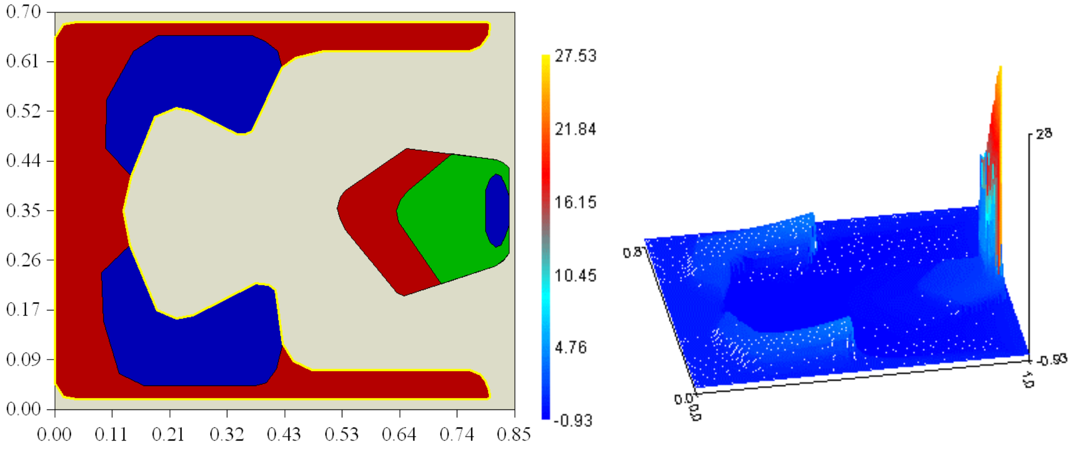

(a) Air bearing surface (b) Pressure profile at middle diameter

Figure 4.30 Air-bearing surface of the Panda III slider

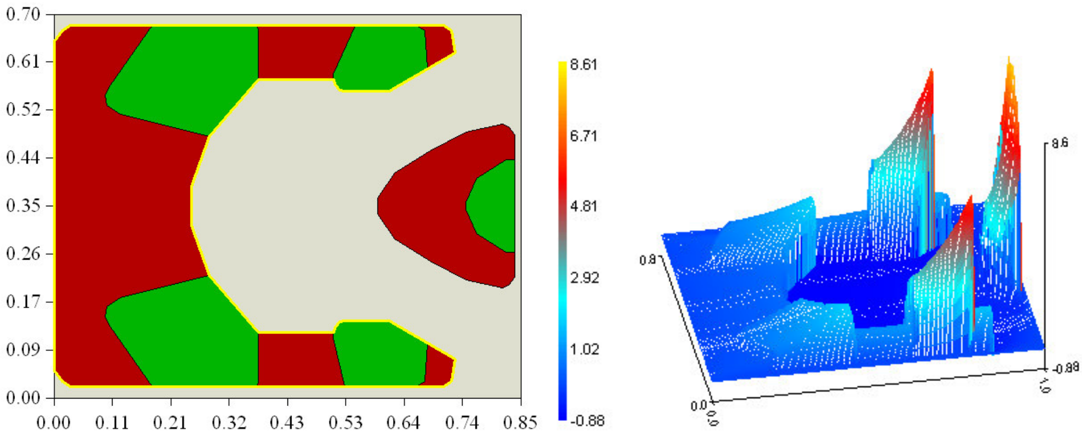

(a) Air bearing surface (b) Pressure profile at middle diameter

Figure 4.31 Air-bearing surface of the two-step-Panda II slider

Table 4.5 Static flying attitudes of three air bearing surface designs

Slider	OD (Radius=27.94, Skew=11.44)			MD (Radius=20.35, Skew=4.26)			ID (Radius=14.83, Skew=-2.45)		
	Gap FH	Pitch	Roll	Gap FH	Pitch	Roll	Gap FH	Pitch	Roll
Two-step	2.84	128.30	4.56	3.66	139.38	3.86	3.00	132.20	-2.55
Panda II	3.45	189.42	2.79	3.55	188.77	0.60	3.47	174.95	-2.23
Panda III	3.51	121.59	-7.64	3.01	121.15	2.71	3.52	116.83	5.01

Then the air bearing modal parameters are estimated using CML Parameter Identification Program simulator. The results are listed in Table 4.6. It is shown that the 2nd pitch mode resonance frequency and damping ratio of the Panda III slider are much higher than those of the Panda II and two-step sliders.

Table 4.6 Estimated Modal Parameters

Slider	Mode #1		Mode #2		Mode #3	
	Freq(kHz)	Damping (%)	Freq(kHz)	Damping (%)	Freq(kHz)	Damping (%)
Two-step	170.3	2.3	239.0	1.1	469.0	1.9
Panda II	135.6	2.7	155.5	2.1	421.9	2.3
Panda III	144.7	1.8	160.6	1.8	584.9	3.1

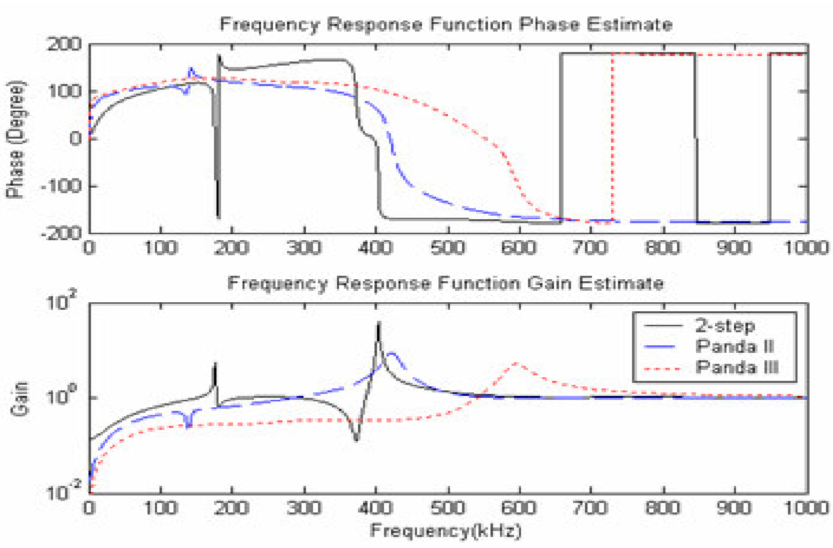

Figure 4.32 The frequency response functions of Panda III, Panda II and two-step sliders

Figure 4.32 shows the simulated frequency response functions of these three kinds of sliders. It is noticed that:

(1) The Panda III slider can better follow low frequency components of the disk waviness than Panda II and two-step sliders. This is obtained by reducing the distance between the head-gap and air bearing center at the trailing pad.

(2) The peak amplitude of the 2nd pitch mode resonance of Panda III is smaller than those of than the Panda II and two-step sliders. This is due to higher coefficient of dampers of the Panda III slider.

(3) The 1st pitch mode resonance of Panda III disappears, which is obtained by adjusting the length of the out-most layer of the trailing pad at 60 μm.

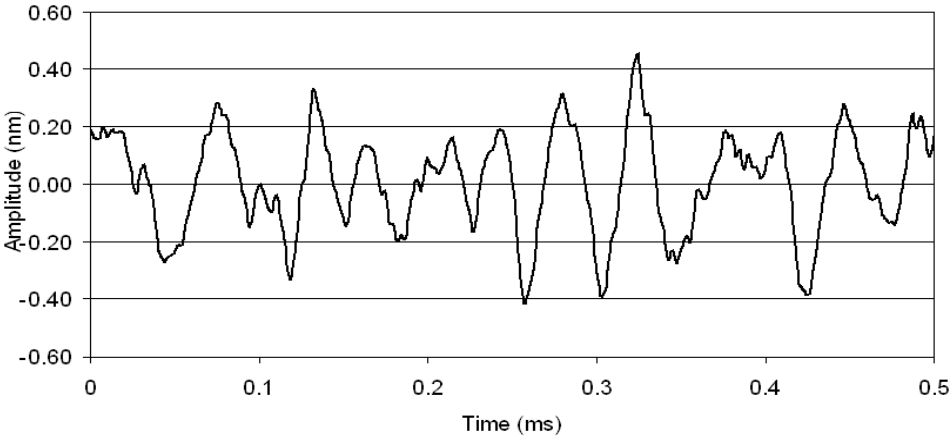

Figure 4.33 Disk surface morphology measured by LDV

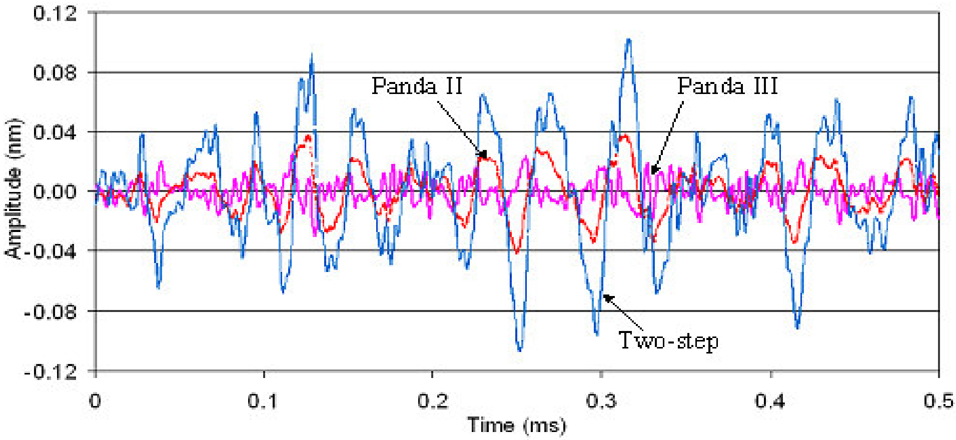

Figure 4.34 Simulation and comparison of flying height modulation with random disk waviness among three types of sliders

Simulations are performed to evaluate the flying height modulations caused by disk waviness of these three kinds of sliders. The disk waviness is obtained from the LDV measurement (as shown in Figure 4.33) and the flying height modulation is simulated using the Dynamic Simulator Program, developed by the Computer Mechanics Lab (CML), the University of California, Berkeley. The results are shown in Figure 4.34 and Table 4.7 lists the standard deviations of the disk waviness and of the flying height modulation as well as the flying height modulation to waviness ratio

ρ . It is obvious that the flying height modulation and the flying height modulation to waviness ratio of the Panda III slider are much smaller than those of the Panda II and two-step sliders.

Table 4.7 Simulation results of flying height modulations

Slider	3σ disk topography	3σ FHM	ρ
Two-step	0.523	0.096	0.183
Panda II	0.523	0.047	0.089
Panda III	0.523	0.025	0.048

4.6 Summary

This chapter aimed at exploring the air-bearing design strategies to significantly reduce the flying height modulation caused by disk waviness. The dynamic response of slider-air bearing designs was investigated. An analytical model was developed and the close-form frequency response function (FRF) was derived to evaluate the waviness following ability of the slider. Then the effects of air bearing stiffness, damping, disk surface features, locations and lengths of air-bearing pads on the flying height modulation due to disk waviness were investigated. The results showed that higher stiffness, larger damping ratio and smaller distance between transducer position and the air bearing center of the trailing pad could induce better waviness following ability of the slider. Optimization was also conducted to optimize the pad locations and sizes to minimize the flying height modulation caused by disk waviness.

Based on the understanding developed in the research activities presented in this Chapter, a three-pad air-bearing surface design was developed successfully. The evaluation results showed that the proposed new slider design was of much better waviness following ability when compared with other slider designs available in the public domain, including the advanced Panda II slider.

Chapter 5

Exploration of Air Bearing Technology to Reduce Flying Height Sensitivity to Altitude Change

Magnetic disk drives, especially mobile hard disk drives are used not only at the sea level, but also at high altitudes environment. Slider's flying attitude is decided by the air-bearing force acting on slider's air-bearing surface. The flying attitude varies when the slider flies from lower altitude to higher altitude, as the air pressure is a function of altitude. Reducing the flying height variation due to altitude change is an important issue in designing the head-disk interface, especially when technology moves towards ultra-low flying height, below 3 nm.

Kohira et al. [49] reported pivot shift approach to reduce the flying height sensitivity to the altitude change. They shifted the pivot loading point of the slider towards the slider's leading edge from the conventional approach of putting the pivot loading point at the geometry center of the slider body. Such a shift increases the pitch moment and such a pitch moment increase tends to compensate the flying height change caused by altitude variation. However, shifting the pivot point to the leading edge also influences the performances of the slider in other aspects. For example, such a shift reduces slider's capability in following up disk's surface morphology.

In this chapter, the mechanism of altitude induced flying attitude (gap flying height and pitch angle) change is investigated, aiming to have a full understanding of the relationship between the flying attitude change and altitude variation. Then a model is introduced to study the effects of the air bearing forces and the force exerting points on the changes of the flying attitude. Possible air bearing surface design strategies are proposed to reduce the flying height sensitivity to the altitude change. Finally a type of air-bearing surface design is developed which shows significant reduction of the gap flying height sensitivity to the altitude change.

5.1 Mechanism of Flying Height Sensitivity to Altitude

5.1.1 The Change of Flying Attitude due to High Altitude

Panda III slider, as reported in Chapter 4 and illustrated in Figure 5.1, is used to investigate the mechanism of the flying height change due to higher altitude. Table 5.1 compares the flying attitudes of the Panda III slider at different radii (outer diameter (OD), middle diameter (MD) and inner diameter (ID)) and at two different altitudes (sea level and at the altitude of 3000 m, industry standard evaluation conditions). The gap flying height listed in column 9 is the flying height at the coordinate of (0.82 mm, 0.35 mm), which is shown in Figure 5.1, and it is very close to the read/write element of the slider. It can be observed that both the gap flying height and the pitch angle reduce when the slider's flying condition changes from the sea level to the altitude of 3000 m. The last column illustrates the percentage of the gap flying height loss from the sea level to the 3000 m altitude (=$\left(FH_s - FH_a\right)/FH_s$. Here, FH_s is the flying height at the sea level, FH_a is flying height at the altitude of 3000 m). It is shown that the flying height loss at the OD is only 14.50 %, while that at the ID can be as high as 32.48 %. In other words, the flying height loss at the ID is much more severe than that at the OD of disk surface. The study presented in the rest part of this section is targeted at identifying the main factor which leads to such a high percentage difference of the flying height change.

Similarly, columns 6 and 8 list the percentages of the pitch angle and roll angle losses from the sea level to the 3000 m altitude, respectively. It can be observed that the variations of the percentages of the pitch angle losses across the disk surface are very small. On the other hand, the changes of the roll angle from the sea level to the 3000 m altitude do not show specific tendency. Though the change of the roll angle is the biggest at the MD, the roll angle itself at the MD is very small.

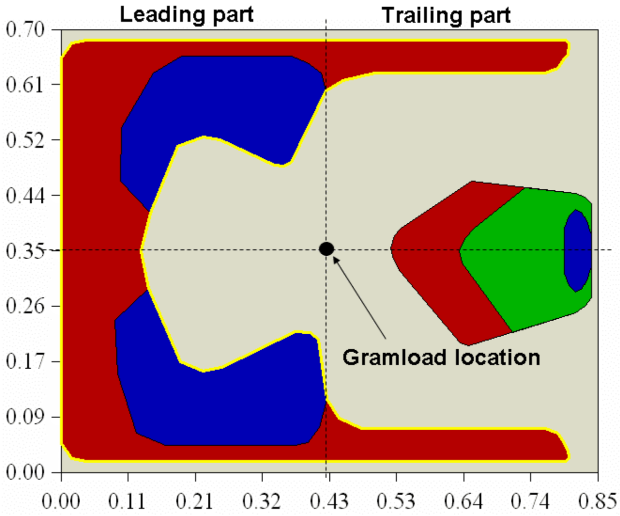

Figure 5.1 Air bearing surface (Panda III slider design, as proposed in Chapter 4)

Table 5.1 Flying attitudes of the sliders at the sea level and the altitude of 3000 m

Radius (mm)	Skew (°)	RPM	Altitude (m)	Pitch (μrad)	Per (%)	Roll (μrad)	Per (%)	FH (0.82, 0.35) (nm)	Per (%)
27.94	11.44	10000	0	146.20		-14.38		3.38	
27.94	11.44	10000	3000	130.71	10.60	-14.99	4.24	2.89	14.50
20.35	4.26	10000	0	142.41		-0.22		2.95	
20.35	4.26	10000	3000	127.39	10.55	-1.53	59.55	2.29	22.37
14.83	-2.45	10000	0	137.04		8.06		3.26	
14.83	-2.45	10000	3000	122.39	10.69	5.61	30.40	2.19	32.48

5.1.2 Effect of Skew Angle on Flying Attitude due to High Altitude

Skew angle is the angle between the slider direction (from slider's trailing edge to its leading edge) and the direction of air flow velocity. The skew angles at different radii are different. Table 5.2 compares the skew angle sensitivity of slider's flying attitude at the sea level and at the altitude of 3000 m. The skew angle is of –2.45° and 11.44°, respectively, --- a representative skew angle range for modern disk drives. It can be observed that the skew angle affects the gap flying height of the slider. However, both cases of -2.45° and 11.44° skew angles would be of the very similar percentages of the flying height losses when the altitude changes from 0 m to 3000 m. Also, similar observation can be made for the pitch angle case. In other words, the skew angle can not be considered as the main factor for the high percentage difference of altitude induced flying height change between ID and OD.

Table 5.2 Skew angle effects on the flying attitude due to high altitude

Radius (mm)	Skew (°)	RPM	Altitude (m)	Pitch (μrad)	Per (%)	Roll (μrad)	Per (%)	FH (0.82, 0.35) (nm)	Per (%)
14.83	-2.45	10000	0	137.04		8.06		3.26	
14.83	-2.45	10000	3000	121.45	10.69	5.61	30.40	2.19	32.82
14.83	11.44	10000	0	130.34		-12.41		3.51	
14.83	11.44	10000	3000	116.88	10.33	-10.78	13.05	2.33	33.62

5.1.3 Effect of Linear Velocity on Flying Attitude due to High Altitude

Disk drive is of constant spindle speeds. Thus, the linear velocity at different radii is different. Supposed the radius is R and the rotation speed of the disk is n (RPM), the linear velocity can be illustrated by:

$$V = \frac{2\pi R \times n}{60} \tag{5.1}$$

Table 5.3 shows the flying attitudes of the slider at outer diameter (OD) and inner diameter (ID) radii, at the sea level and at the altitude of 3000 m. The linear velocities are supposed to be the same (29.25 m/s). If the RPM at OD is 10000, the same linear velocity at ID requires RPM of 18840, according to Eq. (5.1).

From Table 5.3, the flying attitudes and the flying height reductions at OD and ID conditions are similar. Thus it can be concluded that the variations of the flying height losses from the sea level to the altitude of 3000 m at OD and ID conditions shown in Table 5.1 is due to various linear velocities at different tracks of the disk.

Therefore, we can further conclude that the skew angle is not the main factor of the high percentage difference of altitude induced flying height change between ID and OD, if the linear velocity at ID and OD could be kept the same. But the high linear velocity difference between ID and OD is the main reason of high flying height drop difference (percentage) between ID and OD when the altitude is changed.

Table 5.3 Linear velocity effects on the flying height loss due to altitude

Radius (mm)	Skew (°)	RPM	Altitude (m)	Pitch (μrad)	Per (%)	Roll (μrad)	Per (%)	FH (0.82, 0.35) (nm)	Per (%)
27.94	0	10000	0	144.48		9.47		3.22	
27.94	0	10000	3000	129.11	10.64	9.81	-3.60	2.80	13.04
14.83	0	18840	0	143.97		10.14		3.19	
14.83	0	18840	3000	128.93	10.45	9.69	4.44	2.77	13.17

5.1.4 Air Bearing Force Analysis for Flying Height Loss due to High Altitude

The force analysis is aimed at increasing the depth of understanding the flying height loss caused by the altitude change.

The exerting point of the external gram load is considered to be at the center of the backside of the slider. The slider can rotate around this force exerting point in the pitch and roll directions. Thus in the following analysis, we separate the air bearing surface as the trailing part and the leading part from the exerting point of the gram load, the half part that contains the trailing pad is denoted as the trailing part, the other half part containing the leading pads is denoted as the leading part, as illustrated in Figure 5.1.

Tables 5.4 (a) and (b) show the changes of the air-bearing forces and the corresponding effective force exerting points at the leading part and the trailing part of the slider, respectively, when the slider's flying altitude changes from the sea level to the altitude of 3000 m. The third row indicates the amount of force reduction when the slider flies from the sea level to the altitude of 3000 m, and the data in the fourth row are the percentages of the force reduction (= $\left(F_{sea} - F_{3000}\right) / F_{sea}$, where F_{sea} and F_{3000} are the forces at the sea level and the altitude of 3000 m, respectively).

The results of the fifth row are attained at the conditions that the slider flies at the altitude of 3000 m, while assuming the slider flies with the same flying attitude (flying height, pitch angle and roll angle) as that flies at the sea level. This is fulfilled by fixing the flying attitude (nominal flying height, pitch angle and roll angle) during the simulation process. The results of the last row will be discussed in the following section.

Table 5.4 (a): Forces and force loading points at the leading part

Conditions	Positive Force (g)	Center of Positive Force (mm)	Negative Force (g)	Center of Negative Force (mm)
Sea level altitude	1.855	0.250	-0.835	0.291
3000 m altitude	1.465	0.252	-0.583	0.291
Force Reduction	0.390		-0.252	
Force Reduction (%)	21.02		30.18	
3000 m (fix attitude)	1.306	0.252	-0.581	0.293
3000 m (gram load of 0.531 g)	1.304	0.250	-0.580	0.291

(b): Forces and force loading points at the trailing part

Conditions	Positive Force (g)	Center of Positive Force (mm)	Negative Force (g)	Center of Negative Force (mm)
Sea level altitude	1.114	0.800	-1.383	0.588
3000 m altitude	0.877	0.800	-1.016	0.595

Force Reduction	0.237		-0.367	
Force Reduction (%)	21.27		26.54	
3000 m (fix attitude)	0.802	0.799	-0.996	0.598
3000 m (gram load of 0.531 g)	0.807	0.798	-1.000	0.595

From the results listed in Table 5.4, we can observe that:

(1) Relative Sensitivity Comparison

Comparing the fourth rows in the tables, at both the trailing part and the leading part, the reductions of the negative forces (30.18 % and 26.54 %, respectively) are larger than the reductions of the positive forces (21.02 % and 21.27 %, respectively), which means that the negative force is more sensitive to the change of altitude compared with the positive force.

(2) Force Exerting Points at Trailing and Leading Parts

The effective exerting points of both the positive and the negative forces at the leading part and the trailing part of the slider remain almost the same at different altitudes, as can be seen by comparing the second, the fifth and the last rows in Tables 5.4 (a) and (b). In other words, the changes of the exerting centers of the air-bearing forces (both of the positive and negative forces) are negligible.

(3) Air-Bearing Forces at the Trailing and Leading Parts

The positive force at the trailing part (1.114 g at the sea level) is smaller than that at the leading part (1.855 g at the sea level). From Figure 5.1, the maximum pressure at the trailing pad is much higher than those on the other pads, whilst the area size of the leading pads are much larger than the area of the trailing pad. As a result, the total force at the leading part is larger than that at the trailing part. On the other hand, the negative force at the trailing part (-1.383 g) is larger than that at the leading part (-0.835 g), also due to the larger negative pressure area at the trailing part.

The gram load is along the same force direction as the negative air-bearing force. The gram load is applied by suspension to slider body and the gram load force is constant (0.8 g). In the equilibrium state, the slider is balanced by the total positive force, the total negative force and the gram load, which means:

$$F_p - F_n - F_g = 0 \tag{5.2}$$

where F_p, F_n, and F_g represent the total positive force, the total negative force and the gram load, respectively, and F_n only denotes the value of the negative force.

But from the first rows in Tables 5.4 (a) and (b)

$$F_p - F_n = (1.855 + 1.114) - (0.835 + 1.383) = 0.751\,\mathrm{g} \tag{5.3}$$

The difference of the positive force and the negative force is 0.049 g smaller than the applied gram load of 0.8 g, which comes from the simulation resolution or other influencing factors of the CML simulator. In the following analysis, the actual amounts of the force from the CML simulation are utilized.

(4) Further Discussion

From the fifth rows in the Tables 5.4 (a) and (b):

$$F_g = F_p - F_n = (1.306 + 0.802) - (0.581 + 0.996) = 0.531\,\mathrm{g} \tag{5.4}$$

This value of gram load is smaller than that in Eq. (5.3) of 0.751 g, which means that in order to maintain the same flying attitude when the slider flies from the sea level to the altitude of 3000 m, the exerting gram load should be reduced to 0.531 g. Table 5.5 compares the results of the flying attitude with gram loads of 0.751 g and 0.531 g when the slider flies at the altitude of 3000 m. The last row lists the flying attitude of the slider with a gram load of 0.531 g and at the altitude of 3000 m. Comparing the first and the third rows, there are very small differences of the flying attitude of the original slider at the sea level and slider with a gram load of 0.531 g at the altitude of 3000 m.

The force analyses of the slider with a gram load of 0.531 g at the altitude of 3000 m are listed in the last rows in Tables 5.4 (a) and (b). Comparing the second and the last rows of the tables, except for the amount of the positive forces, there are very small variations of the negative forces and the exerting centers of all forces, which means that for the slider with a gram load 0.751 g and flying at the altitude of 3000 m, the extra gram load (0.751-0.531= 0.220 g) is balanced by the positive force, with 0.070 g and 0.161 g (totally 0.231 g) at the trailing part and leading part, respectively. Here the small difference of the force is due to the small variation of the exerting centers of the forces. This change of the gram load can be considered that the net air bearing force ($F_p - F_n$) from the sea level to the altitude of 3000 m is reduced by 0.220 g.

Table 5.5 Flying attitude of the Panda III slider with various gram loads

	Radius (mm)	Skew (°)	RPM	Altitude (m)	Pitch (μrad)	Roll (μrad)	FH (0.82, 0.35) (nm)	Per (%)
Gram load of 0.751 g	27.94	11.44	10000	0	146.20	-14.38	3.38	
	27.94	11.44	10000	3000	130.71	-14.99	2.89	14.50
Gram load of 0.531 g	27.94	11.44	10000	3000	145.29	-15.07	3.48	-2.96

5.1.5 Analytical Model for Flying Height Loss due to High Altitude

The forces as well as the force exerting points (or moments) determine the flying attitude of the slider. A model is proposed to study the effects of the forces and moments on the flying attitude change due to the altitude change.

As shown in Figure 5.2, the positive and negative air-bearing forces at the trailing part and the leading part are denoted as F_{tp}, F_{tn}, F_{lp} and $F_{\ln}$, respectively. The distances from these force exerting points to the center of the slider are indicated as L_{tp}, L_{tn}, L_{lp} and $L_{\ln}$, respectively. The gram load of the suspension is denoted as F_g, which is assumed at the center of the backside of the slider at this time.

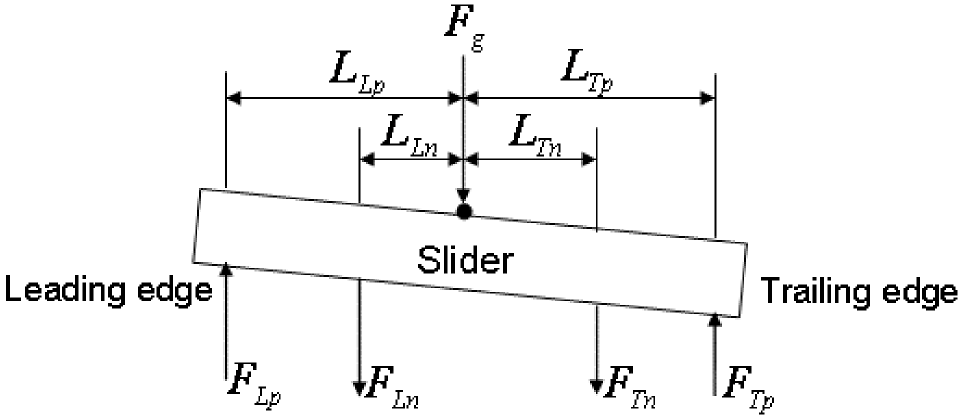

Figure 5.2 Schematic illustration of the forces and force centers

As observed from Table 5.1, both the gap flying height and the pitch angle reduce as the altitude is increased. Comparing the results listed in the first and the second rows in Tables 5.4 (a) and (b), it can be observed that all the forces reduce at a higher altitude. On the other hand, the changes of the distances between the force loading centers and the exerting point of the gram load are rather small and can be neglected. If we suppose the reduction amounts of the forces are indicated as ΔF_{tp}, ΔF_{tn}, ΔF_{lp} and $\Delta F_{\ln}$, respectively, the effects of such force reductions on the changes of the pitch angle and the flying height (FH) can be summarized in Table 5.6. The reduction of F_{tp} or $F_{\ln}$ lead to increased pitch angle and reduced flying height. On the other hand, the reduction of F_{tn} and F_{lp} lead to reduced pitch angle and increased flying height.

Table 5.6 The effects of the force reduction on the changes of the pitch angle and flying height

	Pitch	FH
ΔF_{tp}	Increase	Decrease
ΔF_{tn}	Decrease	Increase
ΔF_{lp}	Decrease	Increase
$\Delta F_{\ln}$	Increase	Decrease

For the Panda III slider, from Table 5.4,

$$\Delta F_{tp} + \Delta F_{\ln} = (1.114 - 0.877) + (0.835 - 0.581) = 0.491\,\mathrm{g}$$

$$\Delta F_{tn} + \Delta F_{lp} = (1.383 - 1.016) + (1.855 - 1.465) = 0.757\,\mathrm{g}$$

$$\Delta F_{tp} + \Delta F_{\ln} < \Delta F_{tn} + \Delta F_{lp} \tag{5.5}$$

Therefore, the pitch angle reduces. In the calculation, only the amount of the negative forces is included.

The flying attitude of a slider is determined by the balance of both forces and moments. For a slider flying in equilibrium, the summation of all the moments in the pitch direction should be equal to zero.

$$\sum M_p = 0$$

or

$$F_{\ln} \times L_{\ln} - F_{lp} \times L_{lp} = F_{tp} \times L_{tp} - F_{tn} \times L_{tn} - M_{sp} \tag{5.6}$$

Here, M_{sp} is the moment due to the static pitch and its value is on the order of 1E-7. In the next analysis it is ignored.

From Table 5.4, we can calculate the values of the changes of moments induced by the changes of the forces:

$$\Delta M_{tn} = \Delta F_{tn} \times L_{tn} = (1.383 - 1.016) \times (0.588 - 0.425) = 0.060 \text{ N.s}$$

$$\Delta M_{tp} = \Delta F_{tp} \times L_{tp} = (1.114 - 0.877) \times (0.800 - 0.425) = 0.089 \text{ N.s}$$

$$\Delta M_{lp} = \Delta F_{lp} \times L_{lp} = (1.855 - 1.465) \times (0.425 - 0.250) = 0.068 \text{ N.s}$$

$$\Delta M_{\mathrm{ln}} = \Delta F_{\mathrm{ln}} \times L_{\mathrm{ln}} = (0.835 - 0.583) \times (0.425 - 0.291) = 0.034 \text{ N.s}$$

$$\Delta M_{lp} + \Delta M_{tn} = 0.128 \text{ N.s}, \ \Delta M_{tp} + \Delta M_{\mathrm{ln}} = 0.123 \text{ N.s}$$

thus $\Delta M_{lp} + \Delta M_{tn} > \Delta M_{tp} + \Delta M_{\mathrm{ln}}$ (5.7)

The result indicates that the changes of the moments also result in the drop of the pitch angle when the slider flies from the sea level to a higher altitude.

From the above analysis, both the force reduction and the moment reduction tend to reduce the pitch angle when the slider flies from the sea level to a higher altitude. It is known that the reduction of the pitch angle tends to increase the gap flying height, if the pivot point (the dimple) remains at the same position. However, the above results indicate that the gap flying height still reduces. This indicates that the reduction of the pitch angle is not big enough to compensate for the reduction of the gap flying height drop caused by the reduced air-bearing force at increased altitude.

5.2 Approaches to Reduce Flying Height Sensitivity to Altitude

There are two types of approaches to reduce the flying height sensitivity to altitude change. One is to adjust the gram load (force and exerting point), the other one is to design the air bearing surface to reduce the loss of the flying height.

5.2.1 Adjusting the Gram Load

1. Adjusting the Gram Load Value

As stated in Table 5.5, when the slider flies from a lower to a higher altitude, the gram load should be reduced in order to maintain the same flying attitude. Thus, a straightforward approach to reduce the flying height sensitivity to the altitude change is to adjust the gram load when the slider flies from a lower to a higher altitude. But this needs methods or technologies to adjust the gram load with different altitudes.

Table 5.7 lists the flying attitudes with various gram loads applied to the slider. It is observed that a smaller gram load can reduce the flying height sensitivity to altitude, but the effect is not significant enough.

Table 5.7 Flying attitudes of the Panda III slider with various gram loads

	Radius (mm)	Skew (°)	RPM	Altitude (m)	Pitch (μrad)	Roll (μrad)	FH (0.82, 0.35) (nm)	Per (%)
Gram load of 0.95 g	27.94	11.44	10000	0	135.74	-13.26	2.96	
	27.94	11.44	10000	3000	118.95	-12.60	2.45	17.23
Gram load of 0.75 g	27.94	11.44	10000	0	146.20	-14.38	3.38	
	27.94	11.44	10000	3000	130.71	-14.99	2.89	14.50
Gram load of 0.55 g	27.94	11.44	10000	0	158.05	-14.46	3.89	
	27.94	11.44	10000	3000	143.73	-16.27	3.43	11.82

2. Adjusting the Loading Point of Gram Load

Another approach is to change the gram load force exerting point to the slider body. Such kind of pivot point shifting has been proposed to reduce the flying height sensitivity due to a higher altitude [47]. Moving the loading point of the gram load to the leading edge would reduce the effect of the gram load moment on the flying height change at the transducer location.

The pivot shift effect can be illustrated using the analytical model, as shown in Figure 5.3. Supposing the pivot shifts towards the leading edge, the amounts of the reduction of the forces are denoted as ΔF_{tp}, ΔF_{lp}, ΔF_{tn} and ΔF_{ln}, respectively and the distances between the loading centers of the forces F_{tp}, F_{tn}, F_{lp} and F_{ln} and the gram load are denoted as L_{tp}', L_{tn}', L_{lp}' and L_{ln}', respectively. It can be noticed that:

$$L_{tp}' > L_{tp},\ L_{tn}' > L_{tn},\ L_{lp}' < L_{lp},\ L_{ln}' < L_{ln} \tag{5.8}$$

As discussed above, the reduction of the gap flying height is induced by $\Delta M_{tp} < \Delta M_{lp}$. When the pivot point moves towards the leading edge, the increase of L_{tp} leads to the increase of ΔM_{tp} and the decrease of L_{lp} leads to the decrease of ΔM_{lp}. The gap flying height will remain the same from the sea level to higher altitude if $\Delta M_{tp} = \Delta M_{lp}$.

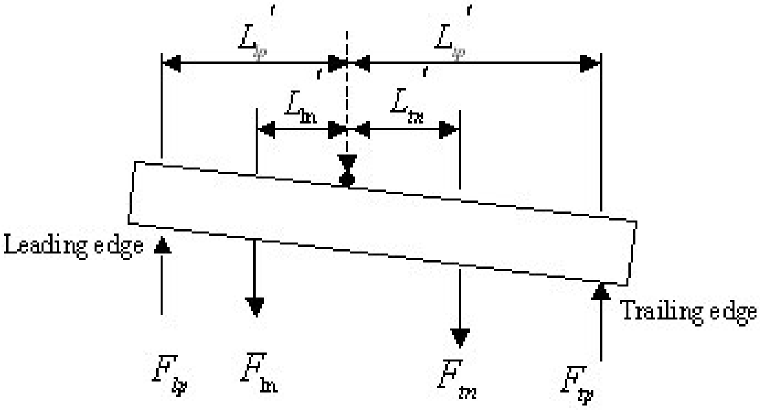

Figure 5.3 Schematic diagram of the forces and force centers of the pitch shift

Table 5.8 (a) Flying attitudes of Panda III (pivot shifts 150 µm to the leading edge)

Radius (mm)	Skew (°)	RPM	Altitude (m)	Pitch (µrad)	Roll (µrad)	FH (0.82, 0.35) (nm)	Per (%)
27.94	11.44	10000	0	129.14	-13.71	3.79	
27.94	11.44	10000	3000	112.16	-13.53	3.39	10.43
20.35	4.26	10000	0	126.65	-0.30	3.34	
20.35	4.26	10000	3000	110.62	-1.11	2.71	18.80
14.83	-2.45	10000	0	121.42	7.17	3.84	
14.83	-2.45	10000	3000	106.60	5.12	2.66	30.66

(b) Flying attitudes of Panda III (pivot shifts 350 µm to the leading edge)

Radius (mm)	Skew (°)	RPM	Altitude (m)	Pitch (µrad)	Roll (µrad)	FH (0.82, 0.35) (nm)	Per (%)
27.94	11.44	10000	0	110.09	-12.79	5.10	
27.94	11.44	10000	3000	92.20	-11.36	5.64	-10.58
20.35	4.26	10000	0	108.46	-1.54	4.61	
20.35	4.26	10000	3000	92.26	-1.01	4.55	1.30
14.83	-2.45	10000	0	102.12	3.93	5.74	
14.83	-2.45	10000	3000	88.38	3.61	4.76	17.07

Tables 5.8 (a) and (b) list the simulation results of the Panda III slider at the sea level and at the altitude of 3000 m, with pivot shifts of 150 μm and 350 μm to the leading edge, respectively. It can be observed that when the pivot shifts to the leading edge, the pitch angle reduces while the gap flying height increases. Comparing the results in Tables 5.8 (a) and 5.1, the percentages of the flying height reductions over the whole disk surface decrease. Comparing the results in Tables 5.8 (b) and 5.1, shifting the pivot towards the leading edge greatly decreases the flying height drop at the inner diameter (ID) condition. However, there is 17 % flying height drop at ID, which is still rather high.

Furthermore, moving the pivot point to the leading edge will affect the other performances of the slider, such as reducing the loading stiffness of the air-bearing surface, and reducing the waviness following ability of the slider.

5.2.2 Increasing the Sensitivity of Pitch Angle to Altitude

Reducing the pitch angle can increase the flying height if the pivot point (the dimple) remains at the same position. Thus one way to reduce the gap flying height loss is to increase the loss of the pitch angle at a higher altitude.

Increasing the reduction amount of the negative air bearing forces at the trailing part of the slider ΔF_{tn} and the positive air bearing force at the leading part of the slider ΔF_{lp} can reduce the pitch angle. Observing the fourth columns in Table 5.4 (b), the reduction amounts ΔF_{tn} show very small changes with different flying attitudes at the altitude of 3000 m. So a more meaningful way is to increase the reduction amount of ΔF_{lp}.

Meanwhile, decreasing the reduction amount of the positive force at the trailing part of the slider ΔF_{tp} and the negative force at the leading part of the slider $\Delta F_{\ln}$ can also reduce the pitch angle. In the same manner, $\Delta F_{\ln}$ varies very small with different flying attitudes at a higher altitude. Thus it is helpful to decrease the reduction amount of ΔF_{tp}.

The positive air bearing force is mainly dependent on the pad size and the etching depth, so is the loss of the positive force.

a) Leading Pads' Size Effect

The sizes of the leading pads are modified, as shown in Figure 5.4. The slider (b) is the original Panda III slider whilst the slider (a) is of larger leading pad and slider (c) is of smaller leading pad. The changes of the gap flying height and the forces at the leading part and the trailing part of the air bearing are listed in Table 5.9.

In the table, PF(L), PC(L), NF(L), NC(L) denote the positive force, positive force exerting point, negative force and negative force exerting point at the leading part, respectively. While PF(T), PC(T), NF(T), NC(T) denote the positive force, positive force exerting point, negative force and negative force exerting point at the trailing part, respectively.

The sizes of the leading pads have a significant effect on the pitch angle. The pitch angle of the slider (a) is more than 170 μrad and that of slider (c) is only about 110 μrad, due to the difference of the leading pad size. But the percentages of the reductions of the pitch angle from the sea level to the altitude of 3000 m only show about 2~3 % difference for these three sliders, for slider (a) is 8.21%, while that of slider (c) is 9.84 %. It means that the effect of the leading pad size on the sensitivity of the pitch angle to altitude is not significant.

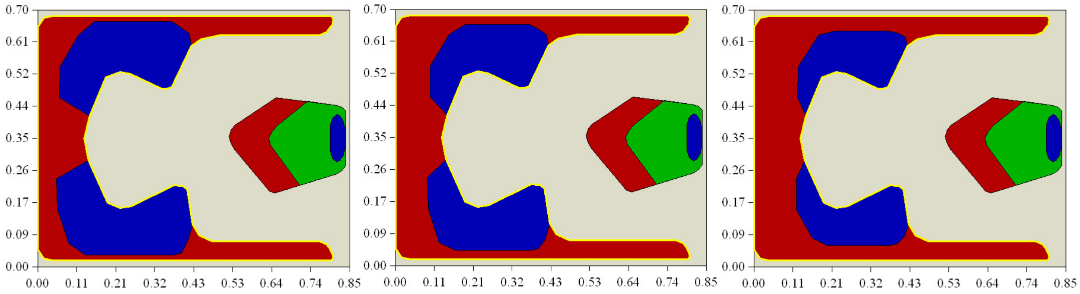

(a) Larger leading pad (b) Original (c) Smaller leading pad

Figure 5.4 Leading pads' size effect on pitch sensitivity to altitude

Table 5.9 Leading pads' size effect on the flying height and forces changes

Slider	Altitude (m)	Pitch (µrad)	Gap FH (nm)	PF(L) (g)	PC(L) (mm)	NF(L) (g)	NC(L) (mm)	PF(T) (g)	PC(T) (mm)	NF(T) (g)	NC(T) (mm)
(a)	0	171.06	3.48	1.78	0.232	-0.82	0.291	1.15	0.802	-1.35	0.588
	3000	157.01	2.92	1.40	0.231	-0.58	0.291	0.91	0.801	-0.99	0.594
Loss (%)		8.21	16.09	21.34							
(b)	0	145.41	3.30	1.85	0.249	-0.84	0.291	1.12	0.800	-1.39	0.588
	3000	129.24	2.80	1.46	0.251	-0.58	0.291	0.88	0.800	-1.02	0.594
Loss (%)		11.20	15.15	21.60							
(c)	0	111.98	3.25	1.92	0.261	-0.85	0.291	1.10	0.800	-1.44	0.589
	3000	100.96	2.82	1.51	0.263	-0.59	0.292	0.87	0.800	-1.05	0.595
Loss (%)		9.84	13.23	21.35							

b) Leading Pads' Etching Depth Effect

Next, the etching depth of the leading pads of the Panda III slider is modified and the results are listed in Table 5.10. Here, slider (-) means that the etching depth of the leading pads is 0.01 µm shallower than the leading pads of Panda III slider, while slider (+) means that the etching depth of the leading pads is 0.01 µm deeper than that of Panda III slider. It is shown that deeper etching depth of the leading pads can increase the sensitivity of the pitch angle to altitude, thus reduce the gap flying height variation. But again the effect is not very significant.

From the analysis results, it can be concluded that it is not easy to significantly increase the ΔF_{lp}, which means that increasing the reduction of positive force at the leading part is not very effective to reduce the flying height sensitivity to a higher altitude.

Table 5.10 Leading pad etching depth effect on the flying height and forces changes

Slider	Altitude (m)	Pitch (μrad)	Gap FH (nm)	PF(L) (g)	PC(L) (mm)	NF(L) (g)	NC(L) (mm)	PF(T) (g)	PC(T) (mm)	NF(T) (g)	NC(T) (mm)
(-)	0	167.30	3.98	1.83	0.252	-0.83	0.291	1.12	0.789	-1.36	0.589
	3000	151.73	3.33	1.45	0.255	-0.58	0.290	0.88	0.789	-0.99	0.595
Loss (%)		9.31	16.33	20.76							
(b)	0	146.20	3.38	1.855	0.250	-0.835	0.291	1.114	0.800	-1.383	0.588
	3000	130.71	2.89	1.465	0.252	-0.583	0.291	0.877	0.800	-1.016	0.595
Loss (%)		10.60	14.50								
(+)	0	113.21	3.17	1.88	0.247	-0.86	0.292	1.15	0.800	-1.44	0.589
	3000	99.5	2.75	1.48	0.249	-0.60	0.291	0.90	0.800	-1.05	0.595
Loss (%)		12.11	13.25	21.27							

c) Trailing Pad Size Effect

The investigations of the trailing pad size effect are focused on the top surface and the sub-shallow surface. This is because most of the positive force at the trailing part is focused on the top surface and the sub-shallow surface at the trailing pad of the slider surface.

The sizes of the trailing pads (top surface and sub-shallow step) are modified, as shown in Figure 5.5. The slider (b) is the original Panda III slider whilst the slider (a) has larger trailing pad and slider (c) has smaller trailing pad. The changes of the gap flying height and the forces at the leading part and the trailing part of the air bearing are listed in Table 5.11.

PF(L), PC(L), NF(L), NC(L) denote the positive force, positive force exerting point, negative force and negative force exerting point at the leading part, respectively. While PF(T), PC(T), NF(T), NC(T) denote the positive force, positive force exerting point, negative force and negative force exerting point at the trailing part, respectively.

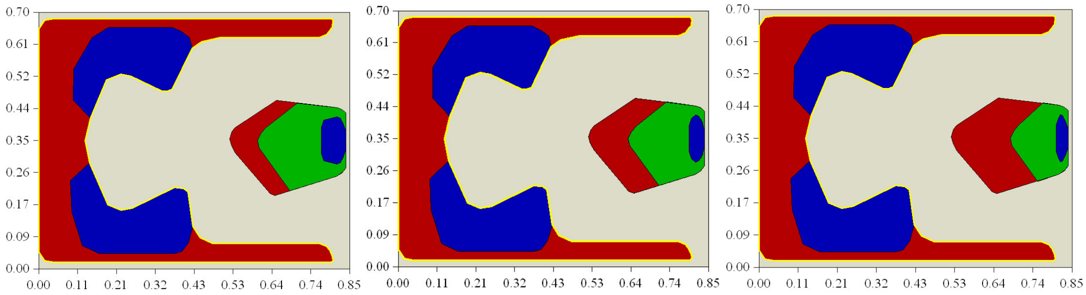

(a) Larger trailing pad (b) Original (c) Smaller trailing pad

Figure 5.5 Trailing pad size effect on pitch sensitivity to altitude

Table 5.11 Trailing pad size effect on the flying height and force changes

Slider	Altitude (m)	Pitch (urad)	Gap FH (nm)	PF(L) (g)	PC(L) (mm)	NF(L) (g)	NC(L) (mm)	PF(T) (g)	PC(T) (mm)	NF(T) (g)	NC(T) (mm)
(a)	0	145.20	4.57	1.824	0.249	-0.837	0.291	1.112	0.789	-1.344	0.587
	3000	130.15	4.01	1.437	0.251	-0.583	0.291	0.879	0.788	-0.989	0.593
Loss (%)		10.36	12.28								
(b)	0	146.20	3.38	1.855	0.250	-0.835	0.291	1.114	0.800	-1.383	0.588
	3000	130.71	2.89	1.465	0.252	-0.583	0.291	0.877	0.800	-1.016	0.595
Loss (%)		10.60	14.50								
(c)	0	141.23	2.53	1.892	0.248	-0.836	0.291	1.145	0.812	-1.451	0.592
	3000	128.76	2.18	1.496	0.252	-0.584	0.291	0.891	0.811	-1.058	0.598
Loss (%)		8.83	13.83								

It is observed that reducing the sizes of the trailing pad decreases the gap flying height and moves the exerting point of the positive force at the trailing part towards the trailing edge. But again, the effect of the sizes of the trailing pad on the sensitivity of the pitch angle to the altitude is small.

d) Etching Depth Effect of the Trailing Pads

Again, the etching depth of sub-shallow step at the trailing pad of the Panda III slider is modified and the results are listed in Table 5.12. Here, slider (-) means that the etching depth of the sub-shallow step at the trailing pad is 0.01 µm shallower than that of the Panda III slider, while slider (+) means that the etching depth of the sub-shallow step is 0.01 µm deeper than that of the Panda III slider.

It is shown that deeper etching depth of the sub-shallow step at the trailing pad can reduce the gap flying height and also move the exerting point of the positive force at the trailing part towards the trailing edge. But the effect on the sensitivity of the pitch angle to altitude is also rather small.

Table 5.12 Leading pad etching depth effect on the flying height and force changes

Slider	Altitude (m)	Pitch (µrad)	Gap FH (nm)	PF(L) (g)	PC(L) (mm)	NF(L) (g)	NC(L) (mm)	PF(T) (g)	PC(T) (mm)	NF(T) (g)	NC(T) (mm)
(-)	0	142.25	4.09	1.828	0.247	-0.835	0.291	1.155	0.788	-1.388	0.588
	3000	128.06	3.03	1.443	0.250	-0.581	0.291	0.908	0.787	-1.018	0.594
Loss (%)		9.97	25.92								
(b)	0	146.20	3.38	1.855	0.250	-0.835	0.291	1.114	0.800	-1.383	0.588
	3000	130.71	2.89	1.465	0.252	-0.583	0.291	0.877	0.800	-1.016	0.595
Loss (%)		10.60	14.50								
(+)	0	141.58	2.91	1.869	0.248	-0.837	0.291	1.107	0.809	-1.396	0.589
	3000	128.31	2.52	1.476	0.251	-0.585	0.291	0.868	0.808	-1.022	0.595
Loss (%)		9.37	13.40								

e) Shifting the Force Centers

As mentioned above, changes of the moments also affect the change of the pitch angle. Last section has discussed the changes of the forces effects on the pitch angle change. Figure 5.6 shows the changes of the force exerting points in order to reduce the pitch angle, if it is assumed that all the forces reductions remain the same. It is observed that increasing L_{lp} and L_{tn} , and reducing L_{tp} and L_{ln} can result in the reduction of the pitch angle.

Increasing L_{lp} and L_{tn} means that the positive force center at the leading part should move to the leading edge and the negative force center at the trailing part should move to the trailing edge. On the other hand, decreasing L_{tp} and L_{ln} means to move the positive force center at the trailing part to the leading edge and the negative force center at the leading part towards the trailing edge.

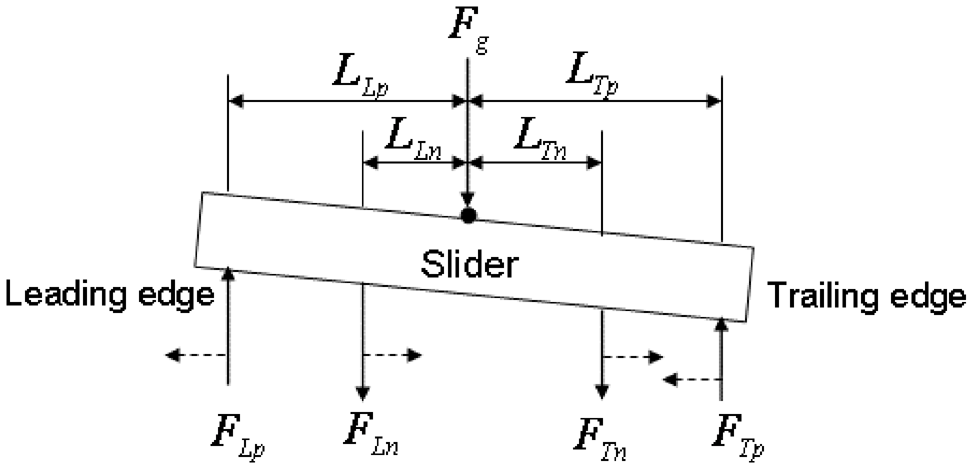

Figure 5.6 Changes of force exerting points on the reduction of the pitch angle

Here, we notice that combination of increasing L_{lp} and decreasing L_{tp} means that the total positive force center should be moved to the leading edge. And combination of increasing L_{tn} and decreasing L_{ln} means to move the total negative force center towards the trailing edge.

A kind of air bearing surface is thus developed, as shown in Figure 5.7, the flying altitude and the forces are listed in Table 5.13 by comparing them with those of the Panda III slider. From the table, it can be observed that the modified design is of smaller flying height loss from the sea level to the altitude of 3000 m. Comparing the loading centers of the positive forces at the trailing part and the leading part, the centers of the modified design are both nearer to the leading edge than those of the Panda III slider. But from the results attained in Chapter 4, such an approach is not the preferred choice in terms of improving the slider's performance in following up the disk waviness when the positive force center at the trailing part moves towards the slider's geometry center.

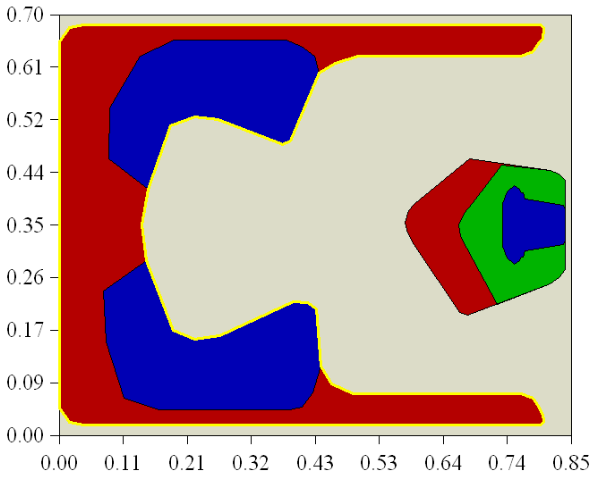

Figure 5.7 Air bearing surface modified from Panda III design

Table 5.13 Flying attitudes and forces analysis of the modified slider

	Altitude (m)	Pitch (μrad)	Gap FH (nm)	PF(L) (g)	PC(L) (mm)	NF(L) (g)	NC(L) (mm)	PF(T) (g)	PC(T) (mm)	NF(T) (g)	NC(T) (mm)
Modified	0	161.60	4.34	1.794	0.248	-0.797	0.290	1.175	0.782	-1.408	0.588
	3000	144.18	3.78	1.412	0.250	-0.552	0.288	0.927	0.780	-1.035	-1.035
Loss (%)		10.78	12.90								
Panda III	0	146.20	3.38	1.855	0.250	-0.835	0.291	1.114	0.800	-1.383	0.588
	3000	130.71	2.89	1.465	0.252	-0.583	0.291	0.877	0.800	-1.016	0.595
Loss (%)		10.60	14.50								

5.2.3 Minimizing the Sensitivity of Pitch Angle and Flying Height to Altitude

The ideal approach of reducing the flying height sensitivity to altitude is to keep both the gap flying height and the pitch angle not much changed when the slider flies from the sea level to a higher altitude.

1. Approaches to Reduce Gap Flying Height Sensitivity to Altitude

As discussed in section 5.1.4, in order to maintain the same flying attitude at the altitude of 3000 m, a gram load of 0.531 g is enough. The remaining 0.220 g of gram load lowers down the flying height and its uneven distribution induces the change of the pitch angle.

If the reduction of the pitch angle is ignored, the amount of the flying height loss due to this variation of 0.220 g gram load will depend on the air-bearing stiffness. Table 5.14 lists the stiffness of the Panda III slider in the flying height direction and in pitch direction at the sea level and at the altitude of 3000 m, respectively. It can be observed that the change of the stiffness is very small when the slider flies from the sea level to the altitude of 3000 m.

Table 5.14 Stiffness at the sea level and at the altitude of 3000 m

Radius (mm)	Skew (°)	RPM	Altitude (m)	Stiffness in FH direction (g/nm)	Per (%)	Stiffness in pitch direction (μN-m/μrad)	Per (%)
27.94	11.44	10000	0	0.377		0.551	
27.94	11.44	10000	3000	0.366	3.13	0.531	3.63

Thus the reduction of the flying height can be illustrated as:

$$\Delta h = \frac{\Delta F}{k} = \frac{0.220}{0.370} = 0.59\ nm \tag{5.9}$$

Comparing to the results in Table 5.1, this value of flying height reduction is larger. It is because that the result in Table 5.1 takes into account the effect of the pitch angle reduction.

In the Eq. (5.9), the ΔF can be considered to be constant from the sea level to a specific altitude by assuming that the slider files with the same flying attitude as it is at the sea level. In order to reduce the variation of Δh, it is helpful to change the stiffness k of the slider.

Supposed the stiffness in the flying height direction at the sea level is k_s and the stiffness at a higher altitude is k_a. They are defined as:

$$k_s = \frac{\Delta F_s}{\Delta h_s} \tag{5.10}$$

$$k_a = \frac{\Delta F_a}{\Delta h_a} \tag{5.11}$$

where Δh_s and Δh_a are small variations of the flying height at the sea level and at the higher altitude, ΔF_s and ΔF_a are the forces which are necessary to achieve flying height variation of Δh_s and Δh_a at the sea level and at the higher altitude, respectively.

Assume that $\Delta h_s = \Delta h_a = \Delta h$, $F_a = F_s - F'$, F' is the net variation of air bearing force from the sea level to the higher altitude (0.220 g for 3000 m), we have:

$$\frac{k_a}{k_s} = \frac{\Delta F_a / \Delta h}{\Delta F_s / \Delta h} = \frac{\Delta F_a}{\Delta F_s} = \frac{\Delta (F_s - F')}{\Delta F_s} = 1 - \frac{\Delta F'}{\Delta F_s} = 1 - \frac{0.220}{0.751} = 70.71\% \quad (5.12)$$

From Eq. (5.12), in order to maintain the same flying attitude at the altitude of 3000 m, the stiffness in the flying height direction at the altitude of 3000 m should be reduced to be 70.71 % of that at the sea level.

2. Approaches to Reduce Pitch Angle Sensitivity to the Altitude Change

Previously, the effect of the stiffness in the flying height direction on the flying height sensitivity to altitude has been discussed. Similarly, supposed the stiffness in the pitch direction at the sea level is kp_s and the stiffness at a higher altitude is kp_a. They are defined as:

$$kp_s = \frac{\Delta T_s}{\Delta p_s} \quad (5.13)$$

$$kp_a = \frac{\Delta T_a}{\Delta p_a} \quad (5.14)$$

where Δp_s and Δp_a are small variations of the pitch angle at the sea level and at the higher altitude, ΔT_s and ΔT_a are the torques which are necessary to achieve the pitch angle variation of Δp_s and Δhp at the sea level and at the higher altitude, respectively.

Assume that $\Delta p_s = \Delta p_a = \Delta p$, from Table 5.4, all the exerting centers of the forces can be considered remain at the same position when the slider flies from the sea level to the altitude of 3000 m. Thus we have:

$$\frac{kp_a}{kp_s} = \frac{\Delta T_a / \Delta p}{\Delta T_s / \Delta p} = \frac{\Delta T_a}{\Delta T_s} = \frac{\Delta((F_s - F') \times L_a)}{\Delta(F_s \times L_s)} = 1 - \frac{\Delta F'}{\Delta F_s} = 1 - \frac{0.220}{0.751} = 70.71\% \quad (5.15)$$

Here, L_s and L_a are the loading centers of the net air bearing force of the slider at the sea level and at the higher altitude. This result means that in order to maintain the same pitch angle from the sea level to the 3000 m altitude, the stiffness in the pitch direction should be reduced to 70.71 % of that at the sea level.

Another approach to reduce the pitch angle sensitivity to a higher altitude can be attained by using the analytical model. From Table 5.1, the pitch angle reduces when the slider flies from a lower to a higher altitude. To minimize the pitch angle sensitivity to a higher altitude, we need to increase the pitch angle when the slider flies at a higher altitude.

Section 5.2.2 has discussed the approaches to increase the pitch angle loss from a lower to a higher altitude. Thus the approaches to reduce the pitch angle loss will be contrary to the approaches discussed in that section. It is needed to decrease the reduction amounts of the negative air bearing force at the trailing part of the slider ΔF_{tn} and the positive air bearing force at the leading part of the slider ΔF_{lp}. And increase the reduction amounts of the positive force at the trailing part of the slider ΔF_{tp} and the negative force at the leading part of the slider $\Delta F_{\ln}$. In the same manner, modifying the forces effects on the pitch angle sensitivity is not significant.

Decreasing L_{lp} and L_{tn}, and increasing L_{tp} and $L_{\ln}$ can lead to the increase of the pitch angle. Decreasing L_{lp} and L_{tn} means that the positive force center at the leading part should be moved to the trailing edge and the negative force center at the trailing part moved to the leading edge. On the other hand, increasing L_{tp} and $L_{\ln}$ means to move the positive force center at the trailing part to the trailing edge and move the negative force center at the leading part towards the leading edge. These movements make the total positive force center be moved to the trailing edge and the total negative force center moved to the leading edge.

5.3 Air Bearing Surface Design to Reduce the Flying Height Sensitivity due to Altitude

5.3.1 Air-Bearing Surface Design Strategies to Reduce the Flying Height Sensitivity to Altitude Change

As discussed above, shifting pivot towards the leading edge reduces the gap flying height sensitivity to the altitude change. However, the improvement is limited. Furthermore, moving the pivot to the leading edge will deteriorate the other performances of the slider, such as the waviness following ability. Also, making the pitch angle loss more sensitive to altitude change is another approach to reduce the gap flying height loss when the slider flies from a lower to a higher altitude. Possible approaches include having more reduction of the positive force at the leading part, moving the total positive force center to the leading edge and moving the total negative force center towards the trailing edge. Again, such kind of approach is not a very effective way to reduce the flying height reduction caused by higher altitude.

Therefore, the author proposed the following air-bearing surface design strategies in order to reduce the flying attitude (flying height and pitch angle) change caused by altitude change:

(1) To move the center of the total positive air bearing force towards the trailing edge, and move the center of the total negative force towards the leading edge of the slider.

(2) To reduce the distances between the loading points of F_{lp} and F_{tn} and the loading point of the gram load and increasing the distances between the loading points of F_{ln} and F_{tp} and the loading point of the gram load can reduce the pitch angle sensitivity to the altitude change.

(3) In order to maintain the gap flying height of the slider from the sea level to the 3000 m altitude, it is needed to reduce the stiffness in flying height direction of the slider, for the Panda III slider and at outer diameter (OD) condition, the stiffness at the altitude of 3000 m should be reduced to about 70.71% of that at the sea level.

5.3.2 Altitude Insensitive Slider Design from the New Design Strategy

(1) Altitude Insensitive Slider Design and Performance Analysis

A new kind of air-bearing surface design, altitude insensitive slider design, is developed based on the above mentioned design strategies, as shown in Figure 5.8. The flying attitudes at the sea level and at the altitude of 3000 m are listed in Table 5.15. The gap flying heights of the slider at outer diameter (OD), middle diameter (MD) and inner diameter (ID) change 2.20 %, 1.62 % and 6.53 %, respectively, when the slider flies from the sea level to the altitude of 3000 m. Such flying height changes are the smallest among all slider designs reported in the public domain up to now. Comparing the results with those in Table 5.1, it can be noticed that the new slider design exhibits significant improvement of the gap flying height stability against altitude change.

One feature of the new slider design is that the pitch angles of the new design is smaller that those of the Panda III slider. The pitch angle is 100 μrad at OD of the altitude insensitive slider, compared with more than 140 μrad of the Panda III slider. The pitch angle is reduced to 60 μrad at ID of the altitude insensitive slider design, compared with 130 μrad of the Panda III slider. The variation of the pitch angle from OD to ID is much bigger for the altitude insensitive slider design, comparing with that of the Panda III slider. In other words, the altitude insensitive slider design shows increased sensitivity of its pitch angle to the linear velocity.

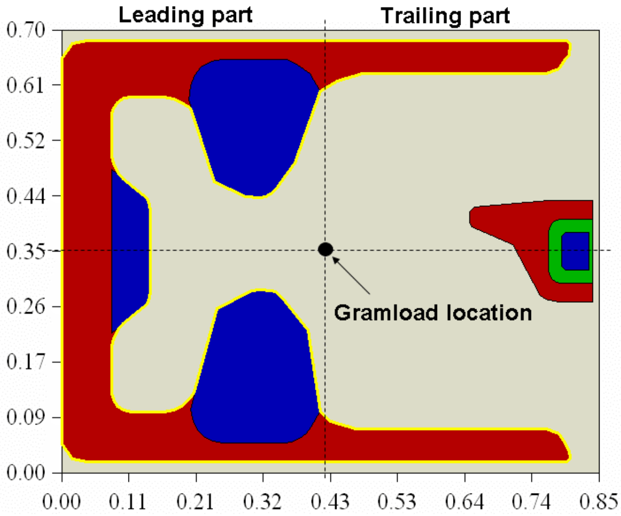

Figure 5.8 Air-bearing surface layout of the proposed altitude insensitive slider design

Table 5.15 Flying attitude of the proposed altitude insensitive slider design

Radius (mm)	Skew (°)	RPM	Altitude (m)	Pitch (μrad)	Roll (μrad)	FH (0.82, 0.35) (nm)	Per (%)
27.94	11.44	10000	0	98.37	-1.14	3.18	
27.94	11.44	10000	3000	94.39	1.42	3.11	2.20
20.35	4.26	10000	0	75.23	-0.48	3.08	
20.35	4.26	10000	3000	71.62	0.60	3.03	1.62
14.83	-2.45	10000	0	60.44	1.17	2.91	
14.83	-2.45	10000	3000	58.76	0.49	2.72	6.53

Table 5.16 Forces and Force loading points of the proposed altitude insensitive slider design and Panda III slider (OD)

	Altitude (m)	Pos (g)	PosC (mm)	Neg (g)	NegC (mm)	Stiffness in FH direction (g/nm)	Stiffness in pitch direction (g/nm)
Altitude insensitive slider	0	2.939	0.483	-2.168	0.512	0.290	0.388
	3000	2.316	0.478	-1.546	0.514	0.226	0.297
Panda III slider	0	2.968	0.454	-2.218	0.474	0.377	0.551
	3000	2.342	0.455	-1.600	0.481	0.366	0.531

(2) Force and Moment Analyses

Table 5.16 listed the forces and the forces' loading centers of the proposed altitude insensitive slider design and those of the Panda III slider. It can be observed that both the values of the positive and negative forces of the two sliders are comparable. So is the reduction amount of the forces when the altitude changes from the sea level to the altitude of 3000 m. However, the centers of both the positive and the negative forces of the proposed altitude insensitive slider design are closer to the trailing edge comparing with those of the Panda III slider, as the geometric center of the slider (the exerting point of the gram load) remains the same. In fact, moving air-bearing force center towards the trailing edge of slider is effectively equivalent to moving the pivot or exerting point of gram load towards the leading edge of the slider.

The last two columns in Table 5.16 list the stiffness in the flying height and the pitch direction of the proposed altitude insensitive slider and those of the Panda III slider. Both the stiffness in the flying height and the pitch direction of the altitude insensitive slider at altitude of 3000 m are reduced to be about 70 % of those at the sea level. However both the stiffness in the flying height and the pitch direction of the Panda III slider at the altitude of 3000 m show very small changes compared with those at the sea level.

Table 5.17 (a) Forces and force centers at the trailing part

	Altitude	Positive force (g)	Center of positive force (mm)	Negative force (g)	Center of negative force (mm)
Altitude insensitive slider	0	1.219	0.810	-1.618	0.603
	3000	0.921	0.810	-1.150	0.607
	Force reduction (%)	24.45		28.92	
Panda III slider	0	1.114	0.800	-1.383	0.588
	3000	0.877	0.800	-1.016	0.595
	Force reduction (%)	21.27		26.54	

(b) Forces and force centers at the leading part

	Altitude	Positive force (g)	Center of positive force (mm)	Negative force (g)	Center of negative force (mm)
Altitude insensitive slider design	0	1.720	0.255	-0.550	0.256
	3000	1.395	0.262	-0.396	0.253
	Force reduction (%)	18.89		28.00	
Panda III slider	0	1.855	0.250	-0.835	0.291
	3000	1.465	0.252	-0.583	0.291
	Force reduction (%)	21.02		30.18	

Tables 5.17 (a) and (b) list the forces and the force loading centers at the trailing part and the leading part of the altitude insensitive slider. The forces and the force loading centers of the Panda III slider are also listed for comparison.

From Table 5.17 (a), both the positive and the negative forces at the trailing part of the proposed altitude insensitive slider design are larger than those of the Panda III slider at the sea level, so is the reduction amount of the forces when altitude increases from the sea level to the altitude of 3000 m. The positive force reduces 24.45 % as compared to 21.27 % of the Panda III slider, and the negative force also reduces about 2 % more than that of the Panda III slider. Furthermore, both the centers of the positive and the negative forces at the trailing part of the proposed altitude insensitive slider design are nearer to the trailing edge than the Panda III slider. As a result, the reduction of moments ΔM_{tp} and ΔM_{tn} of the proposed altitude insensitive slider design is larger than those of the Panda III slider. From these results, more portions of forces and moments are focused at the trailing part for the proposed altitude insensitive slider design than the Panda III slider, so are the reductions of the forces and the moments.

On the other hand, both the positive and the negative forces at the leading part of the proposed altitude insensitive slider design are smaller than those of the Panda III slider, as can be seen in Table 5.17 (b). The negative force at the leading part of the proposed altitude insensitive slider design is only 0.550 g, comparing with 0.835 g of the Panda III slider. Furthermore, the reduction of the forces at the leading part of the proposed altitude insensitive slider design is smaller than those of the Panda III slider. Also, the center of the negative force at the leading part of the proposed altitude insensitive slider design is 0.256 mm from the leading edge, compared with the Panda III slider of 0.291 mm. Such an arrangement makes the distance from the force exerting point to the pivot point almost the same for both the negative force and positive force of the altitude insensitive slider. Thus increases the reduction amount of the moment $\Delta M_{\ln}$, though the reduction of the negative force reduces.

The reductions of the forces and the moments of the proposed altitude insensitive slider design can be calculated as the followings,

$$\Delta F_{tp} + \Delta F_{\ln} = (1.219 - 0.921) + (0.550 - 0.396) = 0.452 \text{ g}$$

$$\Delta F_{tn} + \Delta F_{lp} = (1.618 - 1.150) + (1.720 - 1.395) = 0.793 \text{ g}$$

thus $\Delta F_{tp} + \Delta F_{\ln} < \Delta F_{tn} + \Delta F_{lp}$ (5.16)

This reduction of the forces will reduce the pitch angle, as described in section 5.1.5. But

$$\Delta M_{tn} = \Delta F_{tn} \times L_{tn} = (1.618 - 1.150) \times (0.603 - 0.425) = 0.083 \text{ N.s}$$

$$\Delta M_{tp} = \Delta F_{tp} \times L_{tp} = (1.219 - 0.921) \times (0.810 - 0.425) = 0.115 \text{ N.s}$$

$$\Delta M_{\ln} = \Delta F_{\ln} \times L_{\ln} = (0.550 - 0.196) \times (0.425 - 0.256) = 0.026 \text{ N.s}$$

$$\Delta M_{lp} = \Delta F_{lp} \times L_{lp} = (1.720 - 1.395) \times (0.425 - 0.255) = 0.055 \text{ N.s}$$

thus $\Delta M_{lp} + \Delta M_{tn} < \Delta M_{tp} + \Delta M_{\ln} + M_{sp}$ (5.17)

The change of moments leads to increased pitch angle when the slider flies from the sea level to a higher altitude.

From the results, the proposed altitude insensitive slider design is of much lower flying height sensitivity to the altitude change. Some features of the new design can be summarized as the followings:

(1) Though the total amounts of the positive and the negative forces of the proposed altitude insensitive slider design are comparable to those of the Panda III slider, the trailing part of the proposed altitude insensitive slider carries higher percentage of the total force.

(2) The effective force exerting points of the total positive and the negative forces of the proposed altitude insensitive slider design are more towards the trailing edge of the slider, comparing with the Panda III slider.

5.4 Summary

In this chapter, the mechanism of flying height sensitivity to altitude was investigated. Both the force reduction and the moment reduction tend to reduce the pitch angle and the gap flying height when the slider flies from the sea level to the higher altitude. But the reduction of the pitch angle cannot compensate for the reduction of the gap flying height that leads to the reduction of the gap flying height. A model was used to study the effects of the changes of the forces and moments on the gap flying height changes due to altitude, and strategies of air bearing surface design to reduce the flying height sensitivity to altitude were proposed.

The understandings developed in this chapter were applied to design an altitude insensitive slider. Simulation results indicate that the designed altitude insensitive slider is of significantly reduced gap flying height loss when working altitude increases from the sea level to the altitude of 3000 m.

Chapter 6

Air Bearing Surface Technology Towards Smooth Loading Operations

Another critical aspect for ultra-small head-disk spacing technology is how to smoothly load and unload head-slider from the disk surface as smaller flying height increases the chance of slider-disk contact during the loading and unloading processes.

In this chapter, a new kind of air-bearing surface design is proposed, which has three negative force centers to adjust the built-up time of the air bearing of the slider. The simulation results show that with this kind of air-bearing surface design, the slider can be loaded to the disk with small oscillation and high damping.

6.1 Introduction: From Contact Start-Stop to Load/Unload Operations

Slider flies over disk surface when the disk drive is in its read/write operation status. Slider needs to be at its parking position when the drive is turned off. The traditional approach is to park the slider on a dedicated parking zone of disk surface, called ‘landing zone’ and such a technology is called contact start-stop (CSS) technology [50, 51]. The contact start-stop technology has been the main stream of slider parking technology in HDD industry since the introduction of Winchester drives more than 20 years ago. The slider stays at the landing zone during spinning up and spinning down and moves to the data zone only when the disk RPM reaches the operating conditions. In order to reduce stiction between the slider and the disk, texture zone, usually a regular pattern of bumps created with a laser device, is introduced at the landing zone of the disk. This results in higher head-disk separation and therefore lower areal density. Slider with low flying height at the texture zone also produces high contact force, generating wear debris, which degrades the head disk interface.

Due to those inevitable disadvantages of contact start-stop technology, the dynamic load/unload (L/UL) approach has gained research attentions in the recent years [52-54]. Figure 6.1 shows the load/unload dynamics. In load/unload technology, the slider is moved off the disks prior to power-down and safely positioned onto a cam-like structure. The cam is equipped with a shallow ramp on the side closest to the disk, giving ramp load/unload its name. During a power-on sequence, the read/write heads are loaded by moving the sliders off the ramp, and over the disk surfaces, when the disks reach the appropriate rotational speed.

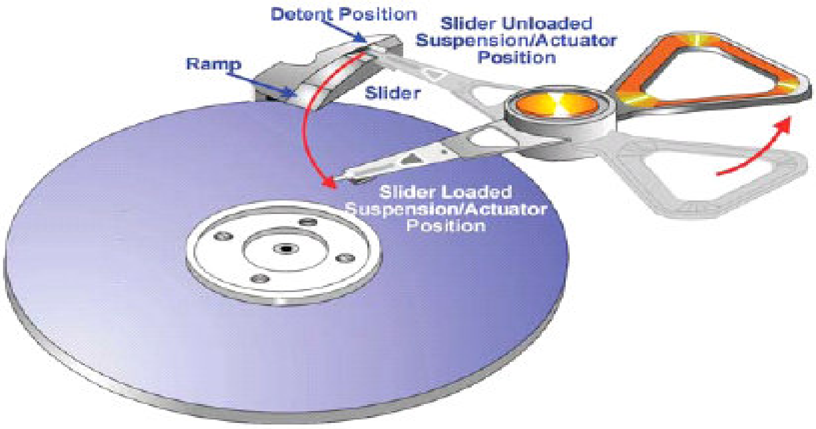

Figure 6.1 Ramp load/unload dynamics [55]

Load/unload technology has many advantages over the contact start-stop (CSS) technology. For example, disk drives with load/unload mechanisms have better shock resistance when the disk drive is not in operation as the head-slider is parked outside disk surface and of no chance to damage disk surface. It is also of lower power consumption, achieved by the elimination of stiction forces, which occurs during a contact start-stop cycle. Most importantly, no slider-disk wear occurs when load/unload is used if the system is designed to avoid contacts. This enables the use of ultra-smooth disks without a special landing zone and with better overall durability. In addition, the landing zone can be freed up for storing more data.

The main design objective of the load/unload mechanisms is to avoid slider-disk contact during load/unload operations. Slider air-bearing surface design, Pitch Static Attitude (PSA), Roll Static Attitude (RSA), gram load, suspension limiters, load/unload velocities and disk rotation speed are the main parameters that affect the load/unload performances of the slider at the head-disk interface (HDI) [56]. Here, we should indicate the definitions of PSA and RSA. When the sliders are mounted to the flexure, there are an initial pitch and roll angles, which are called the pitch static attitude (PSA) and the roll static attitude (RSA).

The sub-ambient pressure (negative pressure) slider shows better load/unload performance as compared to the positive pressure slider. The shallowly recessed cavity of the sub-ambient pressure slider generates larger squeeze flow effect and hence allows the slider to have better cushioning effect [56, 57].

For the loading process, moving the negative air bearing force center to the leading edge will not only induce a negative pitch moment during the early stage but also prolong the pitch-up process. This may result in slider-disk contacts at the leading edge of the slider. A reliable way to load the slider onto the disk is to pitch the slider up rapidly and maintain a positive pitch throughout the loading process.

Q. H. Zeng and D. B. Bogy [57] investigated the effects of the above mentioned design parameters on the load/unload performance by computer modeling. They found that the loading process is much smoother when the spindle speed is reduced, especially for negative pressure sliders. They claimed that the ramps should be carefully and properly designed to improve the loading and unloading performance, especially when the loading velocity is high. The pitch and roll static attitudes (PSA and RSA) have significant effects on the load/unload performance. A positive PSA can improve the loading performance and lead to a smoother unloading process. The RSA also affects the loading performance, but it subjects to the air bearing surface design because there is a skew angle during the load/unload process. Air-bearing surface design is critical for smooth loading process. Their results indicate that the negative force center should be located between the slider's center and the trailing edge, which will result in a positive pitch moment during the entire loading process.

Up to now, researchers are more focused on air-bearing surface designs with negative force center moving to the trailing edge of the slider so as to improve the unloading performance. However, the recent experimental works indicate that the loading process can create more chance of slider disk contact. Also, it is necessary to further investigate the effects of the negative pressure force on the loading performance and to increase the stability of the loading process, especially when the gap flying height is only 3~4 nm.

6.2 Dynamic Loading Process

The Panda II slider developed by the researchers in Data Storage Institute is the first type of slider with flying height being reduced to 3~4 nm [31, 48]. Therefore, such slider is selected to investigate the loading performance at an ultra-low flying height.

The loading analysis in this thesis work is conducted at a disk radius of 18 mm and skew angle 0° --- to reduce the skew angle effect on the loading study. The disk

RPM is 10,000. The slider has a gap flying height (flying height) of 3.3 nm, pitch angle of 185 μrad and roll angle of 4.7 μrad. The pitch static attitude of the slider-suspension assembly is 0.5° and roll static attitude is 0°. The slider is loaded at a vertical velocity of 25 mm/s and the initial nominal flying height is 27 μm.

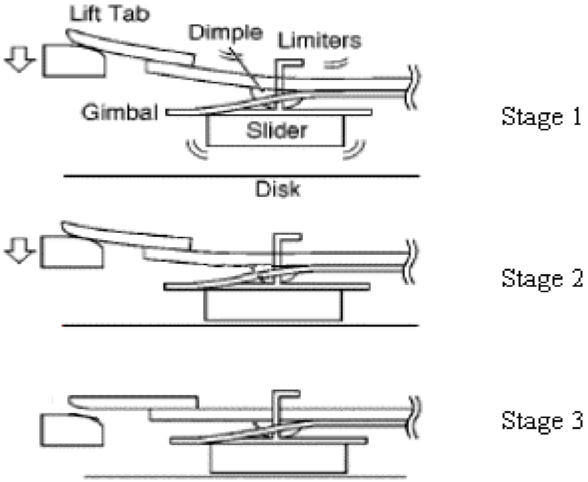

Figure 6. 2 Schematic diagram of loading process

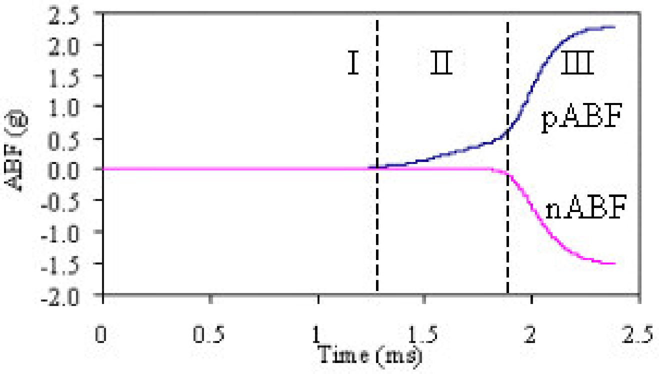

(a) Air bearing force history during loading process

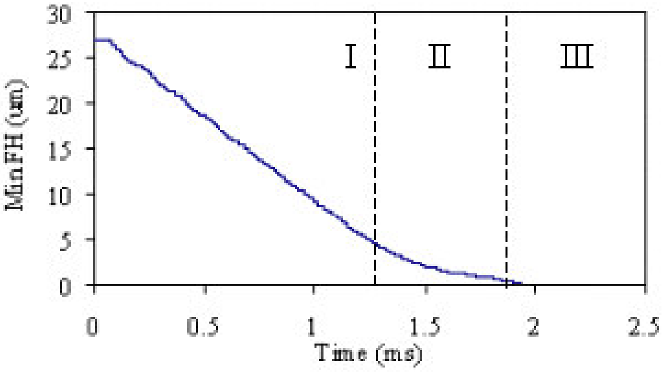

(b) Minimum flying height history during loading process

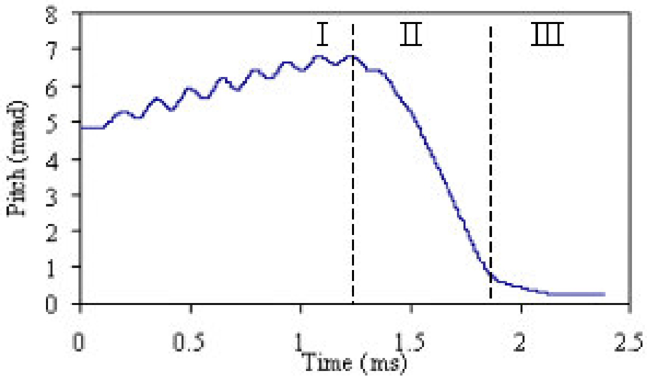

(c) Pitch angle history during loading process

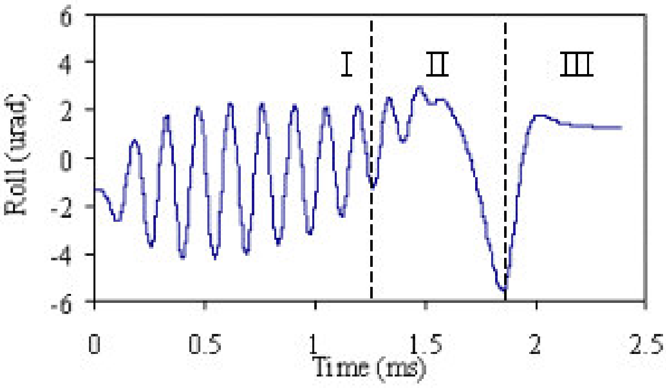

(d) Roll angle history during loading process

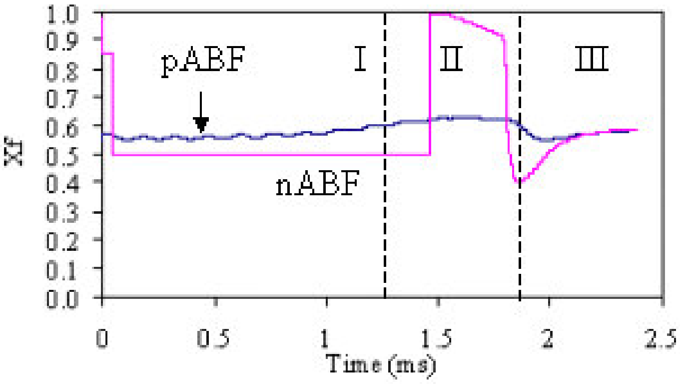

(e) Air bearing force center during loading process

Figure 6.3 Loading process (a) Air bearing force; (b) Minimum flying height; (c) Pitch angle; (d) Roll angle; (e) Normalized force center in X direction

Figure 6.2 shows the schematic diagram of the loading process. The ramp height results in the deflection of the suspension and low pitch angle of the slider at the initial stage of the loading process. The gram load is supported by the ramp on the lift tab. The loading process can be classified as three stages:

In Stage 1 of the loading process, as the suspension moves down the ramp and accelerates from rest to the vertical loading velocity, the pitch angle of the slider increases. This is depicted in Figure 6.3 (c) and indicated as I, when the time is less than 1.3 ms.

Subsequently, in Stage 2, the positive air-bearing force starts to build up and results in reduction of the pitch angle. This occurs when the time is between 1.3 ms and 1.8 ms (indicated as II). The positive air-bearing force arises from the cavity of the slider due to the squeeze flow effect [58, 59]. The squeeze-flow effect is proportional to the vertical velocity of the slider. As the slider loads to a lower flying height, the vertical velocity of the slider reduces and hence the squeeze-flow effect reduces.

In Stage 3, the positive and negative air-bearing forces, which arise from the air flow between the vertically moving slider and the horizontally moving disk, also set in. The share of support of gram load by the air bearing increases until the suspension leaves the ramp. Then, the slider is fully supported by the air bearing force. The slider gradually adjusts itself to the steady state flying height and attitude (indicated as III).

Figure 6.3 (e) shows the normalized force centers in x (slider length) direction. $X_f = 0.5$ means the force center is at the slider center. $X_f < 0.5$ means the force center is between the slider center and the leading edge of the slider and $X_f > 0.5$ means the force center is between the slider center and the trailing edge. It is shown that the positive force center gradually moves to the trailing edge during the loading process. On the other hand, after the negative force starts to build up, the negative force center quickly moves to the trailing edge, and vibrates, then reaches stable state [60].

6.3 Conditions for Optimal Loading Performance

The main requirements for optimal loading process are as follows:

1. No slider-disk contact;
2. Short duration;
3. Minimal oscillations in the vertical, pitch and roll directions, since high degree of oscillations may result in slider-disk contacts and longer loading process.

A safe loading process of a slider ensures that the above requirements are fulfilled. In the evaluation of the loading performance of a slider, the following are determined.

1. Safe range of operating conditions that give no slider-disk contact;
2. Maximum oscillation amplitude in the vertical, pitch and roll directions within the safe range of operating conditions;
3. Time taken for the loading processes within the safe range of operating conditions.

6.4 Triple-Negative-Zone Air Bearing Surface

Short duration is a critical requirement of the loading performance. The long duration is because that the negative force is built-up after the built-up of the positive force, and also due to the long time for the slider to reach stable state. If we can reduce the build-up time of the negative force and increase the damping of the oscillation, we can reduce the duration for the slider to fully load on the disk.

Most of the previous air bearing surface designs have only one negative force area, which determines the built-up time of the negative force and the damping of the loading process. If we design an air-bearing surface with several negative force centers, we can modify and adjust the built-up time of the slider by varying the properties (etching depth and etching area) of the negative force areas.

Thus we propose one concept: triple-negative-zone slider, as shown in Figure 6.4. There are three negative force regions on the air-bearing surface, two regions near the trailing edge (region Ne2) and one near the center of the slider (region Ne1). Suppose the etching depth in regions Ne1 and Ne2 are denoted as E_{Ne1} and E_{Ne2}, respectively, the slider can be denoted as slider (E_{Ne1}, E_{Ne2}) in the following analysis.

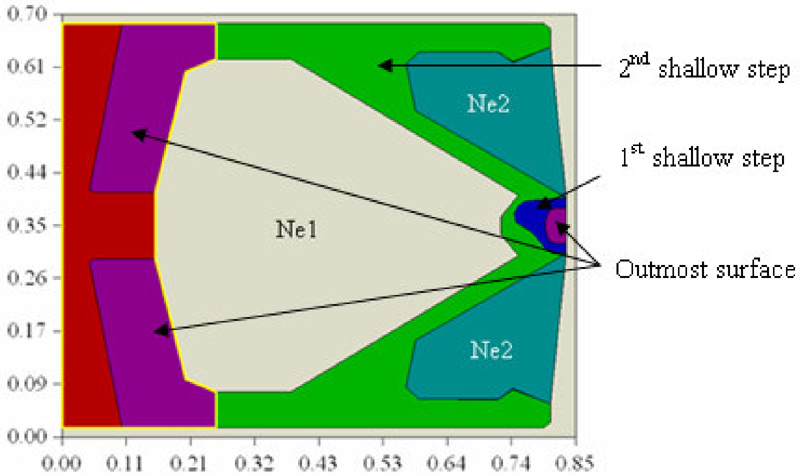

Figure 6.4 Triple-negative-zone air bearing surface

6.4.1 Effect of the Base Recess on the Negative Force

The etching depths of different etching steps of the air-bearing surface determine the amounts of the negative pressure force, especially for the etching depth of the base recess because of its largest area on the air-bearing surface. We first study the effect of the etching depth of the base recess on the static flying attitudes of the sliders and on the change of the negative force, assuming the etching depths in regions Ne1 and Ne2 are the same, as the slider shown in Figure 6.5.

The etching depth of the base recess of the slider shown in Figure 6.5 is varied to be 0.4 µm, 0.8 µm, 1.2 µm, 1.6 µm and 2.0 µm, respectively. Table 6.1 lists the flying attitudes and the positive and the negative forces of the sliders. The etching depth of the base recess has a significant effect on the pitch angle. The pitch angle is the smallest when the etching depth of the base recess is 1.2 μm, the pitch angle increases when the etching depth of the base recess becomes shallower or deeper.

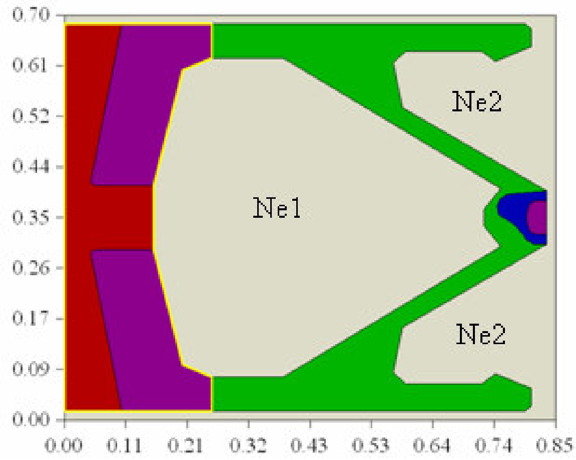

Figure 6.5 Triple-negative-zone slider, regions Ne1 and Ne2 have same etching depth

Table 6.1 Static flying attitude of the sliders

Slider	Pitch (μrad)	Roll (μrad)	Gap FH (nm)	Positive Force (g)	Negative Force (g)
slider(0.4, 0.4)	147.09	-1.48	4.70	2.15	-1.36
slider(0.8, 0.8)	100.16	0.41	3.16	3.09	-2.32
slider(1.2, 1.2)	99.57	0.89	3.63	2.99	-2.21
slider(1.6, 1.6)	115.87	1.60	5.14	2.51	-1.72
slider(2.0, 2.0)	176.14	2.81	13.89	1.78	-0.98

Figure 6.6 shows the effect of the etching depth of the base recess on the negative air bearing force. In the simulation, the etching depths of Ne1 and Ne2 area are the same for all the sliders. In the figure, the denotation of “Free attitude” means that we only modify the etching depths of the base recess of the sliders and let them fly freely, while “Fix attitude” means that we assume all the sliders fly with the same flying attitude as that of the slider with etching depth of the base recess of 1.2 μm. From the plot, the negative force only varies slightly with different flying attitudes. The negative force is mainly dependent on the etching depth of the base recess. The negative force is the biggest when the etching depth of the base recess is 1 μm, and it becomes smaller when the etching depth is shallower or deeper.

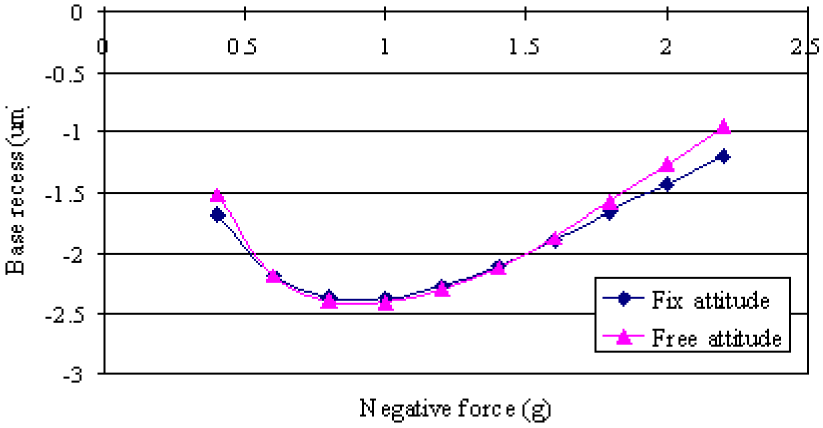

Figure 6.6 Effect of base recess etching depth on the negative force

6.4.2 Effect of the Base Recess on the Loading Performance

1) Force Built-Up and the Depth of Base Recess

The loading processes are also simulated with different etching depths of base recesses (from 0.4 μm to 2.0 μm, denoted as slider (0.4, 0.4), slider (0.8, 0.8), slider (1.2, 1.2), slider (1.6, 1.6) and slider (2.0, 2.0), respectively. Here, all the units for the etching depths are micrometer). The loading zone is at a disk radius of 18 mm and skew angle of 0°. The disk RPM is 10000 and the vertical loading velocity is taken to be 65 mm/s. The pitch static attitudes of the sliders are taken to be 0.5°, roll static attitudes 0° and the sliders are loaded from the initial nominal flying height of 50 μm.

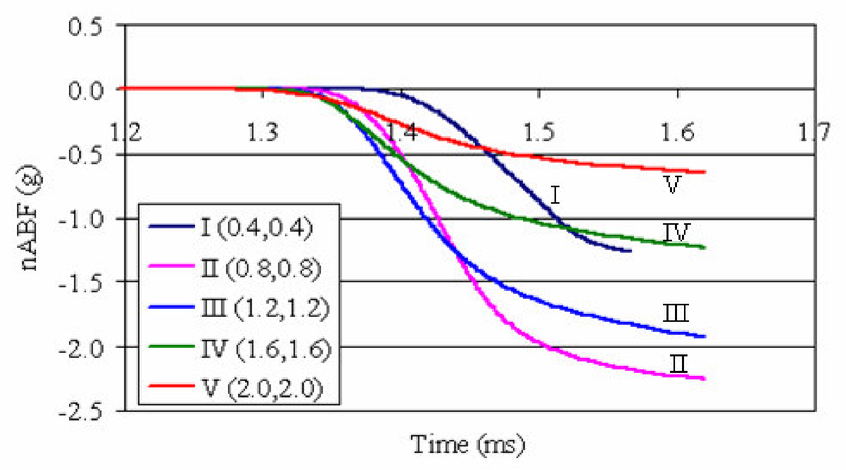

(a) Negative force history of the sliders during the loading process

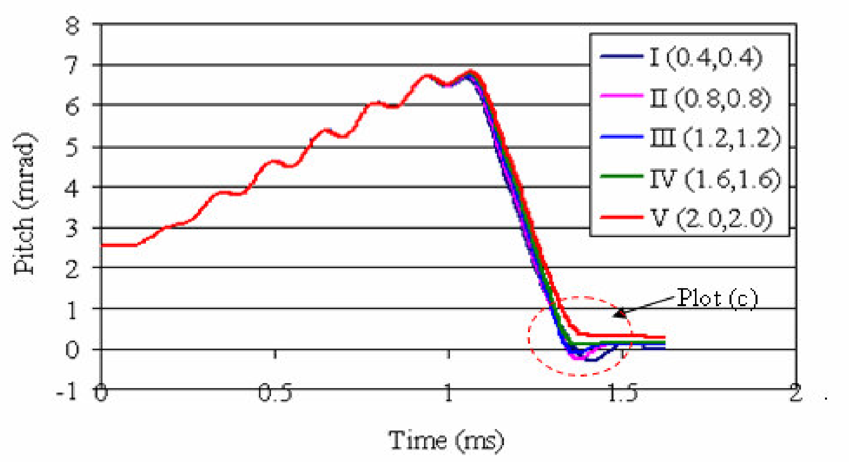

(b) Pitch angle history of the sliders during the loading process

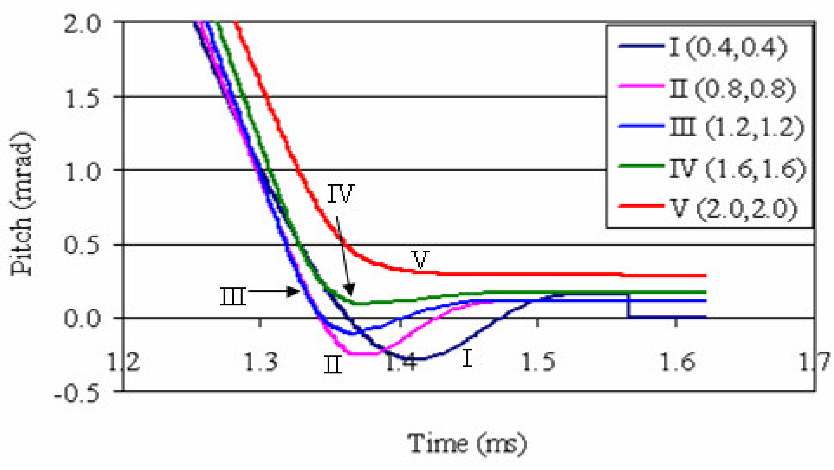

(c) Zoom in plot of (b)

Figure 6.7 Effect of recess etching depth on the negative force and pitch angle history

Figure 6.7 shows the relationship between the etching depth of the base recesses and the parameters histories during the loading process. Plot (a) shows the negative force history of the sliders; (b) is the pitch angle history; (c) is the zoom in plot of (b). Here we notice that:

- Either too shallow a base recess or too deep a base recess leads to reduced negative air bearing force. An etching depth around 0.8~1.1 μm gives the maximum amount of the negative force for the air-bearing surface as mentioned in this section.

- From Figure 6.7 (a), deeper etching depth of the base recess corresponds to shorter built-up time of the negative air bearing force (ABF). It takes longer time for the slider with shallower base recess (for example, the 0.4 μm base recess case) to start build up the negative air bearing force, comparing with deeper base recess sliders. On the other hand, the built-up time difference becomes small when the base recess is deep enough (for example: sliders with 1.2 μm recess and slider with 1.6 μm recess).
- Pitch angle can become negative before reaching its stable value, if the base recess is not very deep. As can be observed from Figure 6.7 (c), the pitch angles of sliders with base recess etching depths of 0.4 μm, 0.8 μm and 1.2 μm can be below 0 μrad before reaching the corresponding stable value.
- Deeper etching depth of the base recess has smoother loading process.

2) Pitch Static Attitude, Base Recess and Slider-Disk Contact

The pitch static attitude (PSA) significantly affects the loading performance. It is the initial pitch angle when the sliders are mounted to the flexure (as mentioned in section 6.1). In order to evaluate the loading performance of the sliders, the effects of the pitch static attitude are simulated. Table 6.2 shows the simulated results of minimum slider-disk clearances during the loading process when the pitch static attitude varies from 0.50° to -0.075°. The symbol "+" refers to a minimum clearance larger than 0 nm or no contact between the slider and the disk during the whole loading process. Symbol "-" refers to a minimum clearance smaller than 0 nm or there is contact during the loading process. It can be observed that there are no contacts for all the sliders when the pitch static attitude is larger than and equal to 0°.

Slider (0.4, 0.4), slider (0.8, 0.8) and slider (1.2, 1.2) contact the disk when the pitch static attitude reduces to –0.05°. The slider (1.6, 1.6) contacts disk as well when the pitch static attitude is further reduced to –0.06°. The results show that the slider (2.0, 2.0) has the best loading performance when considering the pitch static attitude effect.

Table 6.2 Pitch static attitude effects on the minimum clearance

	Etching Depth of base recess (μm)				
PSA (°)	(0.4, 0.4)	(0.8, 0.8)	(1.2, 1.2)	(1.6, 1.6)	(2.0, 2.0)
0.50	+	+	+	+	+
0.25	+	+	+	+	+
0	+	+	+	+	+
-0.05	-	-	-	+	+
-0.06	-	-	-	-	+
-0.075	-	-	-	-	-

6.4.3 Adjusting Loading Performance by Varying Triple-Negative-Zone

From the above analysis, deeper etching depth of the base recess can reduce the built-up time of the negative air-bearing force and lead to a smoother loading process. Actually, the main objective of having multi-negative pressure zones is to have the freedom of assigning different recess depths for different zones. With the triple-negative-zone slider shown in Figure 6.4, if we differ the etching depths in Ne1 and Ne2 areas, the built-up time of the negative force at the Ne1 and Ne2 areas can be different. If the negative force at the Ne2 area is built-up earlier than that in the Ne1 area, a positive pitch moment will be generated which would be helpful to accelerate the loading process.

From Tables 6.1 and 6.2, the static flying attitudes of sliders of etching depth 0.8 μm, 1.2 μm and 1.6 μm are comparable, but slider (1.6, 1.6) has a shorter built-up time of the negative force and smoother loading performance. Thus we take the slider of the base recess of 1.6 μm as the starting design for the exploration of more stable loading performance. We set the etching depth of Ne1 area 1.6 um, while that of Ne2 area 0.8 μm, 1.6 μm and 2.0 μm respectively, thus we get three air bearing surface sliders: slider (1.6, 0.8), slider (1.6, 1.6) and slider (1.6, 2.0). Table 6.3 lists the static flying attitudes and the forces for the sliders. It is shown that compared with slider (1.6, 1.6), slider (1.6, 0.8) is of increased negative force and the negative force center being shifted to the trailing edge. On the other hand, slider (1.6, 2.0) is of reduced negative force and the negative force center shifted forward to the leading edge.

Table 6.3 Static performances of the sliders

Slider	Pitch (μrad)	Roll (μrad)	FH (0.83, 0.35) (nm)	Pos Force (g)	Neg Force (g)	Neg Center (mm)	Neg (2*Ne2)
(1.6, 0.8)	116.86	1.01	4.51	2.58	-1.79	0.44	0.50
(1.6, 1.6)	115.87	1.60	5.14	2.51	-1.72	0.43	0.42
(1.6, 2.0)	115.66	1.34	5.82	2.44	-1.65	0.42	0.37

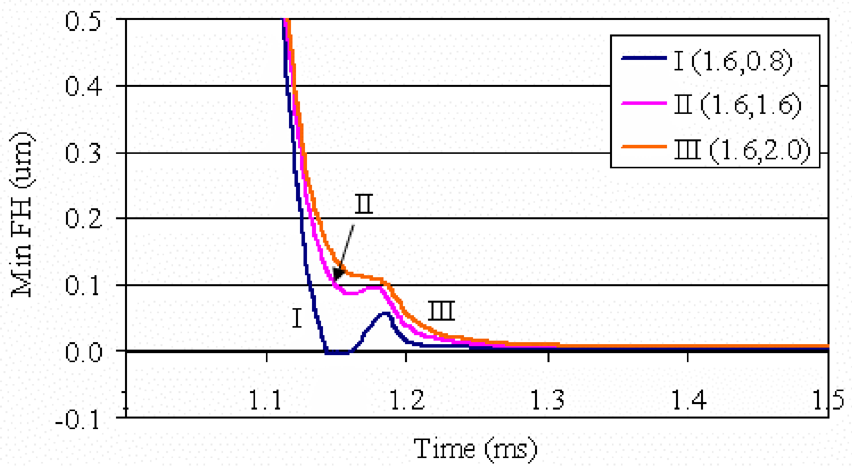

(a) Minimum flying height during the loading process

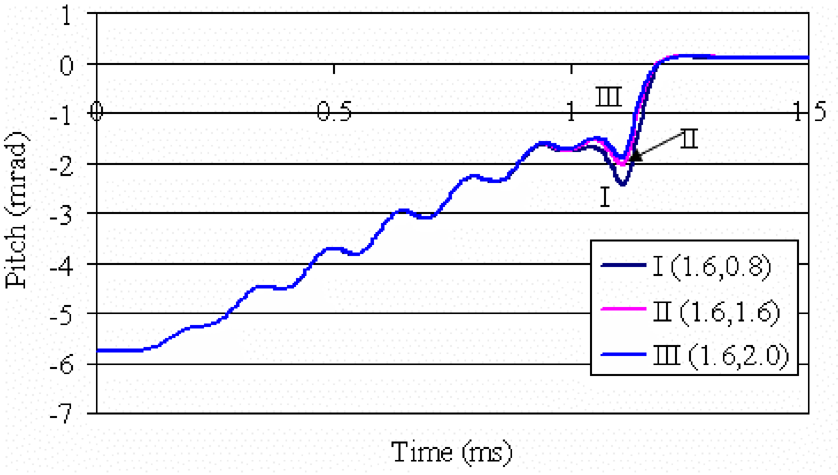

(b) Pitch angle history during the loading process

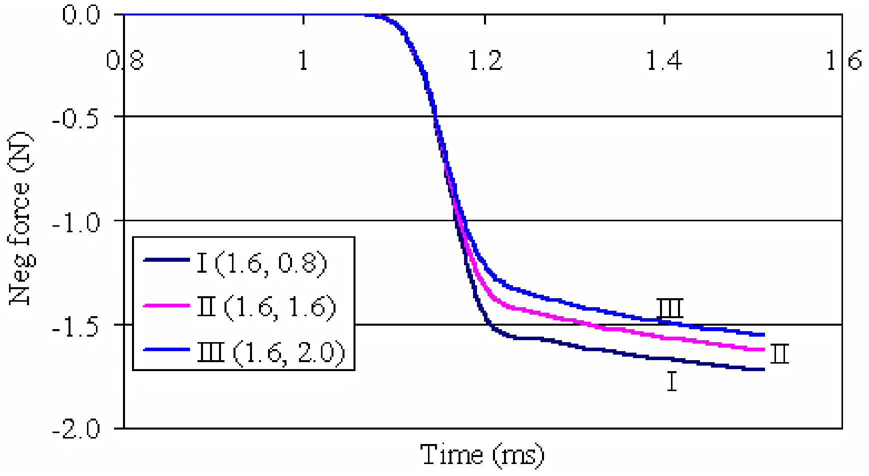

(c) Negative force history during the loading process

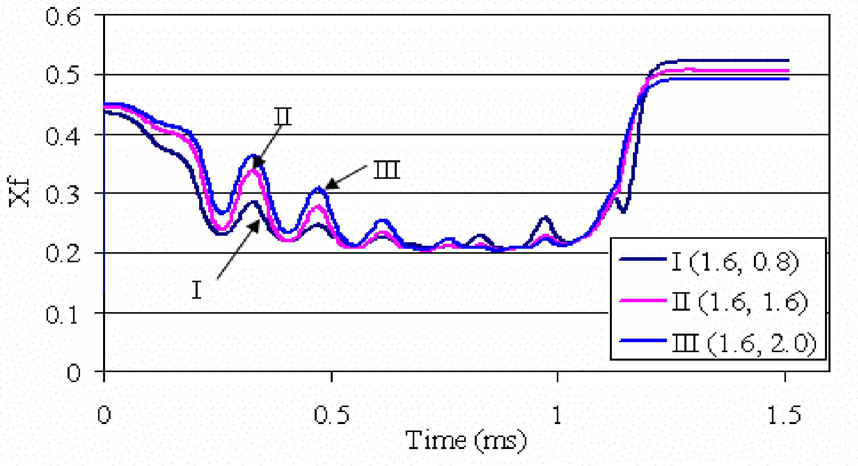

(d) Positive force center history during the loading process

Figure 6.8 The parameters changes during the loading process

Loading performances are simulated with those three sliders. The simulation conditions are the same as in the last section, except that the pitch static attitude is taken to be 0°. Figure 6.8 shows the parameter changes for those sliders during the loading process.

From Figure 6.8 (a), the minimum clearance of slider (1.6, 0.8) is smaller than 0 nm, which means contacts happen during the loading process. The minimum clearances of slider (1.6, 1.6) and (1.6, 2.0) are positive, which means no contact occurs for these two sliders during the loading operation. We can also see that the oscillation of the slider (1.6, 2.0) is smaller than the oscillation of the slider (1.6, 1.6), which means that the loading process of the slider (1.6, 2.0) is smoother. As can also be observed in Figures 6.8 (b) and (d), the slider (1.6, 2.0) shows smaller oscillation of the pitch angle and the positive force centers as well. From Figure 6.8 (c), there is no obvious change of the built-up time of the negative force except the steady value of the negative force.

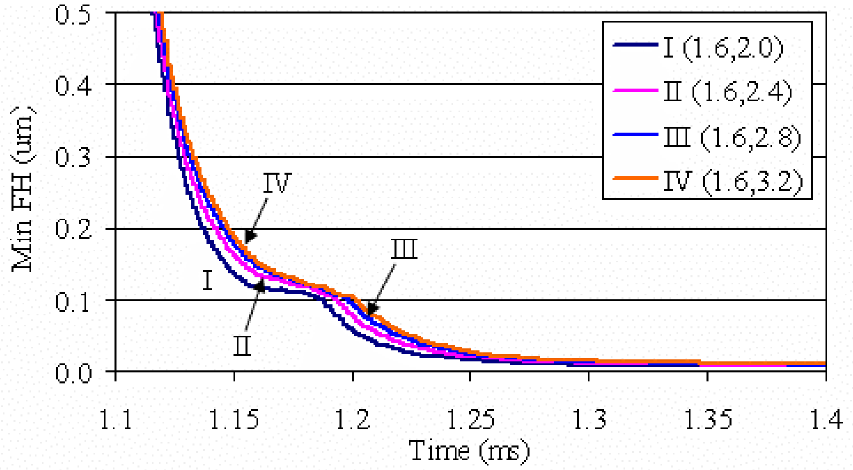

Figure 6.9 Effects of etching depth in Ne2 area on the minimum flying height

From the above analysis, we can conclude that for the triple-negative-zone slider, the etching depth of the base recess of the slider will influence the built-up time of the negative force. If we vary the etching depth of the triple-negative-zone, deeper etching depth in Ne2 area can smooth the loading process. Figure 6.9 shows the minimum clearances of sliders (1.6, 2.0), (1.6, 2.4), (1.6, 2.8), (1.6, 3.2) for the loading process. It can be observed that deeper etching depth in Ne2 area can improve the loading performance, but the difference becomes smaller when the etching depth becomes deeper and deeper.

6.5 Performance Evaluation

The performance comparison is made between the proposed triple-negative-zone slider and the Panda II slider --- mainly comparing the effects of the loading velocity and pitch static attitude on the loading performances for the triple-negative-zone and the Panda II slider.

6.5.1 Effect of Vertical Loading Velocity

The vertical motion of the slider during the loading process introduces a squeeze flow effect, which is directly proportional to the approaching speed between the slider and the disk [9, 10, 23]. A higher loading velocity gives a higher squeeze flow rate and hence a larger positive air bearing force (ABF). This provides greater cushioning effect during the loading process. However, higher loading velocity also expedites the squeeze flow action, leading to an accelerated occurrence of the oscillating motion. It may also cause the slider to hit the disk with a significant momentum impulse.

Y. Hu et al. [57] studied the loading velocity (20 mm/s, 140 mm/s and 300 mm/s) effects on the air bearing pressure profiles. They found that 140 mm/s loading velocity results in larger gap flying height and smaller pitch angle, and the squeeze flow generates more air bearing pressure than that of 20 mm/s loading velocity. But when the loading velocity further increases to 300 mm/s, the flying height further increases and the pitch angle reduces, and the air bearing pressure induced by the squeeze flow becomes smaller than 140 mm/s. This is because of the balanced contribution by the increase in loading velocity and the decrease in the flying attitude.

Thus in the following, the loading processes with vertical loading velocities from 25 mm/s to 265 mm/s are simulated.

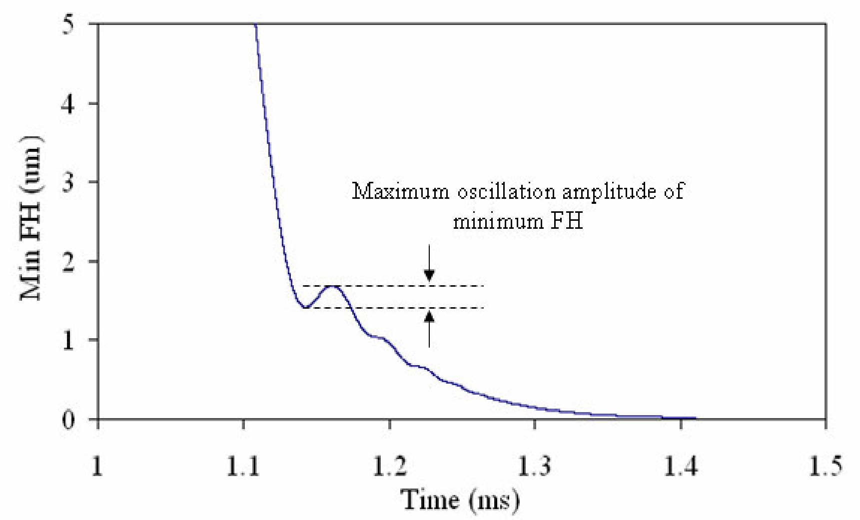

Figure 6.10 Meaning of maximum oscillation amplitude of minimum flying height

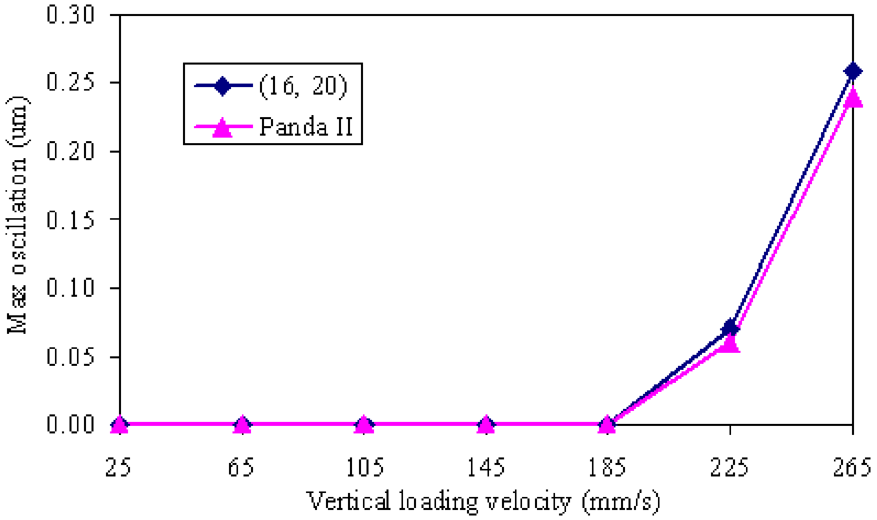

Figure 6.11 Effects of vertical loading velocity on the maximum oscillation amplitude of minimum flying height

For evaluation and comparison, the oscillation amplitude of the minimum flying height is used and the definition is shown in Figure 6.10. Figure 6.11 shows the vertical velocity effect on the maximum oscillation amplitude of the minimum flying height of the triple-negative-zone slider (1.6, 2.0) and the Panda II slider. It is shown that both of the sliders show no oscillation in the vertical direction for loading velocity of 185 mm/s and lower. As the loading velocity increases to above 185 mm/s, the oscillation amplitude of the minimum flying height increases for both the sliders, but the amplitude of the triple-negative-zone slider is slightly larger than that of the Panda II slider.

6.5.2 Effect of Pitch Static Attitude

The pitch static attitude (PSA) of the slider affects their steady flying attitudes, and it significantly affects the load/unload performances. A slider of positive PSA is of less chance of slider-disk contact during the loading operation. A slider which can tolerate more negative PSA is assumed to be more robust in the loading operation. Table 6.4 lists the result of the PSA effects on the minimum flying height for the triple-negative-zone slider (16, 20) and that of the Panda II slider. The loading zone is at disk radius 18 mm and skew angle of 0º. The disk RPM is 10,000 and the vertical loading velocities for the loading process is taken to be 65 mm/s. The slider loading process starts from the initial head-disk spacing of 27.0 μm.

The discussion here starts from a base recess combination of slider (1.6, 2.0). It is shown that no slider-disk contacts occur when the PSA is larger than -0.075^{o} for both the triple-negative-zone slider (1.6, 2.0) and the Panda II slider. But the triple-negative-zone slider contacts the disk when the PSA reaches -0.075^{o}, while there is still no contact for the Panda II slider.

Table 6.4 Static pitch attitude effects on the two kinds of sliders

Pitch static attitude (deg)	Triple-negative-zone slider (1.6, 2.0)	Panda II slider
0.500	+	+
0.250	+	+
0	+	+
-0.050	+	+
-0.060	+	+
-0.075	-	+
-0.090	-	+
-0.100	-	-

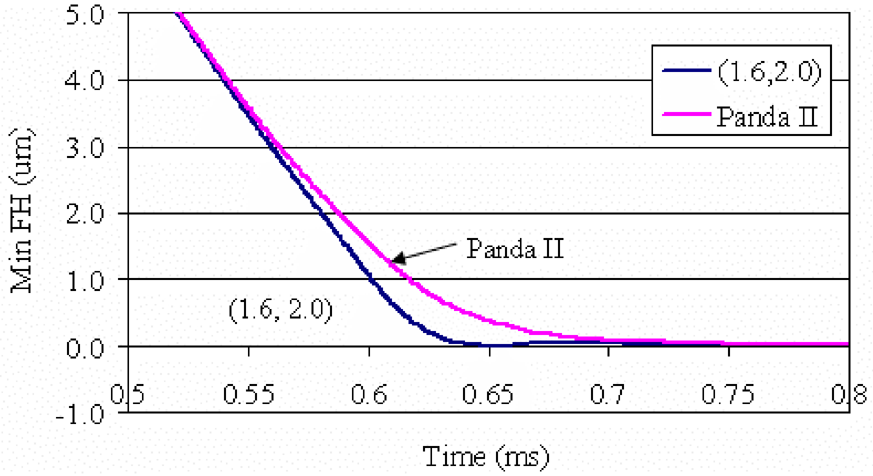

Figure 6.12 Minimum flying heights of the two sliders with PSA of –0.075°

Figure 6.12 shows the minimum clearance for the triple-negative-zone slider (1.6, 2.0) and that of the Panda II slider when the PSA is –0.075°. It is shown that there is still small oscillation for the triple-negative-zone slider (16, 20), but the loading performance of the Panda II slider is smoother.

According to the discussion presented in the previous section, we would like to explore improving the loading performance of the triple-negative-zone slider by increasing the etching depth of Ne2 areas.

Table 6.5 lists the effects of the PSA on the minimum clearance during the loading process with sliders of etching depths at Ne2 areas of 2.0 μm, 3.2 μm, 4.0 μm and 4.8 μm, respectively, comparing with the Panda II slider. The flying height of the sliders are maintained to be within 3.0~4.0 nm. This is achieved by adjusting the etching depth of the 1st shallow step or 2nd shallow step to offset the flying height increase caused by increasing the etching depth in Ne2 area.

From Table 6.5, it can be observed that the slider (1.6, 4.0), slider (1.6, 4.8) and the Panda II slider have comparable loading performance and have smoother loading process than the slider (1.6, 2.0) and slider (1.6, 3.2). There are no contacts for them until the PSA is -0.105°. It is also observed that there is no much obvious further improvement of the loading performance for the slider (1.6, 4.8) when compared to the slider (1.6, 4.0).

Table 6.6 lists the force analyses of these four triple-negative-zone sliders. The first and second columns show the total positive and negative forces, respectively. The third column is the force center of the total negative force. The fourth column is the accumulated negative force at both Ne2 areas and the last column is the percentage of the negative force at Ne2 areas over the total negative force. It is shown that only 12.14 % of the negative force is located at Ne2 areas for the slider (1.6, 4.8), whilst 22.56 % of the negative force at Ne2 areas for the slider (1.6, 2.0).

Increasing the etching depth at Ne2 areas will reduce the negative force near the trailing edge, and thus move the force center of the negative force forward to the leading edge. But moving the negative force to the leading edge will deteriorate the loading performance of the sliders. This movement of the negative force leads to counteract the effect of the etching depth in Ne2 areas and results in no further obvious improvement of the loading performance of the slider (1.6, 4.8) when compared to the slider (1.6, 4.0).

Table 6.5 PSA effects on Min flying height with different etching depth of Ne2 area

	Etching Depth (μm)					
Static Pitch (°)	(1.6, 2.0)	(1.6, 3.2)	(1.6, 4.0)	(1.6, 4.8)	(1.6, 4.8)-I	Panda II
0.500	+	+	+	+	+	+
0.250	+	+	+	+	+	+
0	+	+	+	+	+	+
-0.050	+	+	+	+	+	+
-0.075	-	+	+	+	+	+
-0.090	-	+	+	+	+	+
-0.100	-	-	+	+	+	+
-0.105	-	-	-	-	+	-
-0.110	-	-	-	-	-	-

Table 6.6 Force analysis and loading centre of negative force of the sliders

Sliders	Pos Force (g)	Neg Force (g)	Neg Center (mm)	Neg Force (2*Ne2)	2*Ne2/NegF (%)
(1.6, 2.0)	2.44	-1.64	0.42	0.37	22.56
(1.6, 3.2)	2.29	-1.49	0.39	0.24	16.10
(1.6, 4.0)	2.24	-1.44	0.38	0.20	13.89
(1.6, 4.8)	2.18	-1.40	0.38	0.17	12.14

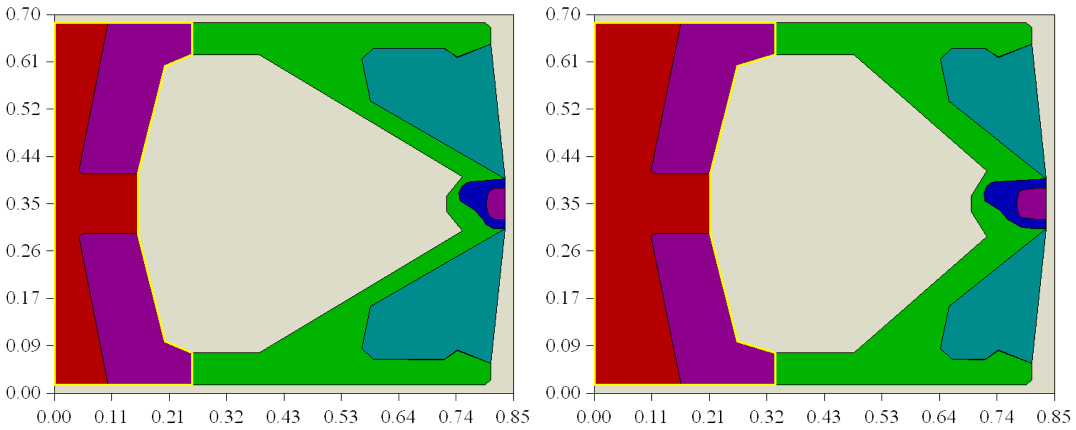

(a) Original triple-negative-zone slider (b) Modified slider (1.6, 4.8)-I

Figure 6.13 Modified air bearing surface design

The above analysis is confirmed by the following practice. The slider (1.6, 4.8) is modified by moving the total negative force towards the trailing edge, which is shown in Figure 6.13. Figure 6.13 (a) is the original triple-negative-zone slider (1.6, 4.8) which is the same as in Figure 6.3. Figure 6.13 (b) is the modified slider (1.6, 4.8)-I. Comparing to the original triple-negative-zone slider (1.6, 4.8), all the pads of slider

(1.6, 4.8)-I are moved backward to the trailing edge, except for the trailing pads. The trailing pads are enlarged in order to maintain the flying height to be around 3.5 nm.

The effect of the pitch static altitude (PSA) on the loading process of the slider (1.6, 4.8)-I are also listed in Table 6.6. It is obvious that slider (1.6, 4.8)-I does not contact the disk even the PSA is -0.105°, which means it has better loading performance than all the other sliders listed in Table 6.6, including the Panda II slider.

Figure 6.14 shows the minimum clearance of the triple-negative-zone slider (1.6, 4.0), the slider (1.6, 4.8)-I and the Panda II slider during the loading process, where PSA is –0.10° and –0.11° for Figures 6.13 (a) and (b), respectively. Table 6.7 list the static flying attitude and the forces of the sliders. It can be seen that these three sliders have comparable gap flying height. But the pitch angle of the Panda II slider is much higher than the slider (1.6, 4.0) and the slider (1.6, 4.8)-I. Another significant difference is that the exerting center of the positive force of the slider (1.6, 4.0) is before the loading point of the gram load. The loading point of the negative force of the slider (1.6, 4.8)-I is behind the loading point of the gram load by modifying the pads, shown in Figure 6.13. But still the loading point of the negative force of the Panda II slider is much nearer to the trailing edge. In other words, the loading performance of the Panda II slider is due to shifting the negative force center to a position beyond the gram load point and towards the trailing edge of the slider. However, the proposed triple-negative-zone approach achieves satisfying loading performance by proper arrangement of recess depth and allows satisfying loading performance even the negative force center is before the gram load point (between leading edge and the gram load point).

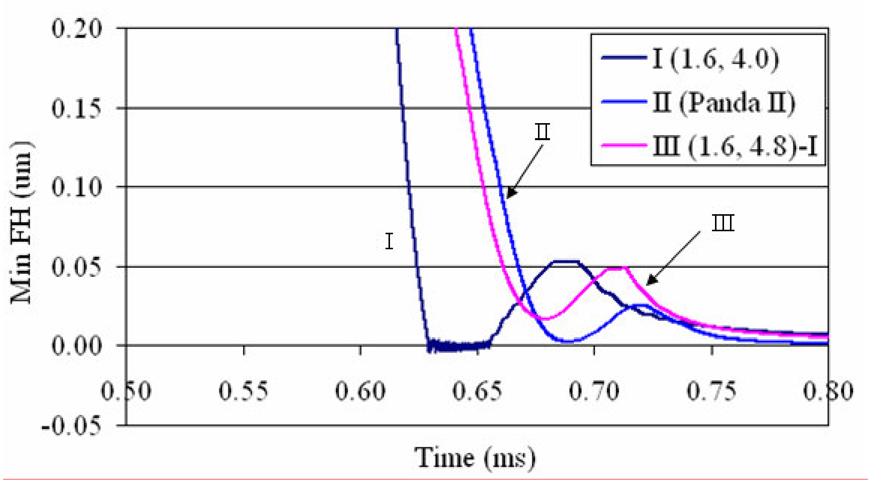

(a) Minimum flying height during loading process with PSA -0.10°

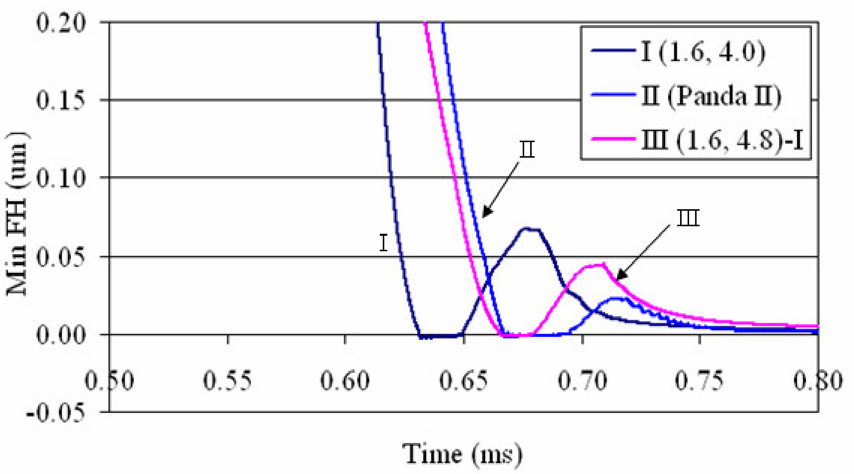

(b) Minimum flying height during loading process with PSA -0.11°

Figure 6.14 Minimum flying heights of the sliders during the loading process

Table 6.7 Static flying height attitude and forces of the sliders

Slider	Pitch (µrad)	Roll (µrad)	Gap FH (nm)	Pos Force (g)	Neg Force (g)	Neg Force Center (mm)
(1.6, 4.0)	124.89	-0.68	3.28	2.21	-1.43	0.381
(1.6, 4.8)-I	143.50	-0.85	3.73	2.32	-1.53	0.426
Panda II	183.62	-1.00	3.50	2.36	-1.58	0.499

From the Figure 6.14 (a), it is observed that there is no contact for both the slider (1.6, 4.8)-I and the Panda II slider, and there is contact for the slider (1.6, 4.0). The before-steady-state oscillation of the slider (1.6, 4.8)-I is comparable to that of the Panda II slider.

From Figure 6.14 (b), all the three sliders contact the disk when the PSA is -0.11°. But here we should note that it takes shorter time for the triple-negative-zone sliders to start to contact the disk, especially for the slider (1.6, 4.0). And furthermore, the contact duration of the sliders (1.6, 4.0) and (1.6, 4.8)-I are both shorter than the duration of the Panda II slider, showing the advantages of the proposed triple-negative-zone slider concept.

6.6 Summary

In this chapter, a kind of triple-negative-zone air-bearing surface design concept is proposed and analyzed. The design is of one negative force zone in the middle of the air-bearing surface and two more negative force zones in the trailing half of the slider body.

The relationship between the etching depth of base recess and the negative force built-up time during the loading process is analyzed. The results show that deeper etching depth of the base recess can shorten the built-up time of the negative air-bearing force.

Then the effects of the etching depth of the negative force zones at the trailing part of the slider on the loading performance are studied. Results suggest that deeper etching depth in Ne2 area can smooth the loading process of the slider.

Investigations confirm that the proposed triple-negative pressure zone approach can achieve satisfying loading performance by proper arrangement of recess depth. It can lead to satisfying loading performance even the negative force center is before the gram load point (between the leading edge and the gram load loading point).

Chapter 7

Nano-Actuator, Proximity-on-Demand and Flying Height Adjustment

An important aspect for ultra-small head-disk spacing technology is how to reduce the chance of the slider-disk contacts and to reduce the head-disk wear, as the occasional contacts between the slider and disk are inevitable when the flying height becomes lower and lower.

In this chapter, a mechanism to realize “proximity-on-demand” interface is proposed which utilizes a piezoelectric actuator (PZT) to adjust the curvature (crown and camber) of the air bearing surface, thus to adjust the flying height. Experimental results confirm the feasibility of such an approach.

7.1 Proximity-On-Demand Technology and Nano-Actuators

7.1.1 Proximity-on-Demand and Necessity of Nano-Actuators

When the flying height is lower than 5.0 nm, it is difficult to prevent the intermittent contact between the head and the disk surface. Such contact will lead to surface wear of both the head and disk surface. Such a surface wear affects the long term robustness of the hard disk drives, especially when the magnetic spacing between the head and the disk is further reduced.

One possible choice for further reducing the magnetic spacing between head and disk is the contact recording technology. Again, one of the major concerns of contact recording is the surface wear.

Wear is a function of time. One approach to reduce the surface wear is to reduce the possible slider-disk contact time during the whole targeted lifespan of the disk drive. Thus, “proximity-on-demand” technology is explored in this thesis. A “proximity-on-demand” interface (shown in Figure 7.1, $FH_i > FH_o$) is the one in which the slider is raised to a safe flying height when it is not in reading or writing. However, the slider will be lowered to proximity to or even partially contact with disk surface during the read/write operation period. Such an approach is expected to significantly decrease the head and disk wear because the actual read/write operation in disk drive is less than 1 % of the total time of the head flying over the disk surface.

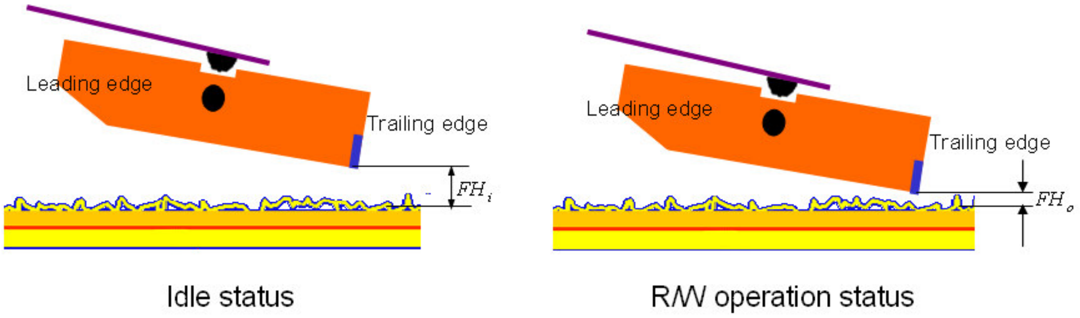

Figure 7.1 “Proximity-on-demand” concept --- the flying height is reduced to its working value only during the read/write operation period whilst the slider will be at high flying height status when the head is not in its read/write operation period

Therefore, a nano-actuator is required for achieving such a “proximity-on-demand” operation. The reason we call the actuator as “nano-actuator” is that the required position change is only a few nanometers --- a mechanical head-disk spacing above 5 nm will be enough to reduce the contact and contact induced wear to a negligible level.

7.1.2 Possible Actuating Principles for Nano-Actuators

1) Piezo-Electric Actuator

The application of an electric field to a piezoelectric material leads to a physical deformation. The common deformation consists of extension mode and shear mode (as will be illustrated in section 7.2). The piezoelectric actuator is of the following advantages: strong force generated by piezoelectric actuator, high response frequency, almost zero power loss, and very high resolution (sub-nanometer). The concern is its large driving voltage for the actuation [61-66].

2) Electro-Static Actuator

The actuation principle of electrostatic actuators is based on the attraction of two oppositely charged plates. The force between two parallel plates is as follow:

$$F_e = \frac{\varepsilon_0 \varepsilon_r A}{2D^2} V^2 \tag{7.1}$$

where $\varepsilon_0\varepsilon_r$ is the dielectric permeability, A is the plate area, V is the voltage applied and D is the distance between the two plates. The concern is the possible breakdown (due to a small air gap), which can damage the slider or disk surface [67-73].

3) Thermal Actuator

Thermal actuation is caused by the difference of the thermal expansion coefficients of two materials or the temperature difference at different positions. These differences make the slider body to be deformed. The thermal actuation has strong force and large displacement. But the response frequency of such actuation is usually not high [74, 75].

7.1.3 Possible Implementation of Flying Height Adjustment

When a slider is flying over a rotating disk, the actual flying height is determined by the forces acting on the slider's air bearing force and the applied gram load. The main parameters of air bearing slider design that affect the flying height are:

1) The shape, depth and wall profile of the rails;
2) Gram load and its loading point;
3) Surface profile of air bearing surface (crown, camber and twist).

Here, crown (full crown) is a description of slider curvature in its length direction, camber is a description of slider curvature in its width direction and the twist is a description of slider curvature across two diagonal corners of a slider, as illustrated in Figure 7.2 [76].

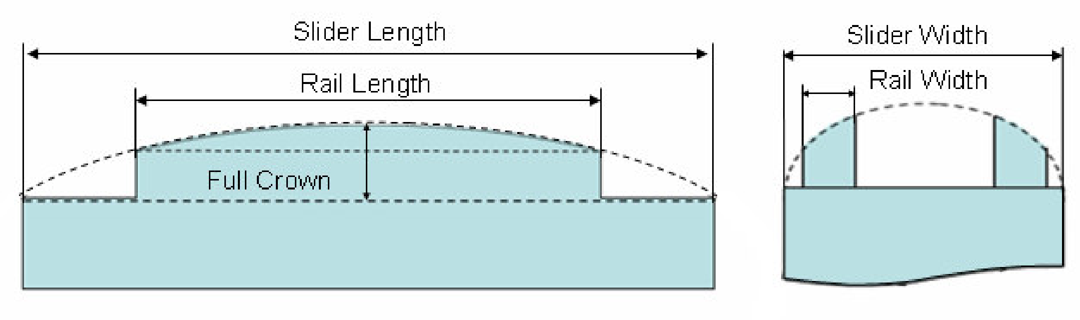

(a) Illustration of crown (full crown) (b) Camber

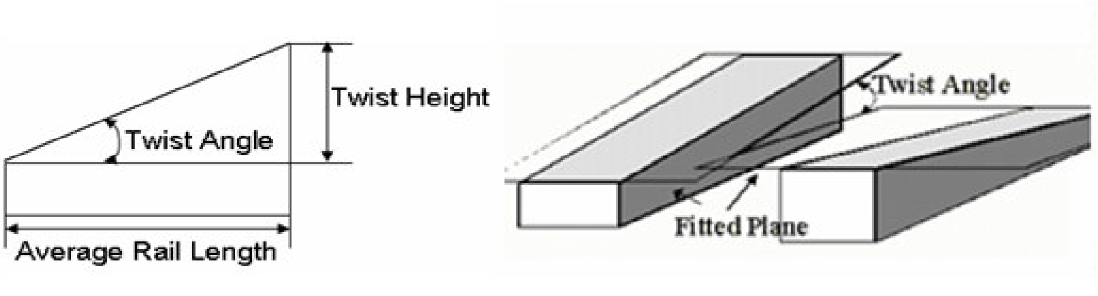

(c) Twist definition

Figure 7.2 Definitions of Crown, Camber and Twist

The main approaches of flying height adjustment can be classified into three groups: adjusting gram load, modifying surface profile of air bearing surface and moving read/write element directly.

1) Adjusting the Force from Suspension to Slider --- Adjusting the Gram Load

Gram load is the loading force applied by a suspension to the slider body. Its direction is towards disk surface. The flying height decreases with an increase of gram load. If one or more piezoelectric actuators are attached to the suspension, the gram load can be actively changed by the applied voltage to the piezoelectric actuator [77].

2) Adjusting the Force from Slider to Disk --- Introducing Electrically Controllable Force between Slider and Disk Surfaces

The flying height can be adjusted if an electrically controllable electro-static force is introduced to the slider-disk interface. In head disk interfaces, the conducting part of the slider body is the Al_2O_3-TiC substrate and the conducting part of the disk close to the slider surface is the magnetic layer. When an electric voltage is applied in head disk interface, the electrical force between the slider and disk will reduce the flying height. But the main problem of the flying height adjustment with electrostatic force is the read head (a GMR sensor) may be damaged by the electro-static discharge [78].

3) Adjusting the Slider Surface Profile to Control the Flying Height

Flying height is the mechanical spacing between the read/write head and the disk. Such a flying height is highly dependent on the profile of the slider air bearing surface. For a given air-bearing surface design and gram load, the flying height will be higher if the slider's crown is increased. Thus the flying height can be adjusted if the surface profile of air bearing surface can be adjusted by a micro-actuator [79].

4) Introducing Relative Motion between Slider and Read/Write Element

The most direct method to adjust the flying height is to attach the read/write head onto a micro-actuator. The micro-actuators move the read/write element directly to change the magnetic spacing between the head and media.

Flying height adjustment by moving the read/write element could be achieved by using piezoelectric materials which are working in the transverse or shear mode [62, 64, 80]. Its driving mechanism is not sophisticated. However, stress control (the stress caused by the PZT in the magnetic material of the read/write element) is not that easy, especially considering that the read/write element can be very close to the actuator.

The electrostatic micro-actuator can also be used to adjust the flying height [81]. Such an actuator can be light in weight and of simple structure. But it is a great challenge to realize compatibility between the read/write head manufacture process and the surface micro-machining process of the electrostatic micro-actuator.

7.2 Structural Design of Active Slider for Adjusting Surface Profile

Among the possible approaches for the flying height adjustment, the author prefers to control slider's geometry so as to control the flying height --- changing the crown and/or the camber of a slider to adjust its flying height. This is because such a slider-suspension system is simple and much easier to be fabricated based on the existing slider manufacturing process.

The requirements for crown adjustment include the followings: (1) high frequency response, (2) large enough crown change (30~60 nm), and (3) easy for fabrication and integration. We found that the piezoelectric actuator based surface profile control approach is the most suitable method. The flying height of the slider is adjusted by changing the crown and the camber of the slider, using a bulk PZT as the actuator.

7.2.1 Crown/Camber Change and Flying Height Variation

The flying height of the slider varies when the crown and/or the camber of the slider changes. A kind of air-bearing surface design, as shown in Figure 7.3, is used for the relationship study between the crown/ camber change and the flying height variation. The working condition parameters used for the investigations include the followings: 17.6 nm gap flying height (pole tip), 20.35 mm working radius, 4.26º skew angle and 5400 RPM disk rotation speed. The static values of the slider's crown and camber are 20 nm and 5 nm, respectively.

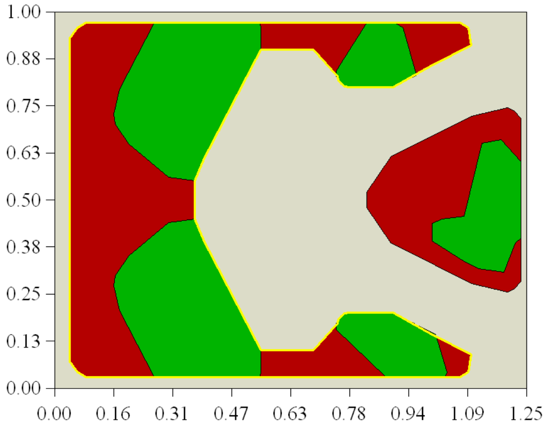

Figure 7.3 Air-bearing surface of the slider used for the analysis of crown/camber change and flying height variation --- sensitivity analysis

The relationships between the flying height and the crown and camber of the slider are plotted in Figures 7.4 and 7.5, respectively. A crown increase of 10 nm results in a flying height change of 2.5 nm. On the other hand, if the camber increases 10 nm, the flying height reduces 1 nm. In order to increase the flying height variation range, we should increase the adjustable range of the slider's crown. Meanwhile, we should reduce the variation of the camber. The results also suggest that the flying height change is not as sensitive to the camber change comparing to the sensitivity to the crown change.

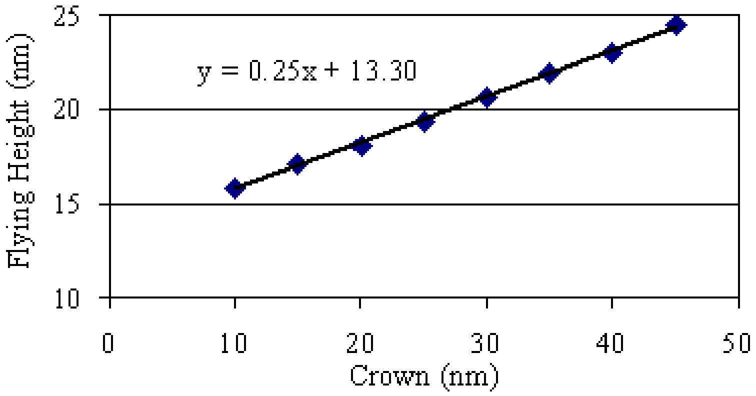

Figure 7.4 Relationship between the change of crown and flying height

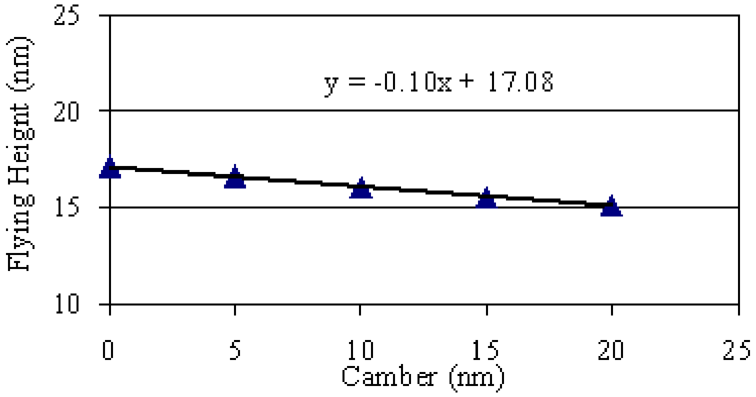

Figure 7.5 Relationship between the change of camber and flying height

7.2.2 Implementation of Flying Height Adjusting Mechanism by Crown Adjustment

The proposed implementation is illustrated in Figure 7.6. A piece of PZT is bonded to the backside of a slider to adjust the crown value of the slider. The length and the width of the slider are 1.25 mm and 1.0 mm, respectively. The total thickness of the active slider is still 0.3 mm, the same as a standard pico slider. Figure 7.7

shows the deformation of the active slider when a voltage potential is applied to the PZT. The deformation is simulated with the finite element analysis software ANSYS. The deformation is small and very similar to a parabolic arch. Thus, the deformation of the slider in the length and width directions can be characterized as the changes of the crown and the camber of the slider.

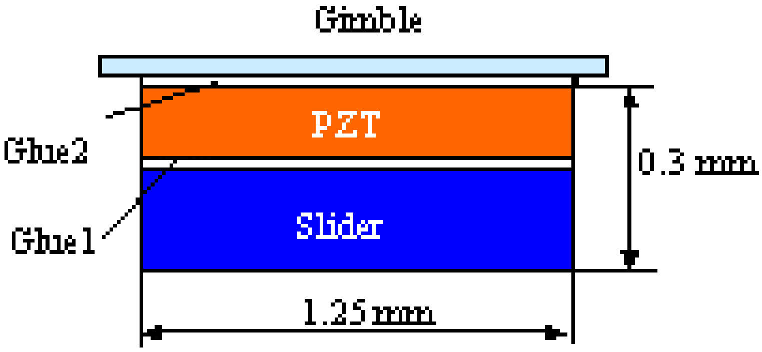

Figure 7.6 Structure design of the active slider

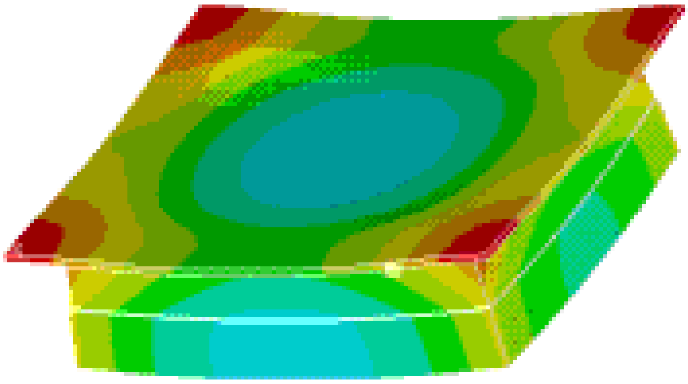

Figure 7.7 Deformation illustration of the active slider

7.2.3 PZT for Crown Adjustment

When certain crystalline ceramic materials are subjected to a mechanical force, the crystals become electrically polarized. Tension and compression generate voltages of opposite polarity. The voltage will be in proportion to the applied force. The converse of such a relationship is also true: if such crystal is exposed to an electric field, it will lengthen or shorten according to the polarity of the field and the lengthened or shortened values will be in proportion to the strength of the electrical field applied. These behaviors are labeled the piezoelectric effect and the inverse piezoelectric effect, respectively [82, 83].

A traditional piezoelectric ceramic is a mass of perovskite crystals, each consisting of a small, tetravalent metal ion, usually titanium or zirconium, in a lattice of larger, divalent metal ions, usually lead or barium, and O_2-ions. At temperature below the Curie point, each crystal has tetragonal or rhombohedral symmetry and a dipole moment (as shown in Figure 7.8). Adjoining dipoles form regions of local alignment called domains. The alignment gives a net dipole moment to the domain and thus a net polarization. The direction of polarization among neighbouring domains is random, so the ceramic element has no overall polarization (Figure 7.9 (a)).

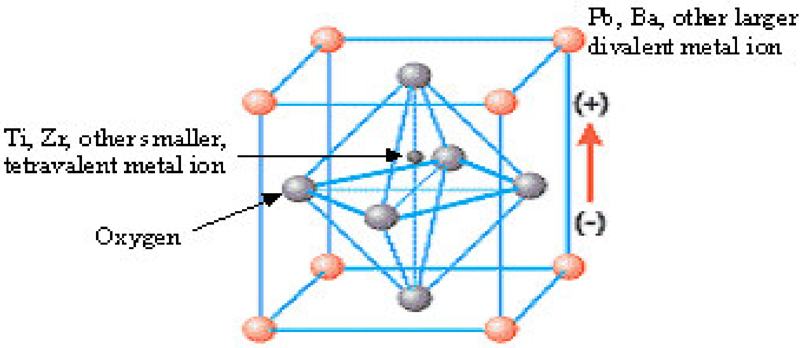

Figure 7.8 Tetragonal lattice, the crystal has electric dipole

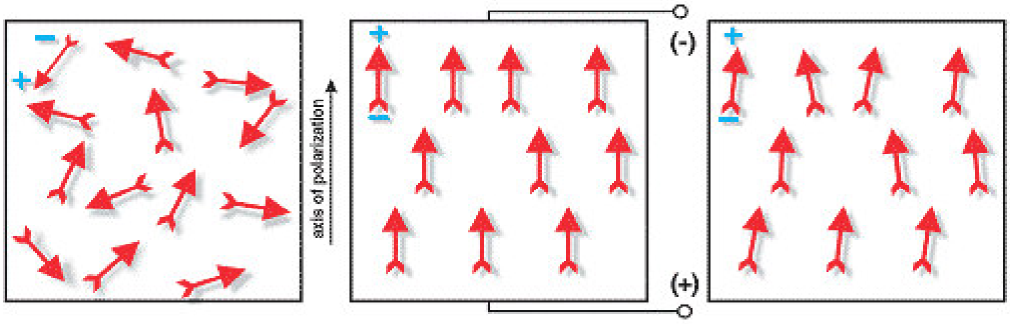

(a) (b) (c)

Figure 7.9 Polarizing (poling) piezoelectric ceramic: (a) random orientation of polar domains prior to polarization; (b) polarization in DC electric field; (c) remanent polarization after electric field removed.

The domains can be aligned by exposing the element to a strong and direct current electric field, usually at a temperature slightly below the Curie point (Figure 7.9 (b)). Through this polarizing (poling) treatment, domains most nearly aligned with the electric field, and the element lengthens in the direction of the field. When the electric field is removed, most of the dipoles are locked into a configuration of near alignment (Figure 7.9 (c)). The element thus has a permanent polarization, the remanent polarization, and is permanently elongated.

Thus mechanical compression or tension on the poled piezoelectric ceramic element will change the dipole moment and create a voltage. On the other hand, if a voltage is applied on the piezoelectric ceramic element, the element will lengthen or shorten.

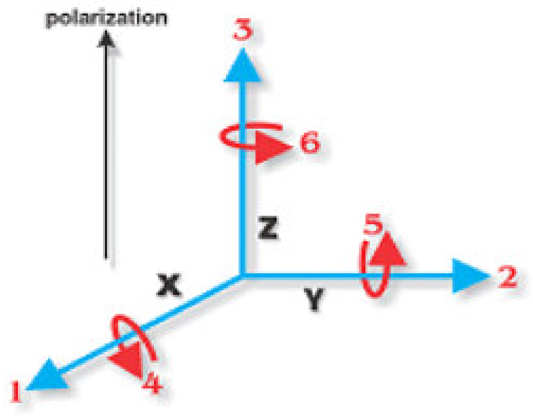

Figure 7.10 Directions of forces affecting a piezoelectric element

A piezoelectric ceramic is anisotropic. Its physical constants relate to both the direction of the applied mechanical or electric forces and the directions perpendicular to the applied force. Consequently, each constant generally has two subscripts that indicate the directions of the two related quantities, such as stress and strain for elasticity. The direction of positive polarization usually is made to coincide with the Z-axis of a rectangular system of X, Y, and Z axes (Figure 7.10). Direction X, Y, or Z is represented by the subscript 1, 2, or 3, respectively, and shear about one of these axes is represented by the subscript 4, 5, or 6, accordingly.

In general, a piezoelectric ceramics plate mainly has three basic modes of vibration: parallel and transverse expansion, shear and bender.

1) Parallel and Transverse Expansion

Figure 7.11 shows the parallel and transverse expansion of the piezoelectric plate. If a voltage of the same polarity as the poling voltage is applied to a ceramic element, in the direction of the poling voltage, the element will be lengthened (Figure 7.11 (b)). If a voltage of polarity opposite to that of the poling is applied, the element will become shorter and broader (Figure 7.11 (c)).

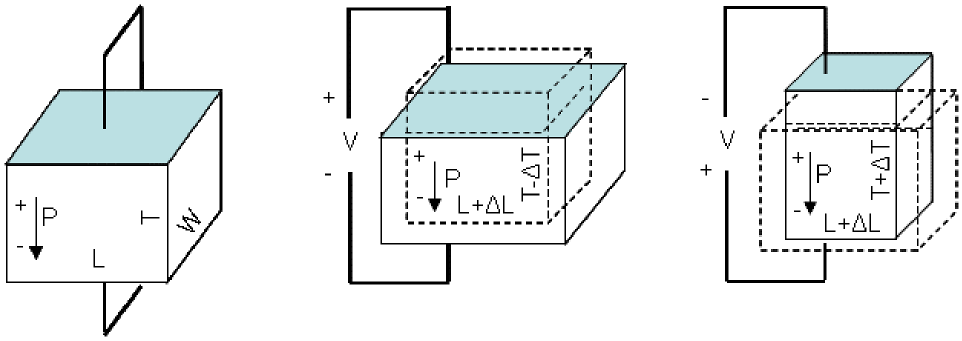

(a) (b) (c)

Figure 7.11 Parallel and transverse expansion of PZT: (a) No voltage is applied; (b) A voltage of the same polarity as the poling voltage is applied; (c) A voltage of opposite polarity to the poling voltage is applied

The parallel expansion is:

$$\Delta T = V \cdot d_{33} \tag{7.2}$$

where

V: the applied voltage;

d_{33}: piezoelectric charge constant (induced polarization in direction 3 (parallel to the direction in which the element is polarized) per unit stress applied in direction 3, or induced strain in direction 3 per unit electric field applied in direction 3).

At the same time, there is transverse expansion:

$$\frac{\Delta L}{L} = \frac{\Delta W}{W} = \frac{V d_{31}}{T} \tag{7.3}$$

where

L: the length of the element perpendicular to the direction of polarization;

W: the width of the element perpendicular to the direction of polarization;

T: the length of the element parallel to the direction of polarization;

d_{31}: piezoelectric charge constant (induced polarization in direction 3 (parallel to the direction in which the element is polarized) per unit stress applied in direction 1, or induced strain in direction 1 per unit electric field applied in direction 3).

2. Shear Mode

When a voltage is applied perpendicular to the direction in which ceramic element is polarized, the shear displacement (Figure 7.12) occurs and it is given by:

$$\Delta x = V \cdot d_{15} \tag{7.4}$$

where, Δx is the strain along poling direction, V is the applied voltage and d_{15} is the piezoelectric charge constant (induced polarization in direction 1 per unit shear stress applied about direction 2 or induced shear strain about direction 2 per unit electric field applied in direction 1).

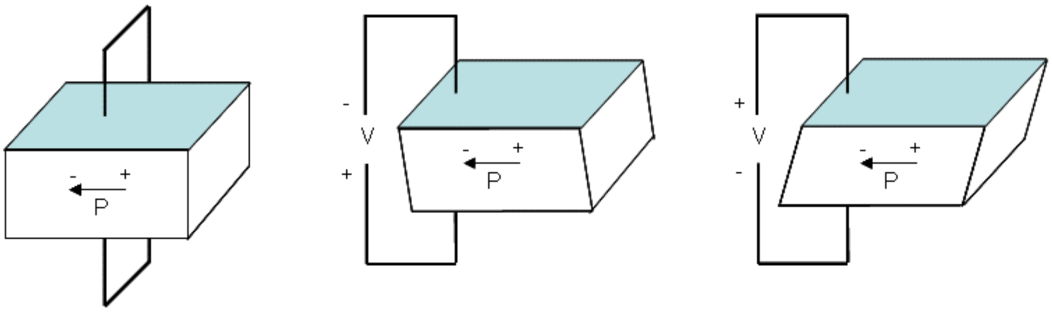

(a) (b) (c)

Figure 7.12 Illustration of shear mode of PZT: (a) No voltage is applied; (b) and (c) A voltage is applied.

7.3 Further Discussion of PZT Based Surface Profile Adjustment

In order to reduce the applied electric voltage, it is necessary to analyze the parameters that affect the deformation of the slider body. In the following simulation, the effect of the gimbal has been considered because the active slider should be bonded to the gimbal of the suspension when the slider is flying over the disk. The thickness of gimbal is 18 μm and its modulus of elasticity is 180 Gpa. Glues between the slider and the PZT, the PZT and the gimbal are also considered. And if it is not specified, the thickness and modulus of elasticity of the glue between the slider and the PZT are 2 μm and 0.255 Gpa, respectively. And the thickness and modulus of elasticity of the glue between the PZT and the gimbal are 2 μm and 0.173 Gpa, respectively. The applied voltage is 20 V.

7.3.1 Effect of PZT Thickness

To obtain a maximum flying height adjustment, the PZT thickness in an active slider should be optimized. The relationship between the changes of the crown and the camber with the PZT thickness is simulated and the result is shown in Figure 7.13. It is observed that the changes of the crown and the camber do not always keep increasing with the increase of the PZT thickness. The largest changes of the crown and the camber occur when the PZT thickness is 0.16 mm. This may be explained that for an applied voltage, the deformation stroke of the PZT increases when its thickness increases. But at the same time, the thickness of the slider body decreases, which results in reducing the deformation stroke of the slider. But the differences of the changes of the crown and the camber are less than 1 nm when the PZT thickness varies from 0.04 mm to 0.16 mm.

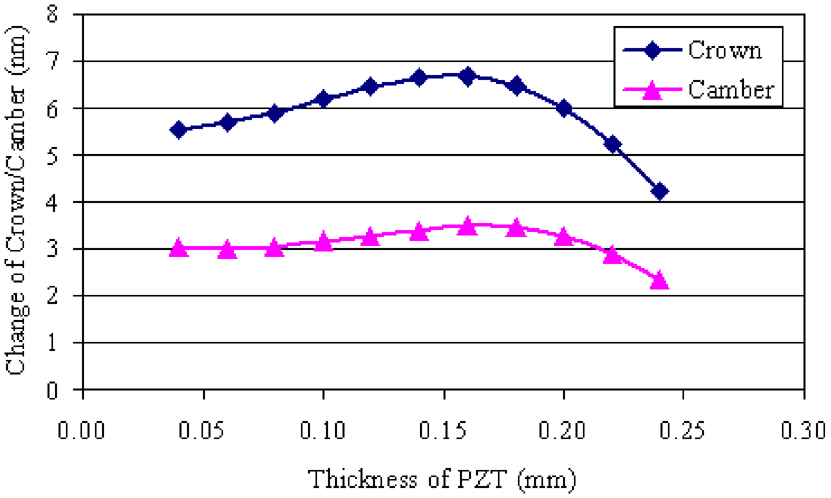

Figure 7.13 Effect of PZT thickness on the changes of crown/camber

7.3.2 Effect of Glue between Slider and PZT

Because there is a large strain in the joint of the slider and the PZT actuator, the glue plays an important role in adjusting the surface profile of the air-bearing surface. Figure 7.14 shows the relationship of the changes of the crown and the camber with the thickness of the glue between the slider and the PZT. The thickness of the slider and the PZT are both of 0.15 mm. It can be observed that the changes of the crown and the camber drastically decrease with the increase of the glue thickness. So it is necessary to make the thickness of the glue between the slider and the PZT as thin as possible in the fabrication of the active slider.

Figure 7.15 shows the relationship between the changes of the crown and the camber and the changes of the elasticity modulus of the glue between the slider and the PZT. It can be seen that the changes of the crown and the camber increase with the increase of the elasticity modulus of the glue. But the increase is small when the elasticity modulus is bigger than 1 Gpa. The glue thickness used here is 2 µm.

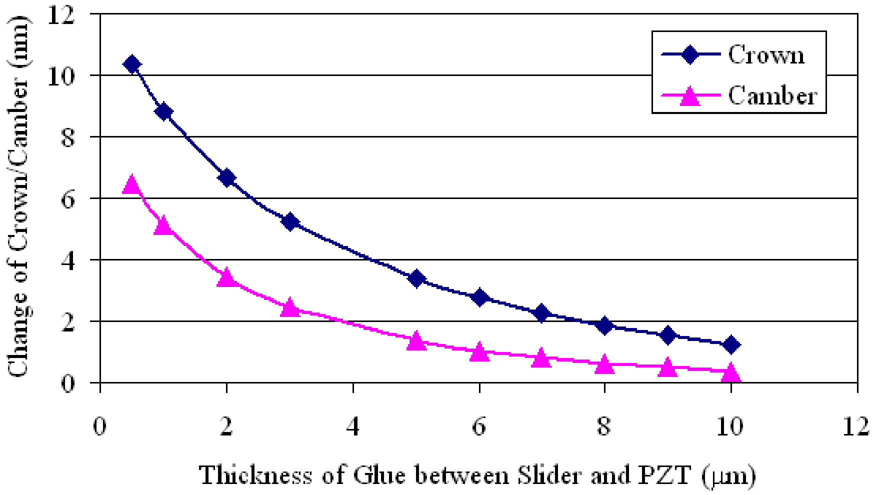

Figure 7.14 Effect of thickness of the glue between slider and PZT on the changes of crown/camber

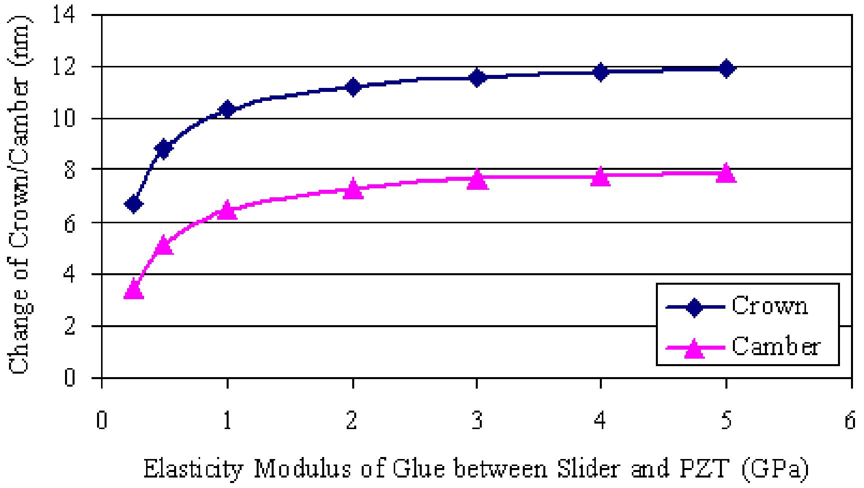

Figure 7.15 Effect of elasticity modulus of the glue between slider and PZT on the changes of crown/camber

7.3.3 Effect of Glue between PZT and Suspension

Figure 7.16 shows the effects of the thickness of the glue between the PZT and the gimbal on the changes of the crown and the camber. In the simulation, the thicknesses of the slider and the PZT are 0.15 mm. It can be seen that the changes of the crown and the camber increase when the glue thickness increases.

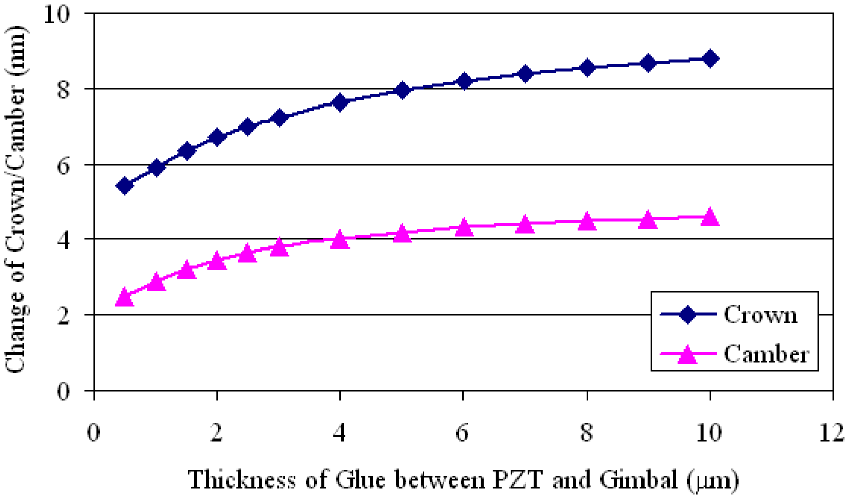

Figure 7.16 Effect of thickness of glue between PZT and gimbal on the changes of crown/camber

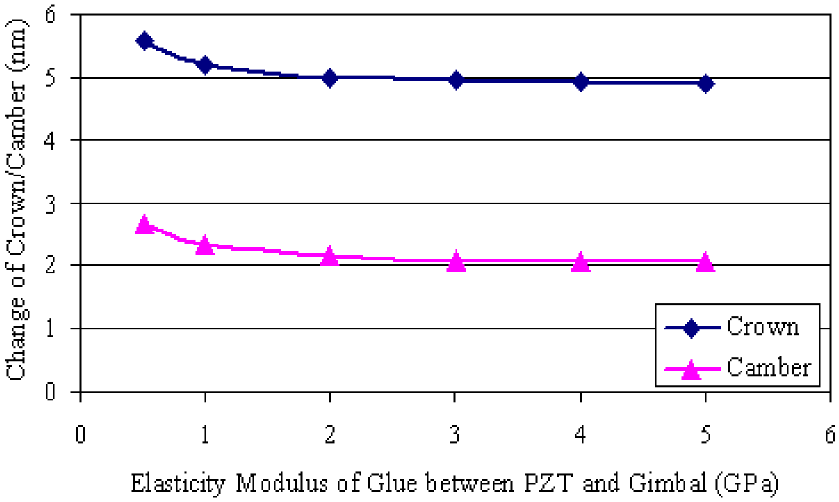

Figure 7.17 Effect of elasticity modulus of glue between PZT and gimbal on the changes of crown/camber

Figure 7.17 shows the relationship of the changes of the crown and the camber with the elasticity modulus of the glue between the slider and the PZT. It can be seen that the changes of the crown and the camber decrease with the increase of the elasticity modulus of the glue. But the increase is very small when the elasticity modulus is bigger than 2 Gpa.

7.3.4 Effect of Applied Voltage

Figure 7.18 shows the simulation results of the slider deformation with the changes of applied voltage, where the thickness of the PZT and the slider are both of 0.15 mm. The thickness and elasticity modulus of the glue between the slider and PZT are 2 μm and 0.255 Gpa, respectively. The thickness and elasticity modulus of the glue between the PZT and gimbal are 2 μm and 0.173 Gpa, respectively.

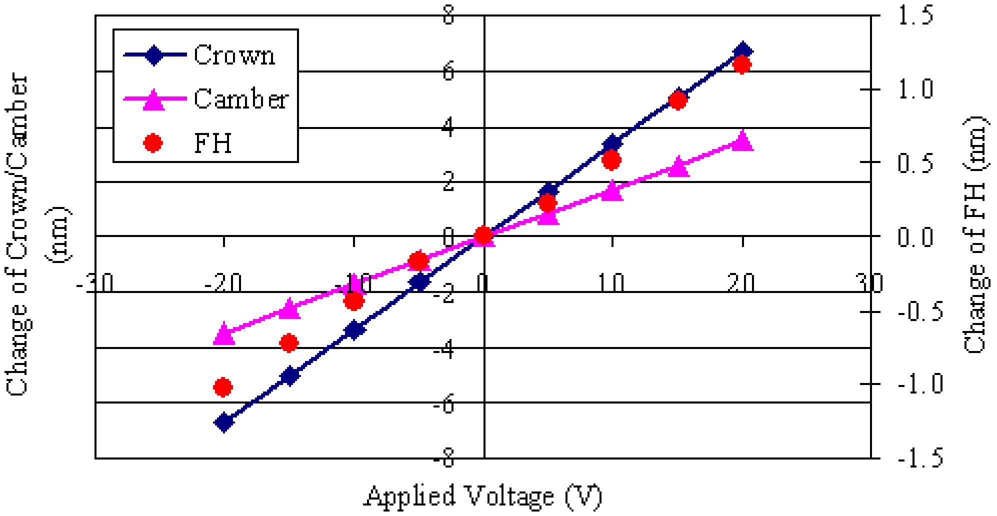

Figure 7.18 Effect of applied voltage on the changes of crown, camber and flying height

It can be observed that the changes of the crown and the camber are almost linear with respect to the applied voltage. When the voltage changes from -20 V to 20 V, the change of the crown increases from -6.69 nm to 6.69 nm and the change of the camber varies from -3.46 nm to 3.46 nm. The corresponding change of the flying height of the slider shown in Figure 7.3 is also plotted in the figure. The change of the flying height varies from -1.33 nm to + 0.92 nm when the applied voltage ranges from -20 V to 20 V.

7.4 Experimental Evaluation of the Active Slider for Flying Height Control

The pico slider shown in Figure 7.3 is fabricated with a PZT bonded to the backside of the slider body and is utilized for the feasibility study of the "proximity-on-demand" interface. The slider material is AlTiC (Al_2O_3/TiC), whose elasticity modulus is 390 GPa. The PZT used in the study is produced by Noliac. The material properties are listed in Table 7.1.

Table 7. 1 Properties of PZT for analysis

$\varepsilon_{1,r}$	1800	s_E^{13} (10^{-12} m^2/N)	-8.61	d_{31}(10^{-12} C/N)	-170
$\varepsilon_{3,r}$	1800	s_E^{33} (10^{-12} m^2/N)	23.2	d_{33} (10^{-12} C/N)	425
s_E^{11} (10^{-12} m^2/N)	17.0	$s_E^{44} = s_E^{55}$ (10^{-12} m^2/N)	43.5	d_{15} (10^{-12} C/N)	506
s_E^{12} (10^{-12} m^2/N)	-6.60	s_E^{66} (10^{-12} m^2/N)	47.1	Density (kg/m^3)	7700

The fabrication processes of the active slider are listed below:

(1) Fabricate the standard pico slider with required air-bearing surface;

(2) Reduce its thickness from 0.3 mm to 0.15 mm from backside by dicing;

(3) Lap the backside to get a smooth surface and reduce stress caused by dicing;

(4) Bond PZT to the backside of the slider with adhesive (Loctite 420, because its viscosity is low, it is relative easy to get thin adhesive layer). The size of the PZT is longer than 1.25 mm in order to have some area for electrical connection of the PZT actuator;

(5) Assemble the active slider onto a suspension;

(6) Bond wire for electrical connection of the PZT actuator.

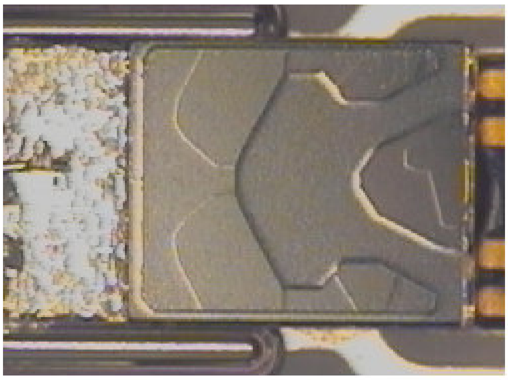

Figure 7.19 Fabricated active slider

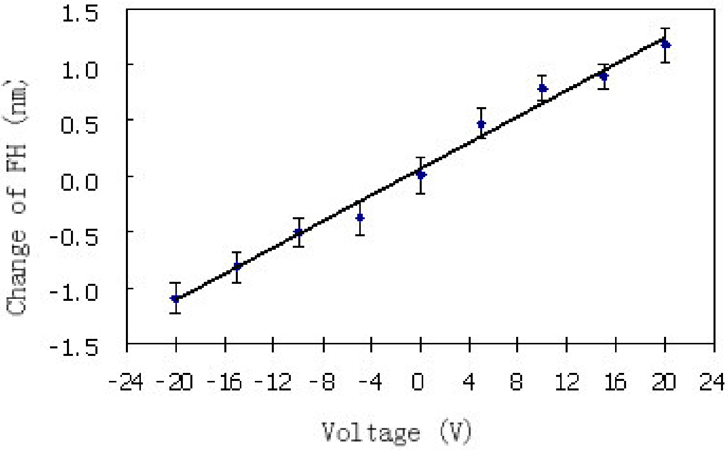

Figure 7.20 Experimental results of adjustment of flying height vs. applied voltage

Figure 7.19 shows the fabricated active slider. Its flying height was tested with the industry standard Phase Metrics Dynamic Flying Height Tester, as discussed in Chapter 2 (tested at the radius of 20.35 mm, 0° skew angle, and 5400 rpm disk rotation speed). The tested flying height for zero potential is 16.8 nm. Figure 7.20 shows the measurement results of the flying height adjustment. The adjustment of flying height gradually increases from –1.1 nm to +1.2 nm with the increase of applied electric potential from – 20 V to + 20 V. The bars are the standard deviation of the measurement during the flying height testing. It can be observed that the tested results correspond well with the simulation results reported in the previous section.

7.5 Towards More Effective Structure Design for the Active Slider

The above simulation and experimental results confirm that it is feasible to adjust the flying height with a PZT bonded on the backside of the slider body. However, it can also be noticed that the required applied voltage of ± 20 V is too high for the actual hard disk drive.

This section discusses how to increase the flying height adjustment with lower applied voltage.

Two approaches can be used to reduce the applied voltage for the active slider: One is to modify the air bearing surface design to increase the flying height sensitivity to the change of the surface profile (crown). Another approach is to modify the structural design of the active slider to increase the slider deformation for a given applied voltage. In the following, a structural design is proposed to reduce the applied voltage for the active slider.

7 5.1 Structural Illustration

Figure 7.21 shows another structural design of the active slider. The length, the width and the total thickness of the active slider are the same as a standard pico slider. Compared with the structure shown in Figure 7.6, a groove is formed on the backside of the slider through the width direction. The slider is bonded to the PZT, and then the PZT is bonded to the suspension. Figure 7.22 shows the deformation of the active slider when a voltage potential is applied to the PZT.

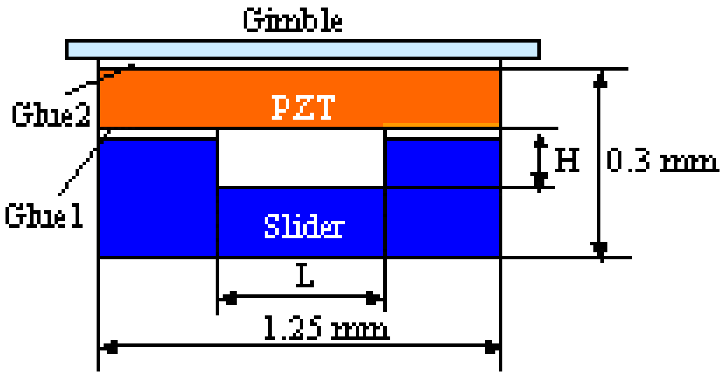

Figure 7.21 Improved structure of the active slider

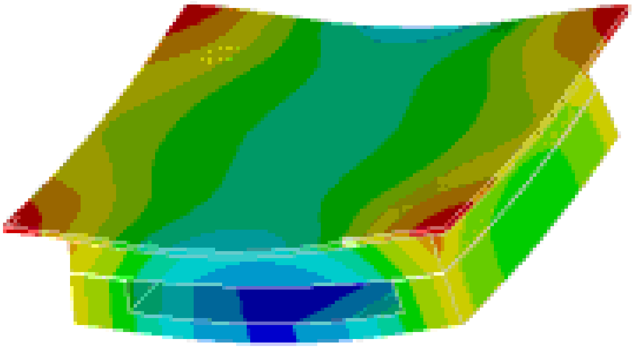

Figure 7.22 Deformation illustration of the active slider

7 5.2 Parameter Analyses

For the structure in Figure 7.21, there are two more parameters that affect the deformation of the slider body: the groove width and depth (L and H in the figure, respectively). For simplicity, the structure shown in Figure 7.6 is denoted as structure I, and the design shown in Figure 7.21 is denoted as structure II.

In the following simulation, if it is not specified, the thicknesses of the PZT and the slider are taken to be 0.15 mm, the groove width and depth are 0.6 mm and 0.08 mm, respectively, the thickness and elasticity modulus of the glue between the slider and the PZT are 2 μm and 0.255 Gpa, respectively, while the thickness and elasticity modulus of the glue between the PZT and the gimbal are 2 μm and 0.173 Gpa, respectively. The applied voltage is 20 V.

Similarly to the last section, the parameters' effects on the changes of the crown/camber are simulated in the following.

1. Effect of PZT Thickness

The relationship of the changes of the crown and the camber with the PZT thickness is shown in Figure 7.23. It is observed that the change of the crown decreases dramatically with the increase of the PZT thickness. When the thickness of PZT increases from 0.04 mm to 0.2 mm, the change of the crown reduces from 32.9 nm to 7.7 nm. On the other hand, the change of the camber is negligible.

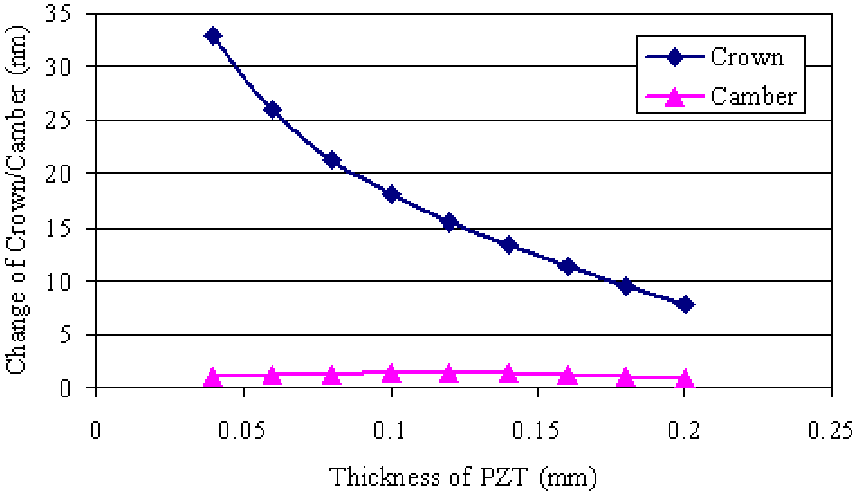

Figure 7.23 Effect of PZT thickness on the changes of crown/camber

2. Effect of the Groove Width and Depth

The groove's parameters will affect the deformation of the slider when the PZT expands or shrinks. Figure 7.24 shows the relationship of the changes of the crown and the camber with the groove width changes. The thicknesses of the slider body and the PZT are both of 0.15 mm. It can be observed that increasing the groove width can increase the change of the crown, while decrease the change of the camber. Both of these are helpful to increase the change of the flying height.

Figure 7.25 shows the effect of the groove depth on the changes of the crown and the camber. Results suggest that increasing the groove depth can increase the change of the crown. The change of the crown ranges from 7.03 nm to 19.36 nm when the groove depth increases from 0.02 mm to 0.16 mm. But the crown change becomes not that sensitive to the further increase of the groove depth when increasing beyond 0.14 mm. On the other hand, the effect of the groove depth on the change of the camber is negligible.

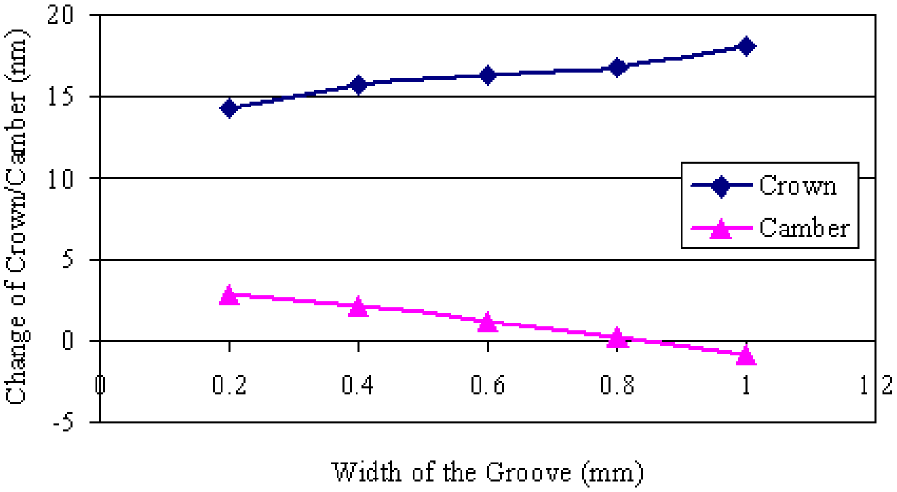

Figure 7.24 Effect of groove width on the changes of crown/camber

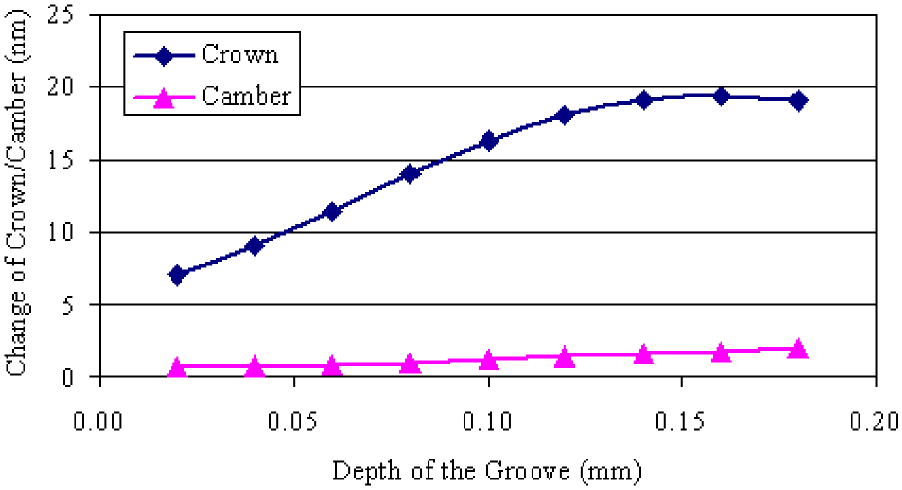

Figure 7.25 Effect of groove depth on the changes of crown/camber

3. Effect of the Glue between Slider and PZT

Figures 7.26 and 7.27 show the changes of the crown and the camber with the changes of the thickness and elasticity modulus of the glue between the slider and the PZT, respectively. It can be observed that reducing the thickness and increasing the elasticity modulus of the glue between the slider and the PZT can increase the changes of the crown and the camber. But the effect of the elasticity modulus of the glue becomes negligible when the elasticity modulus is larger than 2 GPa.

Comparing the results shown in Figures 7.14 and 7.15, the effects of the glues on the changes of the crown and the camber are similar, but the glue's effects of the structure II (the grooved structure) is much smaller than those of the structure I (non-grooved structure). This is because that the contact areas of the glue in the structure II are smaller than those in the structure I, which reduces the effects of the glue on the deformation of the slider.

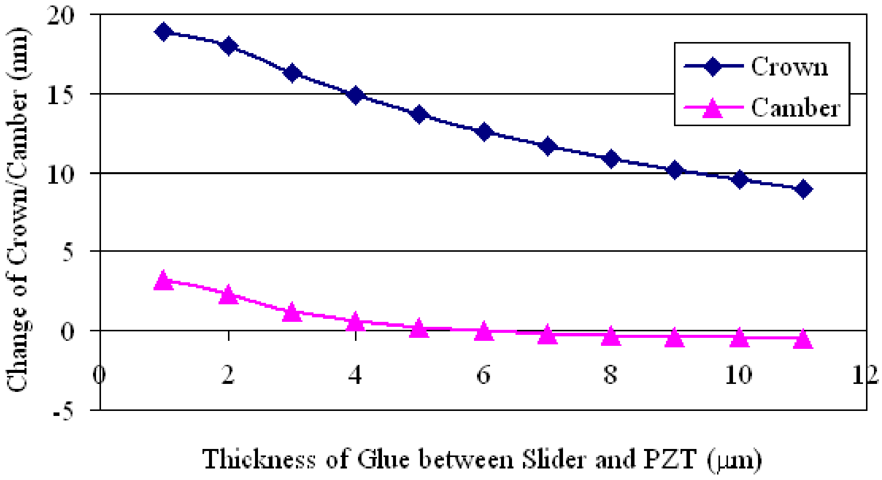

Figure 7.26 Effect of thickness of glue between slider and PZT on the changes of crown/camber

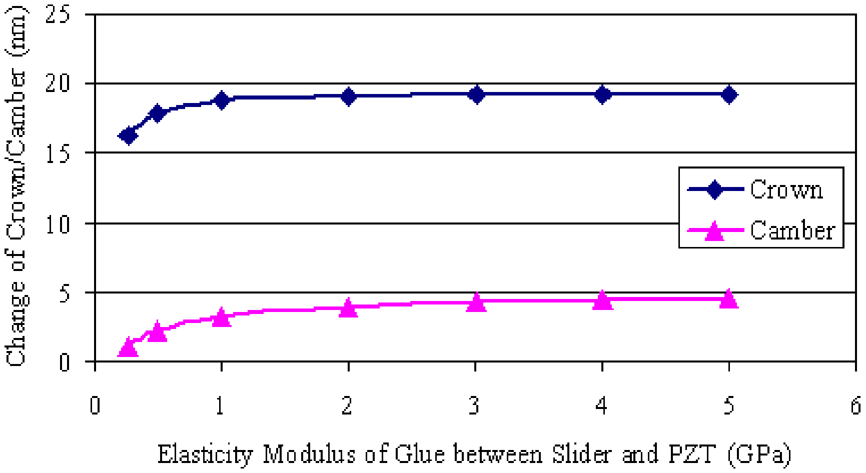

Figure 7.27 Effect of elasticity modulus of the glue between slider and PZT on the changes of crown/camber

4. Effect of the Glue between PZT and Suspension

The relationship of the changes of the crown and the camber with the changes of the thickness and elasticity modulus of the glue between the PZT and the gimbal are shown in Figures 7.28 and 7.29, respectively. It is shown that increasing the thickness and reducing the elasticity modulus of the glue between the PZT and the gimbal can increase the changes of the crown and the camber. But the change of the camber is very small.

Comparing the results to those shown in Figures 7.16 and 7.17, the effects of the glue between the PZT and the gimbal on the changes of the crown and the camber are similar, but the effects of the glue of the structure II is a little bigger than those of structure I, especially the effect on the change of the crown, which is helpful to increase the adjustment of the flying height.

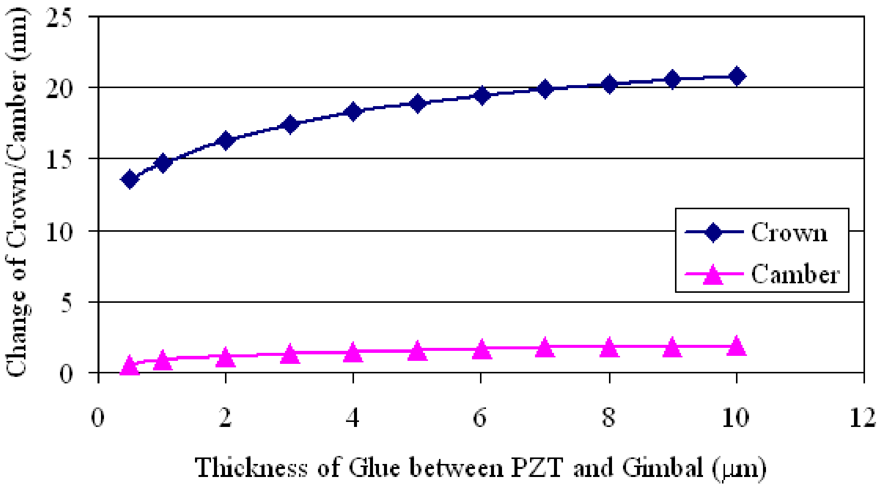

Figure 7.28 Effect of thickness of glue between PZT and gimbal on the changes of crown/camber

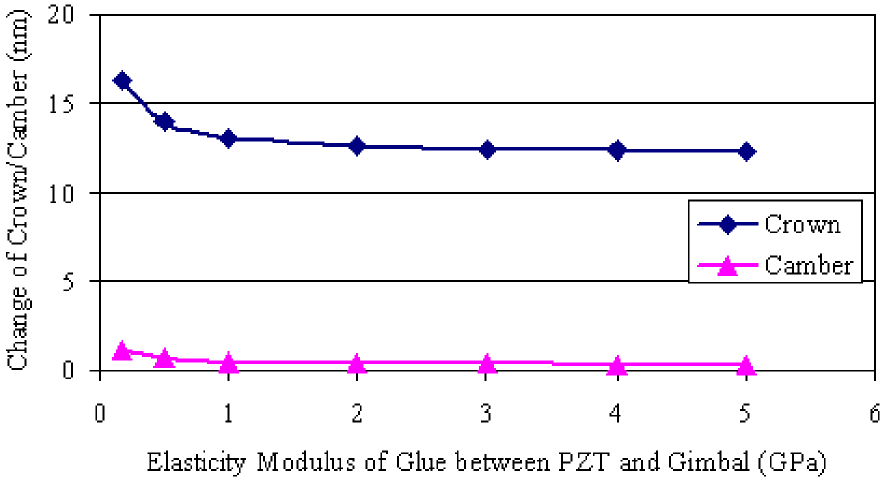

Figure 7.29 Effect of modulus elasticity of glue between PZT and gimbal on the changes of crown/camber

5. Effect of Applied Voltage

Figure 7.30 shows the changes of the crown, camber and the flying height with respect to the applied voltage. Here, the thickness of the PZT is 0.1 mm and the width and depth of the groove are 0.6 mm and 0.1 mm, respectively, the thickness and elasticity modulus of the glue between the slider and the PZT are 2 µm and 0.255 Gpa, respectively, while the thickness and elasticity modulus of the glue between the PZT and the gimbal are 2 µm and 0.173 Gpa, respectively.

It can be observed that the changes of the crown and the camber are almost linear with respect to the applied voltage. When the voltage changes from -20 V to +20 V, the change of the crown increases from -16.31 nm to +16.31 nm and the change of the camber only varies from -1.18 nm to +1.18 nm. The corresponding change of the flying height of the slider shown in Figure 7.3 is also plotted in the figure. It is shown that the change of the flying height varies from -3.38 nm to + 3.83 nm when the applied voltage changes from -20 V to +20 V.

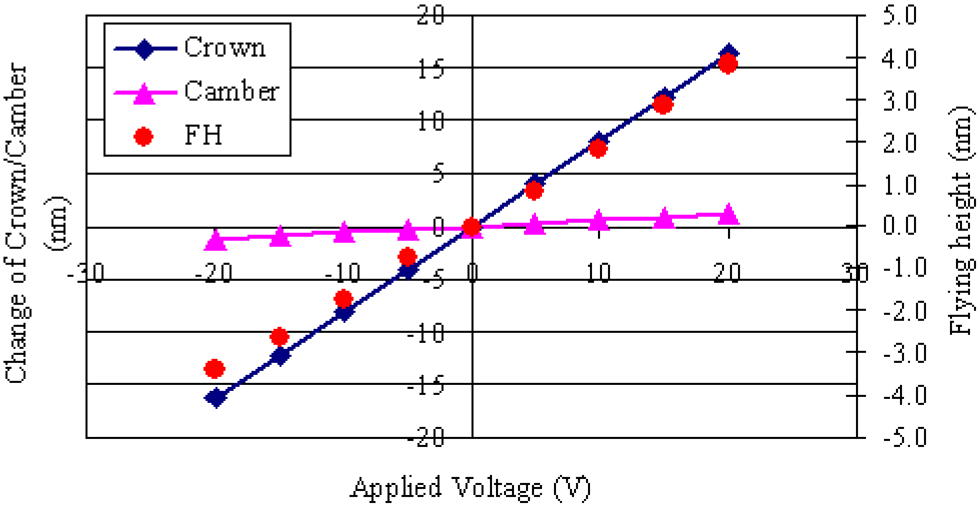

Figure 7.30 Effect of applied voltage on the changes of crown, camber and flying height

Comparing the results shown in Figures 7.18 and 7.30, it can be concluded that with the same applied voltage of -20 V ~ +20 V, the change of the flying height of the structure II (grooved structure) is much larger than the change of the structure I (non-grooved structure). For structure II, an applied voltage range from -7 V to +7 V is enough to obtain the change of the flying height at voltage range of -20 V to 20 V of the structure I. This is because that the groove in the structure II can increase the change of the crown, while reduce the change of the camber with the same deformation of the PZT. Another factor is that the groove in the structure II can reduce the effects of the glue between the slider and the PZT.

7. 6 Summary

In this chapter, an active slider design for “proximity-on-demand” interface was explored. A PZT bulk material was used as a micro-actuator to control the deformation of the slider (crown and camber), and thus to adjust the flying height of the slider. Simulations were carried out to investigate the parameters’ effect on the deformation of the actuator. Slider prototyping and testing results confirmed the feasibility of such an adjusting technology.

An improved structure of the active slider was proposed in order to reduce the applied voltage, where a groove was made across the slider back side in the width direction. Results suggest that grooved slider structure was of significantly increased amount of crown change, thus of the flying height adjustment, for the same voltage applied to the PZT actuator.

The main advantage of using a PZT to control the surface profile of the slider to adjust the flying height is that the structure is very simple to fabricate based on the standard slider fabrication process. And utilizing the improved structure (grooved structure), it was able to reduce the applied voltage in the range of -7 V ~ 7 V to obtain the flying height adjustment of ±1 nm.

Chapter 8

Conclusions and Future Work

This thesis work is focused on the understanding and solution exploration of the key technology challenges for achieving extremely small head-disk spacing so as to further increase the information storage density of modern magnetic hard disk drives.

The areal density of the magnetic hard disk drive during the thesis work period is about 100 Giga-bit per square inch. The work conducted during this thesis work period targeted at exploring technologies to reduce the head disk spacing to 2~4 nm level and push the areal density towards 1000 Giga-bit per square inch (or 1 Tera-bit per square inch).

The major areas of focus of this thesis include technology exploration to minimize the flying height modulation caused by disk waviness, technologies to reduce flying height variation under various possible working altitudes, understanding and exploration of technologies to improve loading performance at extremely low flying height, nano-actuator technology for future flying height control and so on.

It is important to minimize the flying height modulation caused by disk morphology in order to push technology towards 3 nm flying height. Starting from investigating the mechanism of the flying height modulation caused by disk morphology, this thesis investigated the relationship between air-bearing design and flying height modulation. The dynamic response of slider-air bearing designs was investigated. An analytical model was developed and the close-form frequency response function was derived to evaluate waviness following ability of the slider. The analytical results showed that higher stiffness, damping ratio and smaller distance between transducer position and the air bearing force center of the trailing pad could induce better waviness following ability of the slider. Optimization was also conducted to optimize the pad locations and sizes to minimize the flying height modulation caused by disk waviness. Based on these analytical and optimization results, a three-pad air-bearing surface design was developed successfully. The evaluation results showed that new understanding and new technologies proposed in this thesis lead to new slider design which is of much better waviness following ability when compared with any slider designs available in the public domain.

Normally, the flying height drops when the slider flies from lower to higher altitude, due to different air molecule density which leads to the change of the air bearing force. It is important to develop strategies and technologies to minimize the flying height change caused by working altitude, especially when the flying height is around 3 nm only and the allowed maximum flying height change is merely 0.3~0.5 nm. Systematic investigations on the relationship between altitude, air-bearing force on different parts of air bearing surface, and possible air bearing designs were conducted in this thesis. Both the force reductions and the moment reductions tend to reduce the pitch angle and the gap flying height when the slider flies from lower to higher altitude. But the reduction of the pitch angle cannot compensate for the reduction of the gap flying height, which leads to the reduction of the gap flying height. A model was used to study the effects of the changes of the forces and moments on the gap flying height changes due to altitude, and strategies of air bearing surface design to reduce the flying height sensitivity to altitude were proposed. The understandings were applied to the design of the altitude insensitive slider. Results from computer modeling indicate that the designed altitude insensitive slider makes the flying height change negligible at the targeted altitude range.

A multi-negative force zone air-bearing surface, with one negative force zone is in the middle of the air-bearing surface and two more negative force zones in the trailing half of the slider body, was proposed to achieve smooth head-slider loading onto the disk surface. Based on the fact that deeper etching depth of the base recess can shorten the build-up time of the negative air-bearing force, simulation results suggested that deeper etching depth in the negative force zones in the trailing palf of the slider can smooth the loading process of the slider. Investigations confirmed that the proposed triple-negative pressure zone approach could achieve satisfying loading performance by proper arrangement of recess depth. The results of computer modeling showed that sliders designed under such a technology are of obvious advantage in achieving smooth head loading and stable flying status.

A mechanism to realize “proximity-on-demand” interface was proposed which utilizes a PZT to adjust the curvature (crown and camber) of the air bearing surface, thus to adjust the flying height. Slider prototyping and testing results confirmed the feasibility of such an adjusting technology. An improved structure of the active slider was also proposed in order to reduce the applied voltage. Results suggested that this improved slider structure is highly effective in terms of reducing the applied voltage to the range of -7 V~7 V to obtain the flying height adjustment of ±1 nm, which is enough to achieve “proximity-on-demand” interface for flying height of 2~4 nm. The proposed flying height adjusting structure slider is very simple and easy for fabrication by the standard slider fabrication process.

Testing technology is of great importance for such ultra-low flying height systems. Calibration parameters were carefully selected and an optical constant averaging method was developed to improve the testing accuracy in flying height testing process. The experimental studies of the flying height modulation and long-term flyability were conducted with sliders of flying height around 3.5 nm. Results showed that ultra-low flying height could be achieved with satisfying flyability and robustness.

The future research activities may be aimed to further increase the area density, say 5~10 Tera-bit per square inch. The flying height would be further reduced to less than 3 nm, which pushes the head disk interface technology towards intermittent contact or contact recording. With such extremely low flying height, the flying height testing would become more difficult. And many factors, such as intermolecular force and lubricant effects on the flying stability and head disk interface interactions must be taken into account.

Thus the future works may be focused on the following aspects:

- When the flying height reduces to lower than 3 nm, flying height testing would become a critical issue. The calibration process will become more and more difficult using unload technology to capture the minimum and maximum intensity of the calibration curve, because the intermittent contacts and the lubricant effects will deteriorate the smooth unload process and affect the repeatability of the calibration. Thus new calibration methods would be needed to improve the repeatability and accuracy of the calibration process for the flying height testing. Averaging of the optical constants on air bearing surface can improve the flying height testing accuracy around the testing point. But still it may be needed to capture the optical constants at every point on air bearing surface, thus to compensate the effects of optical constants on the testing flying height.
- No matter for intermittent contact or contact recording technology, the surface wear would be the major concerns with ultra small head disk spacing. Nano-

actuator would be an approach to significantly reduce the head-disk contact and surface wear. Now nano-actuators are focused on the flying height adjustment to increase the linear density or adjusting the head-arm or suspension to adjust the head positioning to increase the tracking density. These two adjusting technologies are separate. In the future work, if these two kinds of nano-actuators can be combined together, the movements in the flying height and tracking directions can be adjusted at the same time. Thus can increase both the linear and tracking density.

- With head disk spacing smaller than 3 nm, many factors which can be negligible with higher flying height must be taken into account. The intermolecular force between the air bearing surface and disk surface would become a critical issue when the head disk spacing reduces to a molecular level. Another aspect is to reduce the lubricant effects, such as lubricant modulation, depletion and transfer from the disk surface to air bearing surface, on the interface stability and robustness.

References

[1] Lyman, Peter and Hal R. Varian, “How Much Information”, Retrieved from http://www.sims.berkeley.edu/how-much-info, 2000.

[2] Ed Grochowski, “IBM areal sensity perspective”, Retrieved from http://ssdweb01.storage.ibm.com/hdd/technolo/grochows/g02j.jpg, 2002.

[3] D. A. Thompson and J. S. Best, “The future of magnetic data storage technology”, IBM, J. Res. Develop. Vol, 44, No. 3, pp. 311-322. 2000.

[4] IBM Company Website [Online], http://www.ibm.com, March 2001.

[5] Hitachi Global Storage Technology (HGST) report in 2003.

[6] S. X. Wang and A. M. Taratorin, Magnetic Information Storage Technology, Academic Press, San Diego, 1999.

[7] Ed Grochowski, Receive from http://www.hitachigst.com/hdd/technolo/overview/chart15.html.

[8] B. Liu, M. S. Zhang and S. K. Yu, “Femto slider: fabrication and evaluation”, IEEE Trans. Mag. Vol. 39, No.2, pp.909-914. 2003.

[9] G. E. Sommargren, “Flying height and topography measuring interferometer”, US Patent 5218424, 1993.

[10] P. De. Groot, “Optical gap measuring apparatus and method”, US Patent 5557399, 1996.

[11] C. A. Duran, “Error analysis of a multiwavelength dynamic flying height tester”, IEEE Trans. Magn. Vol. 32, pp. 3720-3722. 1996.

[12] P. De. Groot, “Interferometer and method for measuring the distance of an object surface with respect to the surface of a rotating disk”, US Patent 5600441, 1997.

[13] J. F. Xu and B. Liu, “Flying height modulation and femto slider designs”, Intermag 2003, AB-10, Boston, USA.

[14] J. A. Woollam Co., Inc, Website, http://www.jawoollam.com/m2000_home.html.

[15] H. Tanaka, H. Kohira and M. Matsumoto, "Effects of air-bearing design on slider dynamics during unloading process," IEEE Transactions on Magnetics, Vol. 37, No. 4, pp. 1818-1820. 2001.

[16] C. W. Strunk, C. C. Zahh and P. J. Sides, "Comparison of the Phase Metrics DFHT IV and Zygo Pegasus 2000 flying height testers," Appl. Optics, Vol. 40, No. 25, pp. 4507-4513. 2001.

[17] Bo Liu, Jin Liu, Hui Li et al., "Interface technology of 3 nm flying height and highly stable head-disk spacing for perpendicular magnetic recording", invited talk in PRMRC 2004.

[18] R.Wood, "The feasibility of magnetic recording at 1 Terabit per square inch", IEEE Trans. Magn. Vol 36, No 1, pp. 36-41. 2000.

[19] Pitchford, T., ''Head/Disk Interface Tribology Measurements for 100 Gb/in2,'' Proceedings of the Symposium on Interface Technology Towards 100 Gbit/in2, ASME, New York, TRIB-Vol. 9, pp. 83-90. 1999.

[20] Menon, A., ''Critical Requirements for 100 Gb/in2 Head/Media Interface,'' Proceedings of the Symposium on Interface Technology Towards 100 Gbit/in2, ASME, New York, TRIB-Vol. 9, pp. 1-9. 1999.

[21] Menon, A., ''Interface Tribology for 100 Gb/in2,'' Tribol. Int., 33, pp. 299-308. 2000.

[22] T. Watanabe and D. B. Bogy, "A study of the air bearing effect on the lubricant displacement using an optical surface analyzer", IEEE Trans. Magn., Vol. 38, No. 5, pp. 2138-2140. 2002.

[23] S. Wang, Ying C. Chang and J. J. Liu, "A novel drag test for observing lubricant redistribution due to head-disk interactions", IEEE Trans. Magn, Vol. 35, No 5, pp. 2448-2450. 1999.

[24] X. Ma, D. Kuo and J. Chen, "Effect of lubricant on flyability and read-write performance in the ultra-low flying regime", Journal of Trib. Vol. 124, pp. 259-265. 2002.

[25] X. Ma, H. Tang, and M. Stirniman,"The effect of slider on lubricant loss and redistribution", IEEE Trans. Magn., Vol. 38, No 5, pp. 2144-2146. 2002.

[26] L. Y. Zhu and D. B. Bogy, "Head-disk spacing fluctuation due to disk topography in magnetic recording hard disk files," Tribology and Mechanics of Magnetic Storage Systems, STLE Special Publication SP-26, pp. 160-167. 1989.

[27] W. Yao, D. Kuo and G. Jin, "Effects of disc micro-waviness in an ultra-high density magnetic recording system," Proc. Symp. Interface Technology Towards 100 Gbit/in^2 TRIB 9, pp. 31-37. 1999.

[28] Q. H. Zeng, B. H. Thornton and D. B. Bogy, "Flyability and flying height modulation measurement of sliders with sub-10 nm flying heights", IEEE Trans. Magn., Vol. 37, No. 2, pp.894-899. 2001.

[29] B. H. Thornton, D. B. Bogy and C. S. Bhatia, "The effects of disk morphology on flying height modulation: experimental and simulation," IEEE Trans. Magn., Vol. 38, No. 1, pp. 107-111. 2002.

[30] B. H. Thornton and A. Nayak, "Flying height modulation due to disk waviness of sub-5nm flying height air bearing sliders," Trans. of the ASME, Vol.124, pp. 762-770. 2002.

[31] B. Liu, M. Zhang and S. Yu, "Femto slider: fabrication and evaluation", IEEE Trans. Magn., Vol. 39, No 2, pp. 909-914. 2003.

[32] Shengkai Yu, Bo Liu and Jin Liu, “Analysis and optimization of dynamic response of air bearing sliders to disk waviness”, Tribology International 38, pp. 542-553. 2005.

[33] N. S. Tambe and B. Bhushan, “Durability studies of head-disk interface using padded and load/unload picosliders for magnetic rigid disk drives”, Wear, 255, pp. 1334-1343. 2003.

[34] B. Bhushan and Z. Zhao, “Friction/stiction and wear studies of magnetic thin-film disks with two polar perfluoropolyer lubricants”, IEEE Trans. Magn., 33, pp. 918-925. 1997.

[35] A. Jeff and F. Ian, “Predicting Glide Height Avalanche Performance from the Substrate Through Final Test”, THôT Technologies Report. 2002.

[36] Manual of Candela Instruments- Optical Surface Analyzer.

[37] A. Menon, “Critical requirements for 100 Gb/in2 head/media interface”, in Proc. Symp. Interface Technology Toward 100 Gbit/in2, vol. 9, pp. 1-9. 1999.

[38] S. K. Yu, B. Liu and J. Liu, “Analysis and optimization of dynamic response of air bearing sliders to disk waviness”, Tribology International 38, pp. 542–553. 2005.

[39] Q. H. Zeng and D. B. Bogy, “Stiffness and damping evaluation of air bearing sliders and new designs with high damping”, Journal of Trib. Vol. 121, pp. 341-346. 1999.

[40] Q. H. Zeng and D. B. Bogy, “Experimental evaluation of stiffness and damping of slider air bearings in hard disk drive”, Journal of Trib. Vol. 121, pp. 103-107. 1999.

[41] A. K. Menon and Z. E. Boutaghou, “Time–frequency analysis of tribological systems—part I: implementation and interpretation”, Tribology International Vol. 31, No.9, pp. 501-510. 1998.

[42] K. Ono, K. Takahashi and K. Iida, "Computer analysis of bouncing vibration and tracking characteristics of a point contact slider model over random disk surface", ASME J. Tribology Vol.121, No.3, pp.587-595.

[43] K. Ono, K. Takahashi and K. Iida, "Computer analysis of bouncing vibration and tracking characteristics of a single-degree-of-freedom contact slider model over a random disk surface", JSME Transaction Vol.63, No. 612 (1997-8), pp.2635-2642.

[44] K. Iida and K. Ono, "Analysis of bouncing vibrations of a 2-DOF model of tripad contact slider over a random wavy disk surface", Journal of Trib. Vol. 123, pp. 159-167. 2001.

[45] K. Lida and K. Ono, "Dynamic characteristics and design consideration of a tripad slider in the near-contact regime", Journal of Trib. Vol. 124, pp. 601-606. 2002.

[46] M. Yamane, K. Ono and K. Iida, "Analysis of tracking characteristics and optimum design of tri-pad slider to micro-waviness", ASME J.Tribology, Vol.125, No.1 (2003-1), pp.152-161.

[47] T. Kato, S. Watanabe and H. Matsuoka, "Dynamic characteristics of an in-contact headslider considering meniscus forces: part 2-application to the disk with random undulation and design conditions", Journal of Trib. Vol. 123, pp. 168-174. 2001.

[48] B. Liu, J. Liu and T. C. Chong, "Slider design for sub-3-nm flying height head-disk systems", Journal of Magnetism and Magnetic Materials 287 (2005), pp: 339-345.

[49] H. Kohira, H. Tanaka and J. G. Xu, "Development of novel slider for ultra low flying height", Nippon Kikai Gakkai Joho, Chino, Seimitsu Kiki Bumon Koenkai Koen Ronbunshu, pp. 224-228. 2005.

[50] I. Masanori, "Magnetic disk drive apparatus using contact start/stop mode and head load/unload mode", US patent 5602691, 1997.

[51] Shrinkle, Louis J., “Start/stop architecture for hard disk drive utilizing a magnetoresistive head and zone texture media”, US patent 6061198, 2000.

[52] M. Suk and T.R. Albrecht, “The evolution of load/unload technology,” Microsystem Technologies 8, pp. 10-16. 2002.

[53] T. R. Albrecht and F. Sai, “Load/Unload technology for disk drives,” IEEE Trans. on Magn., Vol. 35, No. 2, pp. 857-862. 1999.

[54] T. R. Albrecht, “Load/unload technology for disk drives”, IEEE Trans. Magn., Vol. 35, No. 2, pp. 857-862. 1999.

[55] Source: http://www.hitachigst.com/hdd/library/whitepap/load/load.htm

[56] Q. H. Zeng and D. B. Bogy, “Effects of certain design parameters on load/unload performance”, IEEE Trans. Magn., Vol. 36, No. 1, pp. 140-147. 2000.

[57] Q. H. Zeng and D. B. Bogy, “Slider air bearing designs for load/unload application”, IEEE Trans. Magn., Vol. 35, No. 2, pp. 746-751. 1999.

[58] Y. Hu, “Ramp-load dynamics of proximity recording air bearing sliders in magnetic hard disk drive”, ASME Journal of Tribology, Vol. 121, pp. 560-567. 1999.

[59] T. G. Jeong and D. B. Bogy, “Numerical simulation of dynamic loading in hard disk drives”, Transactions of the ASME, Vol. 115, pp. 370-375. 1993.

[60] Q. H. Zeng and D. B. Bogy, “The CML dynamic load/unload simulator”, Version 421.40, Computer Mechanics Laboratory, Department of Mechanical Engineering, University of California, Berkeley

[61] A. Mori, T. Munemoto and H. Otsuki, “A dual-stage magnetic disk drive actuator using a piezoelectric device for a high track density”, IEEE Trans. Magn., Vol. 27, No. 6, pp. 5298-5300. 1991.

[62] M. Kurita, T. Yamazaki and H. Kohira, “An active-head slider with a piezoelectric actuator for controlling flying height”, IEEE Trans. Magn., Vol. 38, No. 5, pp. 2102-2105. 2002.

[63] S. Koganezawa and T. Hara, “Development of shear-mode piezoelectric microactuator for precise head positioning”, Fujitsu Sci. Tech. J., 37. 2. pp. 212-219. 2001.

[64] N. Tagawa, H. Seki, and K. Kitamura, “Development of novel PZT thin films for active sliders based on head load/unload on demand systems”, Microsystem Tech. 8. pp. 133-138. 2003.

[65] Y. L. Lou, P. Gao and B. Qin, “Dual-stage servo with on-slider PZT microactuator for hard disk drives”, IEEE Trans. Magn., Vol. 38, No. 5, pp. 2183-2183. 2002.

[66] S. Koganezawa, Y. Uematsu, and T. Yamada, “Shear mode piezoelectric microactuator for magnetic disk drives”, IEEE Trans. Magn., Vol. 34, No. 4, pp. 1910-1912. 1998.

[67] Imamura and T. Koshikawa, “Transverse mode electrostatic microactuator for MEMS-based HDD slider,” IEEE Proc, MEMS Workshop, pp. 216-221. 1996.

[68] D. A. Horsley, M. B. Cohn, and A. Singh, “Design and fabrication of an angular microactuator for magnetic disk drives”, J. Microelectromechanical System, Vol. 7, No. 2, pp. 141-148. 1998.

[69] L. S. Fan, “Design and fabrication of microactuators for high density data storage”, IEEE Trans. Magn., Vol. 32, No. 3, pp. 855-1862. 1996.

[70] T. Hirano, L. S. Fan and T. Semba, “High-bandwidth HDD tracking servo by a moving-slider micro-actuator”, IEEE Trans. Magn., Vol. 35, No. 5, pp. 3670-3672. 1999.

[71] Y. Tang, S. X. Chen and T. S. Low, "Micro electrostatic actuators in dual-stage disk drives with high track density", IEEE Trans. Magn., Vol. 32, No. 5, pp. 3851-3853. 1996.

[72] C. R. Horowitz and R. T. Howe, "Design, fabrication, position sensing, and control of an electrostatically-driven polysilicon microactuator", IEEE Trans. Magn., Vol. 32, No. 1, pp. 122-128. 1996.

[73] D. A. Horsley, N. N. Wongkmet and R. Horowitz, "Precision positioning using a microfabricated electrostatic actuator", IEEE Trans. Magn., Vol. 35, No. 2, pp. 993-999. 1999.

[74] P. Machtle, R. Berger and A. Dietzel, "Integrated microheaters for In-situ flying height control of sliders used in hard-disk drives", IEEE 2001, pp: 196-199.

[75] T. R. Albercht, "Flying height adjustment for air bearing sliders", Patent No: US 6344949, 2002.

[76] CML steady definition, CML air bearing design program use's manual.

[77] M. T. Girard, "Gram load adjusting system for magnetic head suspensions", US Patent 5687597,1997.

[78] Bonin, Wayne A, "Integrated electrostatic slider fly height control", US Patent 6876509, 2005.

[79] M. S. Zhang, Y. S. Hor and G. Han, "Slider curvature adjustment through stress control", IEEE Trans. Magns., Vol. 38, No. 5, pp. 2162-2164. 2002.

[80] C. E. Yeack-Scranton, V. D. Khanna and K. F. Etzold, "An active slider for practical contact recording", IEEE Trans. Magn., Vol. 26, No. 5, pp. 2478-2483. 1990.

[81] T. Imamura, M. Katayama and Y. Ikegawa, "MEMS-Based integrated head/actuator/slider for hard disk drives", IEEE Trans. Magn., Vol. 3, No. 3, pp. 166-174. 1998.

[82] J. R. Phillips, "Piezoelectric technology primer", CTS Wireless Components, 4800 Alameda Blvd. N. E. Albuquerque, New Mexico 87113.

[83] J. S. Harrison. and Z. Ounaies., "Piezoelectric polymers", ICASE Report No. 43. 2001.